

AD-A243 552



✓ (2)

# NAVAL POSTGRADUATE SCHOOL

## Monterey, California



DTIC  
ELECTE  
DEC 20 1991  
C D

# THESIS

FLOW VISUALIZATION AND WAKE ANALYSIS FOR  
STANDARD AND MODIFIED CONFIGURATIONS OF THE  
AN/ALQ-78 ANTENNA POD

by

James F. Small

March 1991

Thesis Advisor:  
Co-Advisor:

S. K. Hebbar  
M. F. Platzer

Approved for public release; distribution is unlimited

91-18401



91 1218 151

UNCLASSIFIED

SECURITY CLASSIFICATION OF THIS PAGE

REPORT DOCUMENTATION PAGE				
1a. REPORT SECURITY CLASSIFICATION UNCLASSIFIED			1b. RESTRICTIVE MARKINGS	
2a. SECURITY CLASSIFICATION AUTHORITY			3. DISTRIBUTION/AVAILABILITY OF REPORT Approved for public release; distribution is unlimited	
2b. DECLASSIFICATION/DOWNGRADING SCHEDULE				
4. PERFORMING ORGANIZATION REPORT NUMBER(S)			5. MONITORING ORGANIZATION REPORT NUMBER(S)	
6a. NAME OF PERFORMING ORGANIZATION Naval Postgraduate School		6b. OFFICE SYMBOL (If applicable) AA	7a. NAME OF MONITORING ORGANIZATION Naval Postgraduate School	
6c. ADDRESS (City, State, and ZIP Code) Monterey, CA 93943-5000			7b. ADDRESS (City, State, and ZIP Code) Monterey, CA 93943-5000	
8a. NAME OF FUNDING/SPONSORING ORGANIZATION		8b. OFFICE SYMBOL (If applicable)	9. PROCUREMENT INSTRUMENT IDENTIFICATION NUMBER	
8c. ADDRESS (City, State, and ZIP Code)			10. SOURCE OF FUNDING NUMBERS	
			Program Element No.	Project No.
			Task No.	Work Unit Accession Number
11. TITLE (Include Security Classification) Flow Visualization and Wake Analysis for Standard and Modified Configurations of the AN/ALQ-78 Antenna Pod				
12. PERSONAL AUTHOR(S) James F. Small				
13a. TYPE OF REPORT Engineer's Thesis		13b. TIME COVERED From To	14. DATE OF REPORT (year, month, day) March 1991	15. PAGE COUNT 159
16. SUPPLEMENTARY NOTATION The views expressed in this thesis are those of the author and do not reflect the official policy or position of the Department of Defense or the U. S. Government.				
17. COSATI CODES			18. SUBJECT TERMS (continue on reverse if necessary and identify by block number)	
FIELD	GROUP	SUBGROUP		
			Three-Dimensional Aerodynamics	
			Vortex Shedding	
			Flow Visualization, Laser Sheet	
19. ABSTRACT (continue on reverse if necessary and identify by block number) A low-speed wind tunnel investigation was conducted to compare the aerodynamic flow field characteristics for standard and modified configurations of a 20 percent scale model of the AN/ALQ-78 electronic support measures system antenna pod. The modification consisted of replacing the standard quasi-conically shaped radome with a cylindrical radome and adapter collar. The research was requested by the Naval Air Systems Command (NAVAIRSYSCOM) as part of a risk and feasibility assessment in preparation for possible full-scale flight tests of the modified configuration. Wake flow visualization was conducted to determine the general characteristics of the flow field. Base pressure measurements were made to assess three-dimensional effects. The presence of coherent vortex shedding in the wake was investigated using a cross-probe constant temperature hot-film anemometer and spectrum analyzer. The Reynolds number varied from $4 \times 10^4$ to $6 \times 10^5$ with the upper value approximately equal to one-eighth that of the full-scale pod in flight. Asymmetric vortex shedding was visualized in the wakes of both configurations at subcritical Reynolds numbers. The modified configuration exhibited a pronounced region of quasi-two-dimensional flow during wake visualization and base pressure tests, indicating a significant increase in the aerodynamic forces acting on the pod structure. Spectral analysis of the hot-film output confirmed the presence of coherent vortex shedding in the wakes of both models at subcritical Reynolds numbers.				
20. DISTRIBUTION/AVAILABILITY OF ABSTRACT <input checked="" type="checkbox"/> UNCLASSIFIED/UNLIMITED <input type="checkbox"/> SAME AS REPORT <input type="checkbox"/> DTIC USERS			21. ABSTRACT SECURITY CLASSIFICATION UNCLASSIFIED	
22a. NAME OF RESPONSIBLE INDIVIDUAL S. K. Hebbar			22b. TELEPHONE (Include Area code) (408) 646-2997	22c. OFFICE SYMBOL AA/Hb

DD FORM 1473, JUN 86

Previous editions are obsolete.  
S/N 0102-LF-014-6603SECURITY CLASSIFICATION OF THIS PAGE  
UNCLASSIFIED

Approved for public release; distribution is unlimited.

Flow Visualization and Wake Analysis for  
Standard and Modified Configurations of the AN/ALQ-78 Antenna Pod

by

James F. Small  
Lieutenant Commander, United States Navy  
B.S., United States Naval Academy, 1978  
M.S., Naval Postgraduate School, 1990

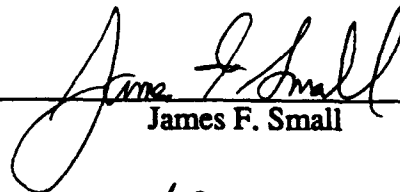
Submitted in partial fulfillment  
of the requirements for the degree of

AERONAUTICAL ENGINEER

from the

NAVAL POSTGRADUATE SCHOOL  
March 1991

Author:

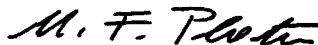


James F. Small

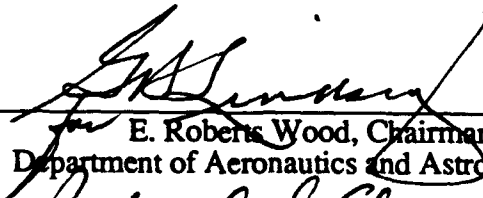
Approved by:



Sheshagiri K. Hebbar, Thesis Advisor



Max F. Platzer, Co-advisor and Second Reader



E. Roberts Wood, Chairman,  
Department of Aeronautics and Astronautics



Richard Elster  
Dean of Instruction

## ABSTRACT

A low-speed wind tunnel investigation was conducted to compare the aerodynamic flow field characteristics for standard and modified configurations of a 20 percent scale model of the AN/ALQ-78 electronic support measures system antenna pod. The modification consisted of replacing the standard quasi-conically shaped radome with a cylindrical radome and adapter collar. The research was requested by the Naval Air Systems Command (NAVAIRSYSCOM) as part of a risk and feasibility assessment in preparation for possible full-scale flight tests of the modified configuration. Wake flow visualization was conducted to determine the general characteristics of the flow field. Base pressure measurements were made to assess three-dimensional effects. The presence of coherent vortex shedding in the wake was investigated using a cross-probe constant temperature hot-film anemometer and spectrum analyzer. The Reynolds number varied from  $4 \times 10^4$  to  $6 \times 10^5$  with the upper value approximately equal to one-eighth that of the full-scale pod in flight. Asymmetric vortex shedding was visualized in the wakes of both configurations at subcritical Reynolds numbers. The modified configuration exhibited a pronounced region of quasi-two-dimensional flow during wake visualization and base pressure tests, indicating a significant increase in the aerodynamic forces acting on the pod structure. Spectral analysis of the hot-film output confirmed the presence of coherent vortex shedding in the wakes of both models at subcritical Reynolds numbers.



Authorization for	
None	<input checked="" type="checkbox"/>
DTIC Tab	<input type="checkbox"/>
Unannounced	<input type="checkbox"/>
Justification	
By	
Distribution	
Availability Codes	
Dist	Avail and/or Special
A-1	

## TABLE OF CONTENTS

I.	INTRODUCTION . . . . .	1
A.	BACKGROUND . . . . .	1
B.	LITERATURE REVIEW . . . . .	7
1.	General . . . . .	7
2.	Two-dimensional Vortex Shedding from Stationary Circular Cylinders . . . . .	8
3.	Strouhal Number . . . . .	10
4.	Two-dimensional Vortex Shedding from Oscillating Circular Cylinders . . . . .	12
5.	Three-dimensional Vortex Shedding . . . . .	13
C.	EXPERIMENTAL APPROACH . . . . .	14
II.	EXPERIMENTAL APPARATUS . . . . .	15
A.	WIND TUNNEL . . . . .	15
B.	ALQ-78 ANTENNA POD MODELS . . . . .	18
C.	MODEL SUPPORT . . . . .	20
D.	FLOW VISUALIZATION INSTRUMENTATION . . . . .	21
1.	Laser and Optics . . . . .	21
2.	Particle Seeding . . . . .	24
3.	Video Imaging System . . . . .	24
4.	Still Imagery . . . . .	26
E.	BASE PRESSURE INSTRUMENTATION . . . . .	26
F.	HOT-FILM ANEMOMETRY . . . . .	26
1.	Probe . . . . .	26
2.	Probe Support . . . . .	27
3.	Traversing System . . . . .	28
4.	Probe Cables . . . . .	30
5.	Hot-film Signal Processing and Display Equipment . . . . .	31
6.	Hot-film Signal Post-processing and Display Equipment . . . . .	32
7.	Coherent Signal Generation Devices . . . . .	35

III. EXPERIMENTAL PROCEDURES	37
A. WAKE VISUALIZATION	37
1. Laser Sheet Generation	37
2. Seed Optimization	37
3. Video Image Optimization	40
4. Still Photography Optimization	40
5. Image Recording	40
6. Turntable Alignment	42
B. BASE PRESSURE MEASUREMENTS	43
1. Base Pressure Coefficient	43
2. Yaw Sensitivity	44
3. Experimental Corrections	44
C. HOT-FILM ANEMOMETRY	46
1. CTA System Configuration	46
2. CTA System Optimization	46
3. Probe Support Dynamics	47
4. Quasi-two-dimensional Cylinder Investigation	48
5. Model Wake Investigation	49
IV. RESULTS AND DISCUSSION	50
A. QUASI-TWO-DIMENSIONAL CIRCULAR CYLINDER	50
1. Vortex Shedding Frequency	50
2. Boundary Layer Tripping Effects	50
3. Three-dimensional Effects	51
B. FLOW VISUALIZATION	52
1. Vortex Formation Region	52
2. Near Wake Region	57
C. BASE PRESSURE COEFFICIENT	61
1. Untripped Boundary Layer	62
2. Tripped Boundary Layer	62
3. Yaw Sensitivity	64
D. VORTEX SHEDDING FREQUENCY	64
1. Standard Configuration	64
2. Modified Configuration	65

V. CONCLUSIONS AND RECOMMENDATIONS . . . . .	69
A. CONCLUSIONS . . . . .	69
1. General . . . . .	69
2. Current P-3C Flight Restriction . . . . .	69
3. Test Instrumentation . . . . .	70
B. RECOMMENDATIONS . . . . .	71
REFERENCES . . . . .	72
APPENDIX A MODEL PRODUCTION DRAWINGS . . . . .	A-1
APPENDIX B DATA REDUCTION SPREADSHEET . . . . .	B-1
APPENDIX C SPECTRUM ANALYZER OUTPUT . . . . .	C-1
APPENDIX D FLOW VISUALIZATION IMAGERY . . . . .	D-1
APPENDIX E BASE PRESSURE COEFFICIENT PLOTS . . . . .	E-1
BIBLIOGRAPHY . . . . .	75
INITIAL DISTRIBUTION LIST . . . . .	79

## TERMS AND SYMBOLS

AN/ALQ-78	Original ESM system installed on the P-3C aircraft
AN/ALR-66(V)3	Improved P-3C ESM system
AN/APS-115B	Standard search radar system on the P-3C aircraft
AN/APS-137(V)	ISAR system with target imaging capability, installed on some P-3C aircraft
CCD	Charge coupled device
$C_{pB}$	Base pressure coefficient
CTA	Constant temperature anemometer
D, d	Reference length, cross-wake dimension of cylinder and model radomes
D', d'	Distance between free shear layers in a wake
ECP	Engineering change proposal
ESM	Electronic support measures
EW	Electronic warfare
FFT	Fast Fourier transform
$f_s$	Vortex shedding frequency
$g_c$	Proportionality constant
H <sub>2</sub> O	Water
ISAR	Inverse Synthetic Aperture Radar
LASC	Lockheed Aeronautical Systems Company, formerly LCC
LCC	Lockheed California Company
NAVAIRSYSCOM	Naval Air Systems Command
NAVAIRTESTCEN	Naval Air Test Center



NPS	Naval Postgraduate School
$P_{atm}$	Atmospheric pressure
$P_{mod}$	Model base static pressure
$P_2$	Wind tunnel test section static pressure
P-3C	Lockheed <i>Orion</i> , four-engine turbo-prop, land-based maritime patrol aircraft
$q$	dynamic pressure
$R$	Gas constant for air
$Re$	Reynolds number
R. H.	Relative humidity
RMS	Root mean square
$S$	Strouhal number
$S'$	Universal Strouhal number
SC	Signal conditioner
SLR	Single lens reflex
SNR	Signal-to-noise ratio
$T$	Temperature
$U_{\infty}$	Wind tunnel freestream velocity
$U_{actual}$	$U_{\infty}$ corrected for tunnel blockage
$\Delta p$	Pressure difference
$\epsilon$	Wind tunnel blockage correction factor
$\rho$	Wind tunnel air density
$\rho_{dry}$	$\rho$ corrected for temperature
$\rho_{obs}$	$\rho_{dry}$ corrected for humidity
$\omega_o$	Natural frequency

## ACKNOWLEDGEMENT

This thesis was sponsored by the Naval Air Systems Command (AIR-546D3B) in support of ongoing P-3C weapons system upgrades. Special thanks are owed to CDR Tom McKannon, who provided invaluable assistance as my NAVAIRSYSCOM point of contact.

My deepest gratitude is extended to Professors S. K. Hebbar and M. F. Platzer, my thesis advisor and co-advisor, for their guidance, encouragement, and sincere interest in completing a project of significant personal importance to me. I would like to express my appreciation to Professor R. M. Howard for his support and advice.

I would also like to thank the professionals of the Department of Aeronautics and Astronautics, in particular Mr. Alan McGuire, Mr. Ronald Ramaker, and Mr. Jack King for their precise and timely technical assistance. The expeditious fabrication of very high quality wind tunnel models was particularly helpful.

Mr. Ivan Sachs of the Lockheed Aeronautical Systems Company provided key assistance on P-3 wing flutter characteristics and was a valuable source of corporate knowledge concerning the structural dynamics of P-3 wing stores. Mr. Sachs also supplied copies of Lockheed flight test reports on the ALQ-78 pod vibrations.

Mr. Larry Meyn, of the NASA Ames Research Center, generously provided hot-film probes, DISA anemometry equipment, a spectrum analyzer, and a video copy processor, without which this project could not have been completed.

I am indebted to Joseph Chlebanowski, David Leedy, and John Sommers for the development and refinement of a working laser sheet flow visualization system which paved the way for my successful flow visualization studies.

## I. INTRODUCTION

### A. BACKGROUND

The U. S. Navy P-3C maritime patrol aircraft underwent a major electronic warfare (EW) upgrade during the mid-1980's in which the AN/ALQ-78 electronic support measures (ESM) system was replaced by the AN/ALR-66(V)3. The ALR-66(V)3 installation included wingtip mounted receiving antennas for threat warning and a modification to the forward AN/APS-115B radar antenna. This modification allowed the radar antenna to serve as both a high gain surveillance and targeting antenna for the ESM system and as a standard search radar antenna. The pod mounted ALQ-78 antenna [Figs. 1 and 2] was removed from the aircraft.

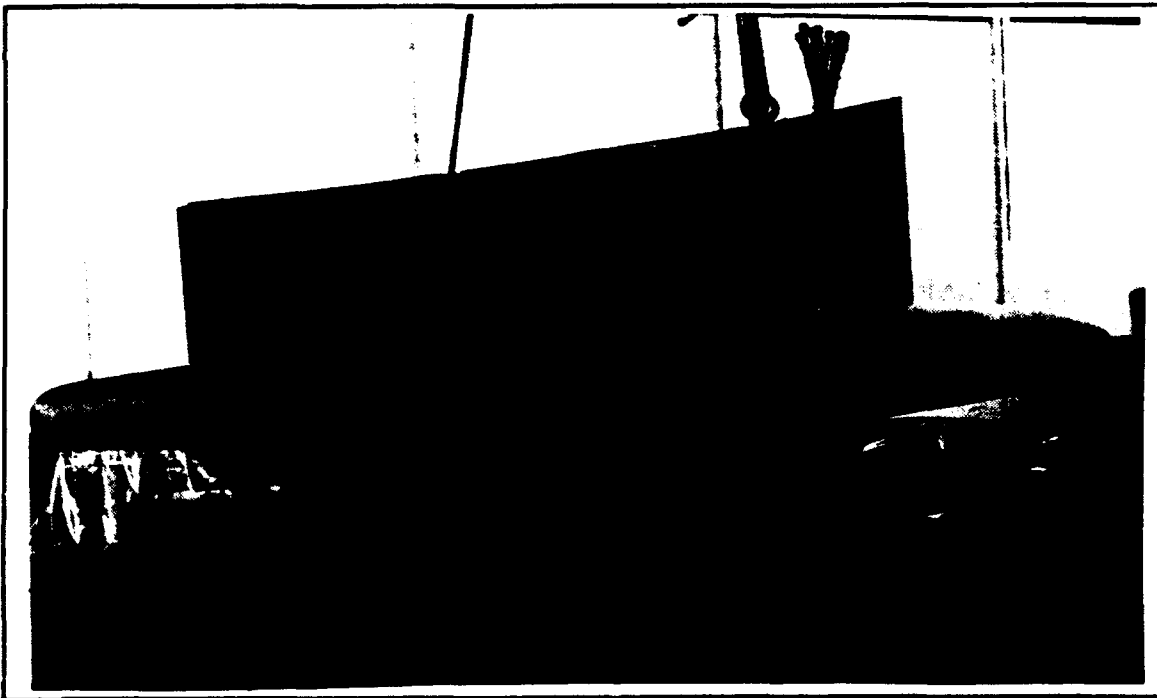


**Figure 1. Standard AN/ALQ-78 Antenna Pod**

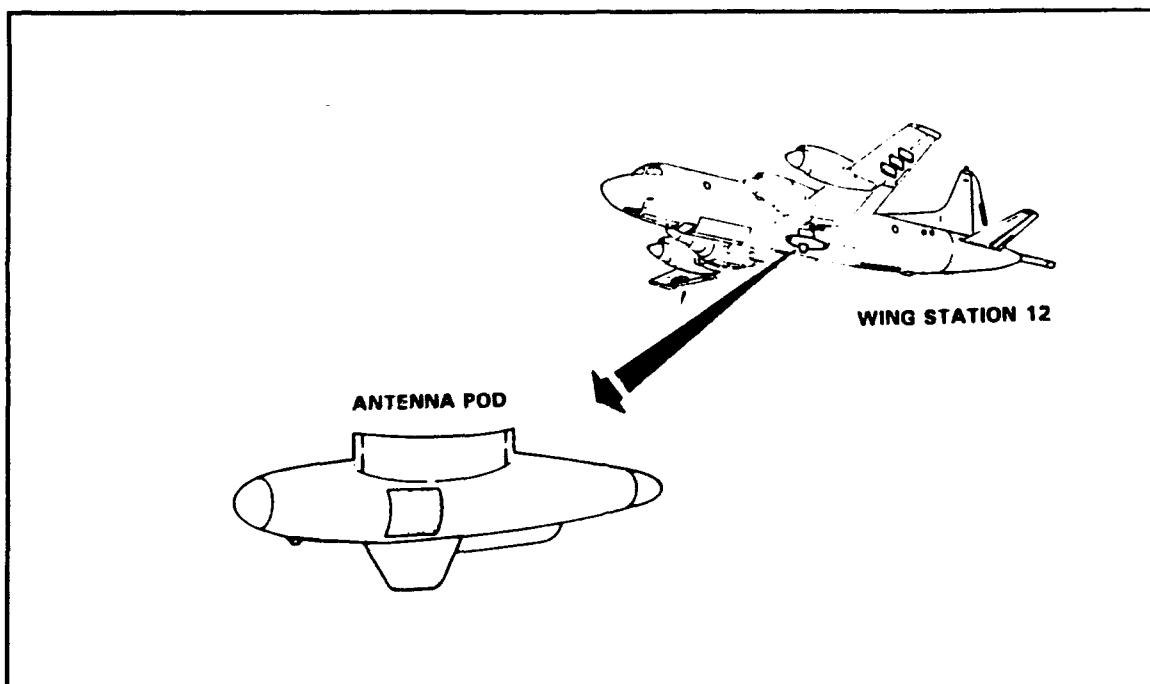


**Figure 2. Location of the AN/ALQ-78 Antenna Pod on the P-3C Aircraft [Rei. 1]**

Developmental and operational testing revealed performance and reliability deficiencies in the modified APS-115B antenna which were verified in service use. An additional drawback of this design is that it is incompatible with the AN/APS-137(V) inverse synthetic aperture radar (ISAR) antenna, precluding installation of the improved ESM system on ISAR equipped aircraft. The Naval Air Systems Command (NAVAIRSYSCOM) received two unsolicited engineering change proposals (ECP's) from industry offering technical solutions to these deficiencies employing proven hardware. Both proposals use a modified ALQ-78 antenna pod with a new antenna, an enlarged radome with improved electrical transmission efficiency, and associated antenna electronics. The new equipment in these proposals had previously been accepted for use in other aircraft programs. Those applications involved mounting the radomes directly on the

fuselage, however; and uncertainty over the aerodynamics and structural dynamics of the pod mounted version was viewed as a technical risk.

NAVAIRSYSCOM requested this study as part of a risk and feasibility assessment in preparation for possible technical evaluation of a modified pod on a Naval Air Test Center (NAVAIRTESTCEN) P-3C aircraft. The technical evaluation will consist of system performance tests for the antenna/radome combination and aerodynamic tests to clear the pod for unrestricted carriage. The P-3C maximum airspeed envelope is shown in Figure 3.

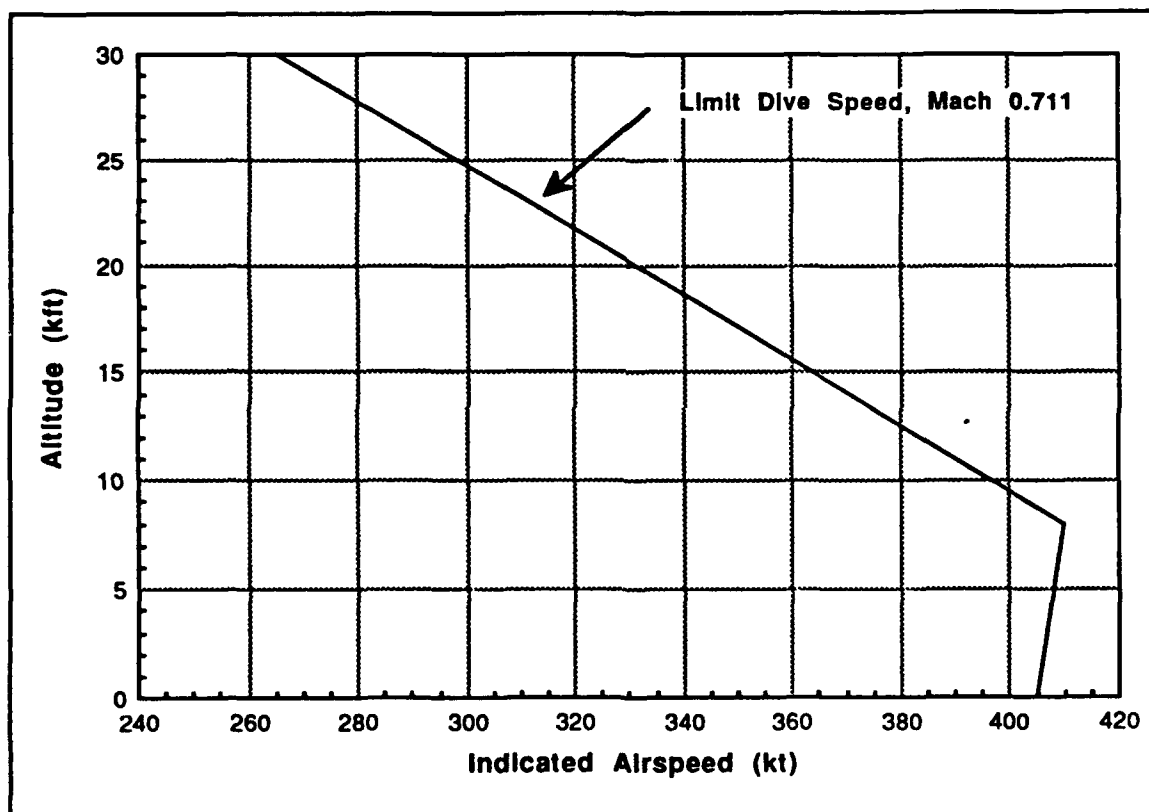


**Figure 3. P-3C Maximum Airspeed Envelope [Ref. 2]**

NAVAIRSYSCOM was particularly interested in determining the feasibility of proceeding directly from scale model aerodynamic tests in a low-speed facility to full-scale engineering flight tests. The pod structure and antenna components have specification

limits for vibration and acceleration which are met by the unmodified configuration. Additionally, the P-3C wing is subject to flutter excitation resulting in catastrophic failure, which places stringent limits on the aerodynamic characteristics and structural dynamics of wing carried stores. Discussions with the Lockheed Aeronautical Systems Company (LASC) flutter group indicated that the small mass of the pod, coupled with the inboard mounting location, eliminates the risk of wing flutter due to pod dynamics [Ref. 3]. Using the standard configuration as an acceptable baseline, this study assessed the aerodynamic effects of the modified configuration using a direct comparison of scale model wake characteristics under identical test conditions. No attempt was made to model the pod structural dynamics or wing flutter response.

The General Instrument Corporation, Government Systems Division ECP was chosen for this study because complete engineering drawings were available for designing the wind tunnel model. The significant aerodynamic feature of the proposed design is the large cylindrical radome and associated adapter collar which mates the radome to the existing structure [Fig. 4]. A comparison of the frontal areas presented by the two radomes is shown in Figure 5.

LASC, formerly the Lockheed California Company, was the principal contractor for the P-3C program. LASC conducted scale model wind tunnel tests and full-scale flight tests on the ALQ-78 pod after vibrations were reported in P-3C aircraft equipped with the ALQ-78 [Refs. 4 through 11]. These tests revealed significant oscillatory stresses and accelerations acting on the pod over a range of flight speeds. The most significant oscillations occurred at frequencies of 30Hz and in a band from approximately 83Hz to 97Hz. The pod and pylon structures were stiffened and the LASC test engineers noted that the 30Hz vibrations persisted in a narrow band of Mach numbers around 0.57. They alluded to compressibility effects as a possible source of the oscillations [Ref. 6] and concluded that the phenomenon occurred at a discrete Mach number of 0.57. A ground

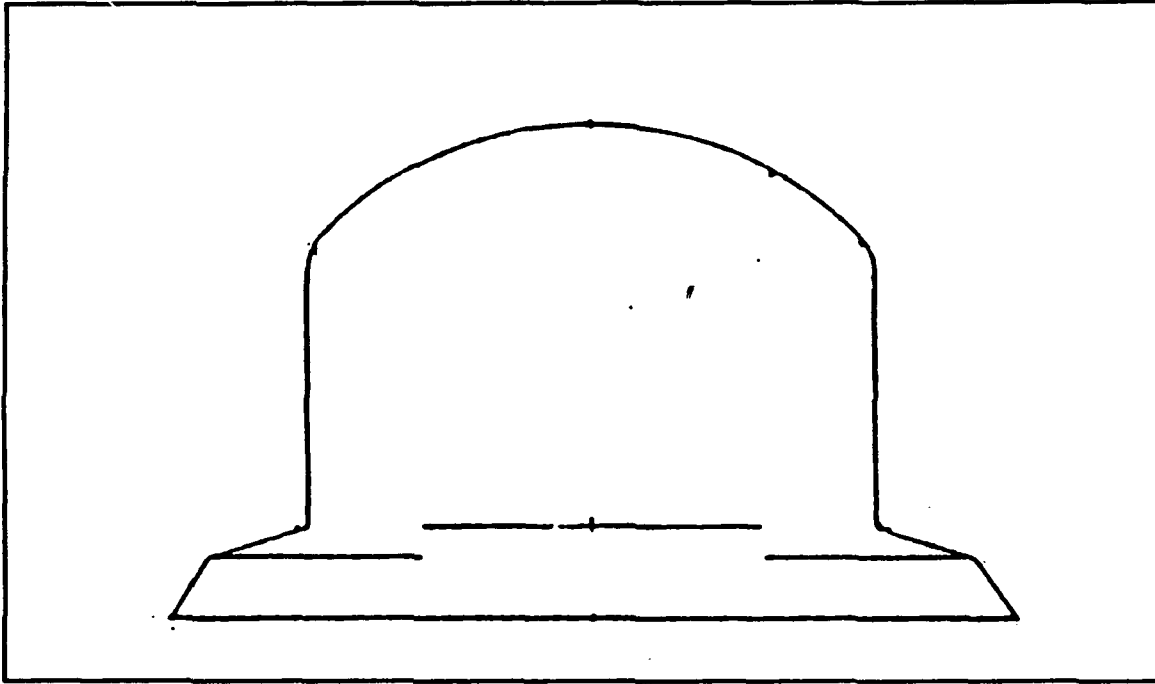


**Figure 4.** Side View of the Modified Radome

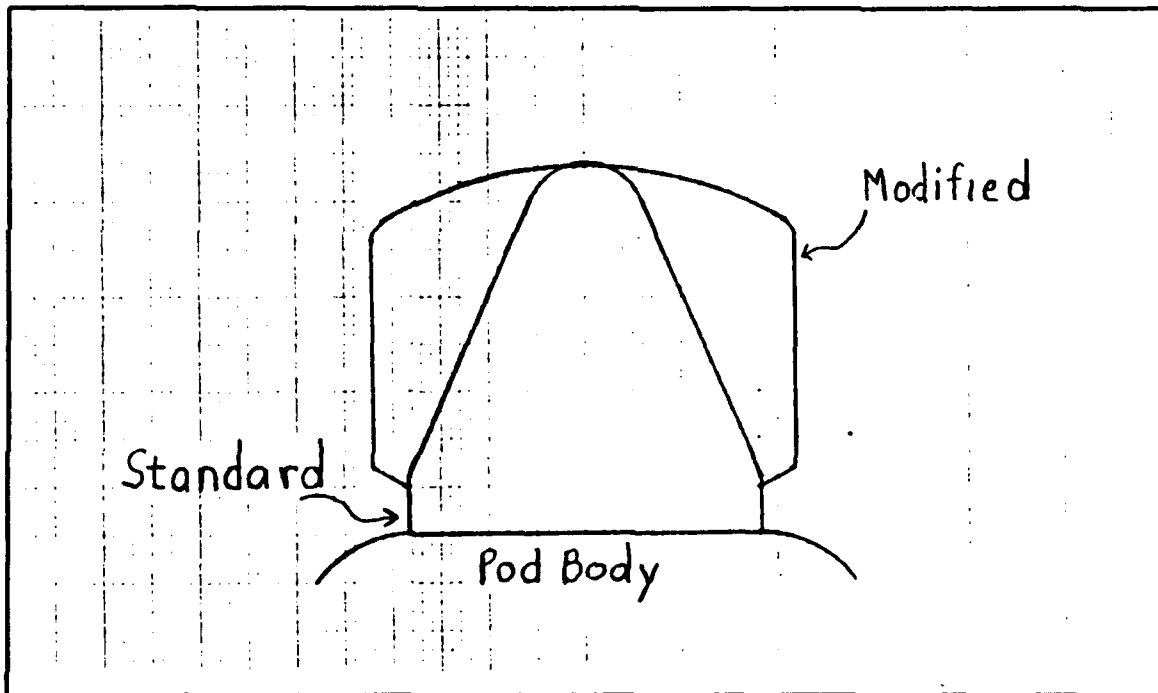


**Figure 5.** Frontal Area Comparison of the Two Radomes.

vibration test was conducted on two different pods installed on production aircraft. These tests documented a pod structural resonant frequency at 30Hz. Subsequent LASC analysis of flight test data indicated that structural oscillations at 90Hz may have excited the 30Hz resonant mode of the pod to produce large amplitude stresses and accelerations at 30Hz.

LASC evaluated a number of candidate solutions to the vibration problem. These included vertical strakes mounted on the radome in various configurations, a large fairing behind the radome, and several different splitter plates. The method used was purely empirical and large splitter plates were found to be the most effective in suppressing vibration. These large splitter plates were more susceptible to 68Hz harmonic vibrations from the constant speed propeller slipstream, however, and were discarded in favor of a small ventral fin [Ref. 12]. This fin did not completely eliminate the 30Hz vibrations and the aircraft flight manual recommends that pilots avoid extended operations at Mach 0.57 when the ALQ-78 pod is installed [Ref. 13].

The LASC flight test results were analyzed in preparation for the experiments described in this thesis. The 30Hz vibrations were actually sustained over a range of Mach numbers, rather than a discrete Mach number, from 0.567M to 0.583M at altitudes from 11,000ft to 15,000ft. These correspond to true airspeeds ranging from 358kt to 366kt (605ft/sec to 619ft/sec). Figure 6 shows the LASC flight test data overlaid on the P-3C maximum range cruise operating envelope. The Mach 0.57 flight restriction is also indicated.

The existence of large oscillatory stresses and accelerations over a narrow range of true airspeeds is consistent with asymmetric vortex shedding induced vibration of a structure at its resonant frequency. The purpose of this research was to investigate these vortices using 20% scale models of the two AN/ALQ-78 antenna pod configurations in the Naval Postgraduate School (NPS) 32x45 in. low-speed wind tunnel.



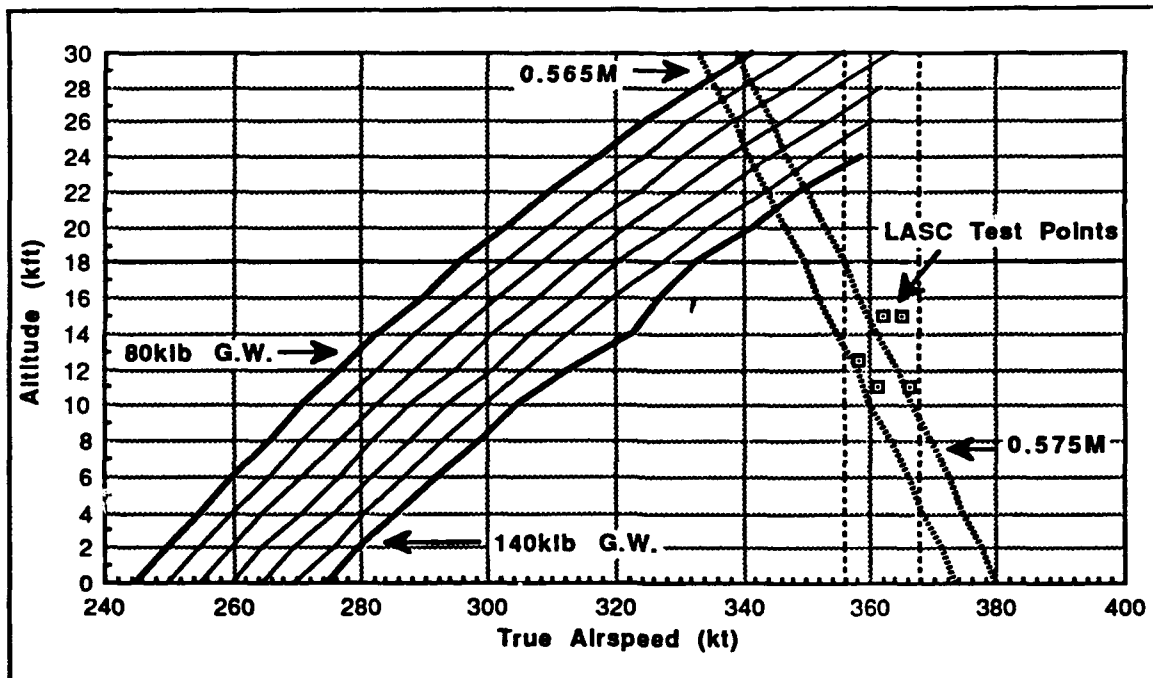


**Figure 6. P-3C Maximum Range Cruise Envelope with Flight Restriction and LASC Vibration Test Points**

## **B. LITERATURE REVIEW**

### **1. General**

The nature of the vibrations described in the LASC reports indicates that asymmetric vortex shedding was the principal cause mechanism. Of particular significance was the effectiveness of classic vortex suppression techniques applied to the pod vibration problem. This experiment was designed to investigate vortex shedding in the ALQ-78 pod's turbulent wake using proven techniques.

The literature contains a wealth of information concerning the vortex shedding phenomenon and experimental procedures for two-dimensional bluff body wakes. There are comparatively few results published for three-dimensional bodies, particularly those with complex shapes. Sarpkaya [Ref. 14] reviewed vortex-induced structural oscillations and included an extensive listing of applicable literature published through mid-1979.

Bearman and Graham [Ref. 15] also provided a comprehensive list of references on the subject. The bibliography lists the resources reviewed in preparation for this research. Not all material was directly cited in this thesis, however the readings provided valuable insight into vortex shedding phenomena.

## 2. Two-dimensional Vortex Shedding from Stationary Circular Cylinders

Periodic vortices were identified in cylinder wakes by Benard in 1908 [Ref. 16]. The formation of a stable vortex street was discovered by von Karman in 1912 [Ref. 16]. The vortex formation is due to boundary layer separation on the rearward half of the body caused by adverse pressure gradients in this region. Figure 7 shows a sequence of pressure fields and vortices during vortex formation. The nature of the vortex street is highly influenced by Reynolds number and four Reynolds number regimes have been identified. The vortex street is completely laminar in the lowest Reynolds number regime

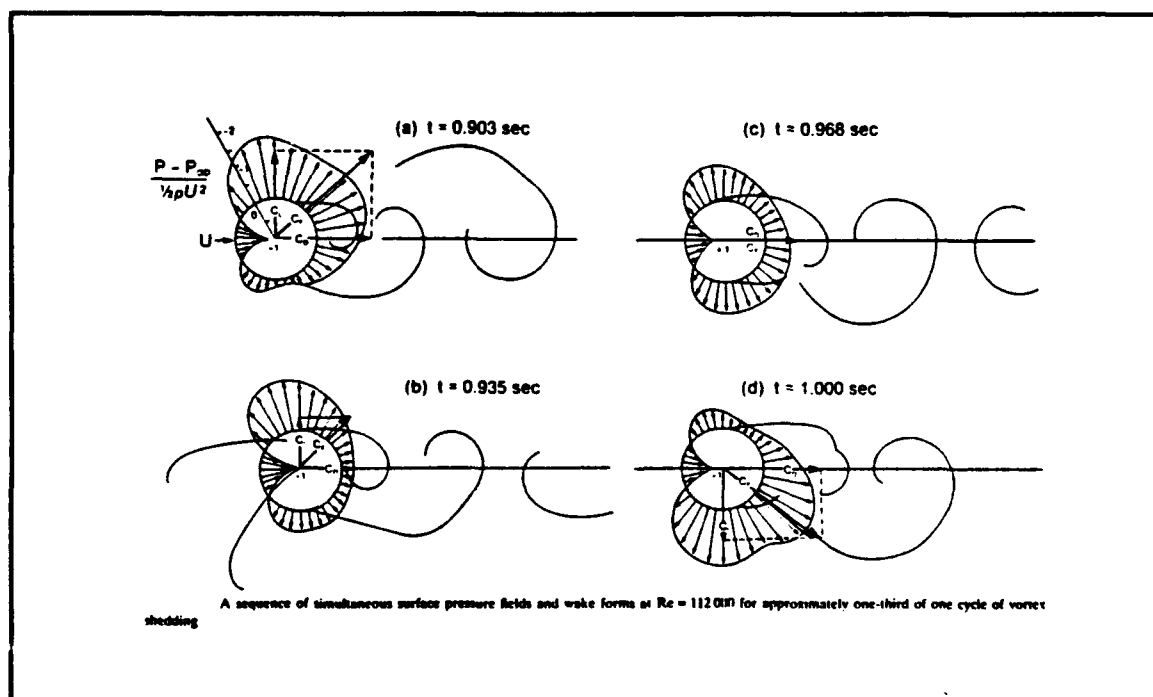


**Figure 7. Surface Pressure Fields During Vortex Formation [Ref. 16]**

( $Re \leq 150$ ). The wake transitions to a turbulent vortex street for  $150 \leq Re \leq 300$ . This is followed by the subcritical regime ( $300 \leq Re \leq 1.5 \times 10^5$ ) characterized by strong periodic vortex shedding. Regular vortex shedding is disrupted in the transitional regime ( $1.5 \times 10^5 \leq Re \leq 3.5 \times 10^6$ ) indicated by a broadened spectrum of shedding frequencies. Strong periodic vortex shedding reappears in the supercritical regime ( $Re > 3.5 \times 10^6$ ). Figure 8 shows the wake patterns in the various Reynolds numbers ranges.

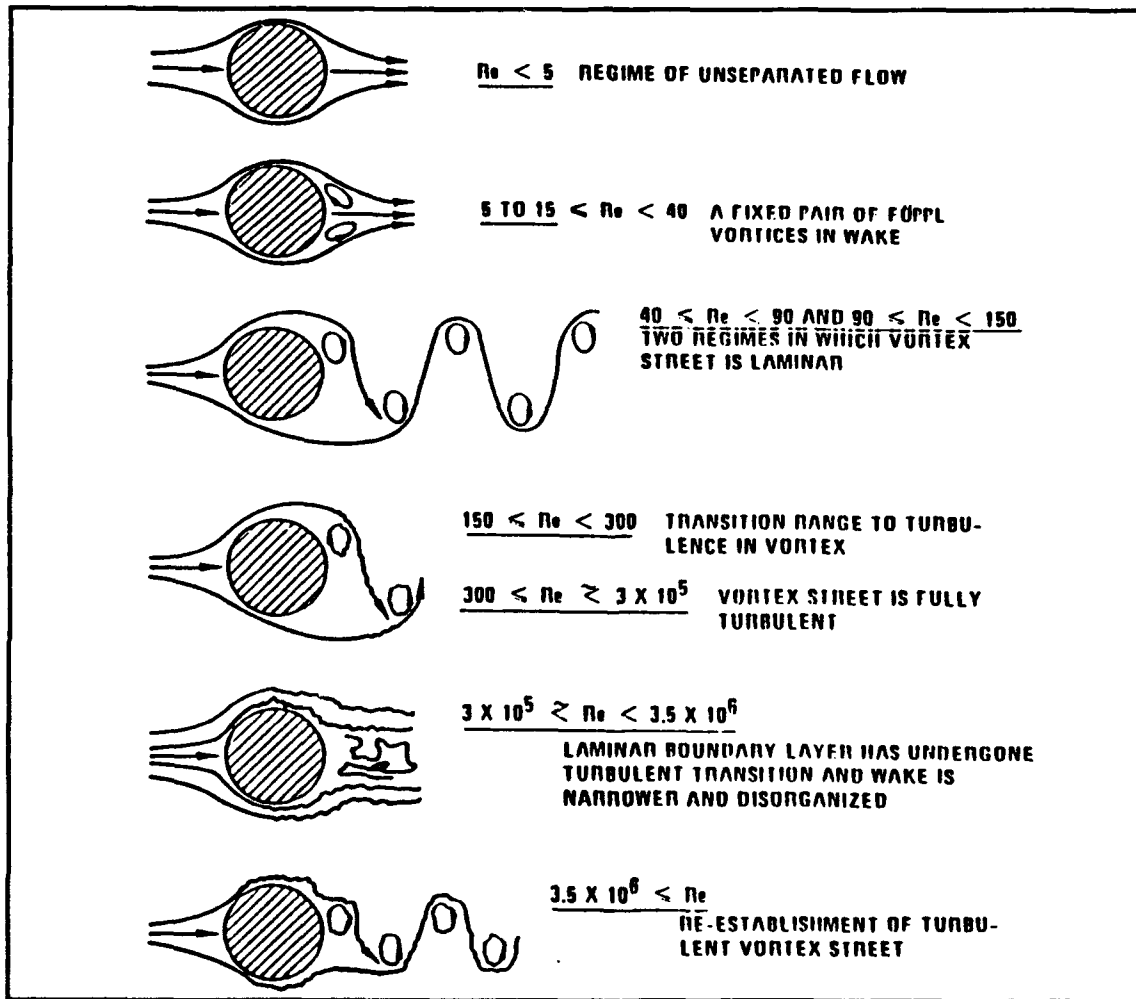


**Figure 8.** Wake Patterns for Different Reynolds Number Flow Regimes [Ref. 16]

### 3. Strouhal Number

The Strouhal number is a non-dimensional constant relating vortex shedding frequency to freestream velocity and the diameter of the two-dimensional cylinder. It is widely used to characterize a particular flow and to compare different flows. The relationship is given by:

$$f_s = \frac{SU}{D} \quad (1)$$

where  $f_s$  = Vortex shedding frequency (Hz)

$S$  = Strouhal number

$U$  = Freestream velocity (ft/sec)

$D$  = Cylinder diameter (ft)

The Strouhal number is not a pure constant. Figures 9 and 10 show the variation of Strouhal number with Reynolds number and body shape. Numerous researchers have noted that the vortex street patterns of two-dimensional bluff bodies are nearly identical, regardless of the body shape. Roshko [Ref. 17] defined a new Strouhal number based on the distance between free shear layers in the wake, rather than on the body diameter:

$$f_s = \frac{S'U}{D'} \quad (2)$$

where  $f_s$  = Vortex shedding frequency (Hz)

$S'$  = New Strouhal number

$U$  = Freestream velocity (ft/sec)

$D'$  = Distance between free shear layers (ft)

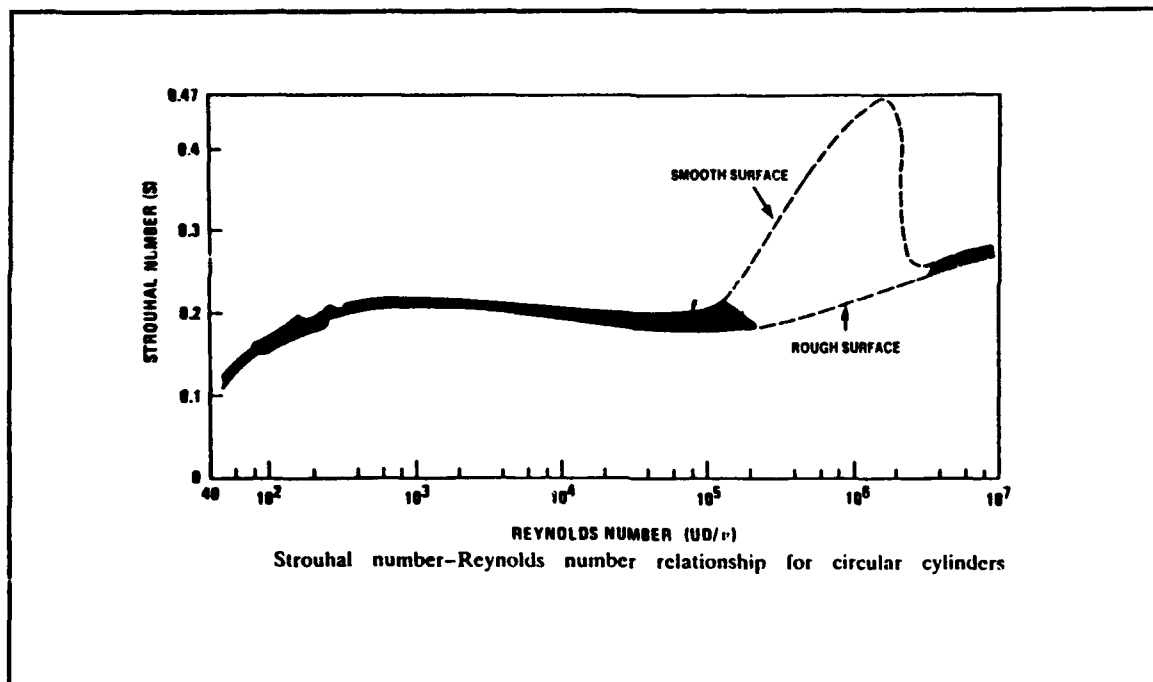


Figure 9. Strouhal number vs. Reynolds number [Ref. 16]

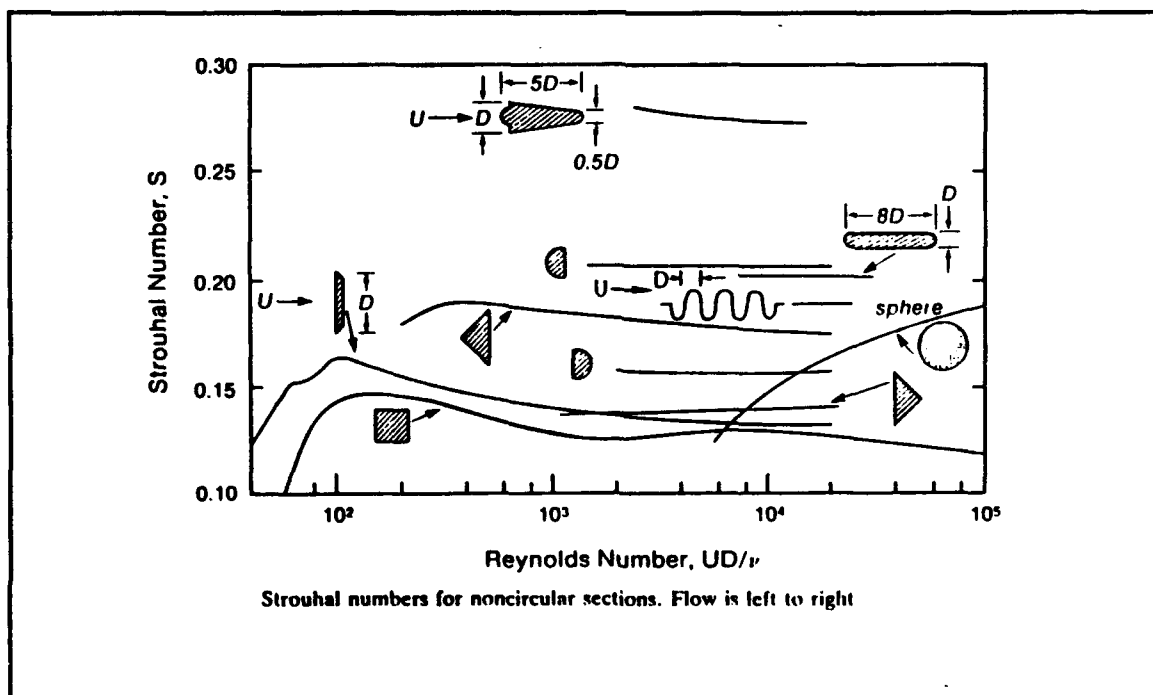


Figure 10. Strouhal numbers for different body shapes [Ref. 16]

Experiments have verified that  $S'$  is nearly constant at approximately 0.2 for a wide variety of body shapes and flow conditions. This concept has been expanded into a wake Strouhal number, or universal Strouhal number, expressed in terms of readily measurable quantities. Calvert [Ref. 18] defined a wake Strouhal number for flow past three-dimensional cones which used wake diameter measured using a hot-wire anemometer and a base pressure coefficient:

$$S^* = S \sqrt{1 - C_{PB}} \left( \frac{d'}{d} \right) \quad (3)$$

where  $S^*$  = Wake Strouhal number  
 $S$  = Strouhal number  
 $C_{PB}$  = Base pressure coefficient  
 $d'$  = Wake diameter (ft)  
 $d$  = Cylinder diameter (ft)

Calvert found the wake Strouhal number to be approximately 0.19 for six different cone configurations.

#### **4. Two-dimensional Vortex Shedding from Oscillating Circular Cylinders**

The vortex shedding phenomenon is considerably more involved for structures which are free to oscillate. Bishop and Hassan [Ref. 19] conducted an extensive study of two dimensional flow past stationary and oscillating cylinders under identical conditions. The complex interaction between the flow field and structural dynamics is beyond the scope of this research, however, it is almost certainly a significant factor for the full-scale antenna pod mounted on the aircraft. Of particular interest is the synchronization of vortex shedding frequency ( $f_s$ ) with the natural frequency of the structure ( $\omega_0$ ). Bishop and

Hassan observed that as the flow velocity approached the value at which  $f_s$  matched  $\omega_o$ , the wake synchronized with the structure and large amplitude oscillations resulted.

Additionally, it was noted that  $f_s$  was "lost" and "lock-in" occurred with vortices shedding at  $\omega_o$  over a range of speeds. Lock-in correlated with an increase in the two-dimensionality of the flow around the cylinder. Lock-in was also noted when  $f_s$  and  $\omega_o$  were harmonically related. Blevins [Ref. 20] provides a very concise discussion of the effects of cylinder motion on the wake.

### **5. Three-dimensional Vortex Shedding**

Calvert [Ref. 18] conducted measurements in the three-dimensional wakes of cones at a Reynolds number of approximately  $5 \times 10^4$ . He observed that the wake was definitely periodic, however the periodicity was not nearly as marked as that for two-dimensional flows at the same Reynolds number. Fiedler and Wille [Ref. 21] investigated the wakes of truncated circular cylinders with aspect ratios of 4 and 8. Working in a Reynolds number range from  $40 \times 10^4$  to  $2.4 \times 10^5$ , they found that the flow over the top of the cylinder provided a downwash into the vortex formation region which tended to suppress vortex shedding. They also noted that increasing aspect ratio and Reynolds number produced flows that were more two-dimensional. Gaster [Ref. 22] studied the wakes of slender cones, perpendicular to the freestream, at very low Reynolds numbers ( $150 \leq Re \leq 600$ ). He observed that the vortices propagated toward regions of higher Reynolds number and tended to concentrate the flow energy toward the base of the cone. Achenbach [Ref. 23] investigated the wakes of spheres at Reynolds numbers from 400 to  $5 \times 10^6$ . He obtained Strouhal numbers varying from 0.13 at very low Reynolds number to 0.20 at a Reynolds number of  $3.7 \times 10^5$ . Vortex shedding was not evident at Reynolds numbers above  $3.7 \times 10^5$ .

## **C. EXPERIMENTAL APPROACH**

A thorough review of the vibration problems documented by LASC, coupled with the results achieved by other investigations of similar wake phenomena, lead to the following set of basic assumptions, experimental approach and limitations.

1. Asymmetric vortex shedding is the principal cause of the ALQ-78 antenna pod vibrations.
2. Similar vortex shedding will be evident at Reynolds numbers achievable in the NPS low-speed wind tunnel.
3. The modified pod will also exhibit vortex shedding.
4. The vortex shedding measured will share many of the characteristics documented by other research.
5. The generalization of the wind tunnel results to the full-scale aircraft will be limited by Reynolds number. The wind tunnel Reynolds Number will be one-eighth or less than that for the full-scale aircraft.
6. Compressibility effects cannot be investigated with the facilities available at NPS.
7. The compressibility contribution to the standard configuration vibrations can be readily determined through a simple flight test.



## II. EXPERIMENTAL APPARATUS

### A. WIND TUNNEL

The experiments were conducted in the NPS 32x45in. low-speed wind tunnel [Ref. 24]. The tunnel is a closed-circuit, single return type designed by the Aerolab Development Company of Pasadena, California and was installed at the school in the mid-1950's. The tunnel arrangement is shown in figure 11.

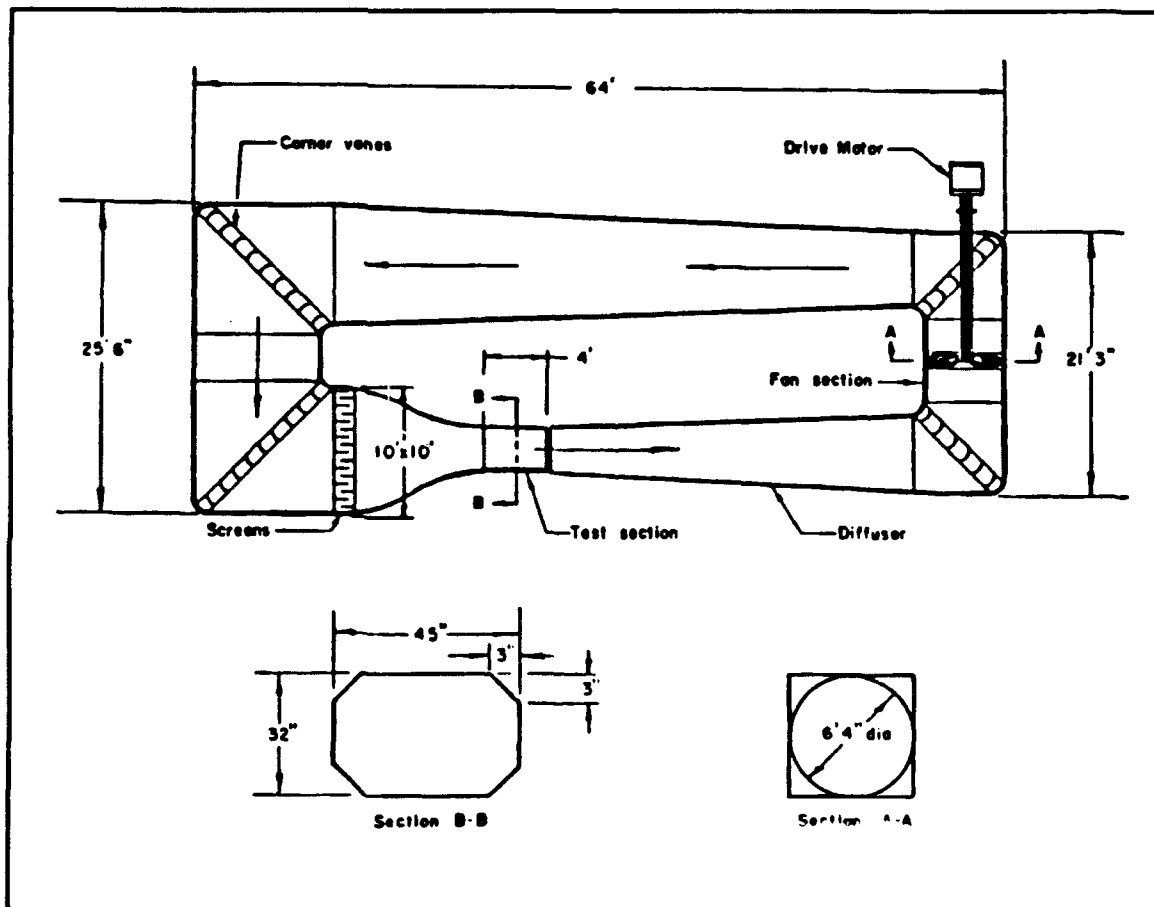


Figure 11. Naval Postgraduate School Low Speed Wind Tunnel Arrangement

The tunnel is powered by a 100hp electric motor coupled to a three-bladed variable pitch fan by a four-speed International truck transmission. The transmission was added after installation to obtain efficient operation for tunnel speeds up to approximately 180mph. The fan is shrouded by a circular duct with a 6ft 4in. diameter. Eight stator blades are located immediately downstream of the fan to remove the fan induced swirl, thus reducing losses and turbulence in the flow.

The tunnel cross section incorporates corner fillets which alleviate synergetic boundary layer effects at the wall intersections. The cross section gradually expands as the flow moves from the fan, through three sets of 90° corner vanes, to a 10×10ft settling chamber. The settling chamber includes two fine wire mesh turbulence screens separated by approximately 6in. These are designed to improve the flow quality by breaking large turbulent fluctuations into small, low energy, fluctuations which are ultimately dissipated as heat. This tunnel has a turbulence factor of 1.04. The settled flow is then smoothly accelerated into the test section through a 10:1 contraction cone.

The 32×45in. test section is 48in. long with slightly divergent walls to counter the effective contraction due to boundary layer growth. Transparent viewing panels are installed in the test section sidewall access doors and in the upper wall. Model illumination is provided by fluorescent lights in the corner fillets. A reflection plane installed on the lower wall provides model attachment points on a remotely controlled turntable with 0.1° angular resolution for rotations about the vertical axis. The reflection plane and corner fillets reduced the cross sectional area to approximately 1251in.<sup>2</sup>.

The test section is designed to operate at atmospheric pressure, resulting in pressures above atmospheric throughout the rest of the circuit. A breather slot, extending completely around the cross section, is installed immediately downstream of the test section. The slot allows air into the circuit to compensate for leakage losses elsewhere, thus ensuring uniform atmospheric pressure in the test section.

A diffuser is installed downstream of the test section to decelerate the flow, converting kinetic energy into pressure and reducing friction losses. A heavy gauge wire screen is installed in the diffuser to prevent damage to the turning vanes and fan in the event of a model failure during tunnel operation. After exiting the diffuser, the flow passes through a fourth set of 90° turning vanes and re-enters the fan.

Tunnel flow instrumentation consists of a settling chamber temperature gauge, a static pressure difference measurement network, and a pitot-static probe. The temperature gauge, located on the settling chamber outer wall, senses settling chamber temperature with a thermocouple and displays the temperature in °F. There are four static pressure taps in the settling chamber wall. These are connected to a common manifold to reduce the effect of local variations. Four additional taps are located in the test section and are also connected to a common manifold. Both manifolds are connected to a precision water manometer and to a pressure transducer with a digital display. These instruments measure the static pressure difference between the settling chamber and test section and, when calibrated, this arrangement provides accurate test section velocity indications. The pitot-static probe, located in the contraction cone upstream of the test section, is connected to an airspeed indicator which provides an approximate test section velocity. Actual test section velocity was calculated using the following equation [Ref. 25]:

$$U_{\infty} = \sqrt{\frac{(2)(2.046)\Delta p}{(0.8881)\rho}} \quad (4)$$

where  $U_{\infty}$  = Velocity (ft/sec)  
 2.046 = Units conversion factor  
 $\Delta p$  = Static pressure difference (cm of water)  
 0.8881 = Tunnel calibration factor  
 $\rho$  = Density (slugs/ft<sup>3</sup>)

The tunnel calibration factor was obtained from Renoud [Ref. 26].

## **B. ALQ-78 ANTENNA POD MODELS**

Twenty percent scale models of the two ALQ-78 antenna pod configurations were used in this investigation. The models were designed using copies of LASC production drawings for the standard configuration and General Instrument engineering drawings for the modified radome. The models are shown in figures 12 and 13. The ventral fin on the

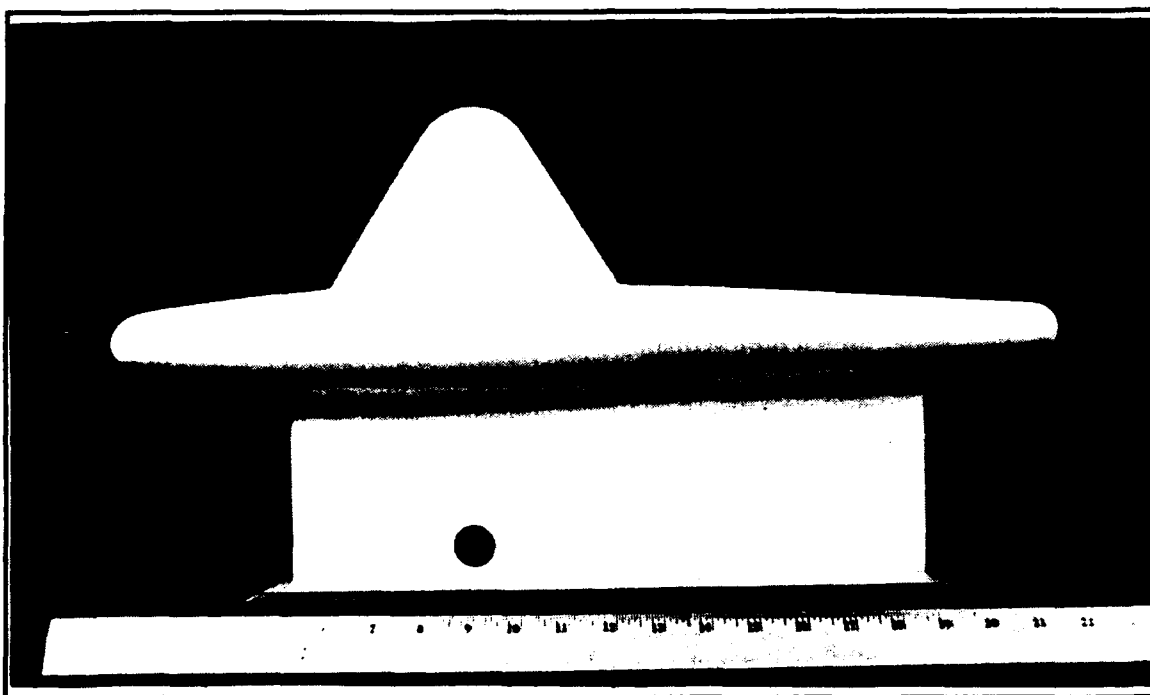


**Figure 12. ALQ-78 Antenna Pod Model, Standard Configuration**

standard configuration was not installed. The 4in. scale pylon height was extended to 6in. in order to place the radome near the center of the test section flow. The top of the model pylon was made parallel to the pod body centerline, rather than shaped to fit the P-3C airfoil section, to mate the model with the installed reflection plane. The model pylon trailing edge was rounded to a  $1/16$  in. radius circle to preclude damage during machining. The ESM test antenna, located on the nose of the pod body and shown in figure 1, was not

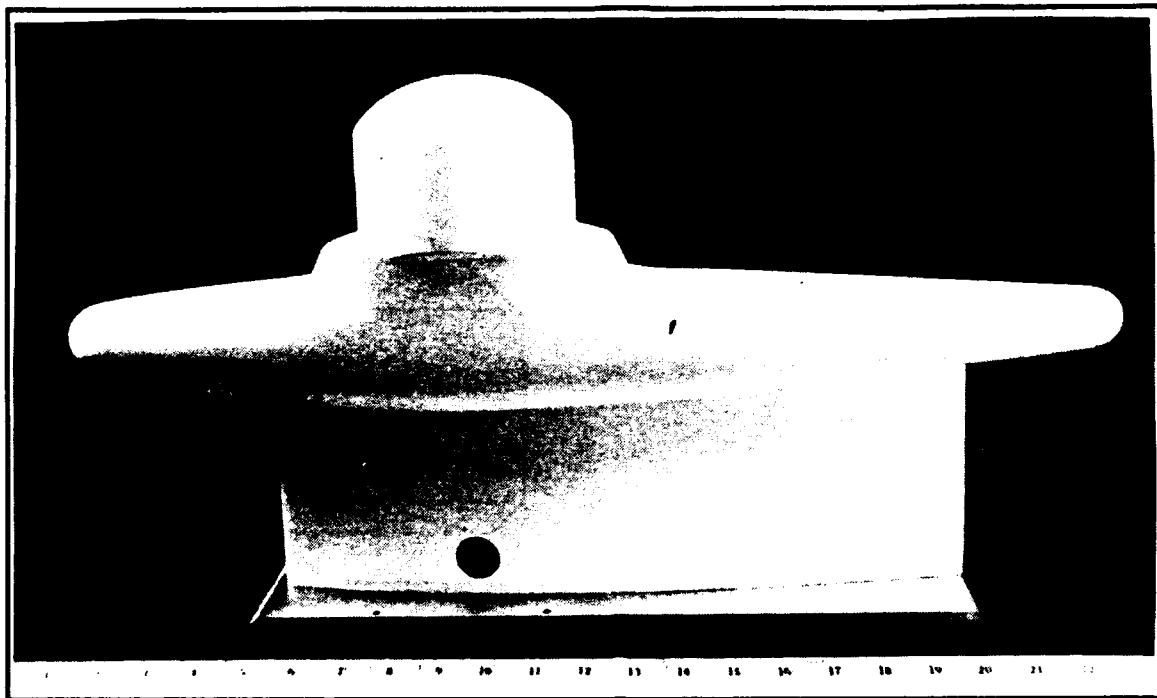


**Figure 13. ALQ-78 Antenna Pod Model, Modified Configuration**

modelled. The small configuration differences between the actual antenna pod and models were not significant for this investigation. Figure 14 shows the location of static pressure taps installed in the rear stagnation region of the radomes to measure base pressure. The pressure taps were connected to a multiple water manometer by flexible plastic tubing. The tubing was routed internally to a 1 in. diameter feed through access hole located at the junction of the pylon and mounting base.

The models were constructed from laminated birch, coated with a polyester based filler, and finished in a matte gray lacquer paint. They were subsequently painted flat black as this color was better suited for flow visualization studies. Design and production tolerances were checked against an actual pod obtained to support the model construction. The pylons and modified radome were within  $1/32$  in. (0.03125in.). The standard radome and pod bodies were within  $1/16$  in. (0.0625in.).

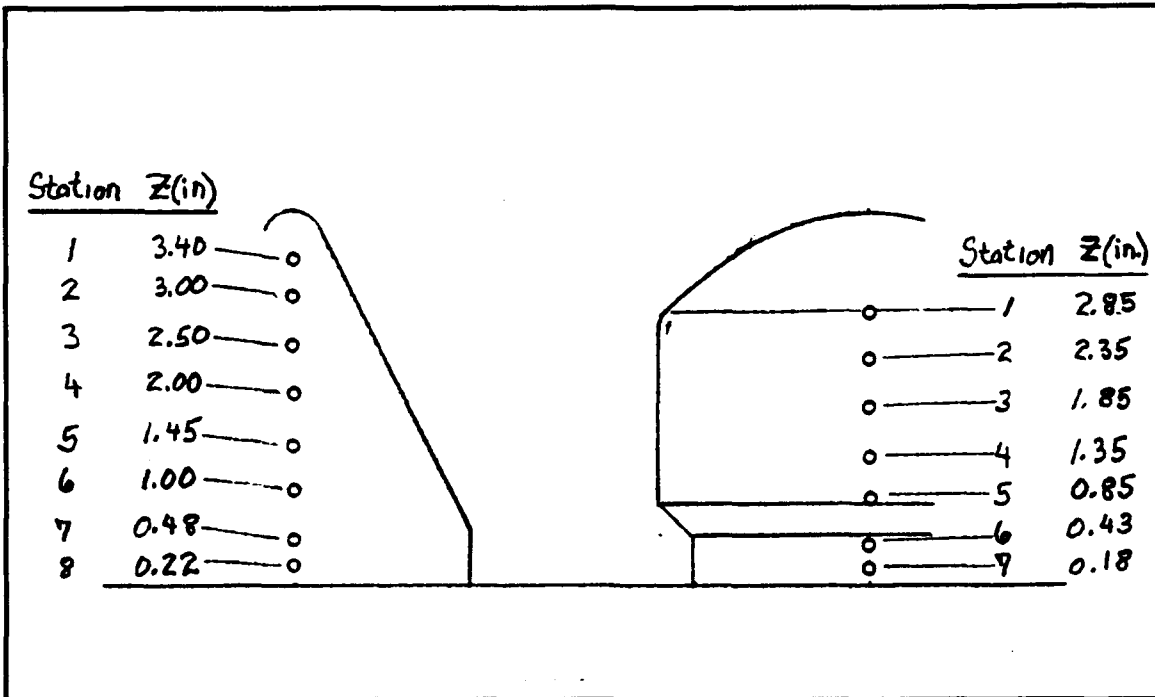


**Figure 14. Location of Static Pressure Taps on the Model Radomes**

Boundary layer trip devices were installed on the radomes during some of the base pressure and flow visualization tests. Piano wire with a diameter of 0.015in. was glued to the surface with cyanoacrylate adhesive.

Model production drawings are included in Appendix A.

### **C. MODEL SUPPORT**

The model was mounted to the reflection plane turntable using an aluminum base plate with mounting holes matched to the turntable. No force balance was used. The remotely controlled turntable enabled model rotations in yaw up to the P-3C envelope limit of 15° in 0.1° increments. Figure 15 shows the model mounted in the wind tunnel.



**Figure 15.** ALQ-78 Antenna Pod Model Mounted in the NPS Low Speed Wind Tunnel

#### **D. FLOW VISUALIZATION INSTRUMENTATION**

##### **1. Laser and Optics**

A laser sheet flow visualization system was developed for the NPS low speed wind tunnel during the late 1980's [Refs. 27 through 29]. The system used for this investigation was essentially identical to the system employed by Sommers [Ref. 29]. The system is shown in figure 16.

A Spectra-Physics Model 164 Argon-ion laser and model 625 power supply were used. The laser output was a nominal 5W blue-green beam with a specified diameter of 1.25mm and a divergence of 0.69mrad. A Spectra-Physics Model 404 laser power meter was used to check the laser output and peak the power. The maximum power measured was 3.9W.

The NPS installation featured a fiber-optic transmission line to transport the beam from the laser to the conversion optics. A Newport Corporation F-LFI laser fiber

illuminator was used. Three components comprised the illuminator. A quick-disconnect coupler head coupled the laser output into the fiber optic cable. The coupler also provided aperture adjustments and a focusing lens to maximize the laser power provided to the fiber. The Newport Corporation Model FA-2UV-10 fiber-optic cable used a 200micron silica fiber with a transmission efficiency of approximately 80%. The cable installed at NPS was approximately 10m long and terminated in an output handpiece. The handpiece contained optics which captured the divergent fiber output and focused it into a collimated beam with a 6mm diameter and 10mrad divergence.

The 10m cable failed early in the flow visualization study and was repaired by the Newport Corporation. In the interim, it was replaced by another F-LFI illuminator with a 3m cable.

The illuminator output was fed into a Newport Corporation Model T81-3X beam expander. The "expander" was reversed in this system and used to contract the beam by a factor of 3. The beam was then fed through a plano-cylindrical lens which formed the actual laser sheet. This investigator was able to form a 1/8in. (3mm) sheet by fine-tuning the focus adjustments on the handpiece and 3X expander.

The power output was peaked at the handpiece using the Model 404 power meter. The maximum power out of the long cable was 2.7W and the maximum out of the short cable was 2.9W. These power levels provided adequate illumination in the test section.

The handpiece, expander, and lens were fixed to a 6in. rail assembly which was mounted on a hand-operated two-dimensional traverse. The traverse enabled positioning the laser sheet in any part of the test section and could be mounted on both the upper and side viewing windows to provide three planes of illumination. The traverse could only be used on the side window when employing the 3m fiber-optic cable.



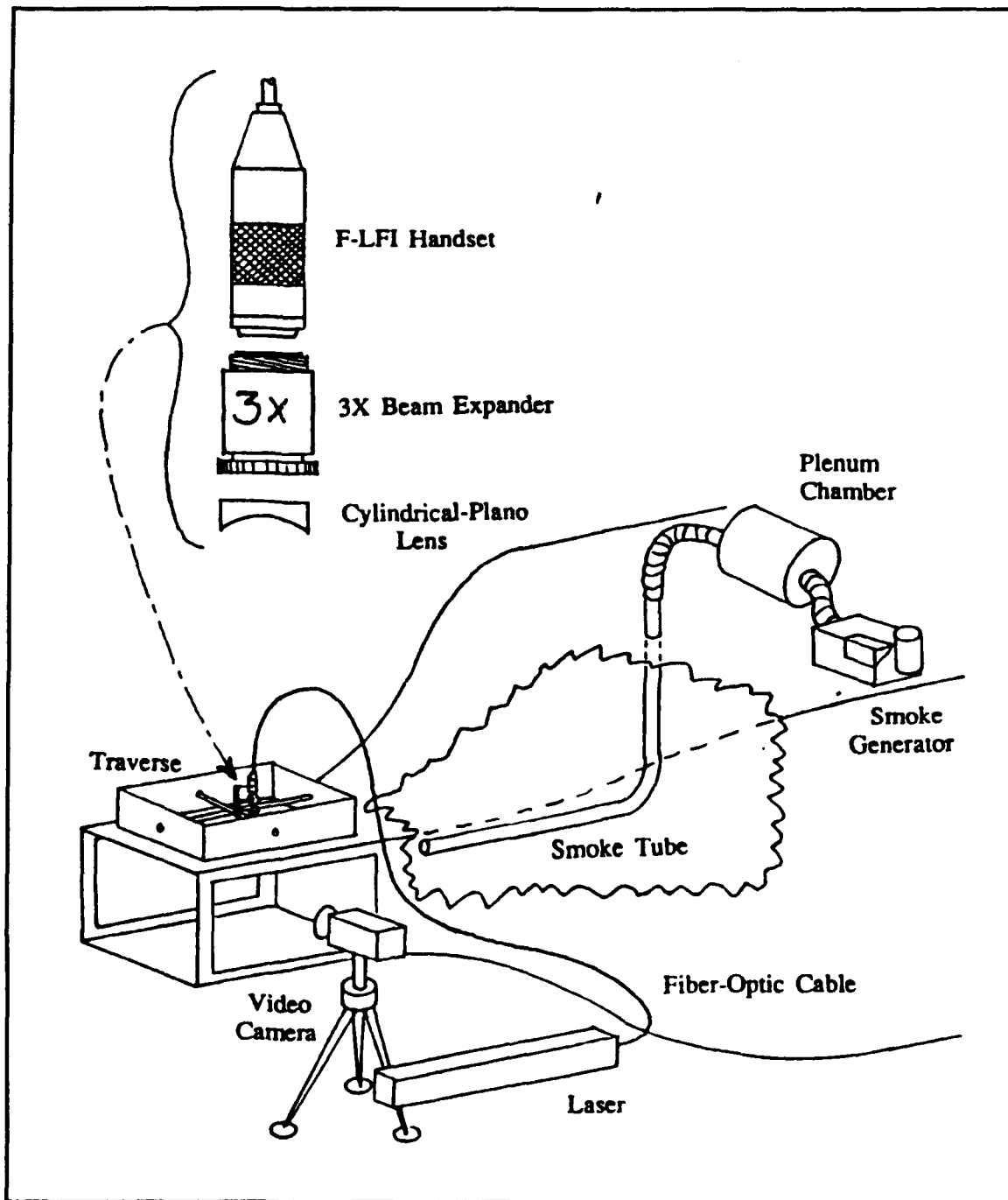


**Figure 16.** Flow Visualization System [Ref. 29]

## **2. Particle Seeding**

Particle seeding for flow visualization was provided by a Rosco Model 1500 theatrical fog/smoke machine. The machine heats and vaporizes Rosco #8207 fog fluid which forms a dense aerosol consisting of 0.5micron to 60micron particles. The smoke is fairly dry and is ideal for flow visualization seeding. The smoke machine was located on top on the wind tunnel settling chamber and was operated by a remote control.

The smoke machine output was fed into a ten-gallon cylindrical plenum chamber to settle the smoke flow and to cool the smoke. Warm smoke would tend to rise in the test section due to buoyancy effects. The plenum exhausted into a flexible hose which was connected to a 1in. diameter copper tube. The copper tube extended into the settling chamber and was gently curved through 90°. The tube extended horizontally to a point 3ft upstream of the test section. The exhaust end of the tube was sharpened and polished to provide a smooth exit for the smoke column. The smoke expanded to a 3-4in. thick column in the test section. The copper tube was clamped in place, permitting vertical adjustment of the smoke column location.

## **3. Video Imaging System**

Flow visualization video was captured using a Sony model DXC-3000A camera. The camera featured a 3-chip Charge Coupled Device (CCD) image sensor, 10mm to 120mm zoom lens with automatic and manual aperture control, and a selectable video output gain level. The video scanning rate was 30Hz.

The camera output was routed to a Sony model VO-5850 U-matic video tape recorder. This broadcast quality recorder featured freeze-frame and video editing capabilities. The imagery was recorded on Sony XBR broadcast quality video tapes. A 19in. Sony Trinitron color monitor was used to display the video.

A Mitsubishi model P71U video copy processor was used to obtain hard copies of selected video frames. Mitsubishi model K70S high resolution paper was used. This system provided remarkably sharp still images of the model wakes. Chapter IV contains several examples of the hard copy video output.

The video recorder, display and video copy processor are shown in figure 17.

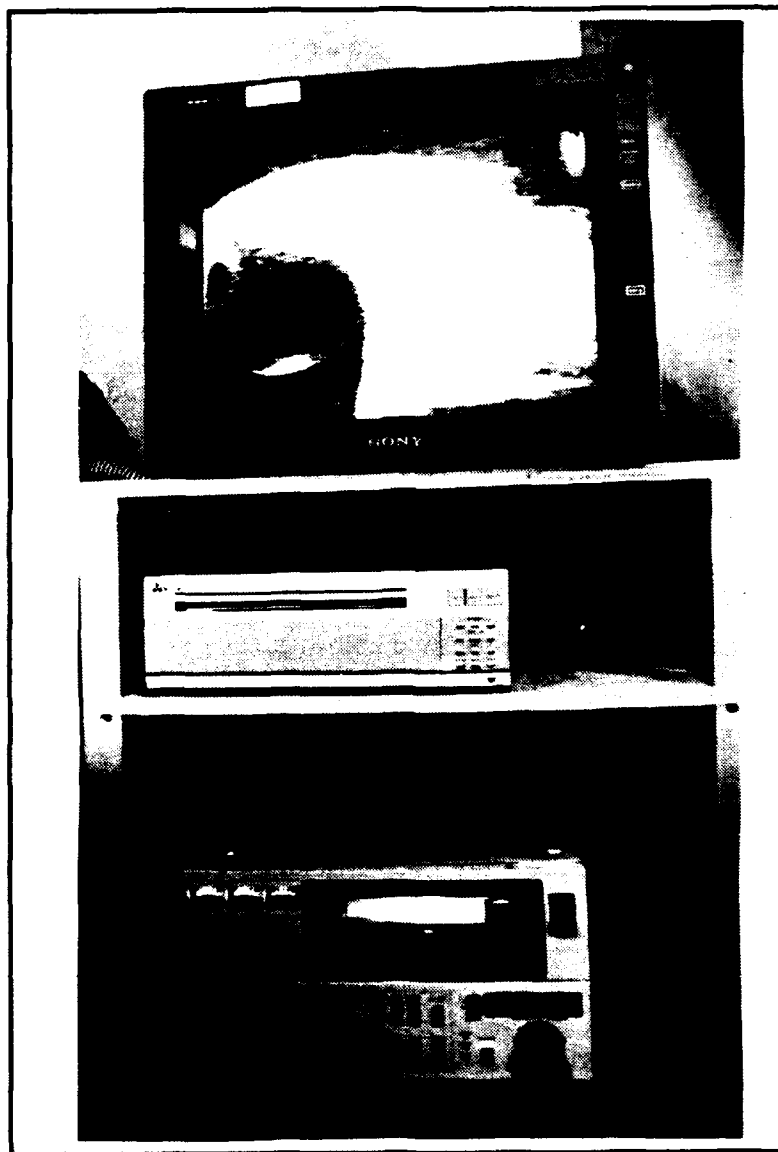


**Figure 17.** Video Monitor, Copy Processor, and Recorder

#### **4. Still Imagery**

A Nikon model N2020 35mm single lens reflex (SLR) camera and Nikkor 50mm/f1.4 lens were used to obtain still photographs of the model wakes. The camera was mounted on a tripod and triggered with a remote shutter release. An Olympus model OM-3 SLR and Olympus 50mm/f1.4 lens were used to photograph the models, instrumentation, and test facilities. Kodak T-Max 400 ISO black and white print film was used. Film processing, printing, and half-toning were performed by the Photographic Division of the NPS Educational Media Department.

#### **E. BASE PRESSURE INSTRUMENTATION**

The static pressure taps located on the rear face of the model radomes were connected to a multiple water manometer with small diameter flexible plastic tubes. Each tube was connected to an individual column on the manometer. Figures 18 and 19 show the manometer installed next to the test section and a typical pressure display. Test section static pressure and atmospheric pressure indications were also provided. The manometer table was canted at 45° to increase the sensitivity of the water columns to changes in static pressure. The water was dyed with green food coloring.

#### **F. HOT-FILM ANEMOMETRY**

##### **1. Probe**

A DISA model 55R51 X-array fiber-film probe was used. The 55R51 contained two 70µm diameter quartz fibers with a 0.5µm nickel film. The probe fibers were 3mm long with the sensing element occupying the central 1.25mm. The hot-film sensor was chosen for this experiment for its excellent low frequency response and robustness in contaminated flows. The NPS tunnel contained some residual smoke particles which could degrade the performance of a hot-wire sensor. This particular X-array probe had one inoperative film so it was used like a single slant-film.

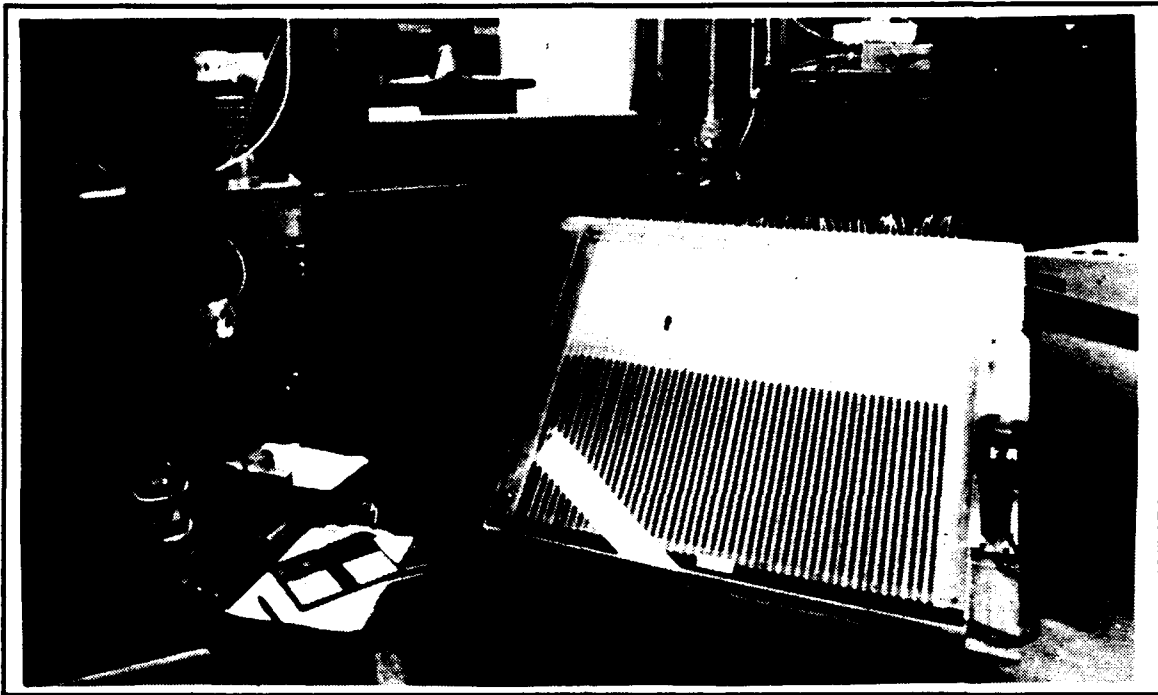


**Figure 18. Multiple Water Manometer Installed Adjacent to the Wind Tunnel Test Section**

## **2. Probe Support**

A DISA model 55H24 probe support was used. The probe support was connected to a DISA model 55H240 right-angle mounting tube for proper orientation in the flow. This assembly was suspended into the test section by a combination of DISA model 55H137 and 55H139 guide tubes. The probe support arrangement can be seen in figure 15. The probe support was approximately 27in. from the point where the guide tube combination was fixed to the traversing mechanism. This extremely long support system was fairly flexible and tended to vibrate at test section velocities above approximately 40ft/sec. The vibration was reduced by positioning the traverse such that the guide tube rested against the tunnel access slots. The test section cover and access slots are shown in figure 20.

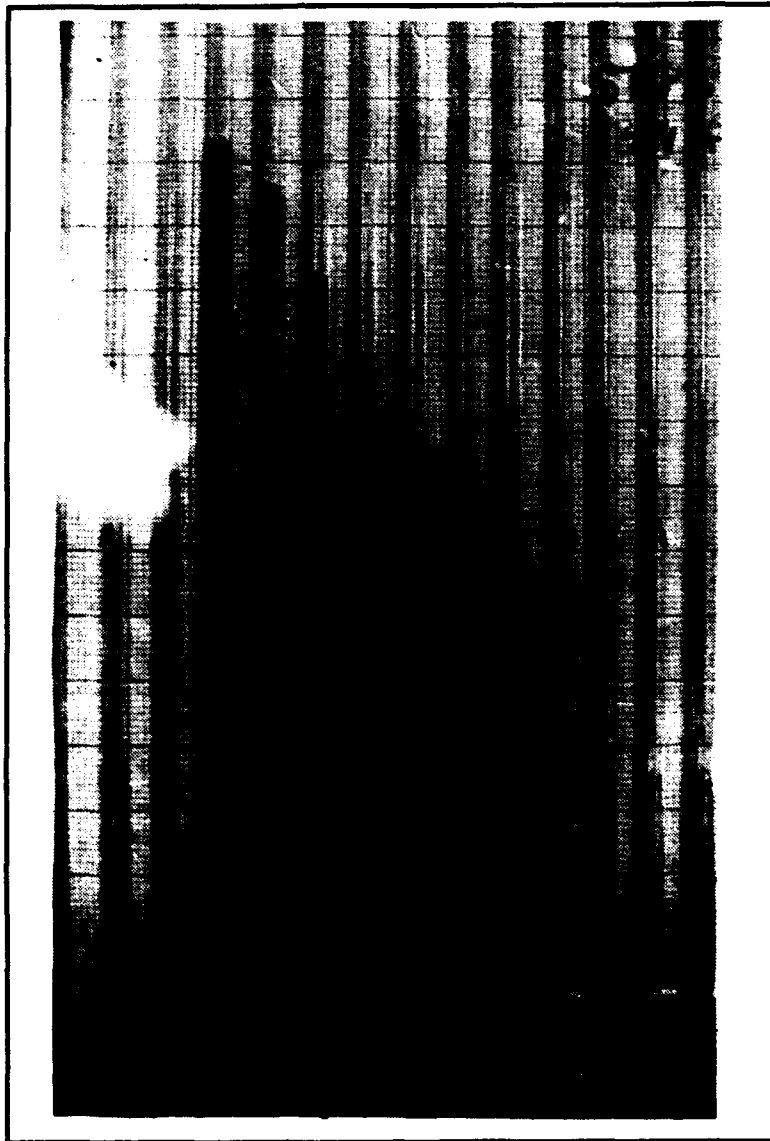


**Figure 19.** Typical Base Pressure Display on the Multiple Water Manometer

### **3. Traversing System**

The probe was positioned in the test section using a Velmex model 8300 three-dimensional stepping motor controller-driver. The Velmex 8300 consists of a 3-D traversing assembly and a motor controller. The system is shown in figure 21. Motion on three orthogonal axes is provided by three stepping motor and jackscrew assemblies. The

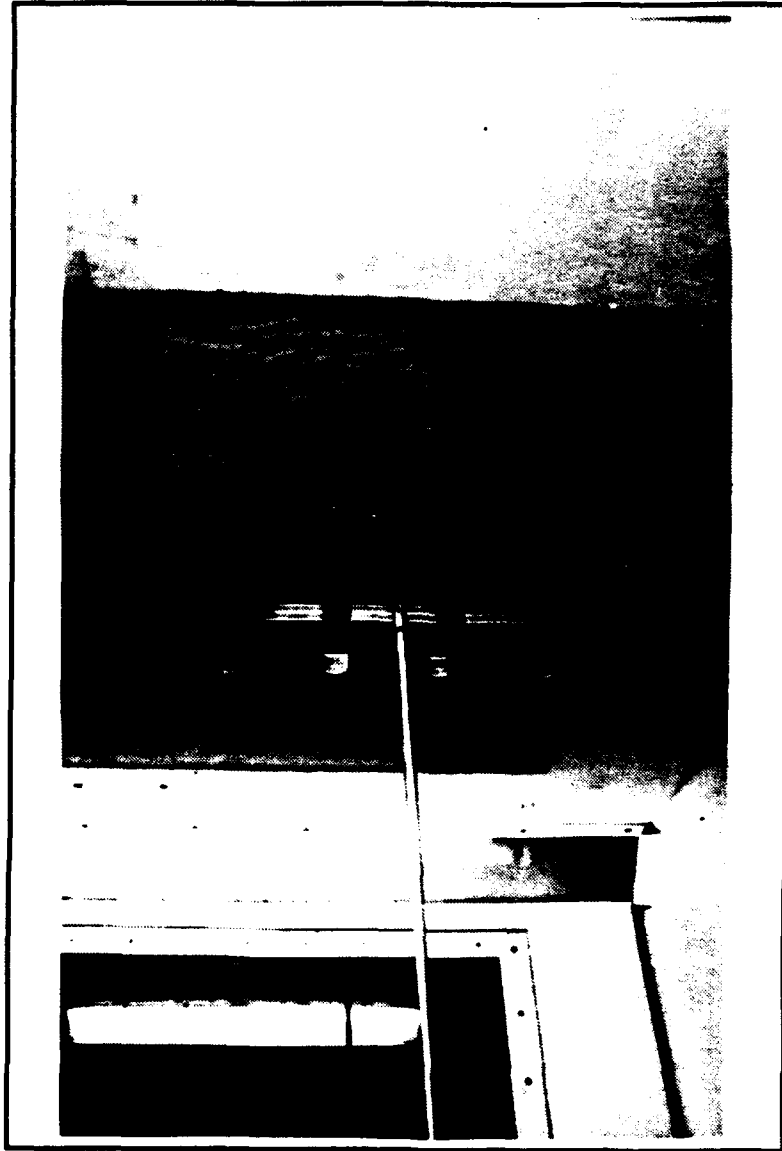


**Figure 20. Test Section Cover and Access Slots**

stepping motors provide 200 steps/revolution with a maximum slew rate of 3000 steps/sec. One step approximately equals 0.000125in. of traverse movement. The traverse is controlled from an IBM PC-AT through an RS-232 interface with the motor controller assembly. A BASIC language control program was used [Ref. 26]. References 26 and 30 contain detailed descriptions of the traversing assembly and listings of the control software.

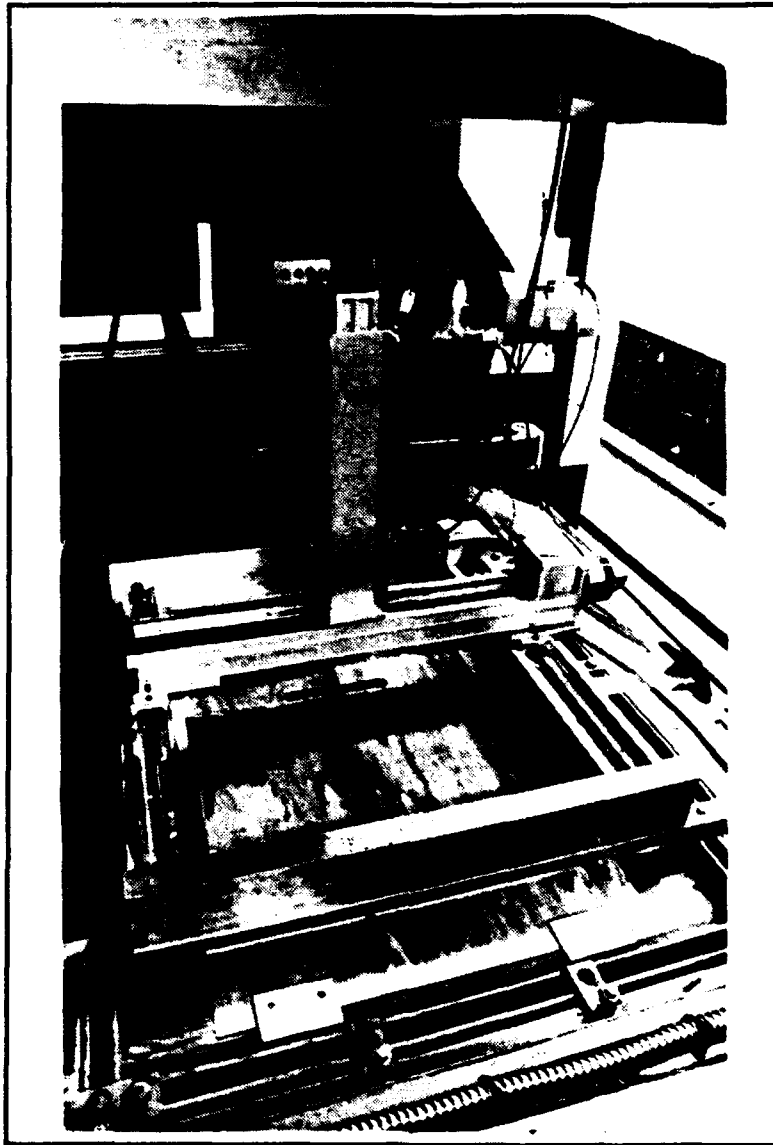


**Figure 21. Velmex 8300 Traversing System**

The PC traverse controller is shown in figure 22.

#### **4. Probe Cables**

The hot-film signals were routed from the probe holder to the anemometer bridge using 20m co-axial cables with BNC type connectors. Two cables were installed although only a single cable was used due to a malfunction of the one of the probe films.



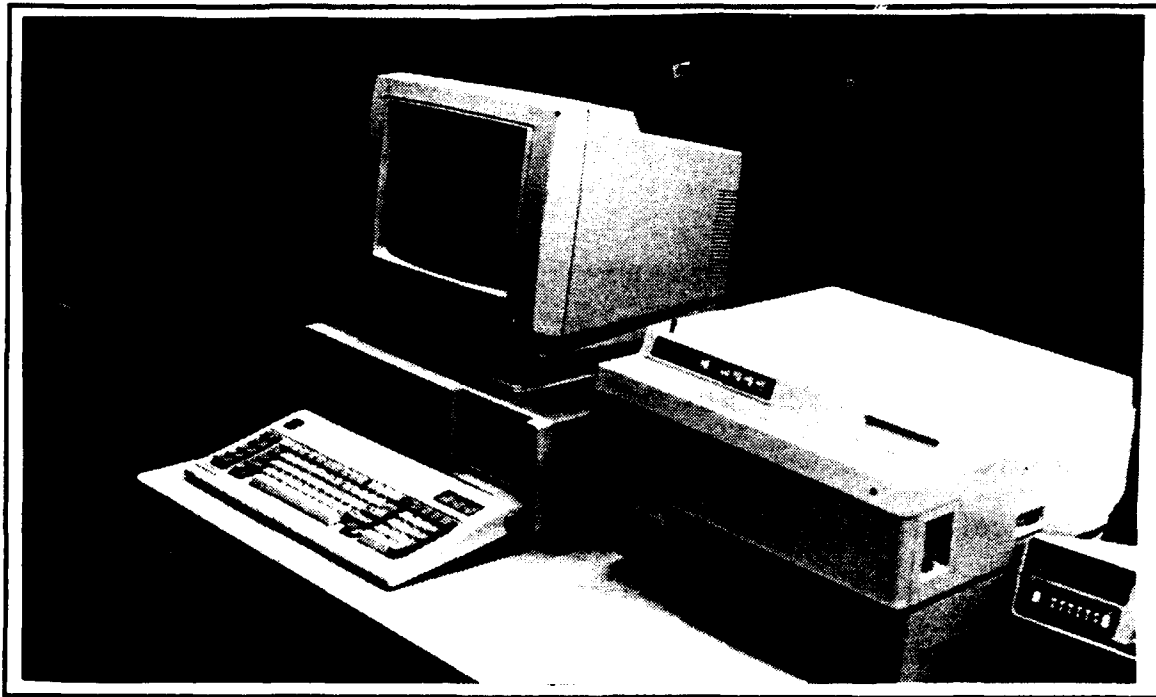


**Figure 22. IBM PC-AT Traverse Control Computer**

### **5. Hot-film Signal Processing and Display Equipment**

The hot-film signals were processed by a constant temperature anemometer (CTA) consisting of a DISA type 56C17 CTA bridge and DISA type 56C01 CTA unit mounted in a DISA type 56B10 main frame. The CTA provided the voltage necessary to keep the hot-film at a constant temperature for varying velocities. The CTA output voltage was proportional to the flow velocity at the probe and was sent to a DISA type 56N21 Linearizer. The Linearizer converted the non-linear CTA voltage output to a voltage which varied linearly with freestream velocity. Five manually set constants were used to calibrate the Linearizer to a generic DISA type 55R01 fiber-film input. In this experiment, the Linearizer was used solely as an interface between the CTA and Signal Conditioner (SC) as the backplane wiring of this particular mainframe unit did not allow a direct connection between the CTA and SC. The DISA type 56N20 Signal Conditioner provided signal filtering and gain selection. A high-pass filter provided selections ranging from DC to

300Hz in discrete steps. A low-pass filter provided selections ranging from 100Hz to 300kHz in discrete steps. These filters could be employed together to create a wide variety of signal bandpass options. The SC also provided additional gain from 1X to 500X. 1X was used for this experiment.

The processed hot-film signals were displayed on a DISA type 56N22 Mean Value Unit and DISA type 56N25 RMS Unit. Operator selection of CTA, Linearizer, and SC outputs was provided. Additionally, these units provided adjustable signal integration times from 0.1sec to 100sec which provided flexible signal smoothing options. The displays provided a digital readout of the signal voltages. The Mean Value Unit had a resolution of 0.1mV and the RMS unit had a resolution of 10mV.

A Tektronix model 465M oscilloscope display was used when making fine adjustments to the CTA bridge gain, filter and high-frequency balance controls.

The mainframe, DISA units, and oscilloscope are shown in figure 23. A DISA type 56N23 Analog Processor Unit was installed in the mainframe but was not used in this experiment.

## **6. Hot-film Signal Post-processing and Display Equipment**

The hot-film signals were post-processed using a GenRad model GR 2512 spectrum analyzer. The GR 2512 is a compact, portable, one-channel spectrum analyzer which uses fast Fourier transform (FFT) techniques for high-speed narrowband analysis of the frequency content of analog or pre-digitized input signals. The input is resolved into 400 separate frequency filters which are equally spaced across selectable analysis ranges of DC to 10Hz through DC to 100kHz. The system features a microprocessor controlled, menu-driven user interface. The spectrum can be viewed in linear or logarithmic frequency display formats. Additionally, the input signal amplitude can be viewed in decibel, volt, volts<sup>2</sup>, volts<sup>2</sup>/Hz, or user defined units. The GR 2512 provides spectrum averaging for up



**Figure 23. DISA Mainframe and Tektronix oscilloscope**

to 1024 display frames. The system also contains a memory which can store one complete averaging run. The system memory and current average frames can be displayed simultaneously and printed.

Selected spectrum analyzer displays were printed using a Tektronix model 4632 Video Hard Copy Unit. The unit was modified for compatibility with the GR 2512 video output signal. The spectrum analyzer and video hard copy unit are shown in figure 24.

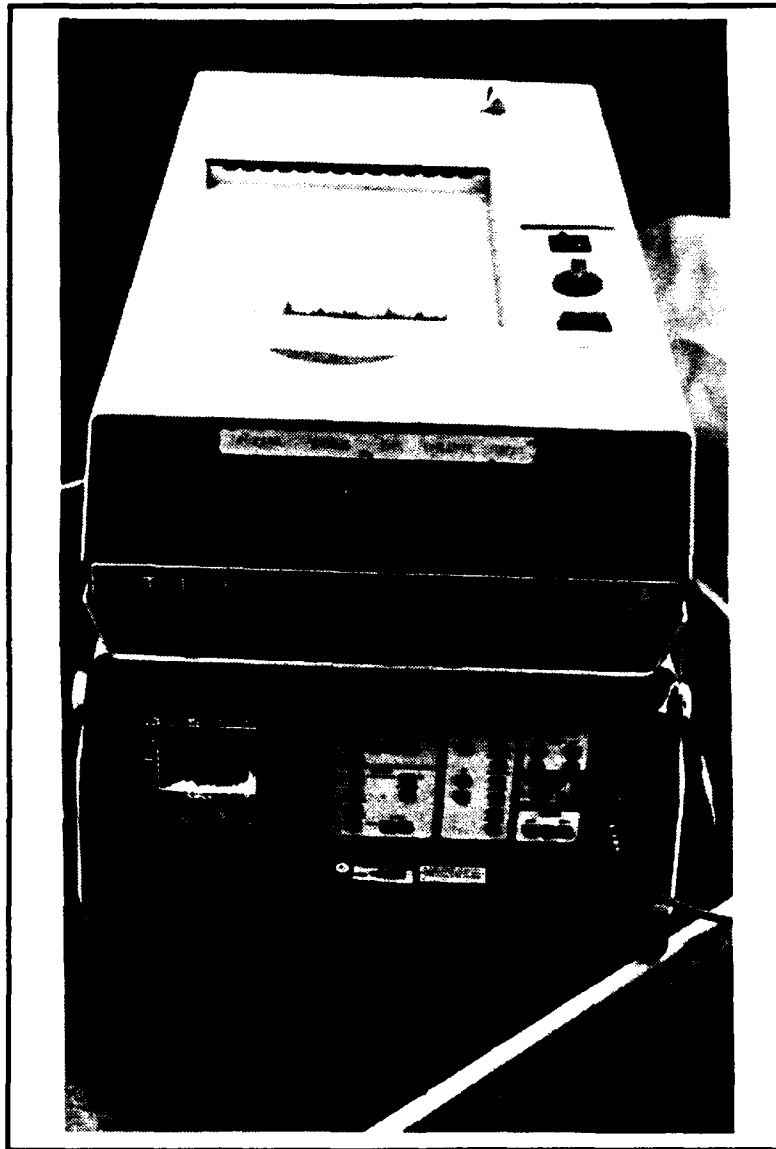


**Figure 24.** GenRad GR 2512 Spectrum Analyzer and Tektronix 4632 Video Hard Copy Unit

## 7. Coherent Signal Generation Devices

The spectra from the initial hot-film surveys in the three dimensional wakes of the pod models were not satisfactory. A two-step approach was designed in which the hot-film output and signal processing equipment were optimized for the detection of periodic wake phenomena. The first step consisted of placing a periodic turbulence generator upstream of the hot-film probe. This device was developed for the experiments conducted by Renoud [Ref. 26]. The device consisted of an 18in. long by 3/8in. diameter cylindrical steel bar attached to a hub. The bar resembled a propeller and was driven by a flexible drive shaft connected to a variable speed DC motor. Figure 25 shows the device installed in the test section. The DC motor was not firmly mounted in the tunnel so the device was

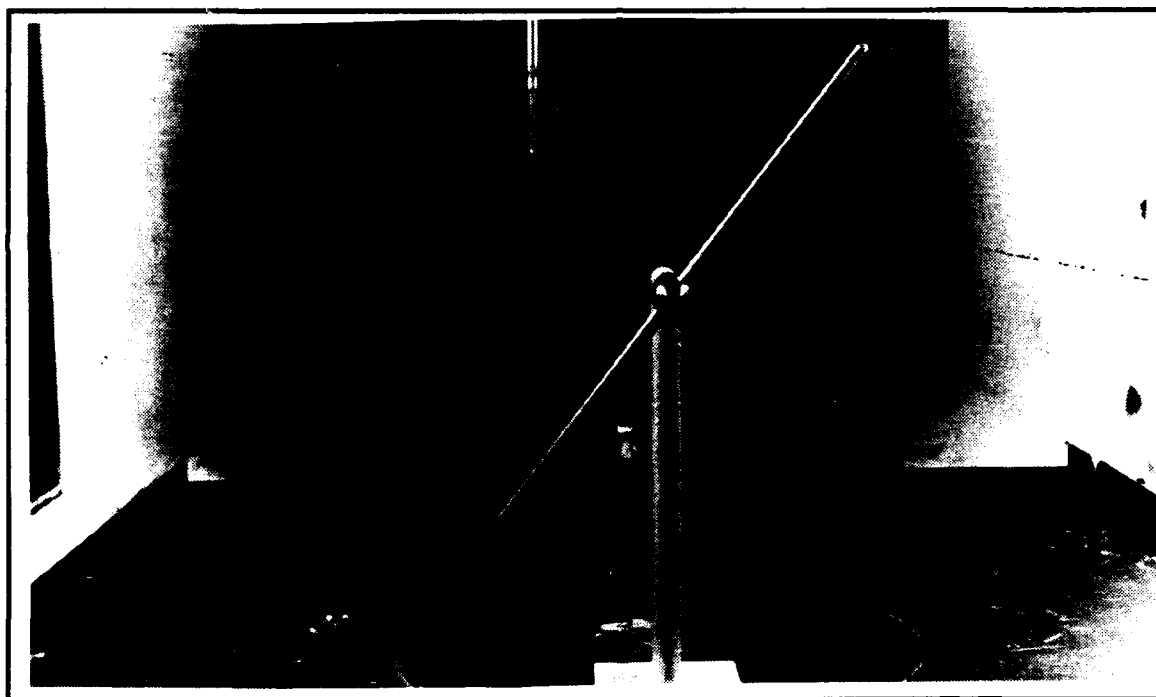


**Figure 25. Periodic Turbulence Generator**

used during low-speed tests only. The turbulence signal generated by this device was displayed as a very narrowband discrete spike on the spectrum analyzer. It was used to investigate optimum settings for the SC filters and spectrum analyzer display modes.

The second device employed was a 14in. long by 1.5in. diameter aluminum cylinder. This cylinder was actually an optics stand which was adapted for this experiment. The cylinder surface was smooth but not polished and the cylinder base was a 3in. diameter flange with holes for mounting bolts. The cylinder was mounted in the tunnel upstream of the hot-film probe. The cylinder wake was investigated for a range of flow speeds and conditions. The wake from the center section of the cylinder was quasi-two-dimensional. The wake near the tip exhibited some three-dimensional effects. Figure 26 shows the cylinder mounted in the test section. The wake spectrum of this device broadened as Reynolds number increased and was used to optimize the hot-film instrumentation for the display of vortex shedding related spectra.

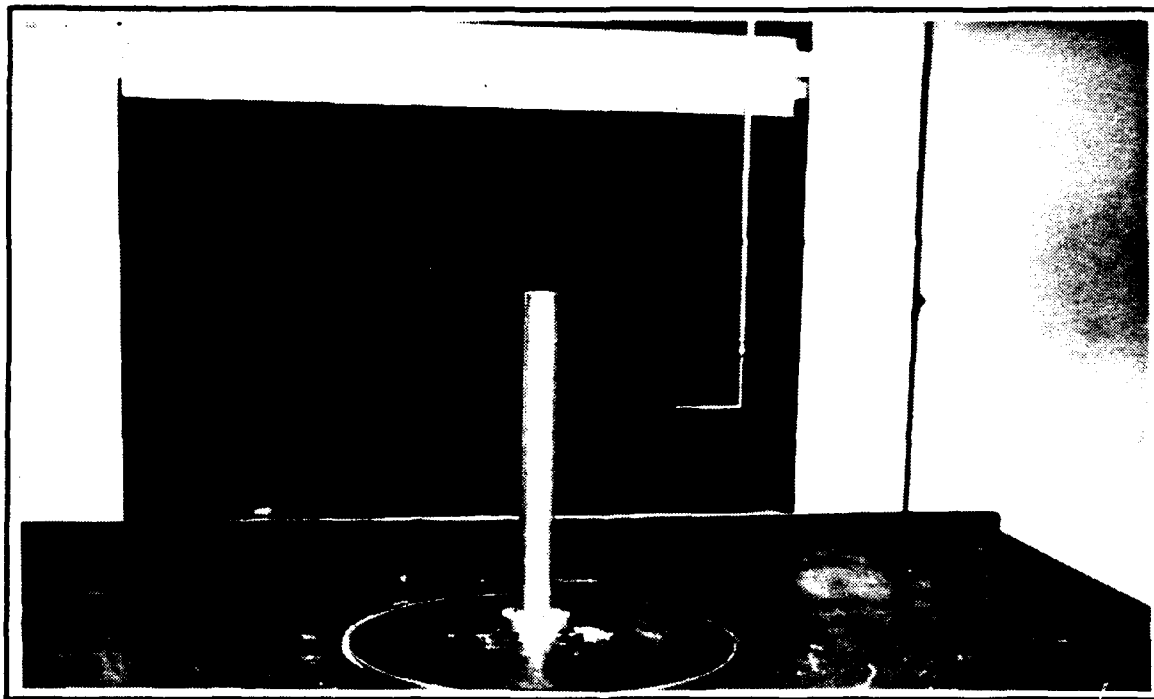


**Figure 26. Quasi-two-dimensional Cylinder**

### **III. EXPERIMENTAL PROCEDURES**

#### **A. WAKE VISUALIZATION**

##### **1. Laser Sheet Generation**

The Spectra-Physics model 164 laser was adjusted for maximum power output using the procedures contained in the operator's manual [Ref. 31]. Specifically, the aperture control was adjusted to eliminate undesirable modality. Single-mode output was verified by observing the "donut" shaped laser output projected onto a distant wall. The reflector assemblies and prism did not require adjustment. The laser power output was measured using a Spectra-Physics model 404 power meter. The laser beam was directed into the meter head through a 0.2-5.0W attenuator and the power was read from the appropriate scale on the meter. A discrepancy was noted between the power output indicated on the model 265 power supply meter and the power measured with the model 404 meter. A calibration curve is shown in figure 27.

The fiber-optic cable was then attached to the laser and adjusted in accordance with the F-LFI instruction sheet. The output of the handpiece was then maximized and measured using the model 404 meter. Minimum power was then set and the beam was then fed through the 3X expander and plano-cylindrical lens. The resulting sheet was focused on the model in the test section. Fine adjustments of the handpiece focus and expander focus produced a thin sheet.

##### **2. Seed Optimization**

A wide range of smoke column quality was observed during the initial flow visualization tests. The optimum quality was obtained by running a series of visualization tests with an empty test section. The smoke tube was placed to provide a column of smoke

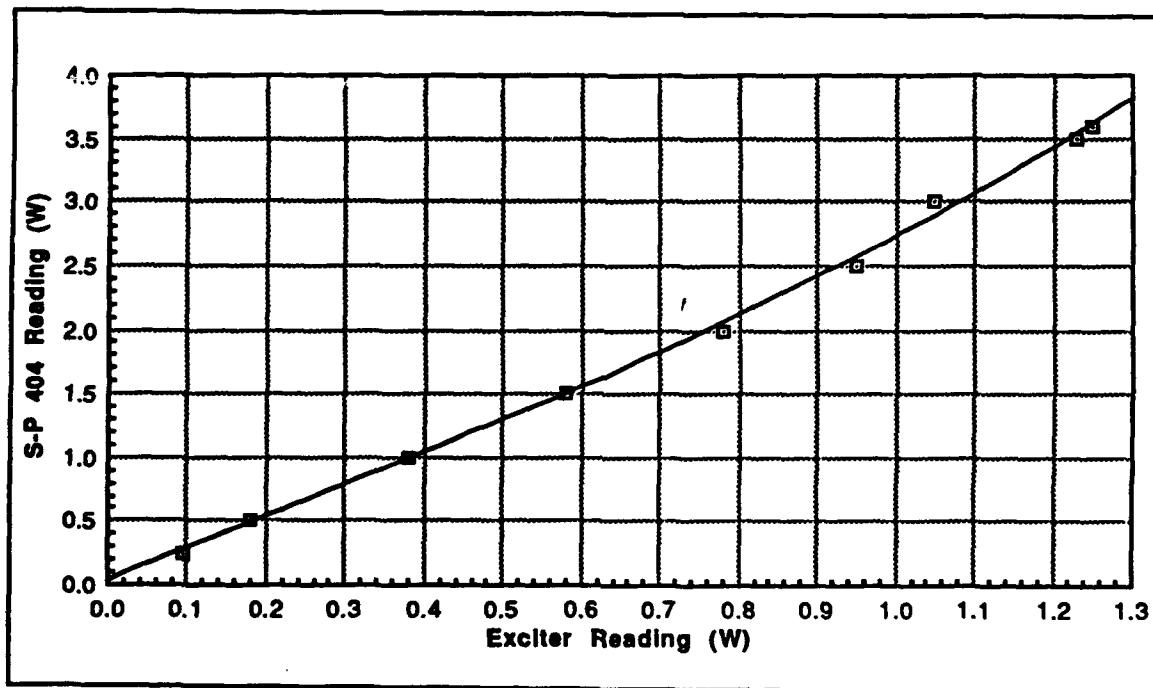


**Figure 27. Laser Output Power Calibration**

in the test section region normally occupied by the model radomes. The video camera was located on top of the test section and focused on the smoke column. Various combinations of tunnel velocity and smoke volume were evaluated.

Tunnel velocities greater than approximately 40ft/sec required large volumes of smoke which quickly filled the tunnel and reduced the image contrast. The best combination was a velocity of 34-35ft/sec with a smoke volume setting of 1.0-1.5. Poor smoke quality was indicated by insufficient volume and/or the presence of irregularities at the edges of the smoke column. Figure 28 shows a smoke column at 34ft/sec with a smoke volume setting of 2.5. The irregularities along the edge could be mistaken for wake phenomena during flow visualization. Figure 29 shows the improvement obtained by reducing the smoke volume setting to 1.0.



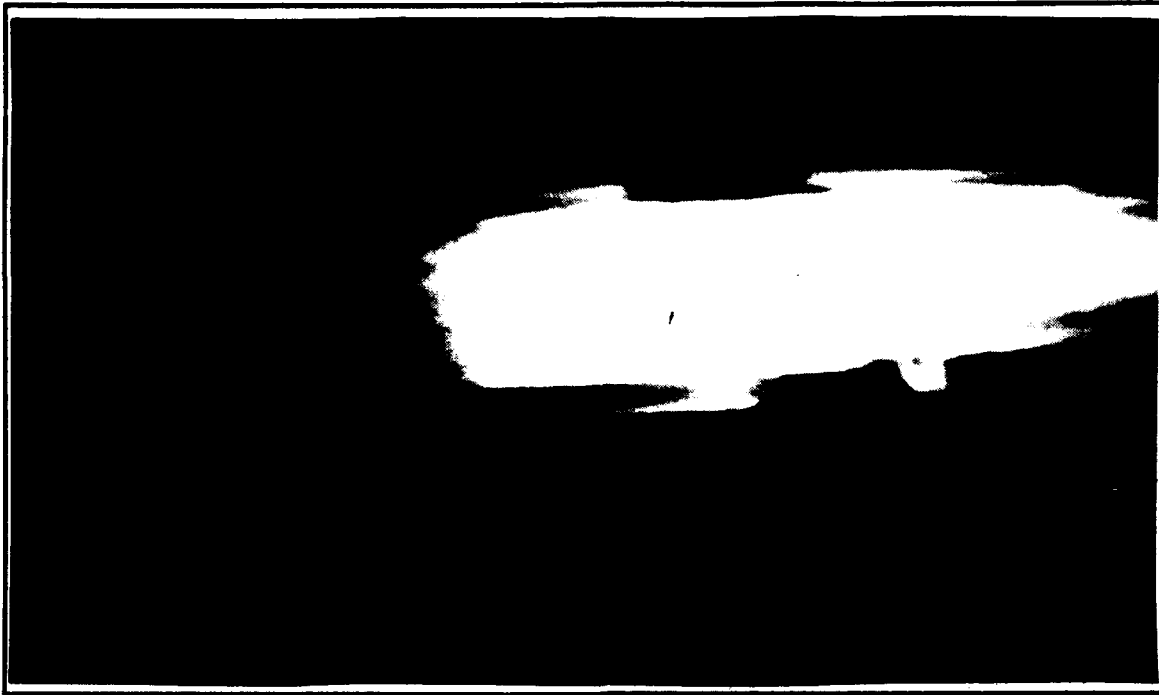


**Figure 28. Smoke Column at 34ft/sec with Smoke Volume Setting of 2.5**

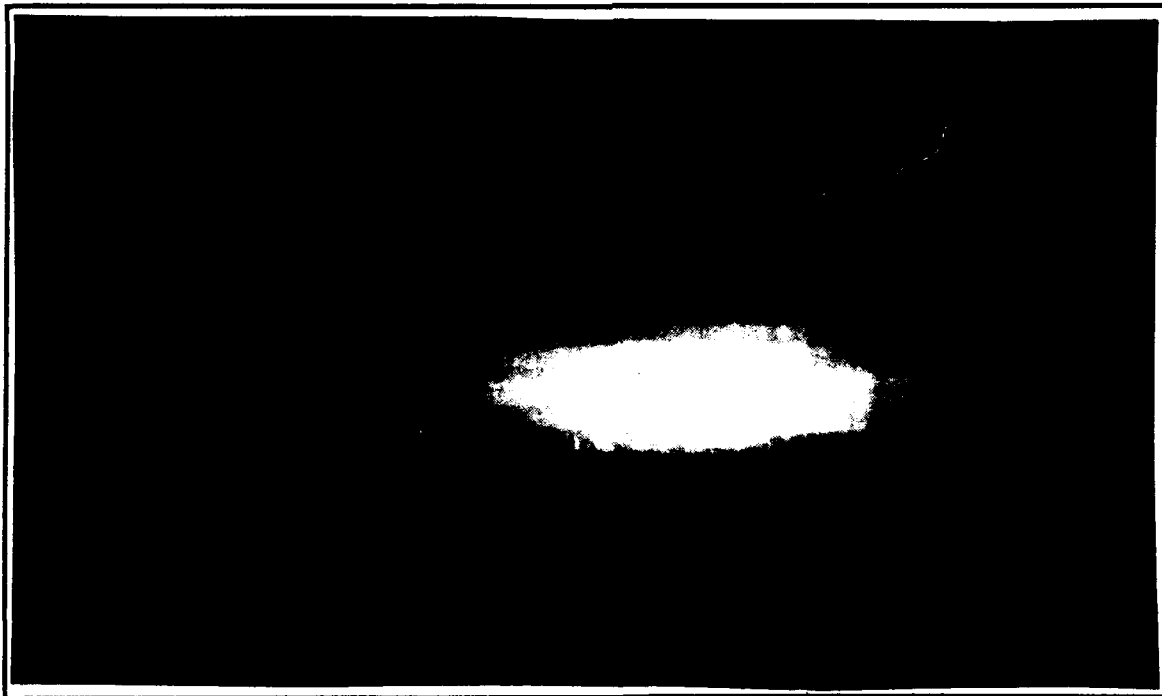


**Figure 29. Smoke Column at 34ft/sec with Smoke Volume Setting of 1.0**

The settling chamber access panel was open for all wake visualization studies. This permitted the use of lower smoke volume settings and also provided some degree of smoke venting as discussed by Sommers [Ref. 29].

### **3. Video Image Optimization**

The video camera was adjusted to provide the best possible output with optimal seeding and the laser set to peak power. The camera video gain was set at 18dB. Two regions were imaged. The vortex formation region was imaged by zooming in such that the field of view encompassed the radome and approximately 1.5 radome diameters downstream. The best camera aperture was found to be an intermediate setting between f2.8 and f4.0. The entire near wake was imaged by zooming out such that the field of view encompassed the radome and the entire region illuminated by the laser. The laser was traversed downstream to a point where the sheet illuminated the back of the radome and as much of the downstream wake as possible. The best aperture for these images was found to be the minimum setting of f1.7.

### **4. Still Photography Optimization**

Several rolls of 400ISO T-Max film were exposed at various exposure settings with the models in the test section. The 50mm focal length lens provided adequate coverage of both the vortex formation region and the near wake from a single position. No reorientation or zooming was required. The best results were obtained with the exposure set to f1.4 and  $1/60$ sec for the vortex formation region and f1.4 and  $1/30$ sec for the near wake.

### **5. Image Recording**

Video and still wake imagery was obtained for all three planes. A set of images was taken with the laser sheet positioned at particular stations on the model. For the

horizontal orientation, the static pressure tap locations served as the stations. Figure 30 shows the locations chosen for the lateral and longitudinal orientations. The smoke column

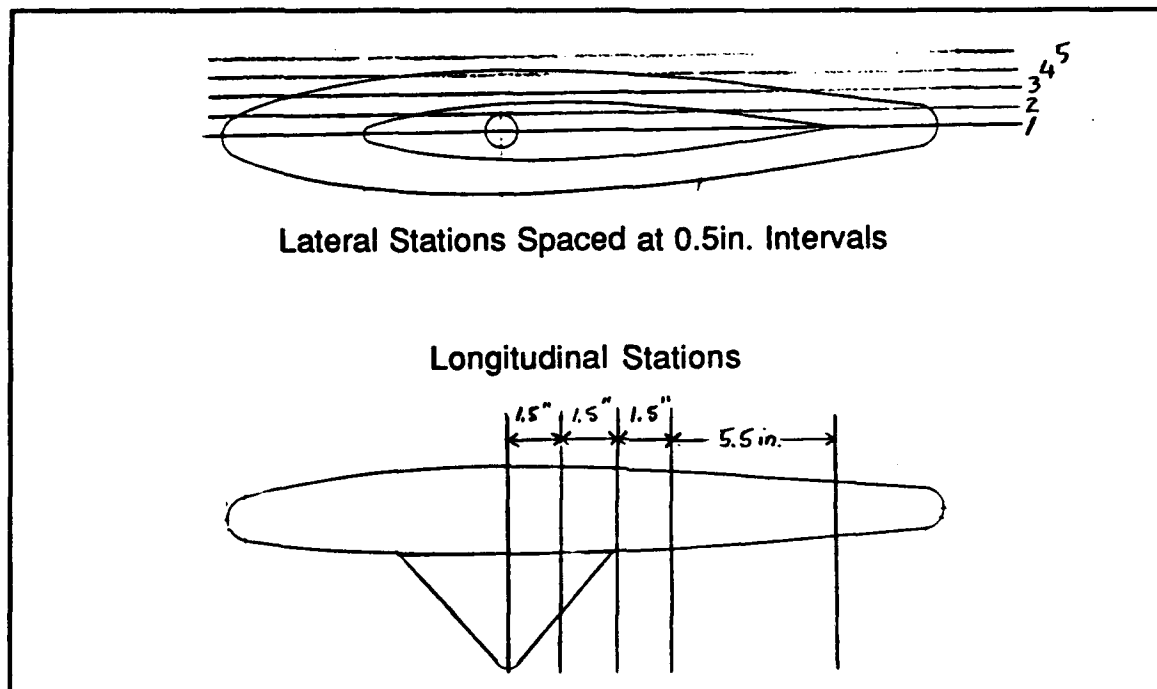


**Figure 30. Lateral and Longitudinal Flow Visualization Stations**

was relatively small and a single smoke tube location did not provide adequate seeding for the entire wake region. Three vertical positions were required and imagery was recorded with the smoke tube in each position. The different smoke tube positions are sketched in figure 31. Laser power was typically 80%-90% of maximum and the smoke volume setting was 1.0-1.5. The video tape recorder and smoke generator were turned on simultaneously. This provided a video recording of the wake as the smoke volume increased to steady state. Many of the images obtained during the smoke build-up showed improved rendition of fine detail. Four still frames were exposed once the smoke had reached steady state. The tape counter, still frame counter, and test conditions were hand recorded on a video log sheet. Five or six consecutive imaging runs could be completed before the tunnel required smoke purging.

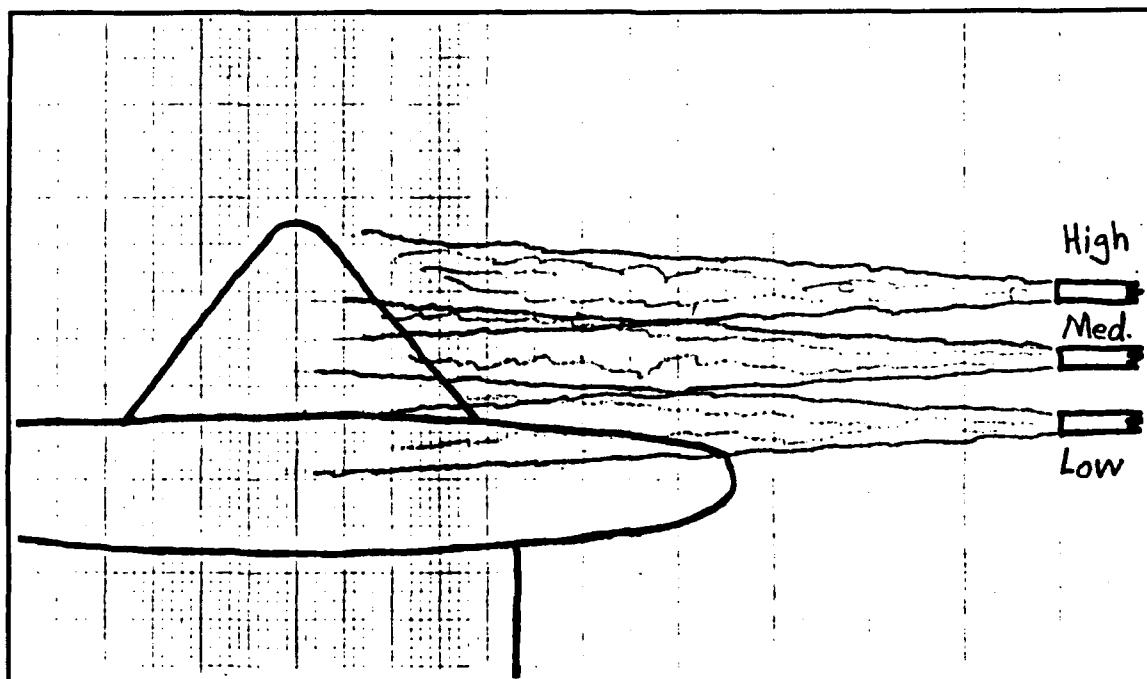


**Figure 31. Smoke Tube Positions**

## **6. Turntable Alignment**

The initial flow visualization tests revealed a skewness in the wake pattern due to a  $1.5^\circ$  turntable misalignment. The turntable orientation was indicated on a rotating bezel with an adjustable index. The index had apparently been moved without realignment, resulting in the skewed wake pattern. The misalignment was corrected by rotating the turntable incrementally until the model attachment sockets were equidistant from the sides of the reflection plane. The new setting was checked by aligning a 3ft. carpenter's level with the attachment sockets and sighting down the test section from a point upstream in the settling chamber. The observer straddled the center static pressure port on the settling chamber floor and visually checked for misalignment. A misaligned turntable was indicated when the level appeared to be at an angle with the longitudinal axis of the test section. Once a satisfactory alignment was achieved, the bezel index was reset and an

alignment mark was etched on the turntable and reflection plane surfaces. This crude procedure provided an alignment good to within approximately 0.2°.

## B. BASE PRESSURE MEASUREMENTS

### 1. Base Pressure Coefficient

The base pressure coefficient ( $C_{pB}$ ) was measured with a multiple water manometer for a range of velocities from 94ft/sec to 270ft/sec. The velocity range was limited by manometer sensitivity on the low end and by maximum tunnel velocity on the high end. The tunnel was stabilized at the desired speed and the following data were hand recorded on prepared data sheets: Atmospheric pressure, test section pressure, model base pressures, settling chamber temperature, and tunnel velocity (cm H<sub>2</sub>O). All pressures were recorded in inches of water. The tunnel velocity and base pressure indications fluctuated at higher speeds. A mean value was recorded in these cases. The settling chamber temperature was kept to within 10°F of the initial value in order to minimize the effect of temperature changes on the air density. Each test velocity was run three times to establish the repeatability of the data and to provide increased confidence in the measured quantities.

The base pressure coefficient was calculated using the pressure difference between the model base and the test section  $P_{mod} - P_2$ . Since the manometer was vented to the atmosphere, the water column height indicated the pressure difference between the model base and the atmosphere ( $P_{mod} - P_{atm}$ ).  $P_{mod} - P_2$  was calculated using the following equation, where the brackets indicate observed quantities:

$$P_{mod} - P_2 = [P_{mod} - P_{atm}] + [P_{atm}] - [P_2] \quad (5)$$

Base pressure was then calculated using:

$$C_{pB} = \frac{(P_{mod} - P_2)}{\frac{1}{2} \rho_{obs} U_{actual}^2} \quad (6)$$

$\rho_{obs}$  and  $U_{actual}$  are defined in the experimental corrections section below.

The data were reduced on a Macintosh® SE computer using the Microsoft® Works version 2.00a spreadsheet. Appendix B contains a sample data reduction spreadsheet. The spreadsheet output was graphed using Cricket Software® Cricket Graph version 1.3.

## 2. Yaw Sensitivity

The sensitivity of  $C_{PB}$  to yaw angle was evaluated at a freestream velocity of 180ft/sec. Data were recorded for yaw angles of 0°, 5°, 10°, and 15°. In view of the excellent repeatability of the 0° yaw data, only one set of data were recorded for each model at other yaw angles. The data were reduced and plotted as above.

## 3. Experimental Corrections

The 45° manometer inclination angle was corrected by multiplying the observed water column height by 0.7071 [Cosine (45°)].

Air density was corrected for atmospheric pressure, relative humidity, and temperature variations. The atmospheric pressure and indoor relative humidity were obtained from meteorological instruments in an adjacent classroom building. Atmospheric pressure and settling chamber temperature were used in the perfect gas equation of state to calculate a dry density ( $\rho_{dry}$ ):

$$\rho_{dry} = \frac{P_{atm}}{RTg_c} \quad (7)$$

where  $\rho_{dry}$  = dry air density (slugs/ft<sup>3</sup>)       $T$  = settling chamber temperature (°R)  
 $P_{atm}$  = atmospheric pressure (lb<sub>f</sub>/ft<sup>2</sup>)       $g_c$  = 32.174 lb<sub>m</sub>/slug  
 $R$  = gas constant for air (ft-lb<sub>f</sub>/lb<sub>m</sub>-°R)

The dry density was corrected for humidity using the following equation [Ref. 32]:

$$\rho_{\text{obs}} = \left[ 1 - \frac{0.378 (\text{R.H.}) (2.685 + 0.003537 T^{2.245})}{P_{\text{atm}}} \right] \rho_{\text{dry}} \quad (8)$$

where  $\rho_{\text{obs}}$  = corrected density (slugs/ft<sup>3</sup>)  
R.H. = relative humidity (fractional value)  
T = settling chamber temperature (°F)

The sensitivity of the data to these corrections was evaluated by comparing the  $C_{pB}$  obtained using standard day conditions to that obtained using corrected conditions. The maximum influence observed was  $\pm 0.001$ .

Tunnel velocity was corrected using equation (4).

A tunnel blockage correction was calculated for each model using the following equation [Ref. 24]:

$$\epsilon = 0.25 \left[ \frac{\text{model frontal area} + \text{instrumentation frontal area}}{\text{test section area}} \right] \quad (9)$$

The calculations are summarized in table I.

The blockage factor was used to calculate actual tunnel velocity as follows:

$$U_{\text{actual}} = (1 + \epsilon) U_{\infty} \quad (10)$$

**TABLE I**  
**BLOCKAGE CORRECTION CALCULATIONS**

Model	Model Frontal Area (in. <sup>2</sup> )	Instrumentation Frontal Area (in. <sup>2</sup> )	Test Section Area (in. <sup>2</sup> )	$\epsilon$
Standard	23.6	1.2	1251	0.00496
Modified	29.4	1.2	1251	0.00611

### **C. HOT-FILM ANEMOMETRY**

#### **1. CTA System Configuration**

The CTA system was configured for hot-film anemometry in accordance with the DISA operator's manuals [Refs. 33 through 35]. The #2 sensor on the hot-film probe was faulty and was not used. The probe was employed as a single slant-film sensor as no replacement probe was available. The #1 sensor provided an acceptable output.

#### **2. CTA System Optimization**

The initial hot-film surveys of the model wakes were unsatisfactory. No coherent spectra were evident. The CTA system was then optimized for detection of coherent spectra by injecting known signals into the flow. A periodic turbulence generator was employed upstream of the probe in a 34ft/sec flow. This device produced very sharp spikes on the spectrum analyzer at the fundamental frequency and several harmonic frequencies. Figures C1 and C2 of Appendix C show the spectrum analyzer display for the periodic turbulence generator. Figure C3 of Appendix C shows the tunnel spectra at 34ft/sec with the periodic turbulence generator off. The tunnel spectrum was remarkably clean. Figure C1 is the output from the CTA. Figure C2 is the linearized and conditioned



output from the SC. The processed SC output signal level was approximately 8dB higher than the CTA output. The signal-to-noise ratio (SNR) was approximately 27dB in both cases. Figure C2 also shows the effect of the SC high-pass filter set at 10Hz.

### **3. Probe Support Dynamics**

The probe support structure was quite flexible and vibrated noticeably at freestream velocities greater than 40ft/sec. The vibration was observed in the longitudinal direction only. A zero velocity investigation of the probe support dynamics was conducted. The support was plucked repeatedly in the longitudinal axis while the spectrum analyzer recorded the CTA output. Figure C4 of Appendix C shows the result. The probe support tended to oscillate with a fundamental frequency of approximately 11Hz. A strong second harmonic was noted at 21.5Hz. The test was repeated in the lateral direction with the results shown in figure C5. The lateral spectrum was more definite with oscillations at 15Hz and 30Hz.

The probe support dynamics were then evaluated with flow. Figure C6 shows the spectrum obtained at 34ft/sec. The spectrum was flat. Freestream velocity was then increased to 94 ft/sec and the probe vibrated approximately  $\pm 0.25$ in. longitudinally. No lateral vibration was discernable. Figure C7 shows the resulting spectrum. Numerous spikes were present with a 20Hz fundamental and 13-14 harmonics. The probe support was then traversed downstream approximately 0.3in. until it rested firmly against the tunnel access slot. This provided additional stiffening of the support structure. Figure C8 shows the resulting spectrum. The spectrum was once again flat. This procedure was repeated at intervals up to a maximum velocity of 240ft/sec. The results were identical for tunnel velocities up to 200ft/sec. Above this speed, the spectrum signal levels for the freely vibrating support were less than that for the stiffened case.

#### **4. Quasi-two-dimensional Cylinder Investigation**

Vortex shedding in the 2-D cylinder wake was investigated for freestream velocities from 114ft/sec to 241ft/sec. The tunnel was stabilized at the desired speed and the probe was moved to a position well away from the cylinder wake. The CTA high-frequency balance was adjusted using the built-in square wave test to provide an optimum output response. The hot-film probe was then positioned in the center of the cylinder span, one cylinder diameter (1.5in.) downstream from the rear stagnation point and one-half diameter in the cross-stream direction. The initial placement is sketched in figure 32.

The probe was then moved incrementally in the cross-stream direction until the DISA RMS Unit showed a maximum RMS voltage. This indicated a region of maximum turbulence. The probe position was further refined until the coherent signal displayed on the spectrum analyzer was maximized. The volts<sup>2</sup> display was used as the spectrum analyzer manual recommended this display for periodic signals. This investigator found it to be superior to the other display options. The spectrum analyzer averaging function was then activated and 128 frames were averaged. The resulting display was printed. The tunnel was then stabilized at a new speed and the process was repeated. As tunnel velocity increased, the location of maximum turbulence tended to move slightly downstream and slightly toward the center of the cylinder. This migration was not precisely measured, however, it is indicated in figure 32. Shedding frequency was then plotted as a function of freestream velocity.

The effect of boundary layer tripping was investigated at a freestream velocity of 94ft/sec. A spectrum was first obtained as described above for the cylinder without boundary layer tripping. Boundary layer trips were then installed and the test was repeated.

Three-dimensional effects were evaluated at a freestream velocity of 201ft/sec. The high velocity was chosen in anticipation of minimal 3-D effects. The probe was

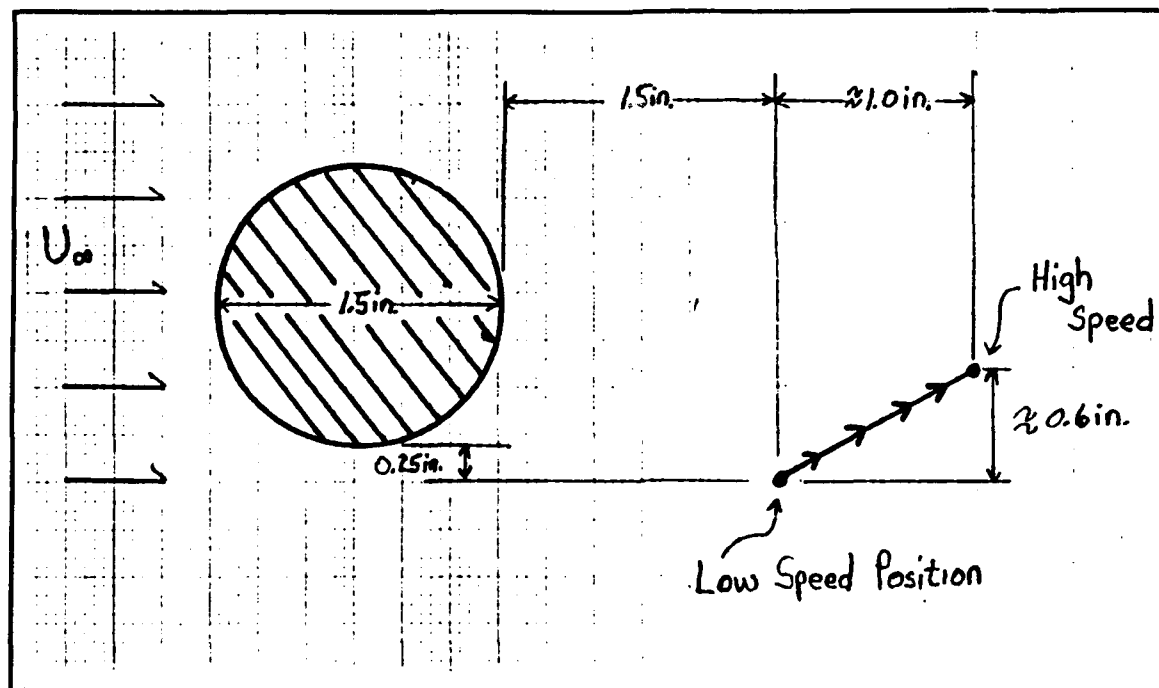


**Figure 32.** Hot-film Survey Position for the 2-D Cylinder Showing the Migration of the Position for Maximum Hot-film Signal Fluctuation

slewed vertically 2in. toward the cylinder tip and the test was repeated. The probe was slewed another 2in. toward the tip and a third test was run.

## 5. Model Wake Investigation

The procedures refined during the 2-D cylinder investigation produced acceptable results when used for the model wake surveys. The freestream velocities ranged from approximately 20ft/sec to 80ft/sec. The upper limit was due to the loss of coherent spectra as Reynolds number increased into the critical range. Wake spectra were obtained for vertical stations 2, 3, 5 and 7 on the standard model. Wake spectra were obtained for station 3 and a location midway between stations 6 and 7 for the modified model. The vertical stations are shown in figure 14. The spectrum analyzer prints were used to construct plots of shedding frequency vs. freestream velocity for both models.

## **IV. RESULTS AND DISCUSSION**

### **A. QUASI-TWO-DIMENSIONAL CIRCULAR CYLINDER**

Although the study of two-dimensional cylinder wakes was not the focus of this research, these results are presented here for comparison with the results obtained in the model wakes. The two-dimensional cylinder tests were limited to hot-film wake surveys.

#### **1. Vortex Shedding Frequency**

The two-dimensional cylinder vortex shedding frequency was measured for tunnel speeds from 33ft/sec to 241ft/sec, corresponding to Reynolds numbers from  $2.7 \times 10^4$  to  $1.9 \times 10^5$ . Figures C9 through C19 of Appendix C show the resulting spectrum analyzer displays. Some broadening of the spectrum was evident as Reynolds number increased, however the spectrum remained well defined throughout the range of velocities tested. Figure 33 is a plot of frequency  $\times$  diameter vs. velocity for the two-dimensional cylinder. Frequency  $\times$  diameter was chosen for the vertical axis because the slope of the resulting first-order curve fit represents the Strouhal number. The plot showed a linear change in frequency as velocity increased with a Strouhal number of 0.174. There was very little scatter in the data. These results demonstrated that, after optimization, the instrumentation could detect a coherent structure in a cylinder wake and display the vortex shedding frequency with acceptable precision.

#### **2. Boundary Layer Tripping Effects**

Boundary layer tripping effects were evaluated at a tunnel velocity of 94ft/sec ( $Re = 7.4 \times 10^4$ ). Figures C20 and C21 of Appendix C show the resulting spectrum analyzer displays. Although the display scales differed, it was evident that the tripping

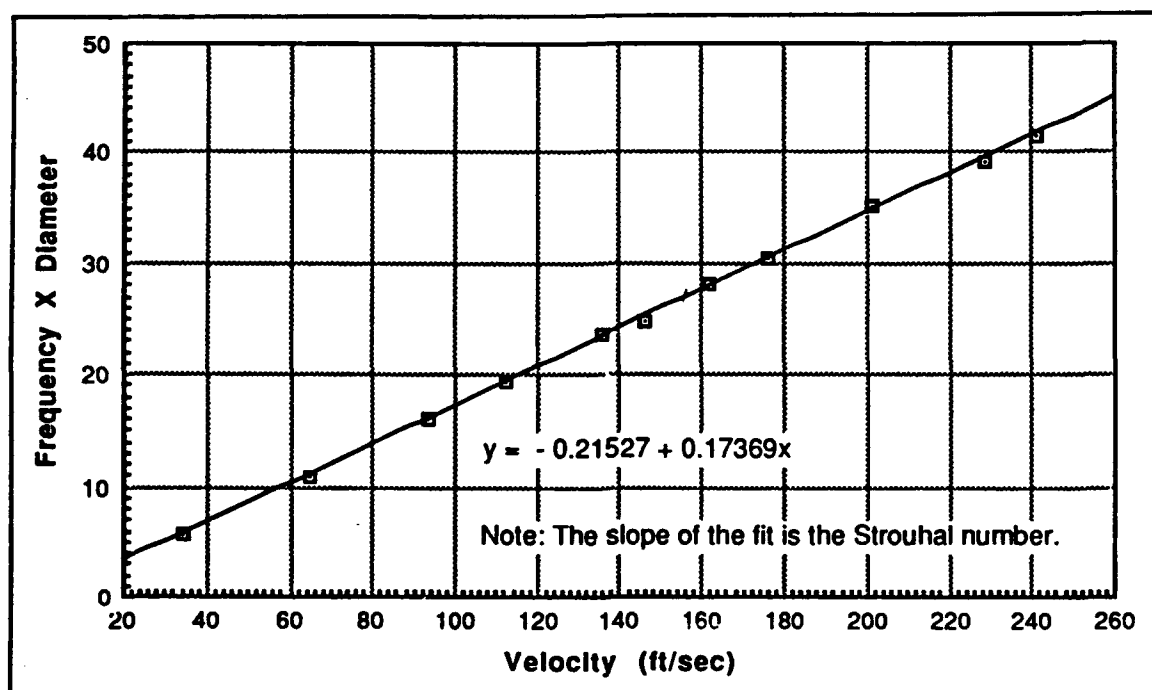


**Figure 33.** Frequency X Diameter vs. Velocity for the Quasi-two-dimensional Cylinder

devices had effectively transitioned the boundary layer and that the cylinder wake was fully turbulent. No coherent spectra were discernable. The boundary layer tripping devices installed on the pod models for base pressure tests were removed for the hot-film surveys based on these results.

### 3. Three-dimensional Effects

Three-dimensional effects were evaluated by obtaining vortex shedding spectra for three separate vertical positions in the cylinder wake at a test velocity of 201 ft/sec ( $Re = 1.6 \times 10^5$ ). This Reynolds number was approximately equal to the maximum Reynolds number for which vortex shedding spectra were obtained for the pod models. The resulting 2-D cylinder spectra are shown in figures C22 through C24 in Appendix C. A 2 in. vertical probe movement toward the cylinder tip resulted in a significant reduction in signal amplitude. The center frequency of the shedding spectra increased by approximately

10Hz [Fig. C23]. An additional 2in. vertical probe movement further reduced the signal amplitude, resulting in a poorly defined, broadband spectrum. The center frequency again increased by approximately 10Hz, although the precise center frequency location was difficult to determine [Fig. C24]. These results showed significant three-dimensional effects in the wake of the quasi-two dimensional cylinder. Accordingly, particular attention was given to the hot-film probe's vertical position for measurements in the model wakes.

## **B. FLOW VISUALIZATION**

### **1. Vortex Formation Region**

The vortex formation region for the standard configuration is shown in figure 34. Vortex shedding was evident in the wake of this model; however, obtaining well

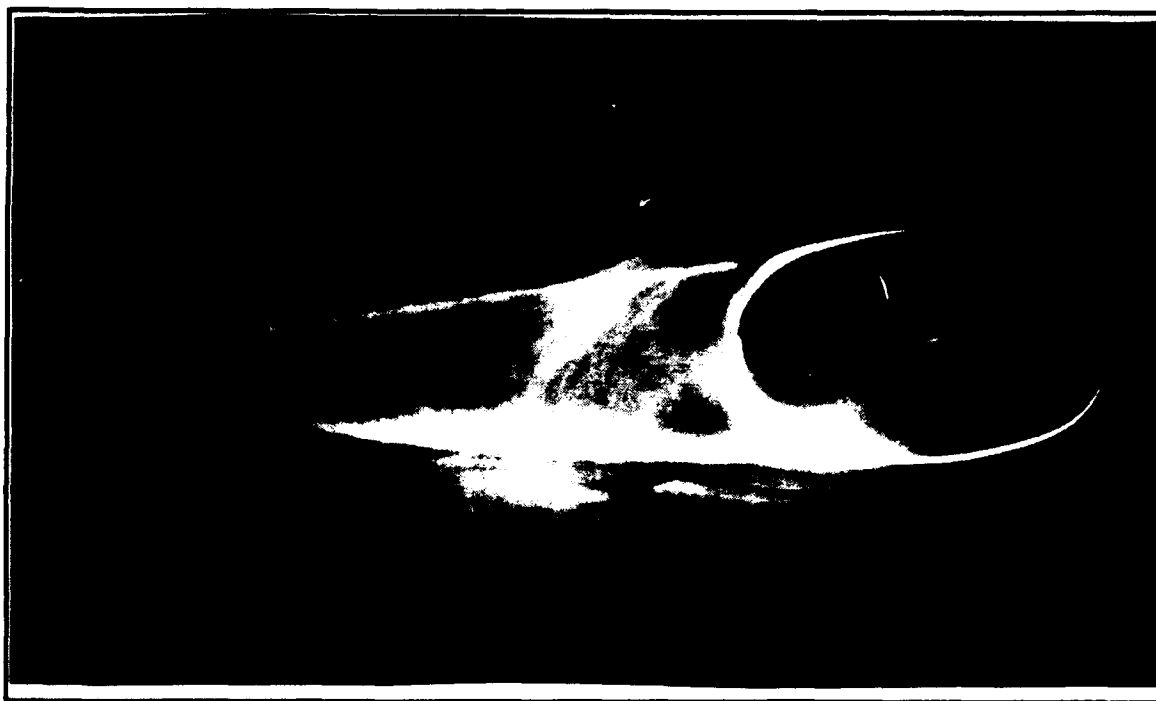


**Figure 34. Vortex Formation Region, Standard Configuration, Vertical Station 7**

defined vortex formation images was difficult. Vortex shedding was visualized at vertical stations 6 through 8. A symmetric pair of attached Föppl vortices was imaged at stations 2

through 5 [Fig. 35]. These vortices are normally associated with flows at a much lower Reynolds number. It is possible that downwash from flow coming over the tip of the

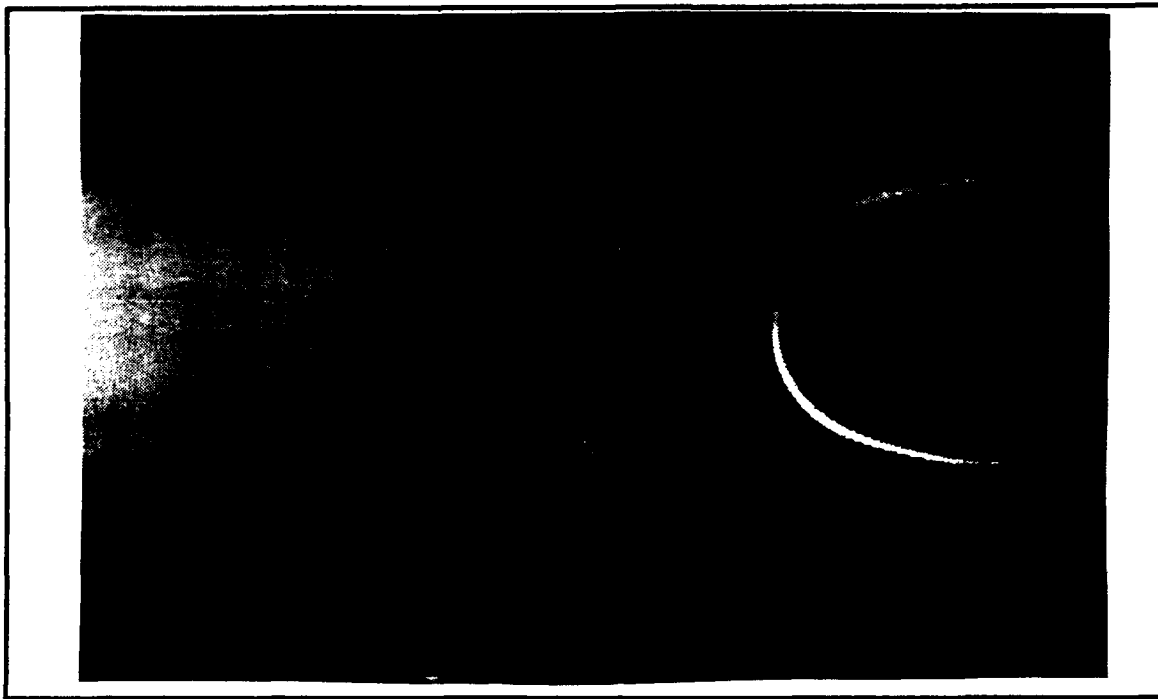


**Figure 35. Vortex Formation Region, Standard Configuration, Vertical Station 4**

radome [Fig. 36] decreased the effective Reynolds number at those locations. The wake had a decided laminar appearance in this region. Imagery obtained using a lateral laser sheet orientation confirmed that the flow just downstream of the radome had the same general appearance of the undisturbed flow upstream of the model; as evidenced by the tight circular shape of the smoke column [Fig. 37]. The wake from the radome base region had an entirely different appearance [Fig. 38]. The flow was separated and the smoke column was not visible in the wake. Additional views of the standard model vortex formation region are shown in figures D1 and D2. of Appendix D.

Imaging the vortex formation region of the modified model was comparatively simple. Figure 39 shows a typical frame. The general appearance was unchanged for the entire vertical extent of the cylindrical portion of the radome as shown in figures D3



**Figure 36. Vortex Formation Region, Standard Configuration, Lateral Station 1**

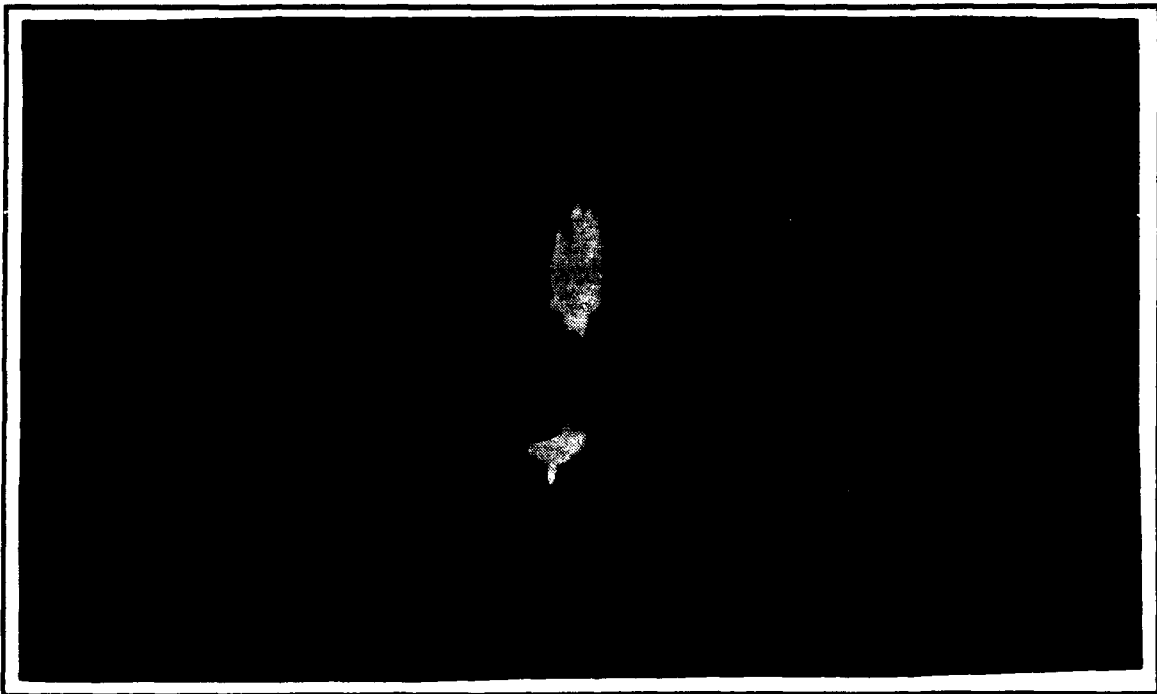


**Figure 37. Vortex Formation Region, Standard Configuration, Longitudinal Station 3, Smoke Tube "High"**



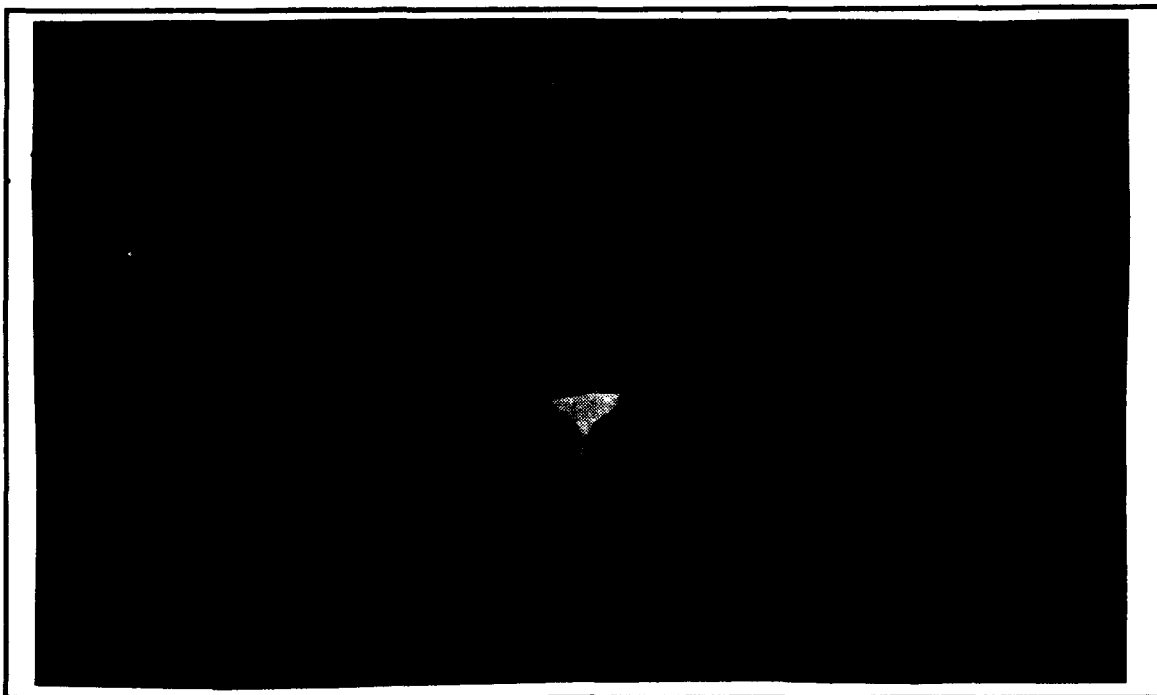


**Figure 38.** Vortex Formation Region, Standard Configuration, Longitudinal Station 3, Smoke Tube "Low"

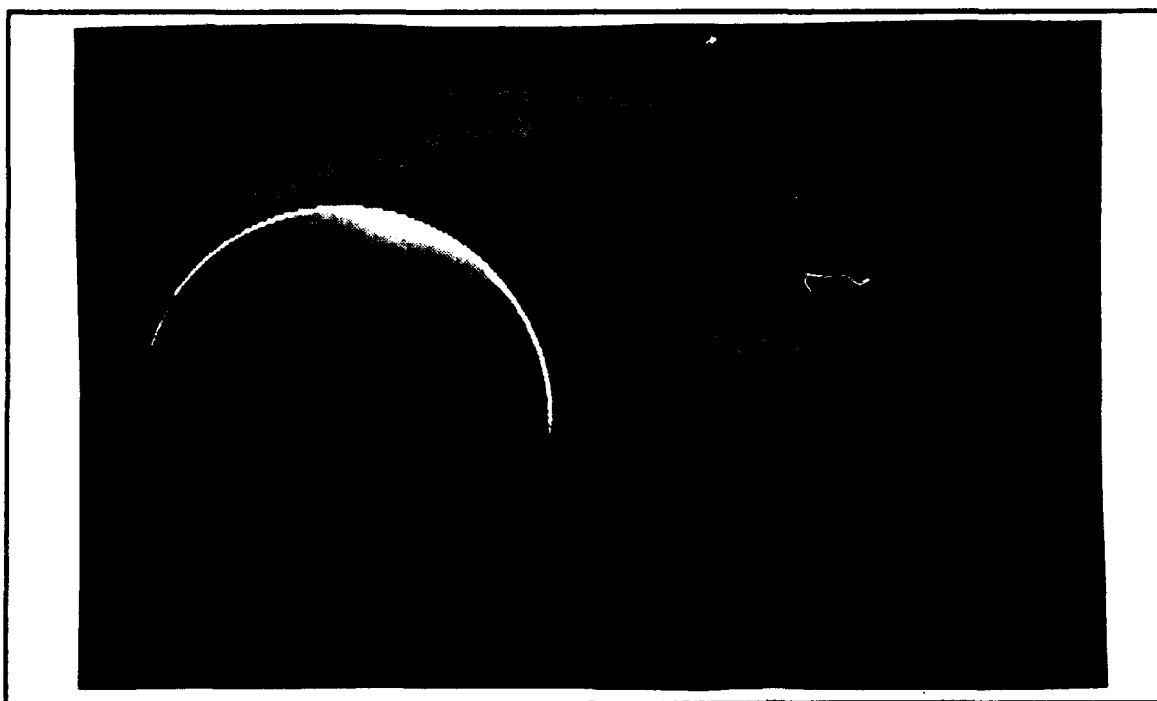


**Figure 39.** Vortex Formation Region, Modified Configuration, Vertical Station 1

through D6 of Appendix D. This indicated that the wake of the modified configuration was significantly more two dimensional than was the wake of the standard configuration.

Vortex shedding was also imaged in the base region [Figures D7 and D8]. The modified configuration exhibited considerably less downwash [Fig. 40] which may account for the strong vortex shedding imaged at vertical station 1. Figure 41 shows the dispersal of the

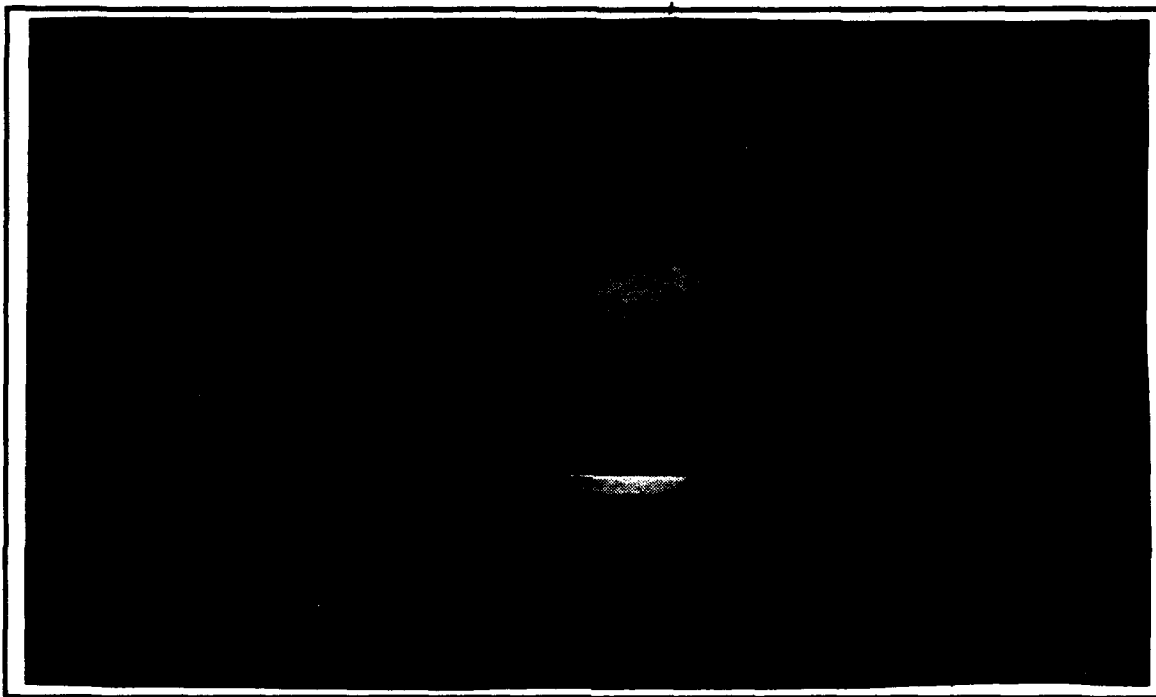


**Figure 40. Vortex Formation Region, Modified Configuration, Lateral Station 1**

smoke column just downstream of the modified radome. The image resembles that seen in the standard radome wake [Fig. 37].

In summary, vortex formation was confined to the base region on the standard configuration. These vortices were fairly difficult to image. The modified configuration exhibited strong vortex shedding over its entire vertical extent.

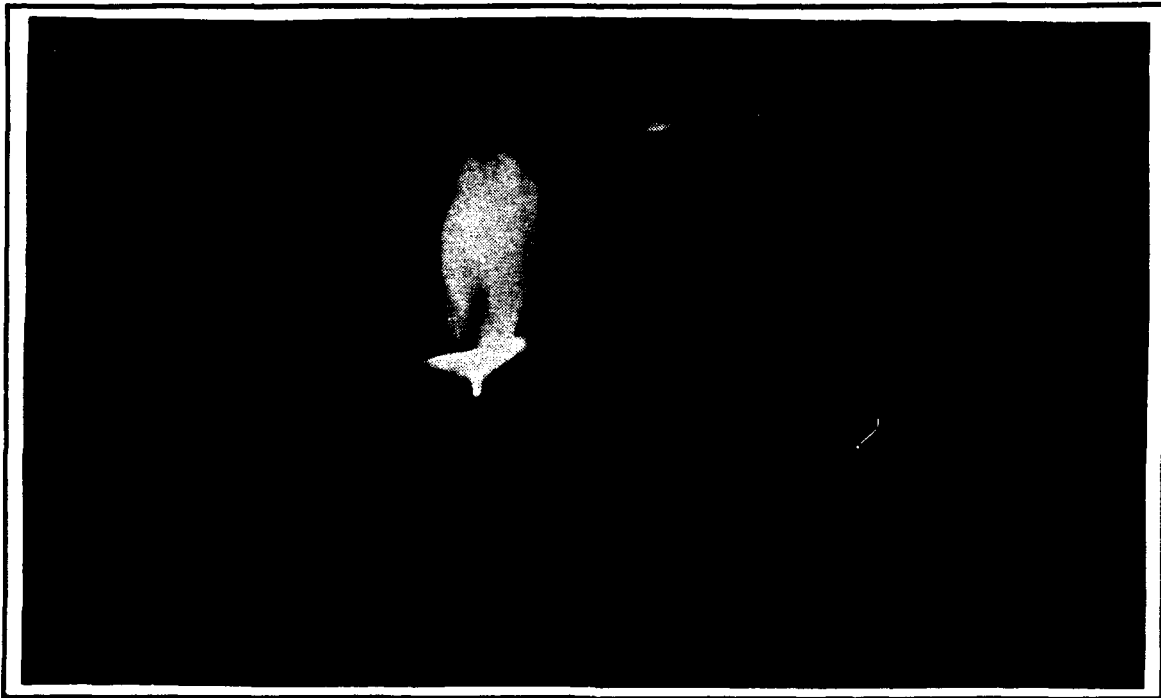


**Figure 41. Vortex Formation Region, Modified Configuration, Longitudinal Station 3, Smoke Tube "Medium"**

## **2. Near Wake Region**

The appearance of the standard configuration's near wake varied considerably along the model's vertical extent. Figure 42 shows the wake typical of vertical stations toward the radome tip. The flow appeared to be laminar with a very well defined smoke tube and some wake necking downstream of the model. The Föppl vortices were discernable as well. The wake near the base contained vortices which altered the appearance significantly [Fig. 43]. Alternating vortices generated lateral excursions in the wake producing an image resembling a classic Karman vortex street. Obtaining still images of these vortices was difficult, however, slow motion replays of the video tape recordings showed a definite pattern as the vortices shed from alternate sides of the radome. The wake "snaked" or "fishtailed" behind the radome in a cyclic manner. Figures 44 and 45 show the downstream appearance of the near wake. The stem-like structure connecting the smoke

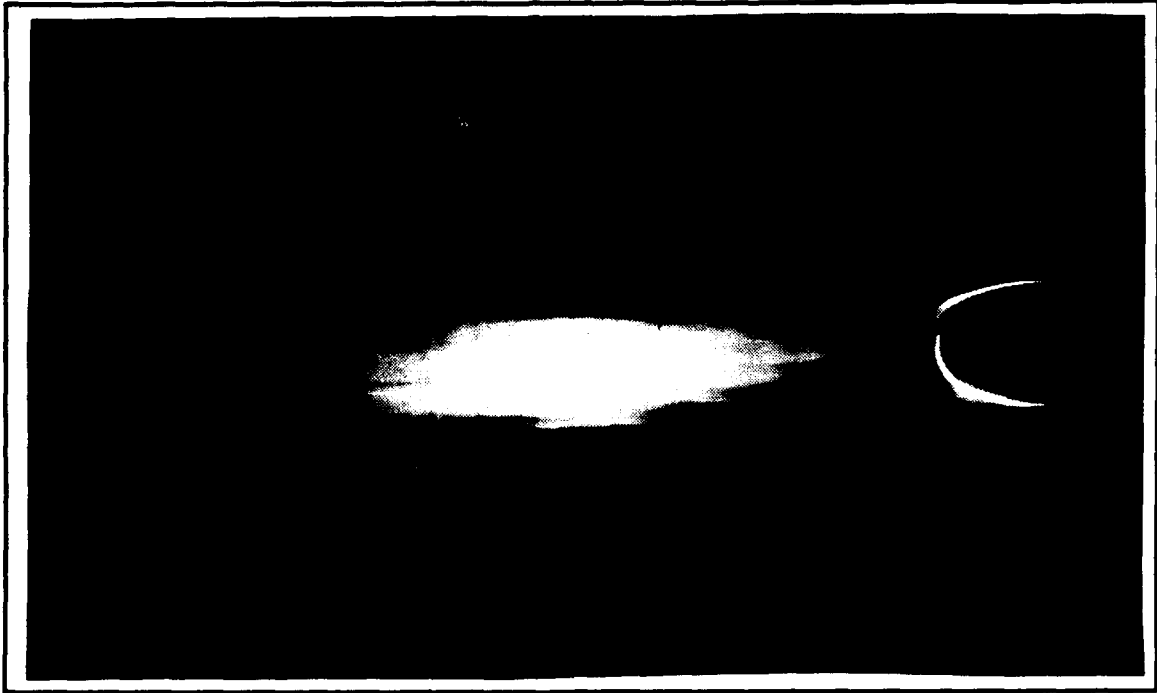


**Figure 42.** Near Wake Region, Standard Configuration, Vertical Station 3

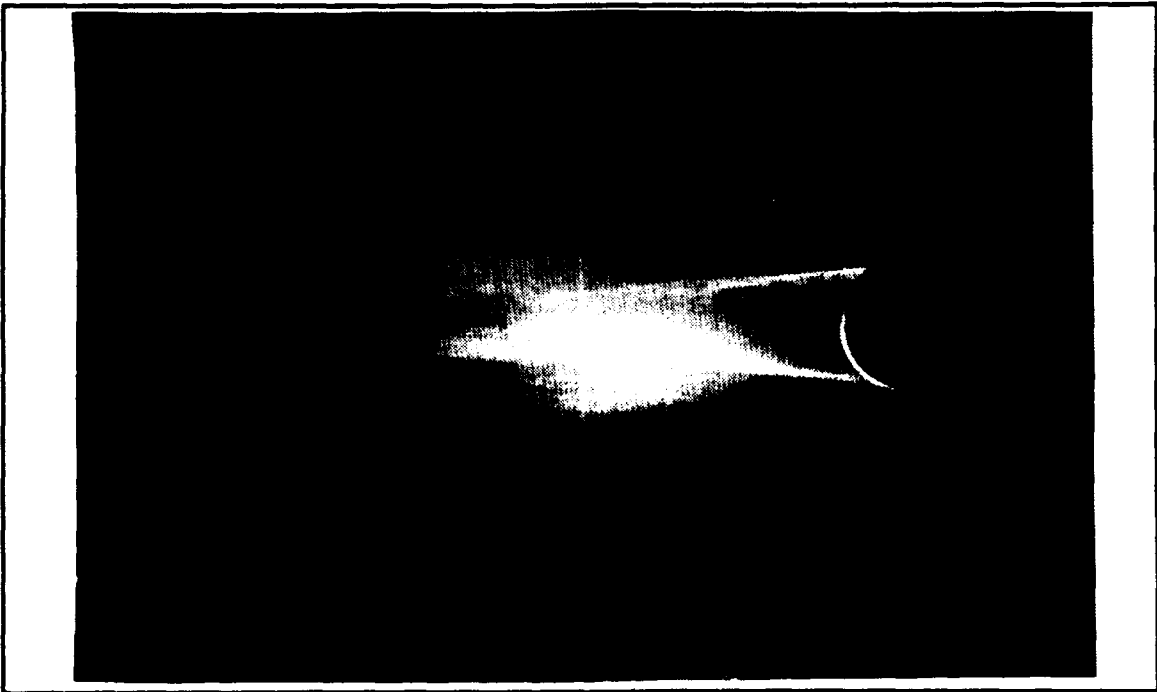


**Figure 43.** Near Wake Region, Standard Configuration, Vertical Station 7

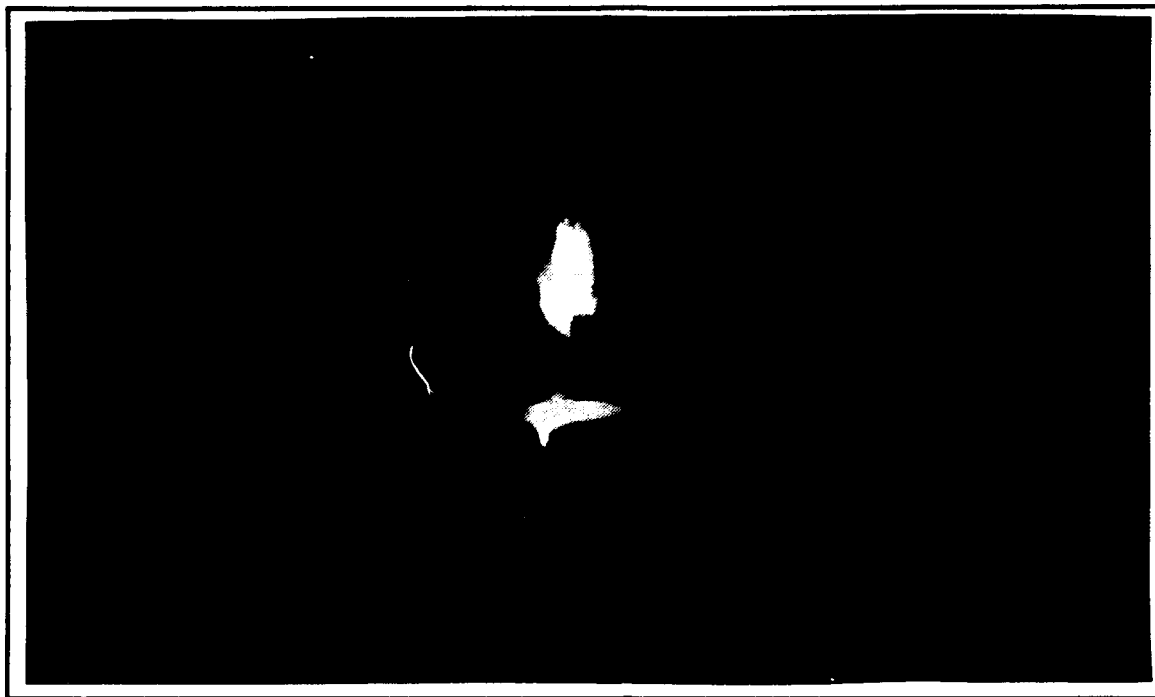


**Figure 44.** Near Wake Region, Standard Configuration, Longitudinal Station 4, Smoke Tube "High"

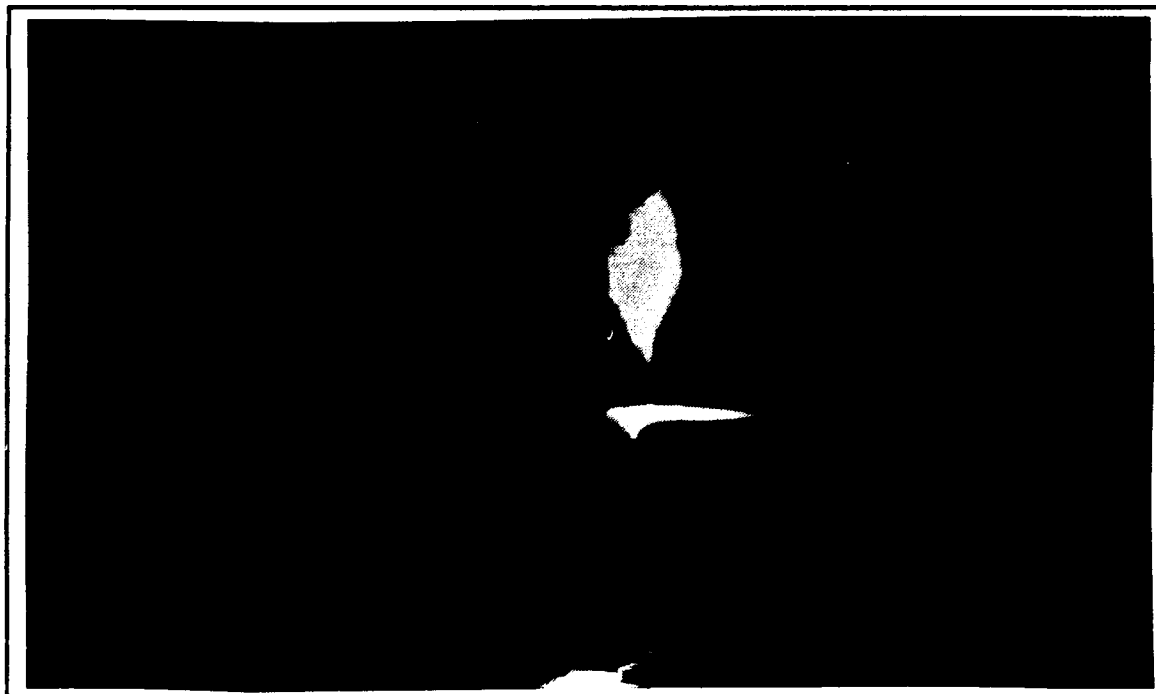


**Figure 45.** Near Wake Region, Standard Configuration, Longitudinal Station 5, Smoke Tube "High"

tube to the pod body was located on the model centerline and alternated slightly from side to side. A frame by frame comparison of the video tape recording of the stem alternating and the recording of the vortex shedding near the radome base was conducted. The vortex shedding frequency and stem alternating frequency were quite close with approximately 4 to 5 video frames required for each cycle. Figure 45 also shows vortices rolling up into the radome wake from the pod body and pylon.

A vortex street was quite evident in the modified configuration's near wake [Figures 46 and 47]. Additional views are shown in figures D9 and D10 of Appendix D.

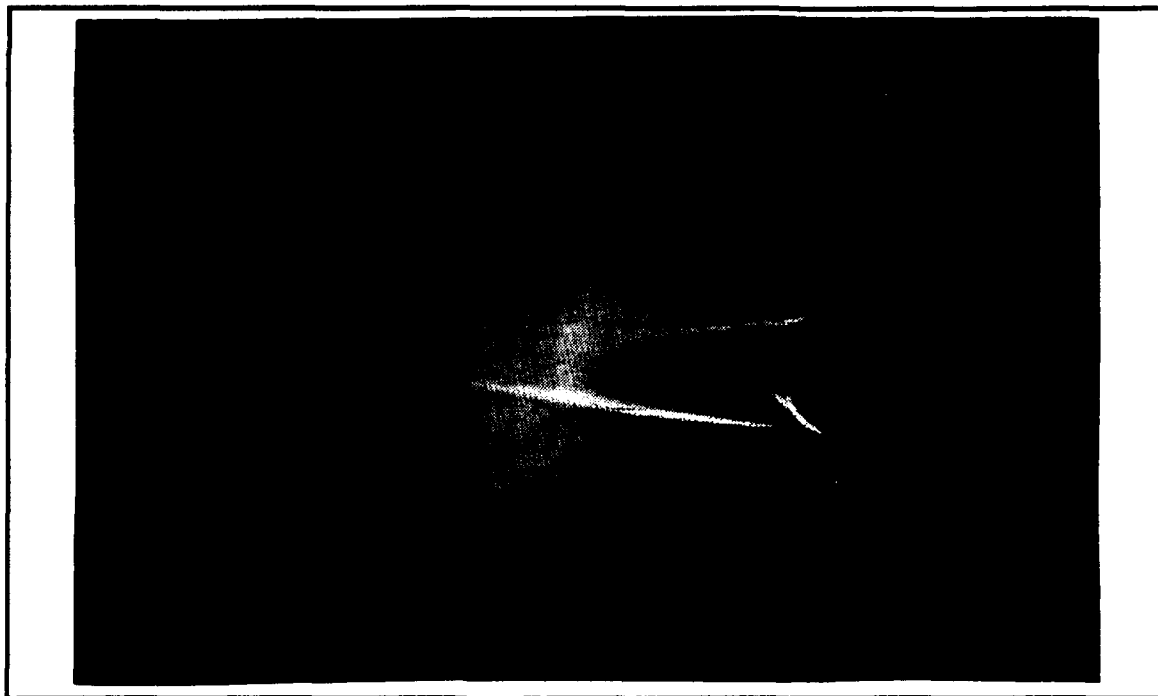


**Figure 46. Near Wake Region, Modified Configuration, Vertical Station 6**

A well-defined street was imaged for all vertical stations of the modified configuration, indicating that strong vortex shedding was occurring along the complete vertical extent of the model.

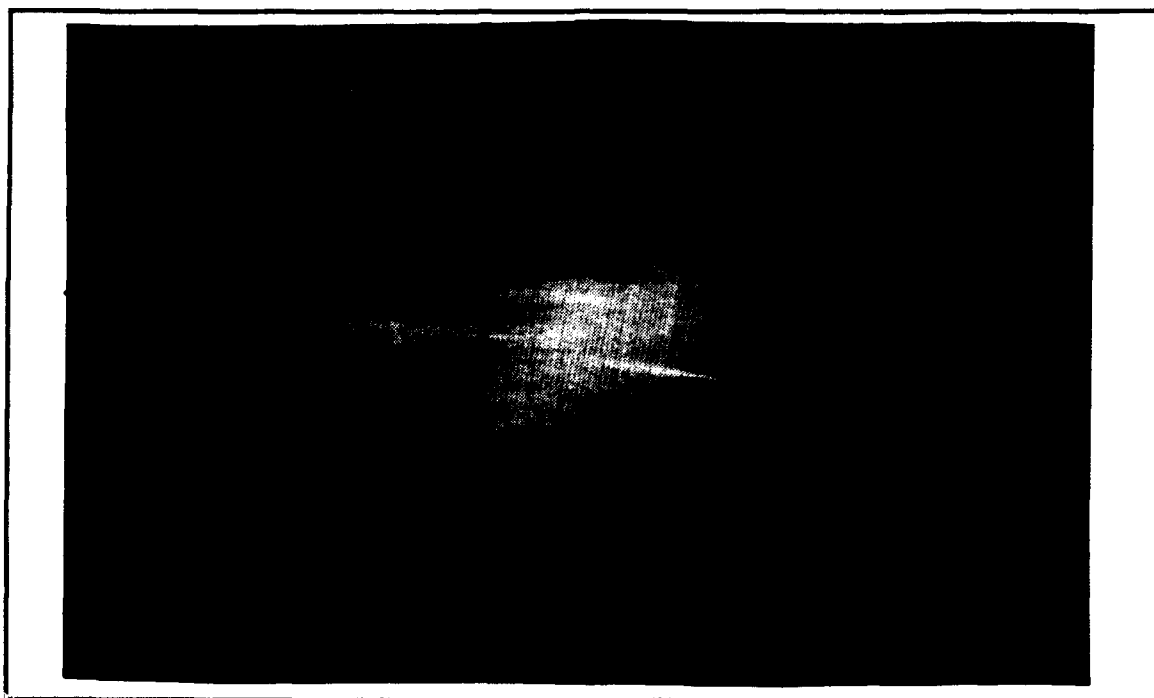


**Figure 47. Near Wake Region, Modified Configuration, Vertical Station 3**

In summary, the near wake flow visualization results reinforced the results obtained in the vortex formation region. The modified configuration exhibited much more significant vortex shedding.

### **C. BASE PRESSURE COEFFICIENT**

The base pressure coefficient provides some insight into the three-dimensional effects present in a flow. The base pressure coefficients for the pod models were obtained for tripped and untripped boundary layer conditions at freestream velocities of 93ft/sec to 270ft/sec. Three data samples were recorded for each velocity. The resulting base pressure coefficients were averaged and plotted. A standard deviation was calculated for each set of three samples. The maximum standard deviation was in the third decimal place, indicating that the data were quite repeatable.

## **1. Untripped Boundary Layer**

The base pressure coefficients for the standard configuration without boundary layer tripping are shown in figure E1 of Appendix E. The non-dimensional vertical coordinate was obtained by dividing the vertical height of the associated pressure tap by the vertical height of the radome (3.9in.). The significant variation in  $C_{pB}$  exhibited in this plot was attributed to inconsistent boundary layer transition points on the radome. End effects, evidenced by suction maxima at the radome tips and suction minima at the radome bases, were also observed. The boundary layer appeared to be well into transition at a freestream velocity of 203ft/sec. Above this speed, the base pressure coefficient plots began collapsing toward a single line; however, the boundary layer did not fully transition in these tests.

The base pressure coefficients for the modified configuration without boundary layer tripping were more varied than those of the standard configuration [Fig. E2]. The abrupt changes in radome cross section near the base appeared to heavily influence the base pressure measurements. The boundary layer did not appear to reach full transition in this case either.

## **2. Tripped Boundary Layer**

The results obtained from the untripped tests indicated that boundary layer tripping would be required for consistent base pressure measurements. Since the full-scale pod boundary layer is fully tripped in the flight velocity regime of interest, it was decided that tripped model results would be more significant. Boundary layer tripping devices were installed on the model radomes and the tests were repeated.

Figure E3 of Appendix E shows a marked change in the base pressure coefficient plot for the standard configuration. Stations 2 through 5 appeared to be fully transitioned, with nearly constant values of  $C_{pB}$  as velocity increased. There was a marked



break point at station 5 and the flow appeared to become two-dimensional for stations 5 through 7. The base pressure coefficients for these stations were nearly constant at a given speed. Stations 1 and 8 showed end effects similar to those observed in the untripped tests.

The base pressure coefficients for the modified model with boundary layer tripping are shown in figure E4 of Appendix E. These results differed considerably from the untripped case. Two distinct flow regions were evident. In the first region, the wake behind the radome cylinder became more two-dimensional as Reynolds number increased. The second region was near the model base. The  $C_{pB}$  plot for this area had the same general appearance as the that of the standard radome's base region.

Figures E5 and E6 of Appendix E show  $C_{pB}$  plotted as a function of local Reynolds number. A local Reynolds number was calculated for each vertical station using the radome width at that station as the characteristic length. Quasi-two-dimensional flow is indicated by coincident plots. Stations 5, 6, and 7 formed a quasi-two-dimensional flow region on the standard model [Fig. E5]. Stations 2 through 4 formed a quasi-two-dimensional flow region on the modified model [Fig. E6]. The  $C_{pB}$  for station 1 collapsed to the same value as stations 2 through 4 at higher Reynolds numbers.

The base pressure coefficient tests indicated that both models had quasi-two-dimensional flow regions in their wakes. This was limited to the radome base area for the standard configuration. The modified configuration exhibited extensive quasi-two-dimensional flow regions, both in the wake behind the radome base and in the wake behind the cylindrical radome. This concurred with the flow visualization results, indicating that the modified configuration wake was significantly more two-dimensional than was the standard configuration wake.

### 3. Yaw Sensitivity

The sensitivity of  $C_{pB}$  to yaw angle was evaluated for both configurations with boundary layer tripping at a freestream velocity of 180ft/sec. The base pressure coefficients of both configurations were insensitive to yaw angles less than  $2.5^\circ$ . Figures E7 and E8 of Appendix E show the  $C_{pB}$  plots for yaw angles up to  $15^\circ$ .

Increased yaw angle eliminated the two-dimensional flow region near the base of the standard radome [Fig. E7]. Interestingly, LASC test pilots reported that slight yaw angles eliminated pod vibrations on some of the ALQ-78 pod test flights.

The  $C_{pB}$  of the modified configuration was not particularly sensitive to increased yaw angle [Fig. E8]. The value of  $C_{pB}$  changed considerably; however the shape of the curve was unchanged. This is not surprising, given the cylindrical shape of the modified radome.

### D. VORTEX SHEDDING FREQUENCY

Vortex shedding frequency was measured in the wakes of both models for freestream velocities of 20ft/sec to approximately 80ft/sec. Using a logarithmic frequency scale and wider bandwidth on the spectrum analyzer enhanced the display of weak, broadband spectra. This enabled vortex shedding frequency measurements at velocities where a linear scale and narrow bandwidth produced a noiselike display with no coherent spectra. Coherent vortex shedding could not be detected above 82 ft/sec ( $Re \approx 1.9 \times 10^5$ ). A wake Strouhal number could not be calculated since the velocity regimes for the  $C_{pB}$  and hot-film measurements did not overlap.

#### 1. Standard Configuration

Vortex shedding frequencies for the standard configuration were measured at vertical station 7. The resulting spectrum analyzer displays are shown in figures C25 through C33 of Appendix C. A coherent structure was present in the wake at velocities up

to approximately 69ft/sec ( $Re \approx 1.3 \times 10^5$ ). A discrete shedding frequency could not be measured at higher velocities. Figure C27 shows an overlay plot of the spectra obtained at two different velocities. Frequency  $\times$  Diameter is plotted as a function of velocity in figure 48. The first-order fit indicated that the Strouhal number for this flow was 0.297. The data scatter was minimal.

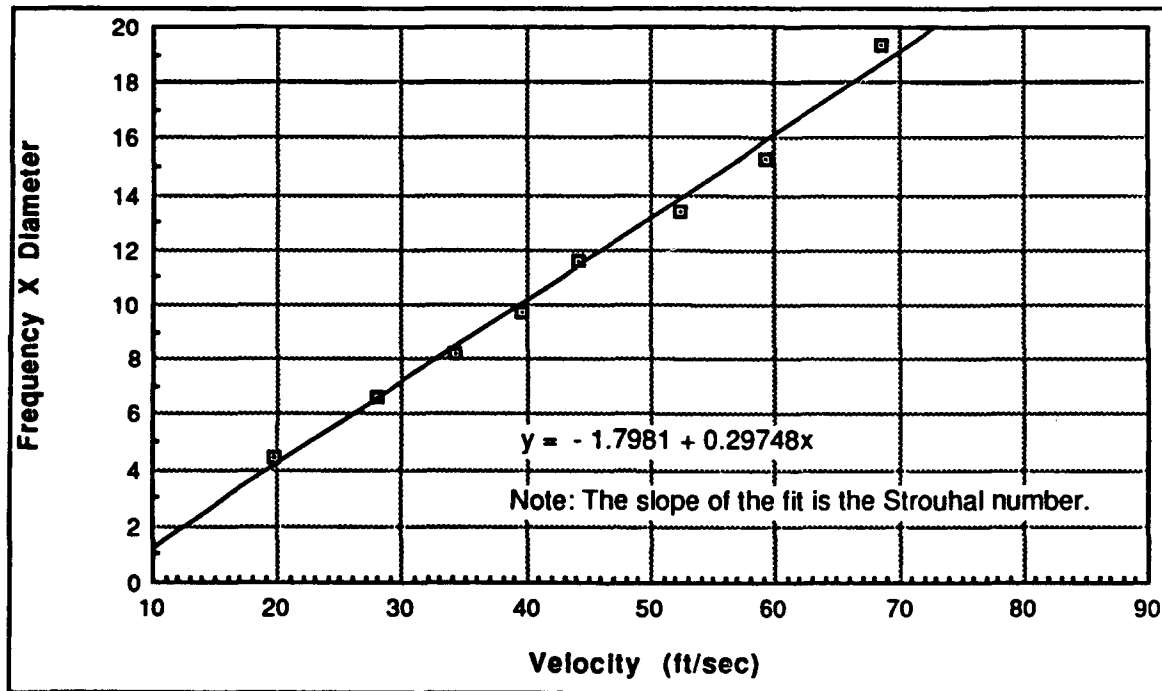


**Figure 48.** Frequency  $\times$  Diameter vs. Velocity for the Standard Configuration

## 2. Modified Configuration

Vortex shedding frequencies for the modified configuration were measured at vertical station 3 and at a location between vertical stations 6 and 7. The spectrum analyzer displays for the radome wake (vertical station 3) are shown in figures C34 through C42 of Appendix C. The vortex shedding signals were stronger than those found in the standard configuration wake and had narrower bandwidths. Frequency  $\times$  Diameter is plotted as a function of velocity in figure 49. The first-order fit indicated that the Strouhal number for this flow was 0.143. Again, the data scatter was minimal.

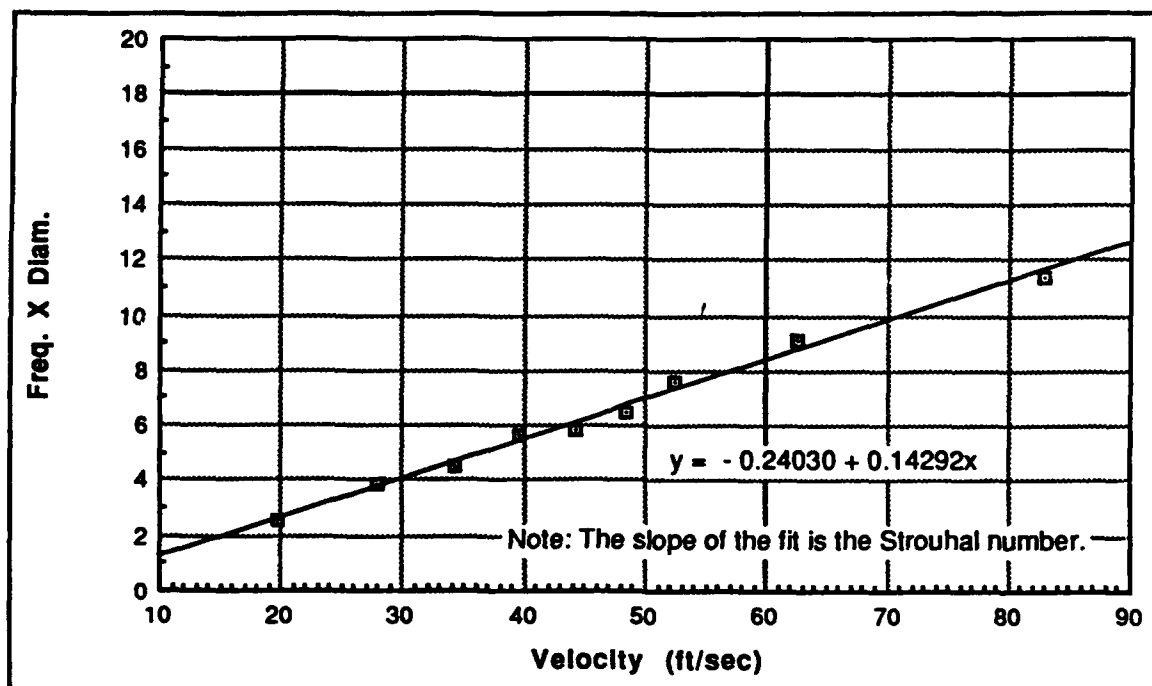


**Figure 49.** Frequency x Diameter vs. Velocity for the Modified Configuration, Radome Wake

The spectrum analyzer displays for the adapter collar wake (between vertical stations 6 and 7) are shown in figures C43 through C48 of Appendix C. The vortex shedding signals were similar to those found in the standard configuration wake, although the shedding frequency was considerably lower. The flow was probably three-dimensional, with the spectra dominated by the radome wake and pod body signals. This may have precluded discrete measurements of adapter collar wake vortex shedding frequency in this region. Frequency x Diameter is plotted as a function of velocity in figure 50. The first-order fit indicated that the Strouhal number for this flow was 0.124. The data scatter was also minimal. Theory suggests that the Strouhal number should be higher, due to the smaller body diameter in this region.

Figure 51 is a composite plot of the three data sets. The significant difference between the Strouhal numbers for the two model configurations is unexplained. It is

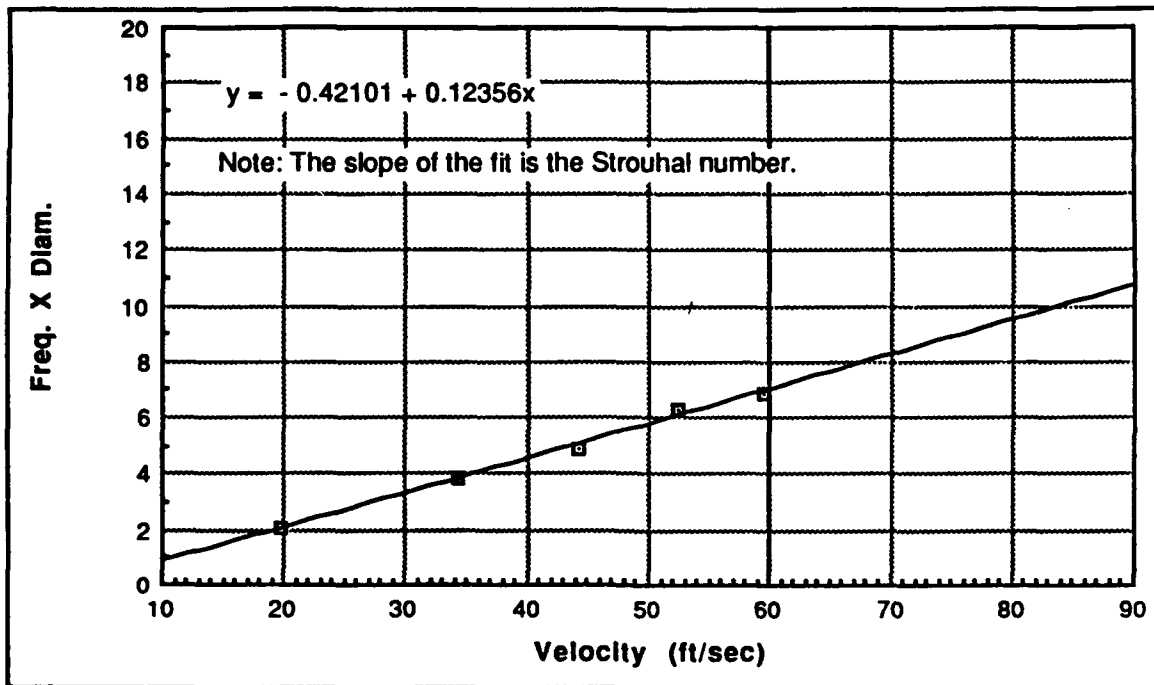


**Figure 50.** Frequency x Diameter vs. Velocity for the Modified Configuration, Adapter Collar Wake

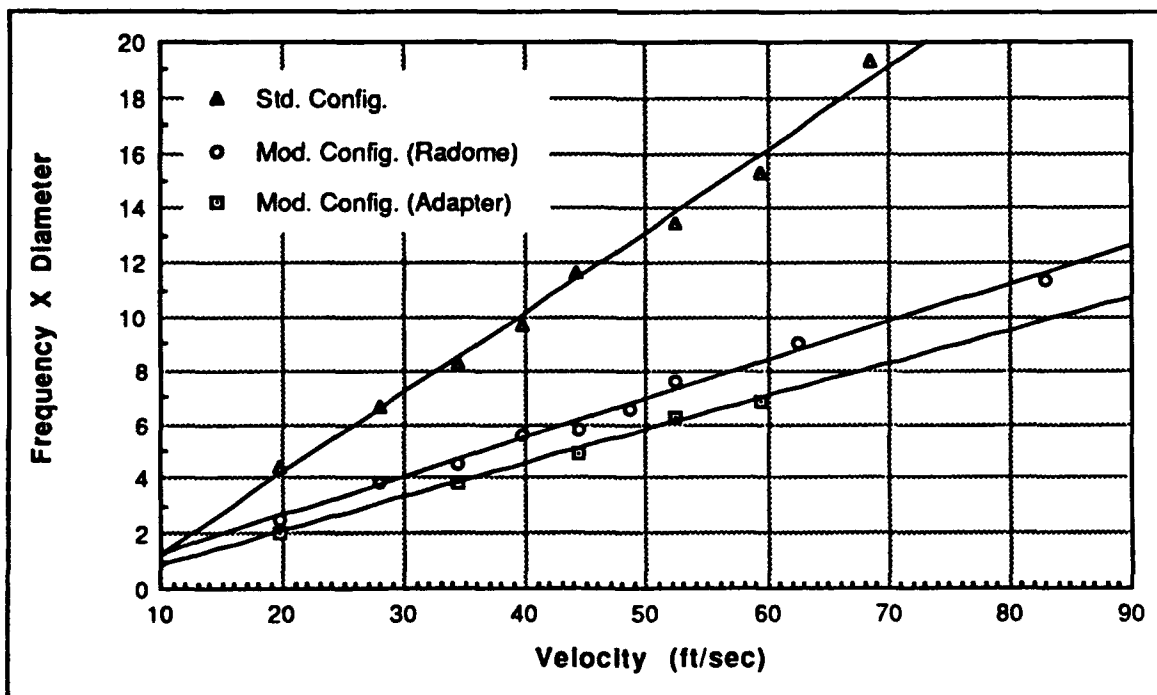


**Figure 51.** Composite Plot of Frequency x Diameter vs. Velocity

possible that wake Strouhal numbers, had they been available, would have collapsed to a single value.

## **V. CONCLUSIONS AND RECOMMENDATIONS**

### **A. CONCLUSIONS**

#### **1. General**

The vortex shedding phenomenon observed in the model wakes was in agreement with well established theory for three-dimensional bluff body flows. The modified configuration's wake was more two-dimensional than that of the standard configuration and contained stronger vortices. The standard configuration shed vortices at approximately twice the frequency of the modified configuration.

Extending these general scale model results to the full-scale case, it is expected that the modified configuration will experience flow-induced vibrations caused by asymmetric vortex shedding. These vibrations can be expected to be stronger than those documented by LASC for the standard pod configuration. The airspeed at which vortex shedding "locks-in" with the pod structure's natural frequency could be considerably higher for the modified configuration, based on the very low Strouhal number observed during these tests. It is also likely that the vortex shedding from the modified configuration will excite the 60Hz second harmonic of the pod natural frequency.

Using an airspeed envelope build-up flight test methodology, the General Instrument design could be flown in a research and development flight test program with acceptable risk.

#### **2. Current P-3C Flight Restriction**

The contribution made by compressibility to the standard configuration's vibration problem has not been adequately established. As a result, the Mach restriction contained in the aircraft manual may be in error. If the pod vibrations are indeed caused by

asymmetric vortex shedding, the Mach 0.57 flight restriction fails to adequately protect the pod over much of the aircraft's operating envelope while simultaneously restricting flight in the heart of the maximum range cruise regime [Fig. 6].

The roles played by compressibility and asymmetric vortex shedding could be investigated in a simple flight test program using a suitably instrumented ALQ-78 pod with a standard radome. Removing the ventral fin should allow sufficient pod vibration for definitive results. A test altitude of 2,000ft would provide an adequate margin between the true airspeed corresponding to Mach 0.57 (approximately 376kt) and the true airspeed for vibration onset measured during the LASC flight tests (approximately 358kt). The low altitude also ensures that the Reynolds number will be sufficiently high for supercritical vortex shedding. A build-up method could be employed to gradually increase the flight test velocity while documenting pod vibrations. If the pod vibrations are caused by vortex shedding, the shedding frequency should lock-in with the third harmonic of the pod's resonant frequency at a true airspeed of approximately 358kt. If, on the other hand, the vibrations are compressibility related, the lock-in should not occur until approximately 376kt true airspeed.

This flight test program could accomplish two significant objectives. First, it could confidently establish a valid flight restriction for aircraft equipped with the standard ALQ-78 pod. Second, it could provide valuable insight into the characteristics of the flow around the pod which could be used in the development of pod modifications.

### **3. Test Instrumentation**

The available test instrumentation was adequate for this research with the exception of the particle seeding technique for the laser sheet flow visualization system. The smoke generator and tube arrangement restricted the flow visualization tests to a very narrow speed range, resulting in a very limited characterization of the flow field. This



limitation was discussed in some detail by Sommers [Ref. 29].

The Mitsubishi video copy processor provided high quality prints of video images. This was a significant enhancement to the laser sheet flow visualization system.

The spectrum analyzer and video hard copy unit provided by the NASA Ames Research Center significantly enhanced the results achieved in these experiments, providing flexible and straightforward documentation of the hot-film output.

## **B. RECOMMENDATIONS**

The following recommendations are based on the results of this investigation:

1. Conduct a flight test program to establish a valid flight restriction for P-3C aircraft equipped with a standard ALQ-78 antenna pod.
2. Acquire an improved seeding system for use with the laser sheet.
3. Acquire a spectrum analyzer and video hard copy unit for permanent use in the NPS low-speed wind tunnel.

## REFERENCES

1. NAVAIR 01-75PAC-1.1, *NFO/Aircrew NATOPS Flight Manual, Navy Model P-3C Aircraft*, p. 8-298, 15 February, 1986, Change 3 dated 30 January, 1990.
2. *Ibid.*, Figure 1-87, p. 1-165.
3. Telephone conversation between Mr. Ivan Sachs, LASC Flutter Group, and the author, 8 November 1990.
4. LASC Contractor's Flight Test Report, AER-REP-AC-1, Summary Report 29, pp. A-1 through A-21, 24 October 1969.
5. LASC Contractor's Flight Test Report, AER-REP-AC-1, Summary Report 43, pp. A-2 through A-17, 8 May 1970.
6. LASC Contractor's Flight Test Report, AER-REP-AC-1, Summary Report 44, pp. A-1 through A-2, 22 May 1970.
7. LASC Contractor's Flight Test Report, AER-REP-AC-1, Summary Report 48, p. B-5, 17 July 1970.
8. LASC Contractor's Flight Test Report, AER-REP-AC-1, Summary Report 49, pp. B-19 through B-26, 31 July 1970.
9. LASC Contractor's Flight Test Report, AER-REP-AC-1, Summary Report 57, p. A-1, 20 November 1970.
10. LASC Contractor's Flight Test Report, AER-REP-AC-1, Summary Report 58, pp. C-1 through C-7 and p. D-1, 5 February 1971.
11. LASC Contractor's Flight Test Report, AER-REP-AC-1, Summary Report 59, pp. B-1 through B-3, 26 January 1971.
12. LASC Report LR 25050, *Estimated Effects of Special Stores on the Flight Characteristics of the P-3 Aircraft*, by C. F. Friend, p. 4, 7 January 1972.
13. NAVAIR 01-75PAC-1, *NATOPS Flight Manual, Navy Model P-3C Aircraft*, p. 4-6, 1 December, 1983, Change 4 dated 30 January, 1990.
14. Sarpkaya, T., "Vortex-Induced Oscillations - A Selective Review," *Transactions of the ASME, Journal of Applied Mechanics*, v. 46, no. 2, pp. 241-258, 1979.
15. Bearman, P. W., and Graham, J. M. R., "Vortex Shedding from Bluff Bodies in Oscillatory Flow: A Report on Euromech 119," *Journal of Fluid Mechanics*, v. 99, pt. 2, pp. 225-245, 1980.

16. Blevins, R. D., *Flow-Induced Vibration*, 2d ed., Van Nostrand Reinhold, 1990.
17. NACA Report 1191, *On the Development of Turbulent Wakes from Vortex Streets*, by A. Roshko, 1954.
18. Calvert, J. R., "Experiments on the Low-Speed Flow Past Cones," *Journal of Fluid Mechanics*, v. 27, pt. 2, pp. 273-289, 1967.
19. Bishop, R. E. D., and Hassan, A. Y., "The Lift and Drag Forces on a Circular Cylinder in a Flowing Fluid," *Proceedings of the Royal Society, London, Series A*, v. 277, pp. 32-75, 1964.
20. Blevins, pp. 54-58.
21. Fiedler, H. E., and Wille, R., "Some Observations in the Near Wake of Blunt Bodies," *AIAA Journal*, v. 8, no. 6, pp. 1140-1141, 1970.
22. Gaster, M., "Vortex Shedding from Slender Cones at Low Reynolds Numbers," *Journal of Fluid Mechanics*, v. 38, pt. 3, pp. 565-576, 1969.
23. Achenbach, E., "Vortex Shedding from Spheres," *Journal of Fluid Mechanics*, v. 62, pt. 2, pp. 209-221, 1974.
24. *Laboratory Manual for Low Speed Wind Tunnel Testing*, Department of Aeronautics, Naval Postgraduate School, Monterey, California, October, 1983.
25. *Laboratory Manual for Low Speed Wind Tunnel Testing*, Department of Aeronautics and Astronautics, Naval Postgraduate School, Monterey, California, September, 1989.
26. Renoud, R. W., *Boundary Layer Response to an Unsteady Turbulent Environment*, Master's Thesis, Naval Postgraduate School, Monterey, California, December 1988.
27. Chlebanowski, J. S., *Flow Visualization by Laser Sheet*, Master's Thesis, Naval Postgraduate School, Monterey, California, March 1988.
28. Leedy, D. H., *An Experimental Investigation of a Fighter Aircraft Model at High Angles of Attack*, Master's Thesis, Naval Postgraduate School, Monterey, California, September 1988.
29. Sommers, J. D., *An Experimental Investigation of Support Strut Interference on a Three-Percent Fighter Model at High Angles of Attack*, Master's Thesis, Naval Postgraduate School, Monterey, California, September 1989.
30. Kindelspire, D. W., *The Effects of Freestream Turbulence on Airfoil Boundary Layer Behavior at Low Reynolds Numbers*, Master's Thesis, Naval Postgraduate School, Monterey, California, September 1989.

31. Spectra-Physics, Inc., *Instruction Manual for Models 164, 166, 167, and 168 Ion Lasers with Model 265 Power Supplies*, 1980.
32. United States Naval Test Pilot School Class Notes, *Pitot-static Systems*, by J. J. McCue, June, 1982.
33. DANTEC Documentation Department, Scientific Research Equipment Division, *Instruction Manual, DISA Type 56C17 CTA Bridge*, July, 1984.
34. DANTEC Documentation Department, Scientific Research Equipment Division, *Instruction Manual, DISA Type 56N21 Linearizer*, September, 1984.
35. DANTEC Documentation Department, Scientific Research Equipment Division, *Instruction Manual, DISA Type 56N20 Signal Conditioner*, February, 1985.

**A-1**

### Figure A2. Pod Body Sections



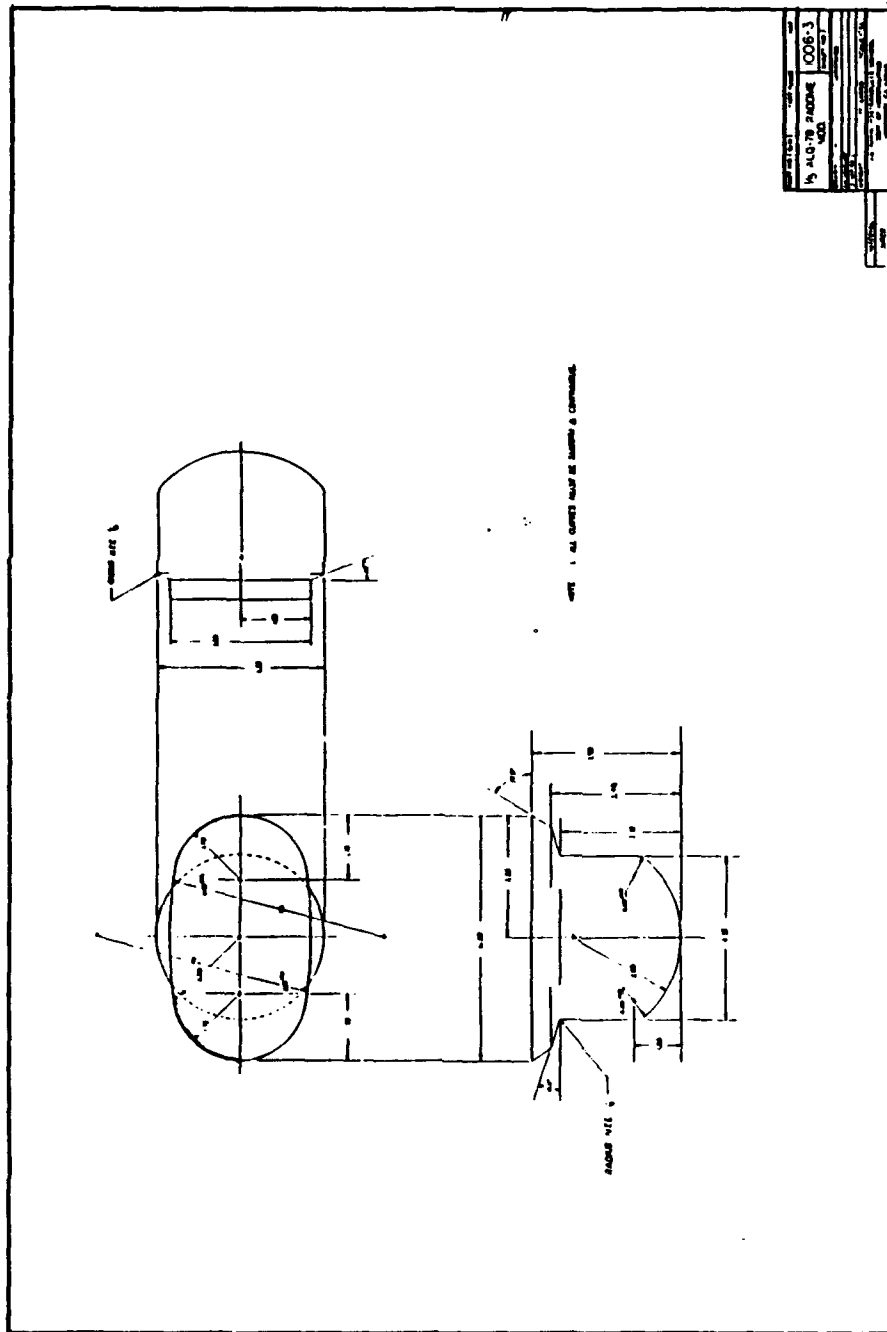


Figure A4. Modified Radome



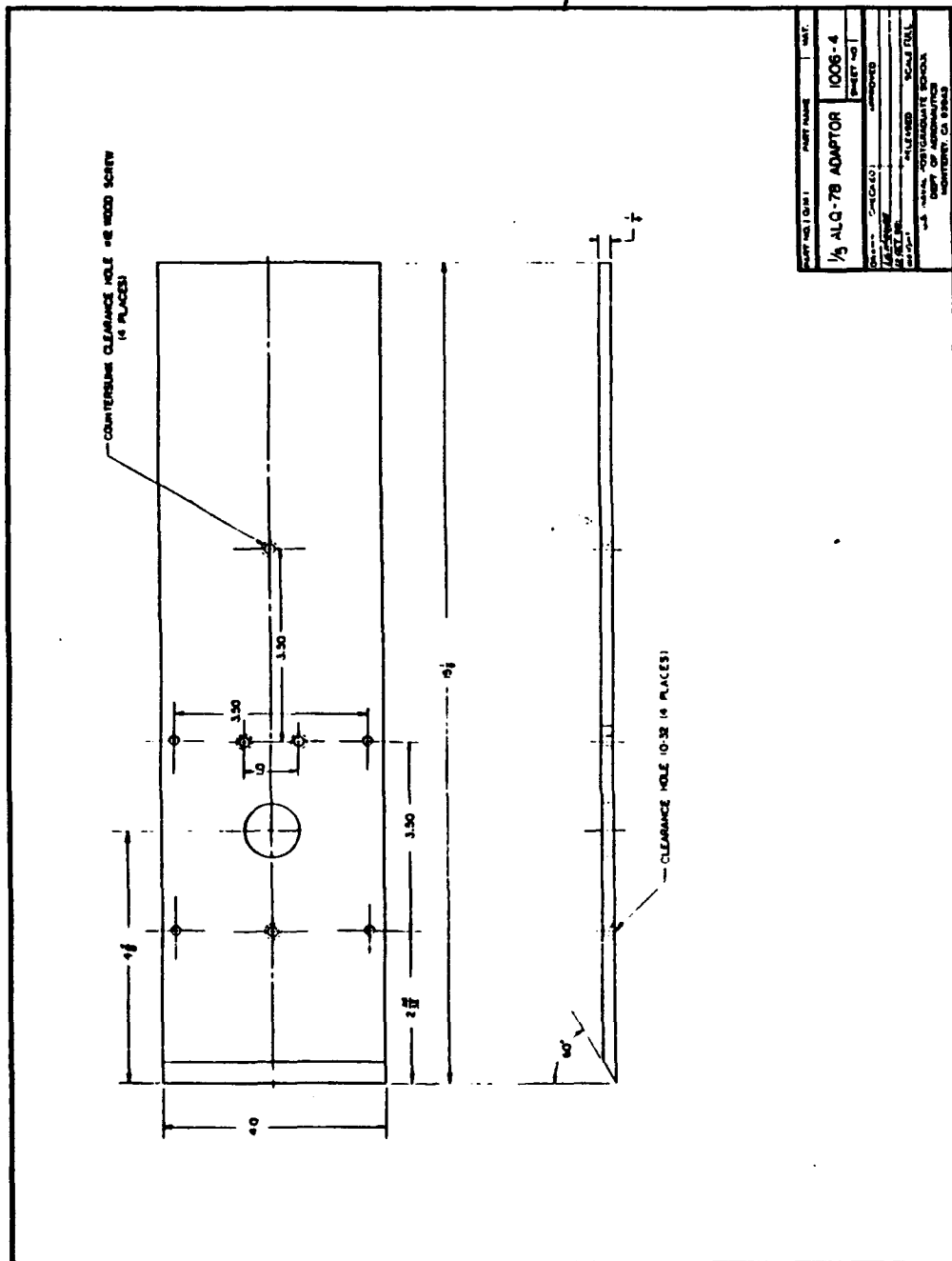


Figure A5. Mounting Plate

# APPENDIX B DATA REDUCTION SPREADSHEET

Run #	Model Conf.	Block. Corr.	Date	Time	Film #	Exposure	Frame #	Manom. Angle (deg)
ST11A	Std. Tripped	0.0049562	2/12/91	2010	N/A	N/A	N/A	45
Tunnel Δp (cm H2O)	Corr. Vel. (ft/sec)	Baro. Press. (mbar)	Baro. Press. (lb/ft <sup>2</sup> )	Temp. (deg F)	Rel. Humidity (%)	Dry Density (slugs/ft <sup>3</sup> )	Obs. Density (slugs/ft <sup>3</sup> )	Obs. Viscosity (slugs/ft-sec)
36.40	271.9	1015	2120	76	61	0.0023060	0.0022906	3.8382124E-07
								q (lb/ft <sup>2</sup> ) 84.69

Station #	Char. Width (in.)	Patm (in. H2O)	P2 (in. H2O)	Pmod - Patm (in. H2O)	Pmod - P2 (in. H2O)	Pmod - P2 (lb/ft <sup>2</sup> )	Base Press. Coeff.	Reynolds Number
1	1.24	0.07	0.70	-9.80	-10.43	-38.33	-0.453	1.68E+05
2	1.58	0.07	0.70	-6.34	-6.97	-25.62	-0.302	2.14E+05
3	2.02	0.07	0.70	-4.22	-4.85	-17.82	-0.210	2.73E+05
4	2.45	0.07	0.70	-2.31	-2.94	-10.81	-0.128	3.31E+05
5	2.91	0.07	0.70	-0.43	-1.06	-3.90	-0.046	3.94E+05
6	3.32	0.07	0.70	-1.30	-1.93	-7.09	-0.084	4.49E+05
7	3.66	0.07	0.70	-0.89	-1.52	-5.59	-0.066	4.95E+05
8	3.66	0.07	0.70	2.50	1.97	7.24	0.085	4.95E+05

Figure B1. Data Reduction Spreadsheet, Boxed Fields Indicate Observed Quantities

APPENDIX C  
SPECTRUM ANALYZER OUTPUT

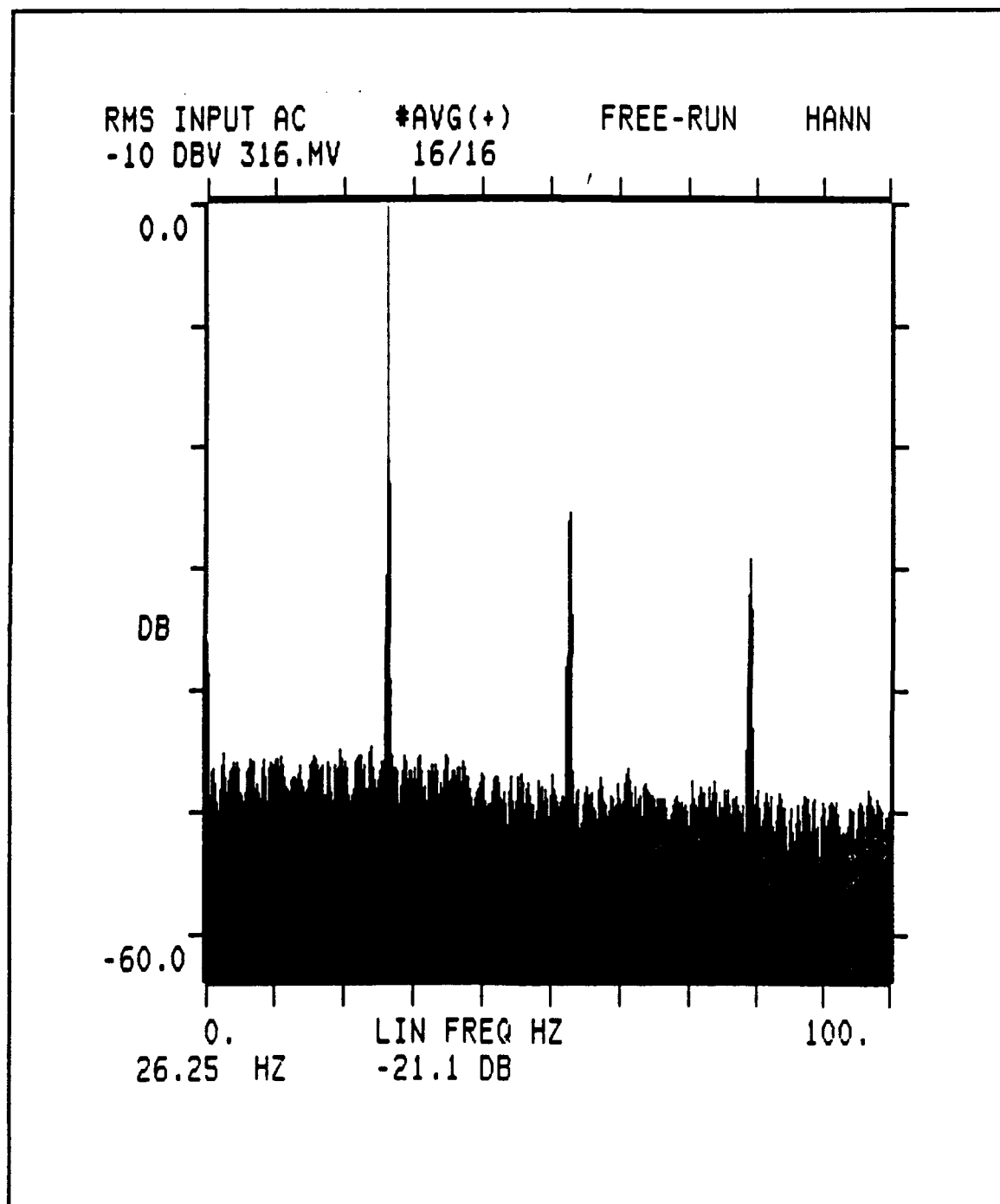
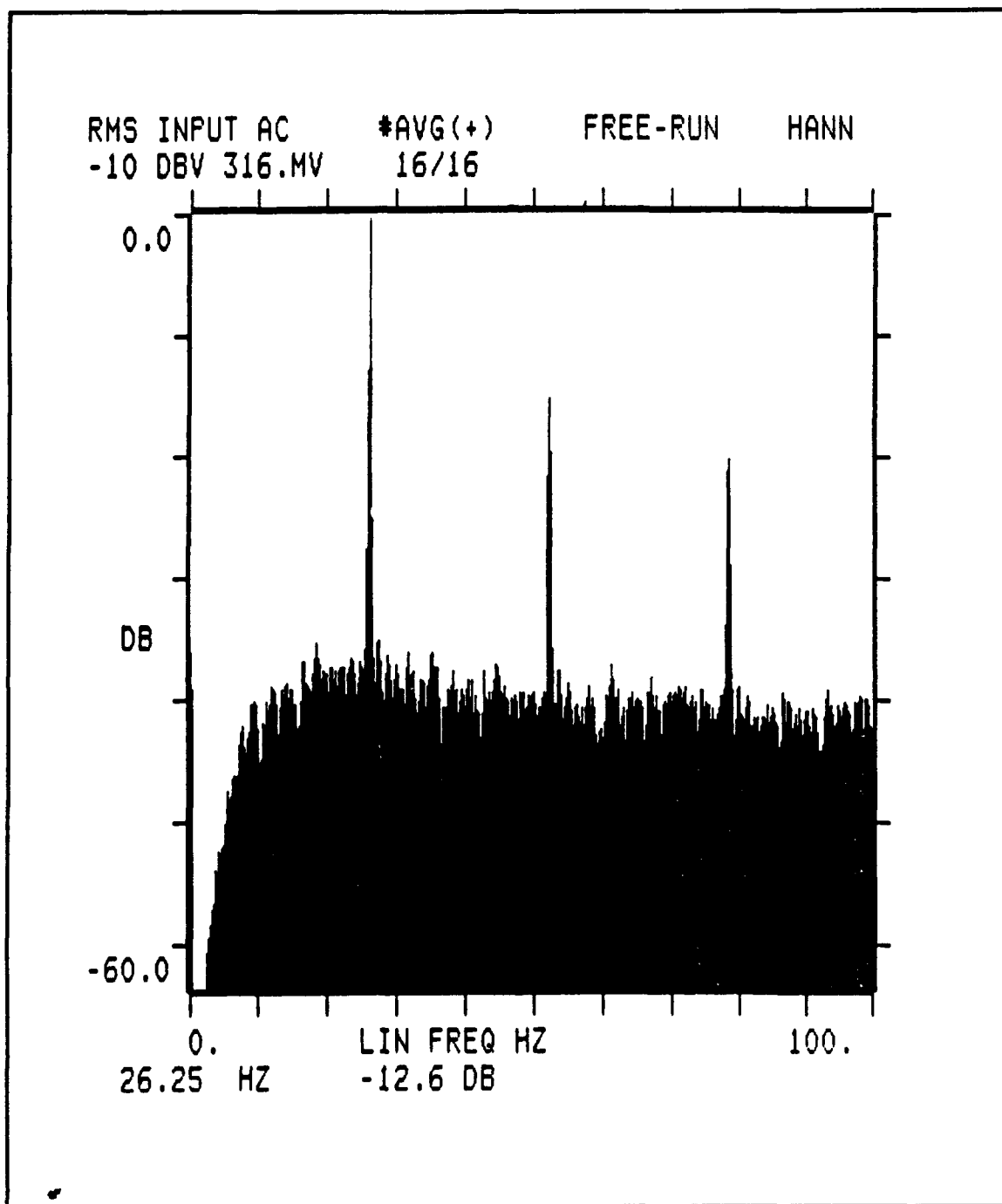
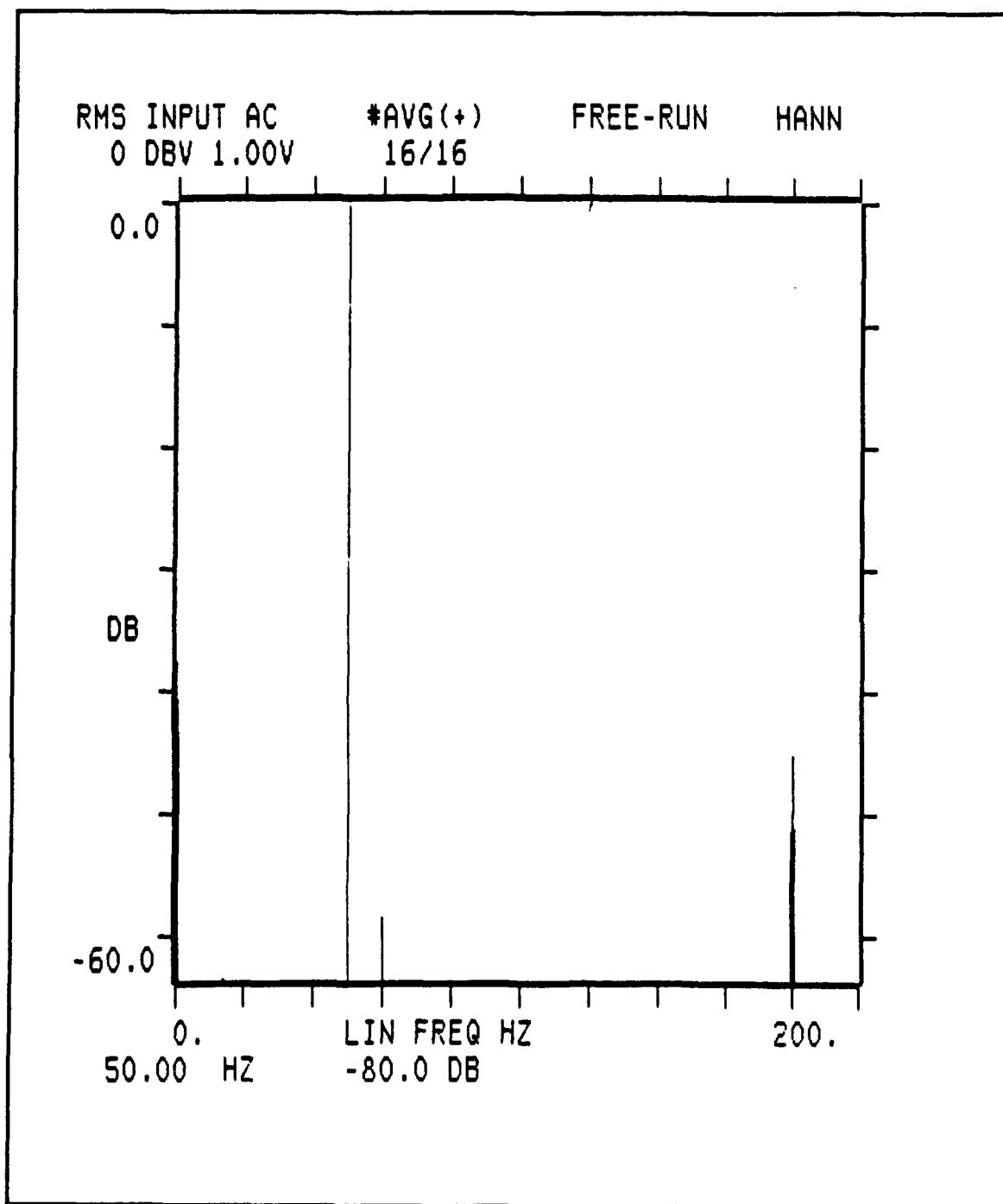


Figure C1. Spectrum Analyzer Display, CTA Output,  $U_{\infty} = 34\text{ft/sec}$ , Turbulence Generator Rotating at Control Setting of 40



**Figure C2.** Spectrum Anaylzer Display, SC Output, SC Bandpass 10Hz to 1kHz, SC Gain = 1,  $U_{\infty} = 34\text{ft/sec}$ , Turbulence Generator Rotating at Control Setting of 40



**Figure C3.** Spectrum Analyzer Display of Tunnel Spectrum, SC Output, SC Bandpass 10Hz to 300Hz, SC Gain = 1,  $U_\infty = 34\text{ft/sec}$ , Turbulence Generator Not Rotating

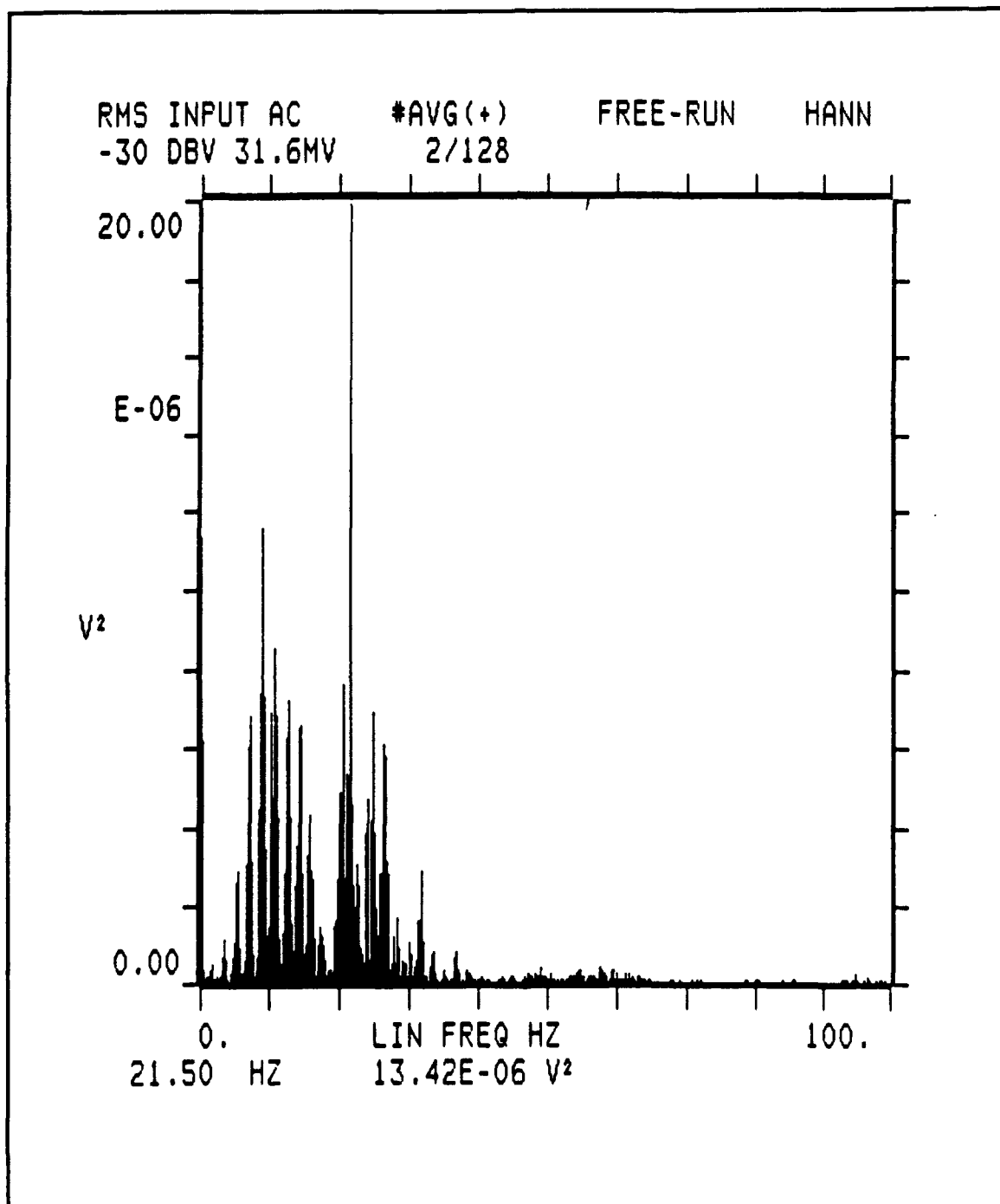


**Figure C4.** Spectrum Analyzer Display for Longitudinal Pluck of Probe Support, CTA Output,  $U_\infty = 0$  ft/sec

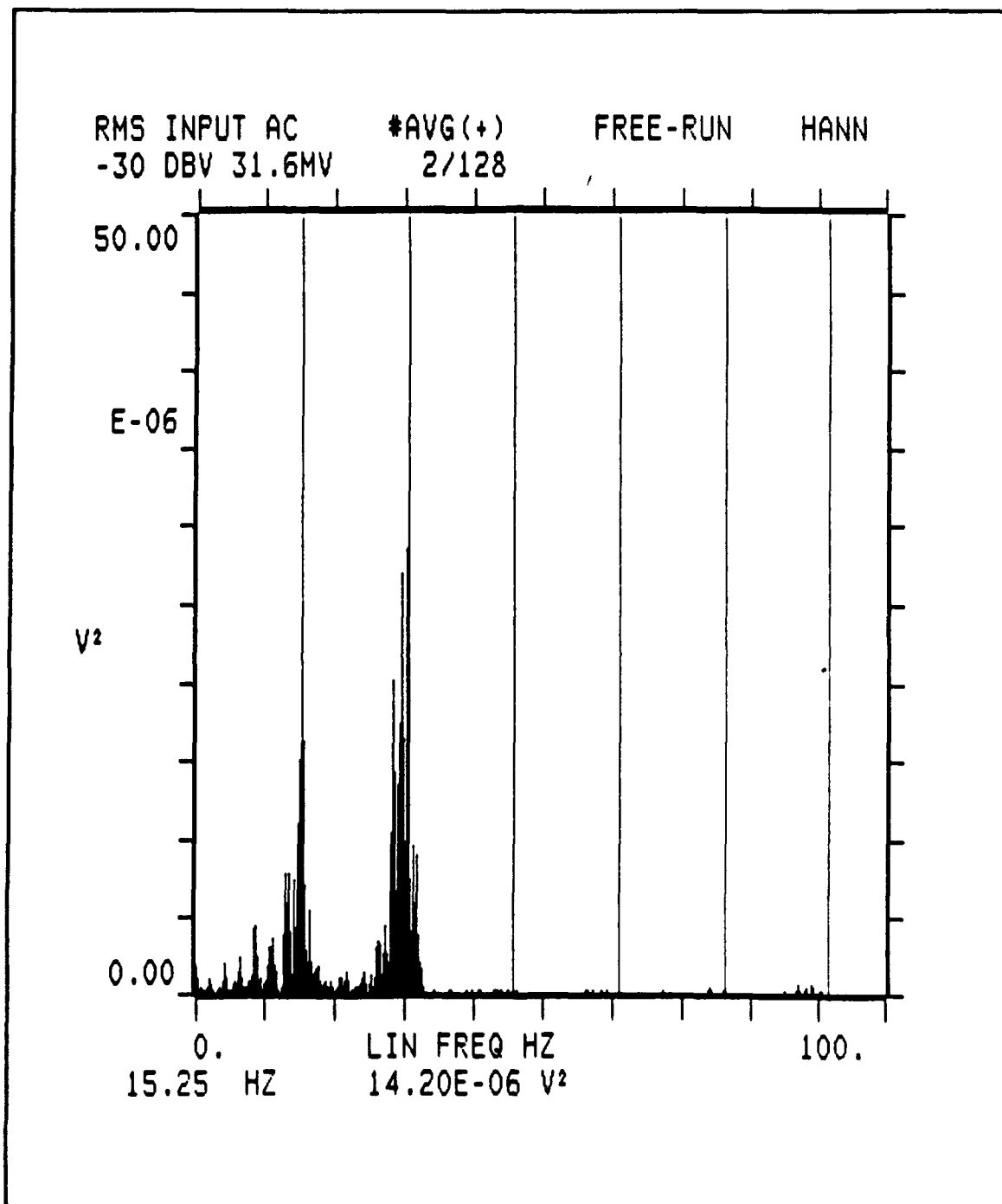


**Figure C5.** Spectrum Analyzer Display for Lateral Pluck of Probe Support,  
 $U_{\infty} = 0\text{ft/sec}$

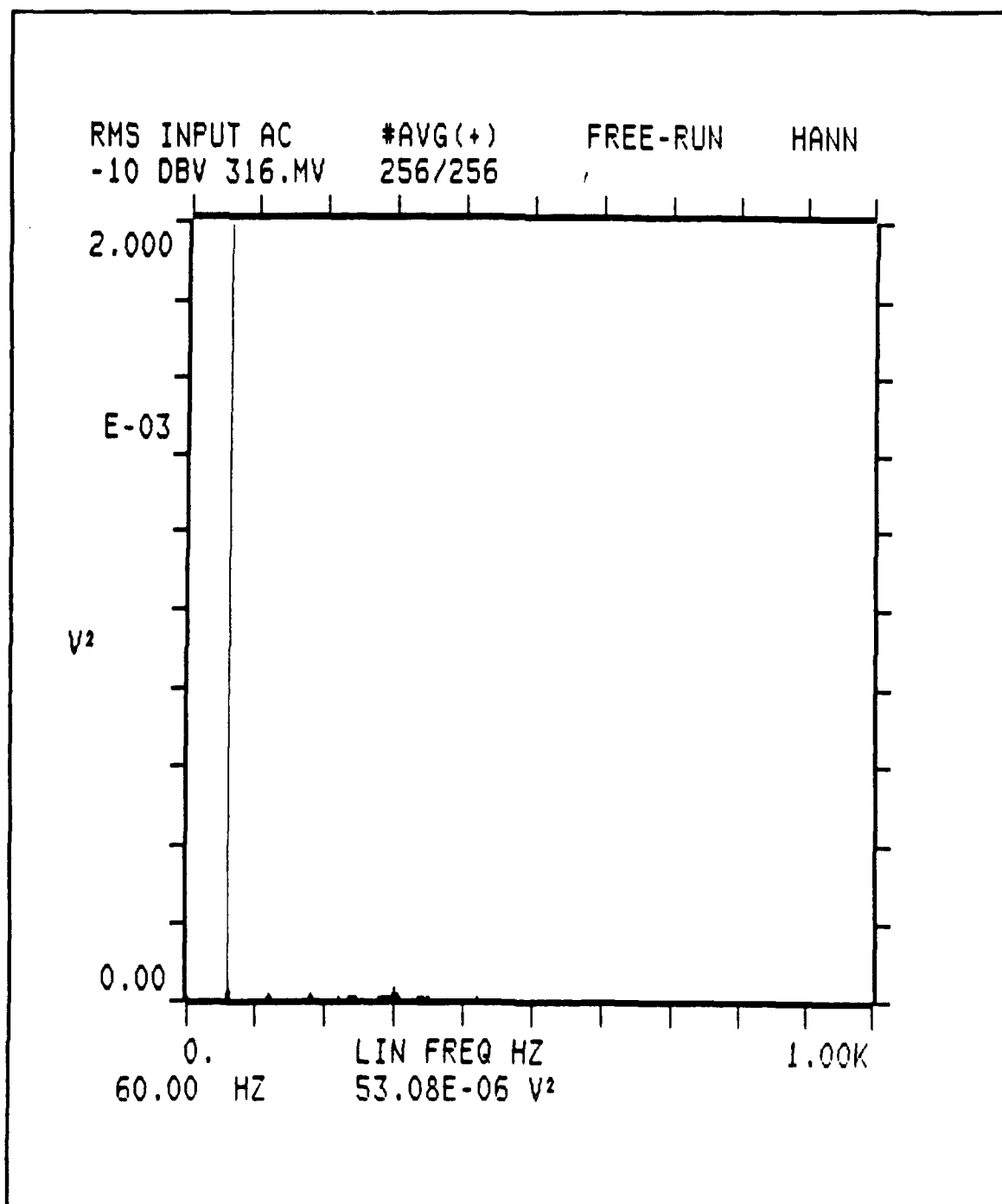


Figure C6. Spectrum Analyzer Display for Free Probe Support,  $U_\infty = 34\text{ft/sec}$



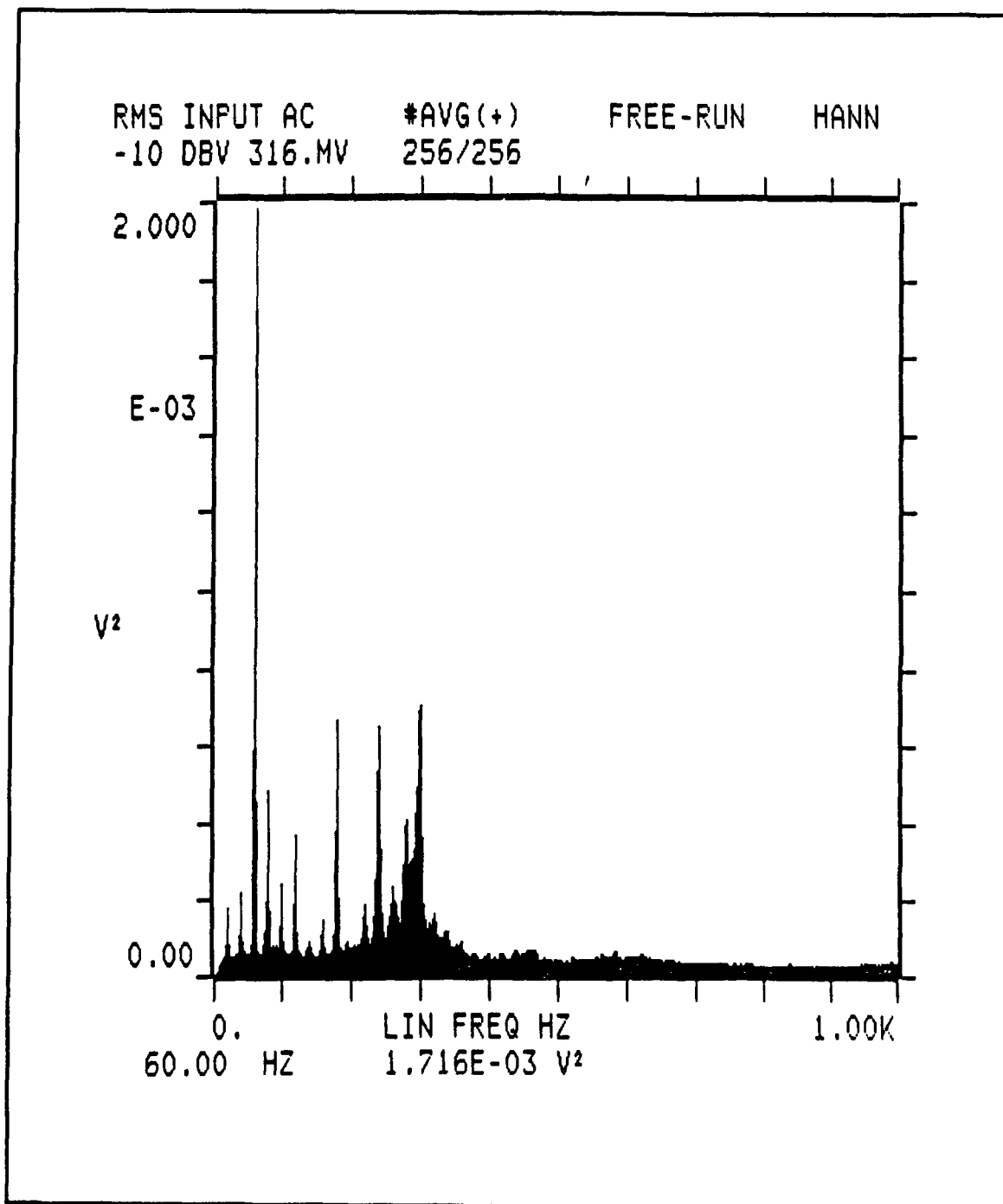


Figure C7. Spectrum Analyzer Display for Free Probe Support,  $U_\infty = 94\text{ft/sec}$

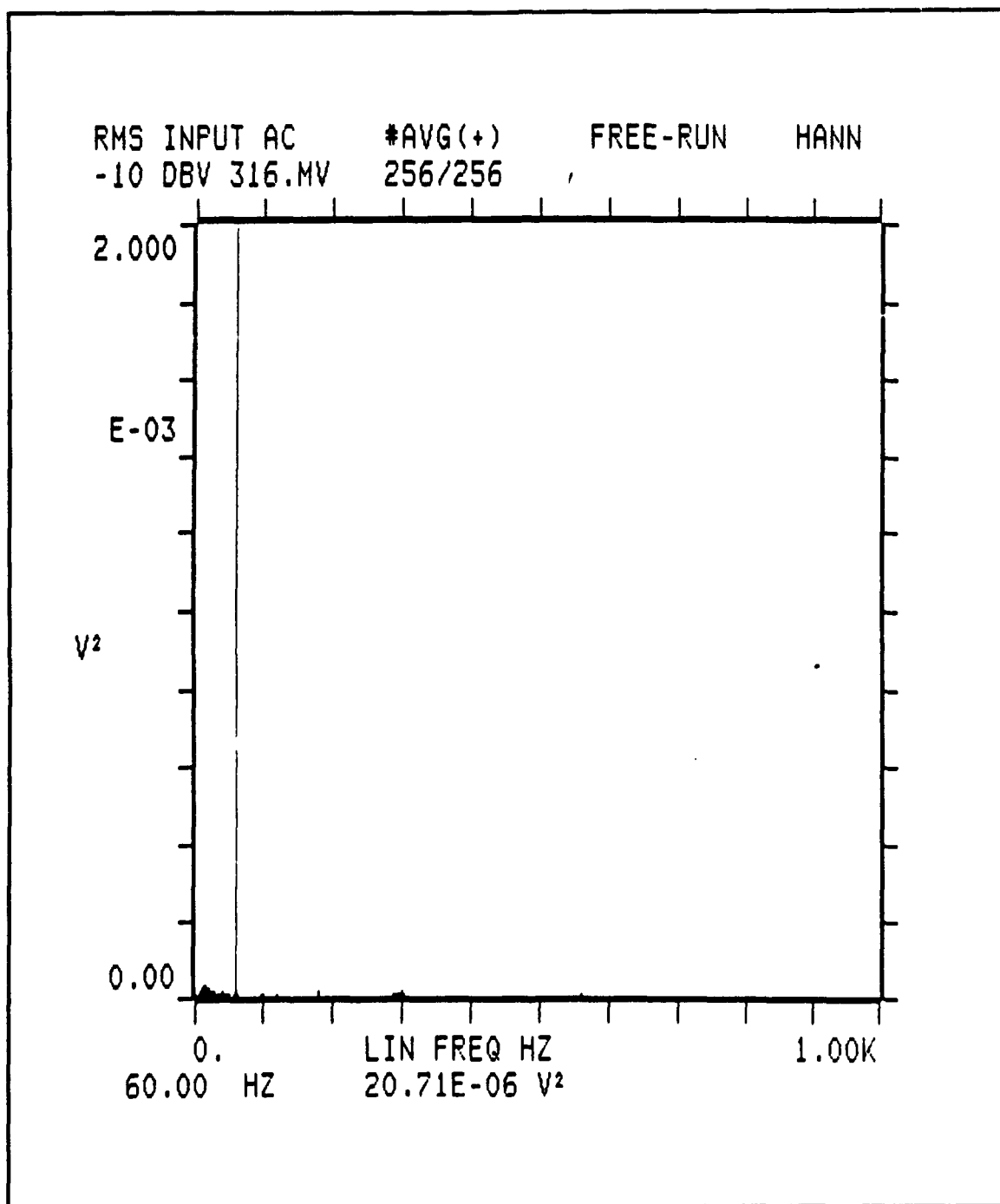
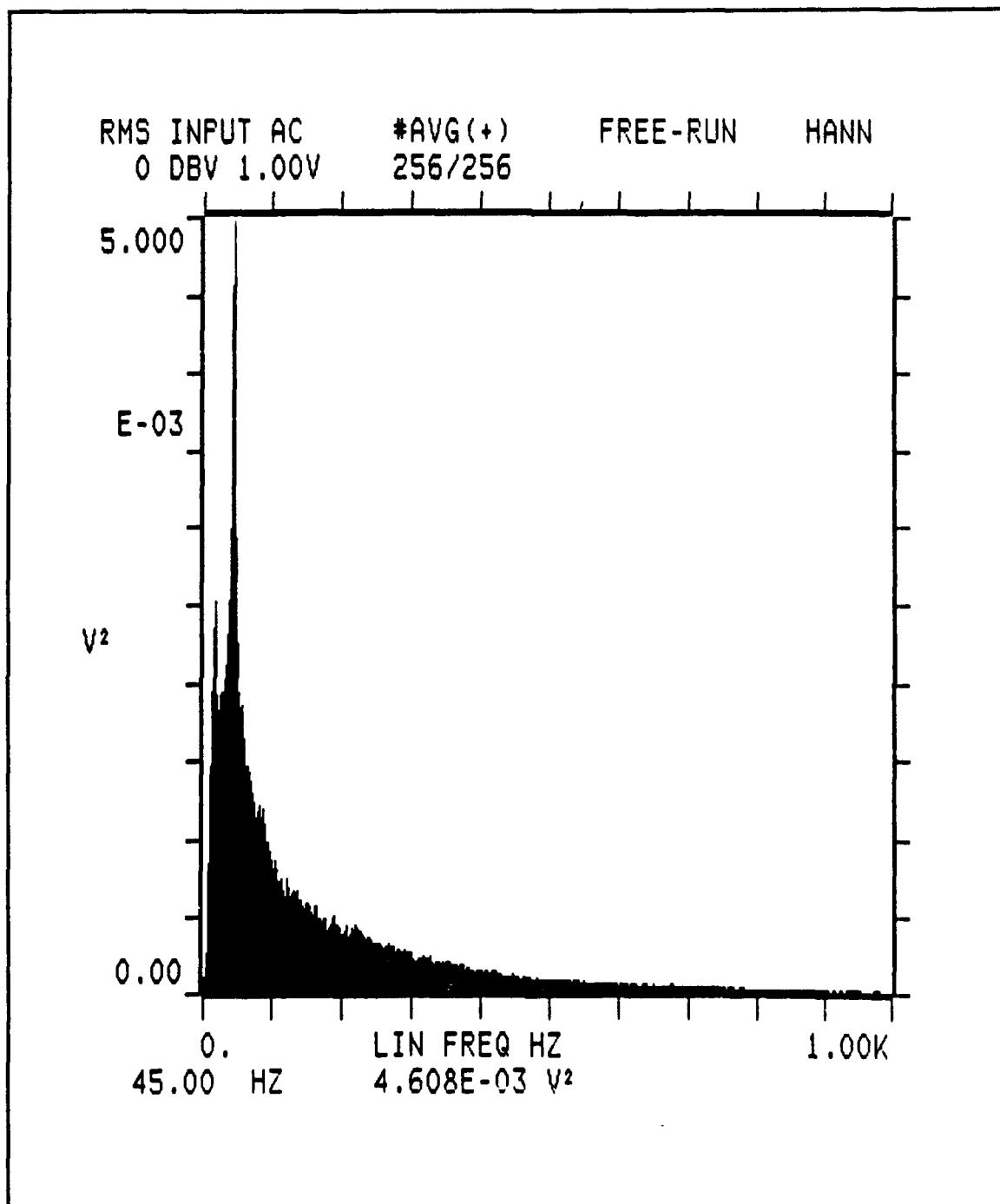
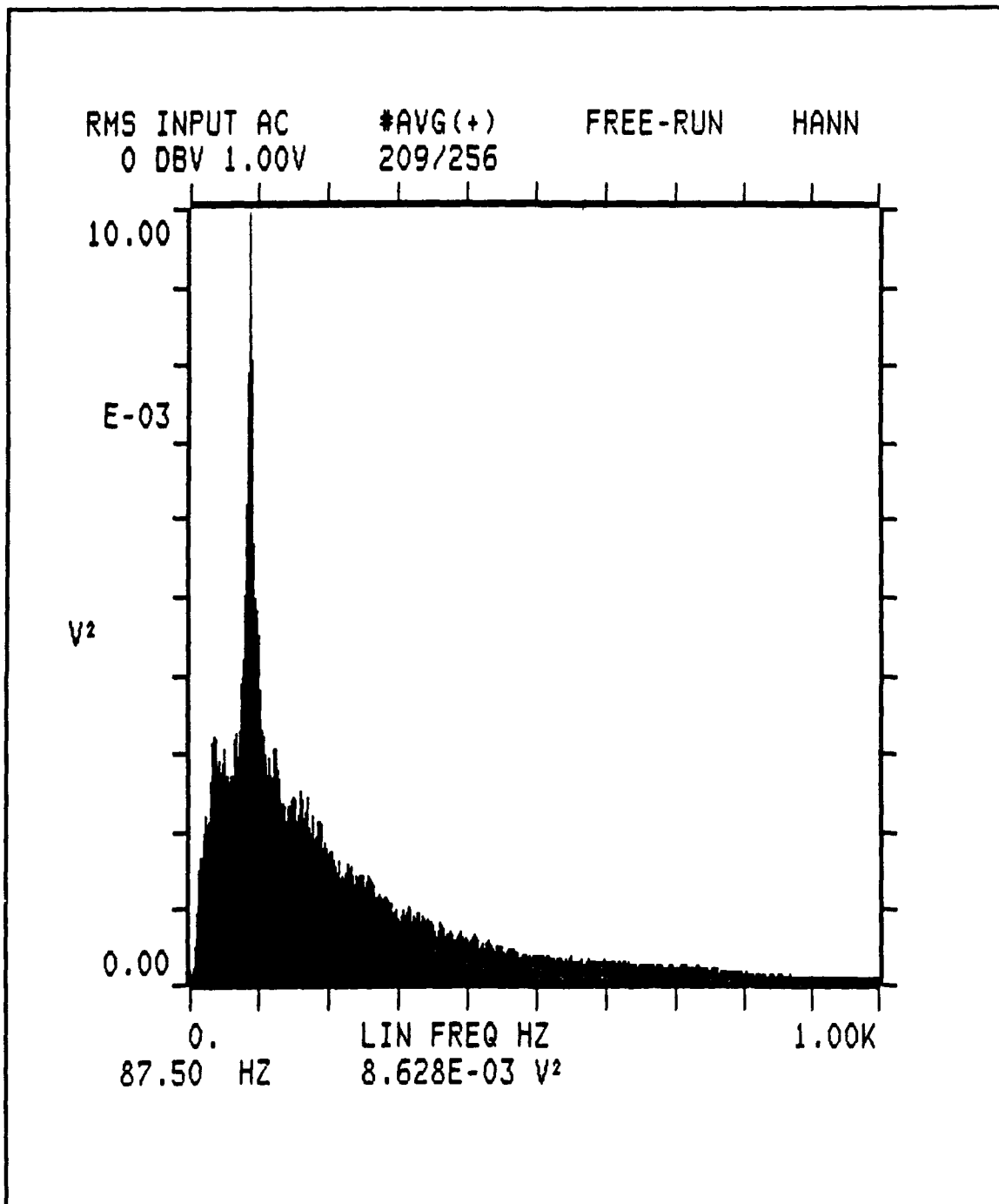


Figure C8. Spectrum Anaylzer Display for Bound Probe Support,  $U_\infty = 94\text{ft/sec}$



**Figure C9.** Spectrum Analyzer Display for Quasi-two-dimensional Cylinder,  
 $U_{\infty} = 34.1\text{ft/sec}$ , Probe at Mid-span



**Figure C10.** Spectrum Analyzer Display for Quasi-two-dimensional Cylinder.  
 $U_{\infty} = 65.0\text{ft/sec}$ , Probe at Mid-span

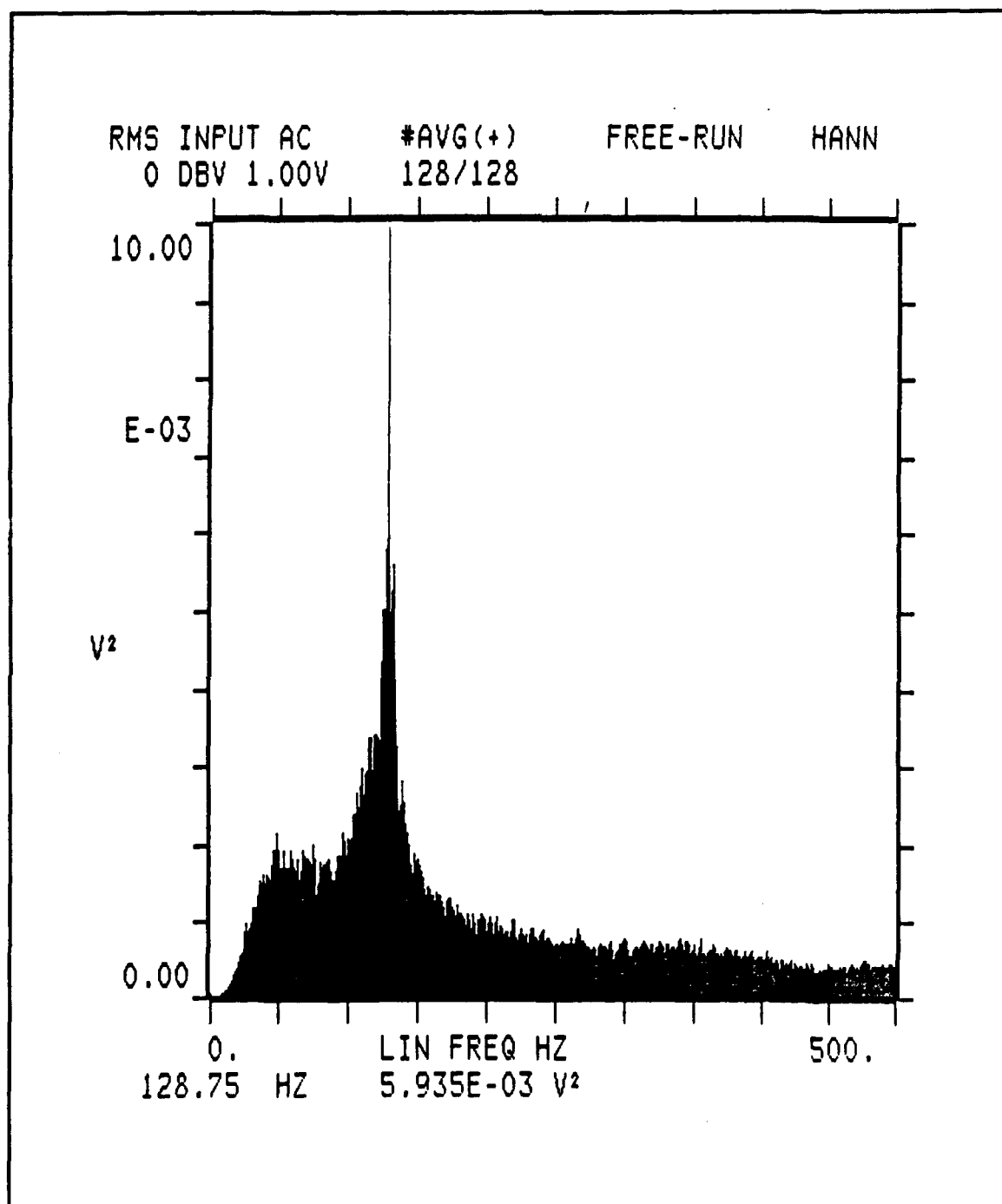


**Figure C11.** Spectrum Analyzer Display for Quasi-two-dimensional Cylinder,  $U_{\infty} = 93.4\text{ft/sec}$ , Probe at Mid-span

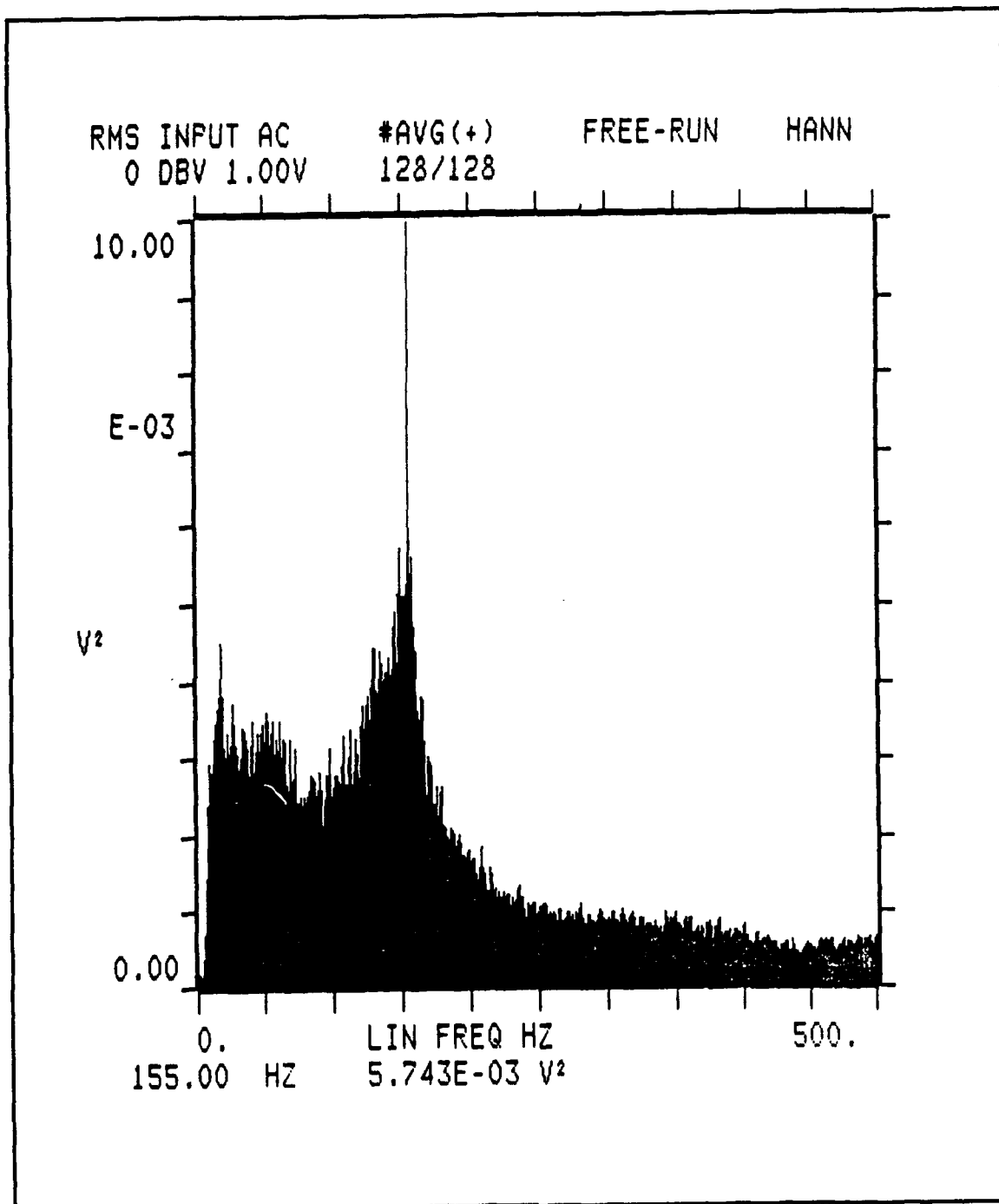


**Figure C12.** Spectrum Analyzer Display for Quasi-two-dimensional Cylinder,  
 $U_{\infty} = 112.3\text{ft/sec}$ , Probe at Mid-span

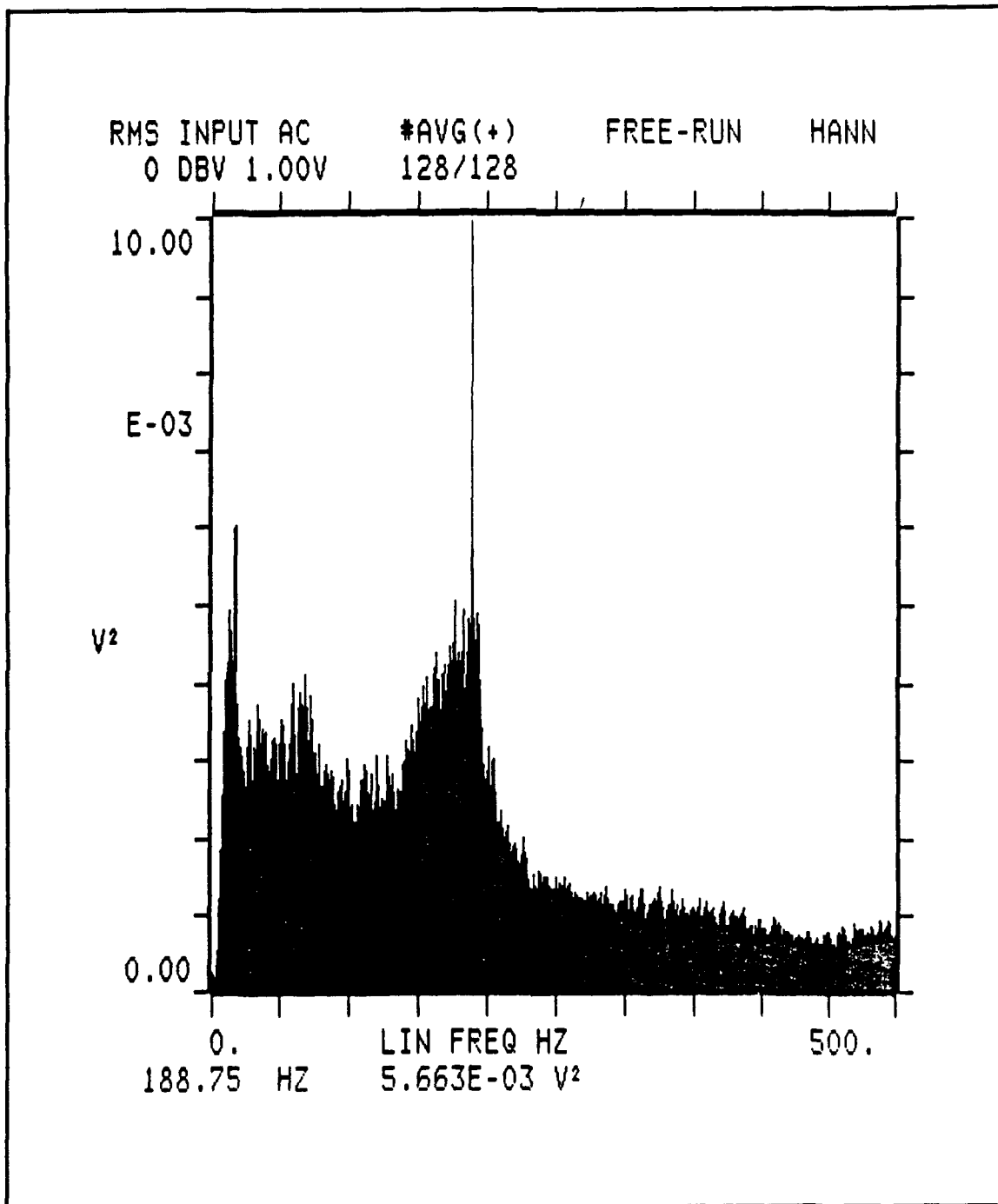


**Figure C13.** Spectrum Analyzer Display for Quasi-two-dimensional Cylinder,  
 $U_{\infty} = 135.7\text{ft/sec}$ , Probe at Mid-span

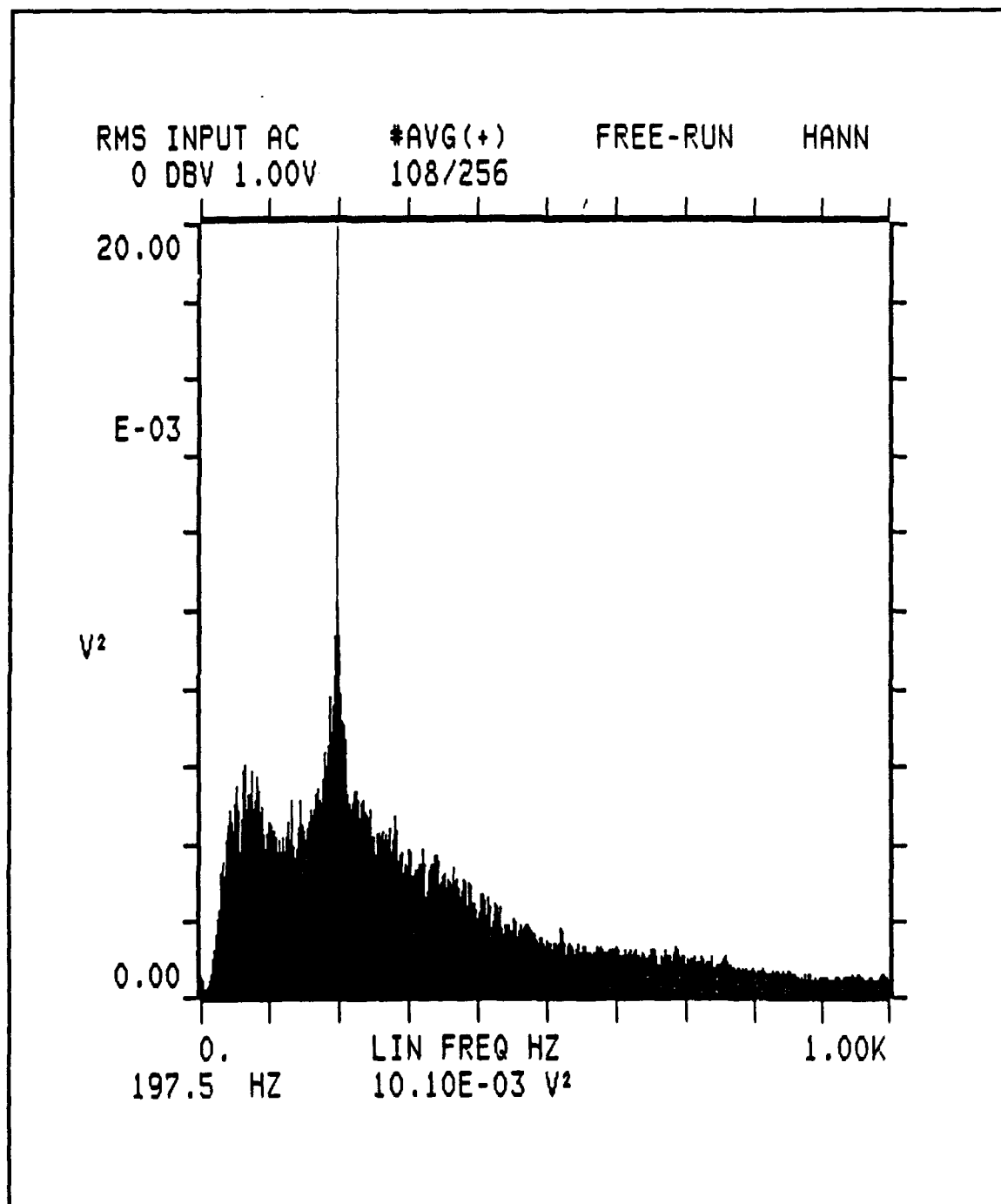


**Figure C14.** Spectrum Analyzer Display for Quasi-two-dimensional Cylinder,  
 $U_{\infty} = 146.0\text{ft/sec}$ , Probe at Mid-span



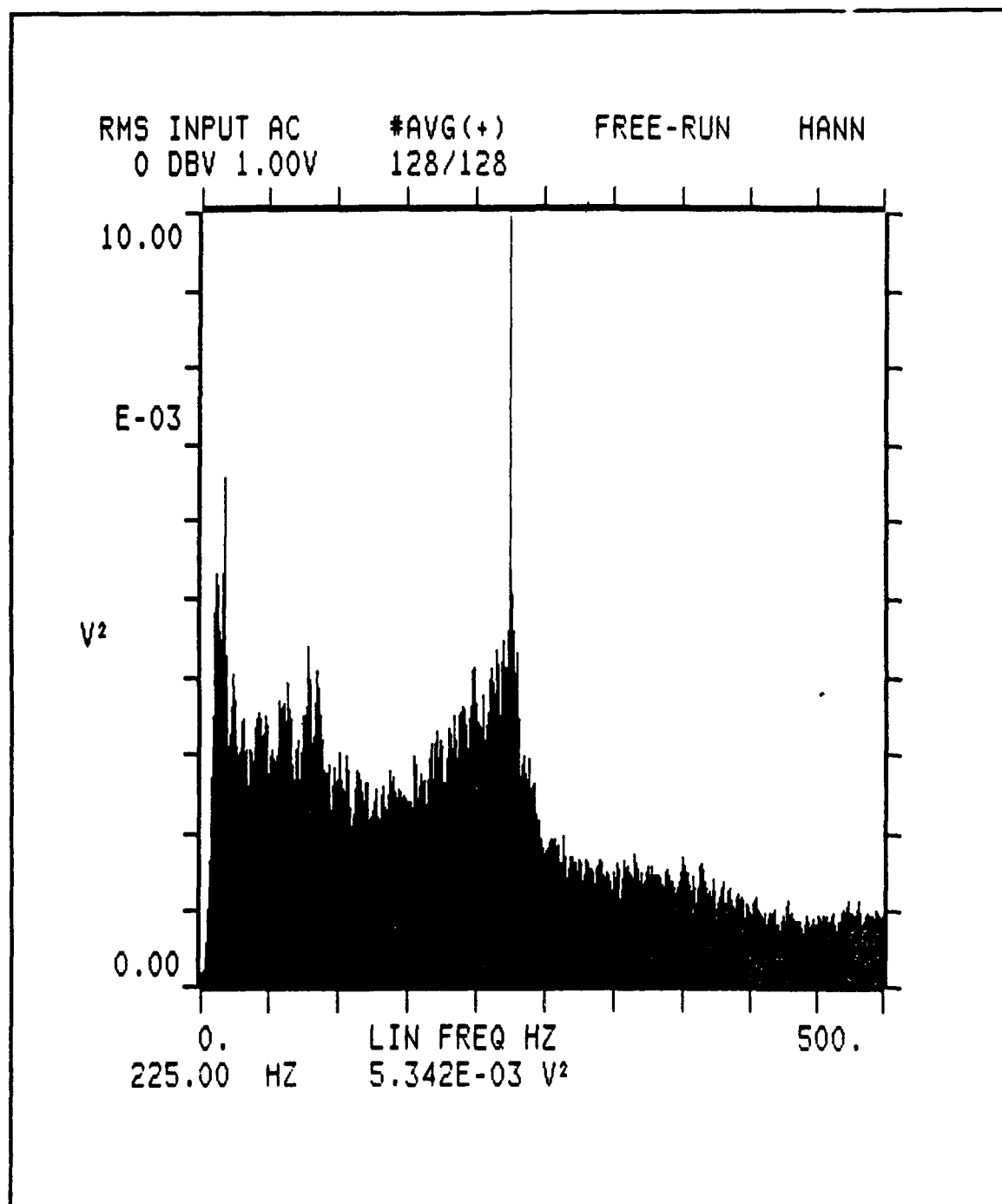


**Figure C15.** Spectrum Analyzer Display for Quasi-two-dimensional Cylinder,  
 $U_{\infty} = 161.8\text{ft/sec}$ , Probe at Mid-span

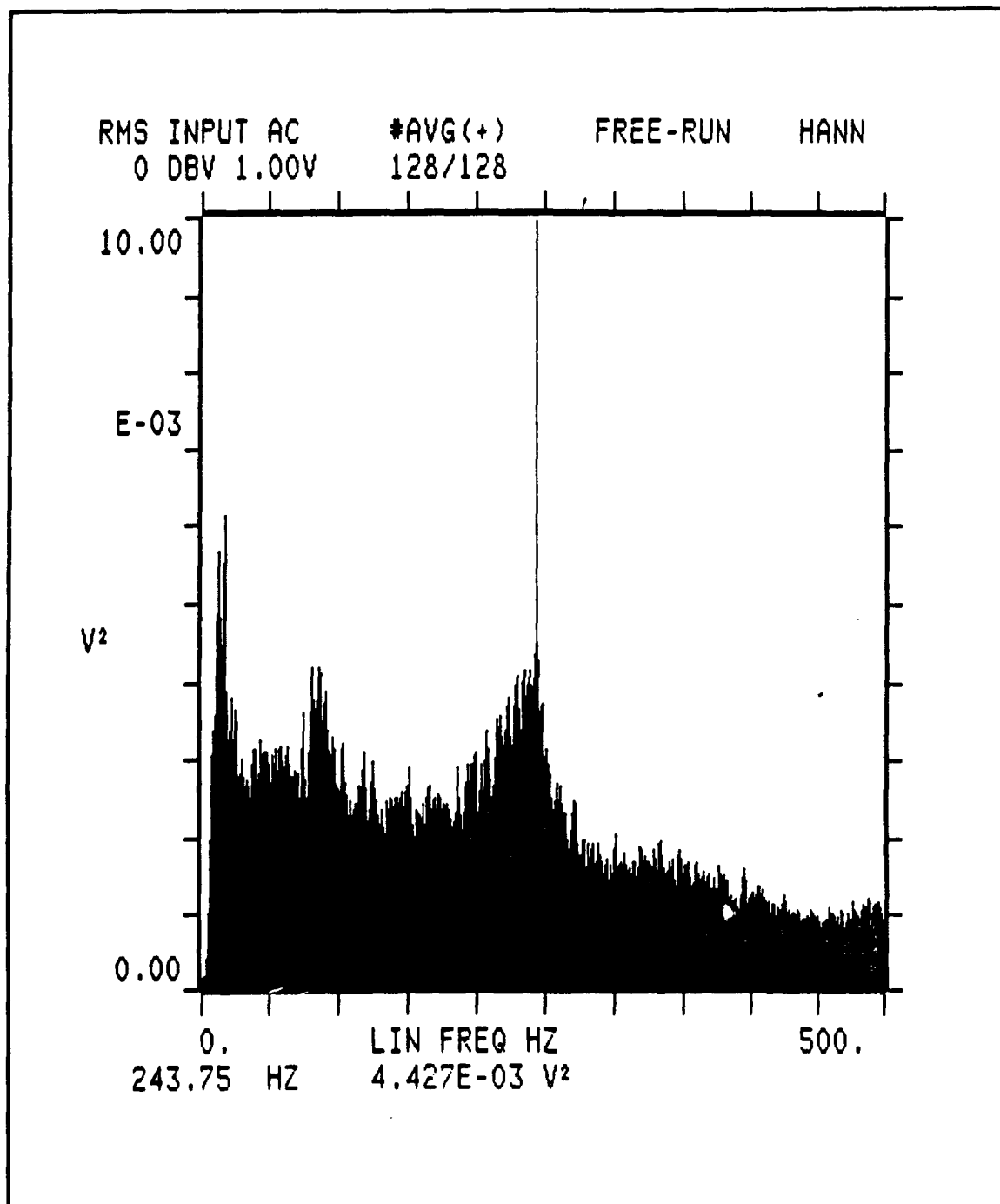


**Figure C16.** Spectrum Analyzer Display for Quasi-two-dimensional Cylinder,  
 $U_{\infty} = 176.1\text{ft/sec}$ , Probe at Mid-span

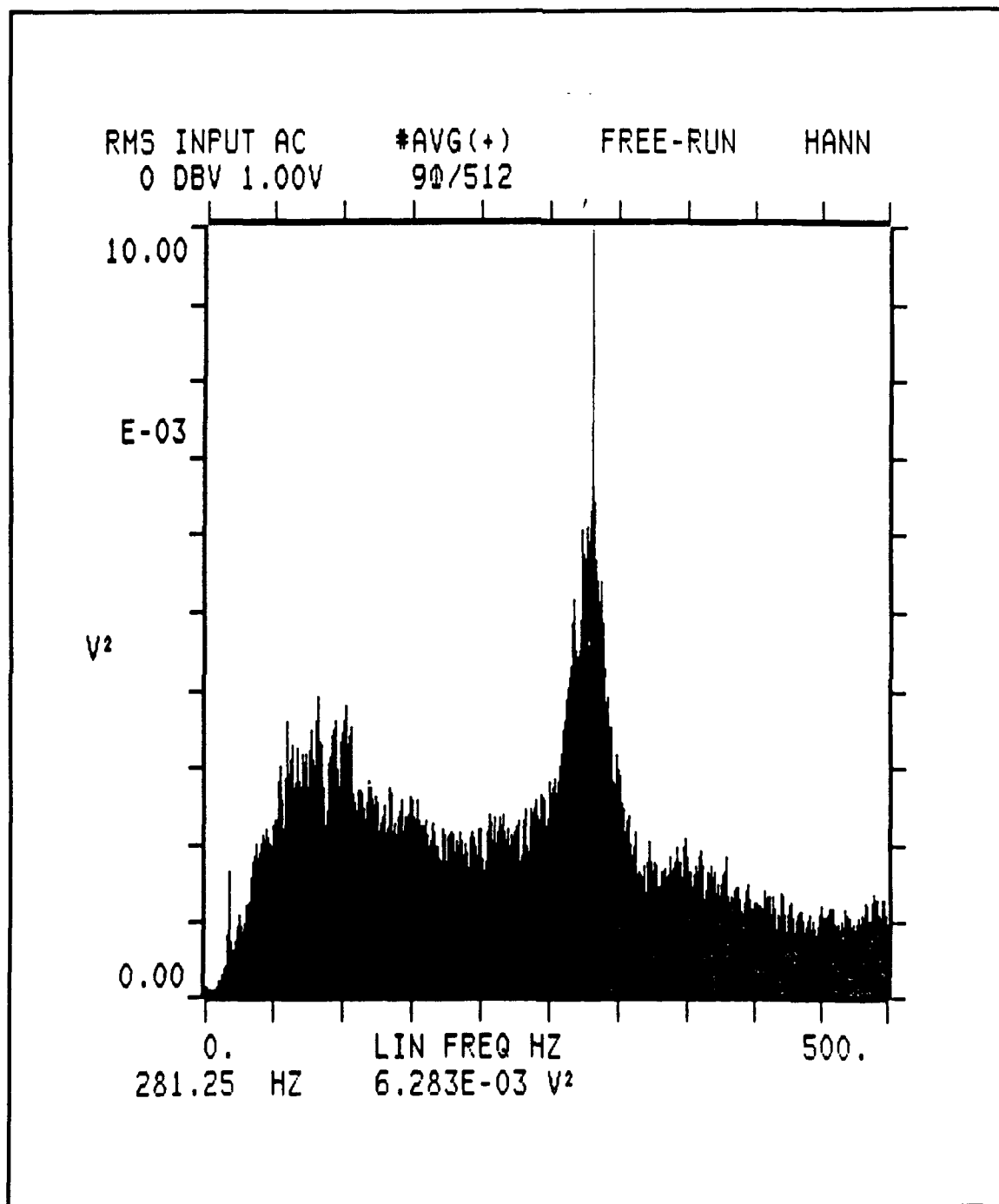


**Figure C17.** Spectrum Analyzer Display for Quasi-two-dimensional Cylinder,  $U_{\infty} = 201.8\text{ft/sec}$ , Probe at Mid-span

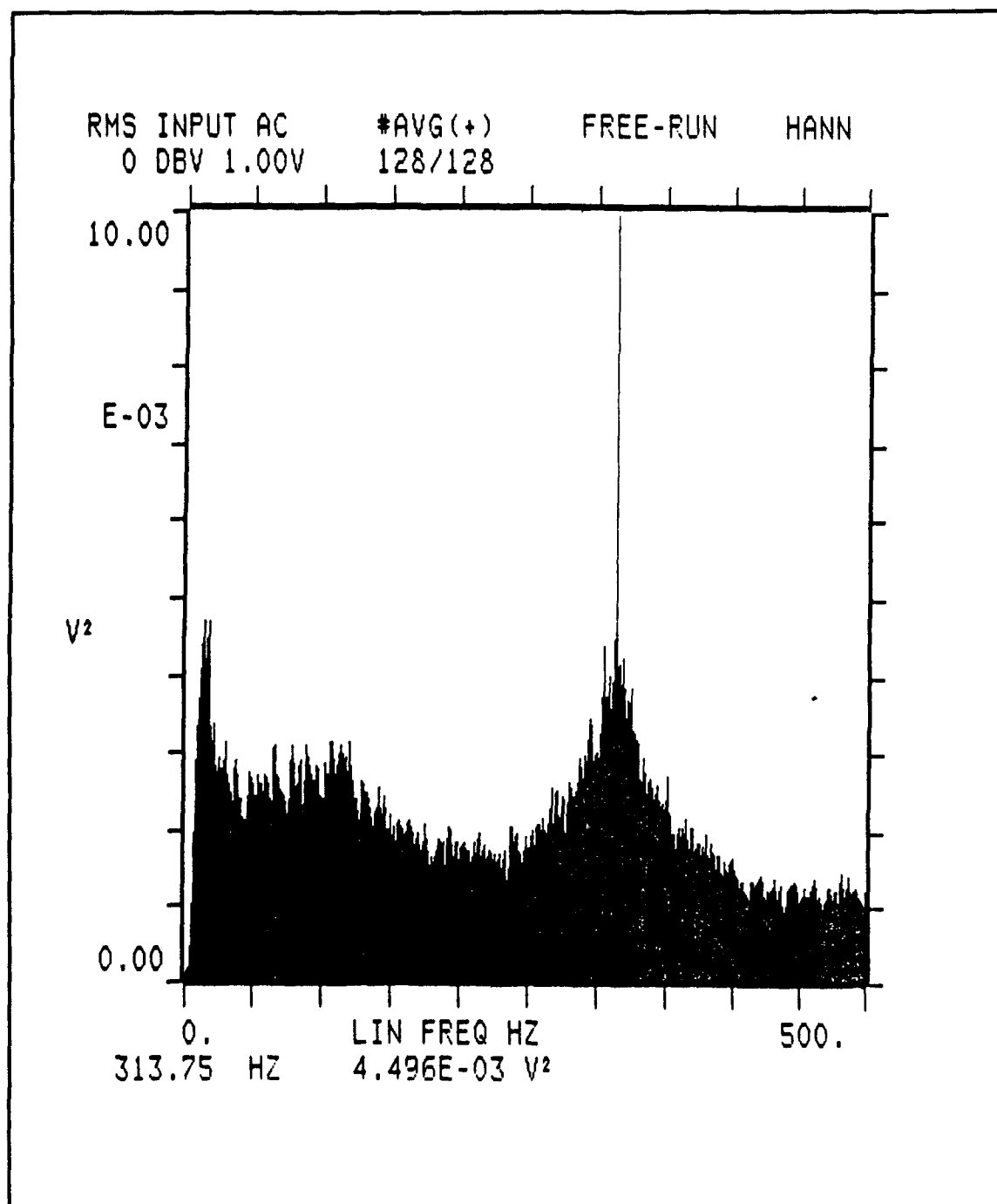


**Figure C18.** Spectrum Analyzer Display for Quasi-two-dimensional Cylinder,  
 $U_{\infty} = 228.8\text{ft/sec}$ , Probe at Mid-span

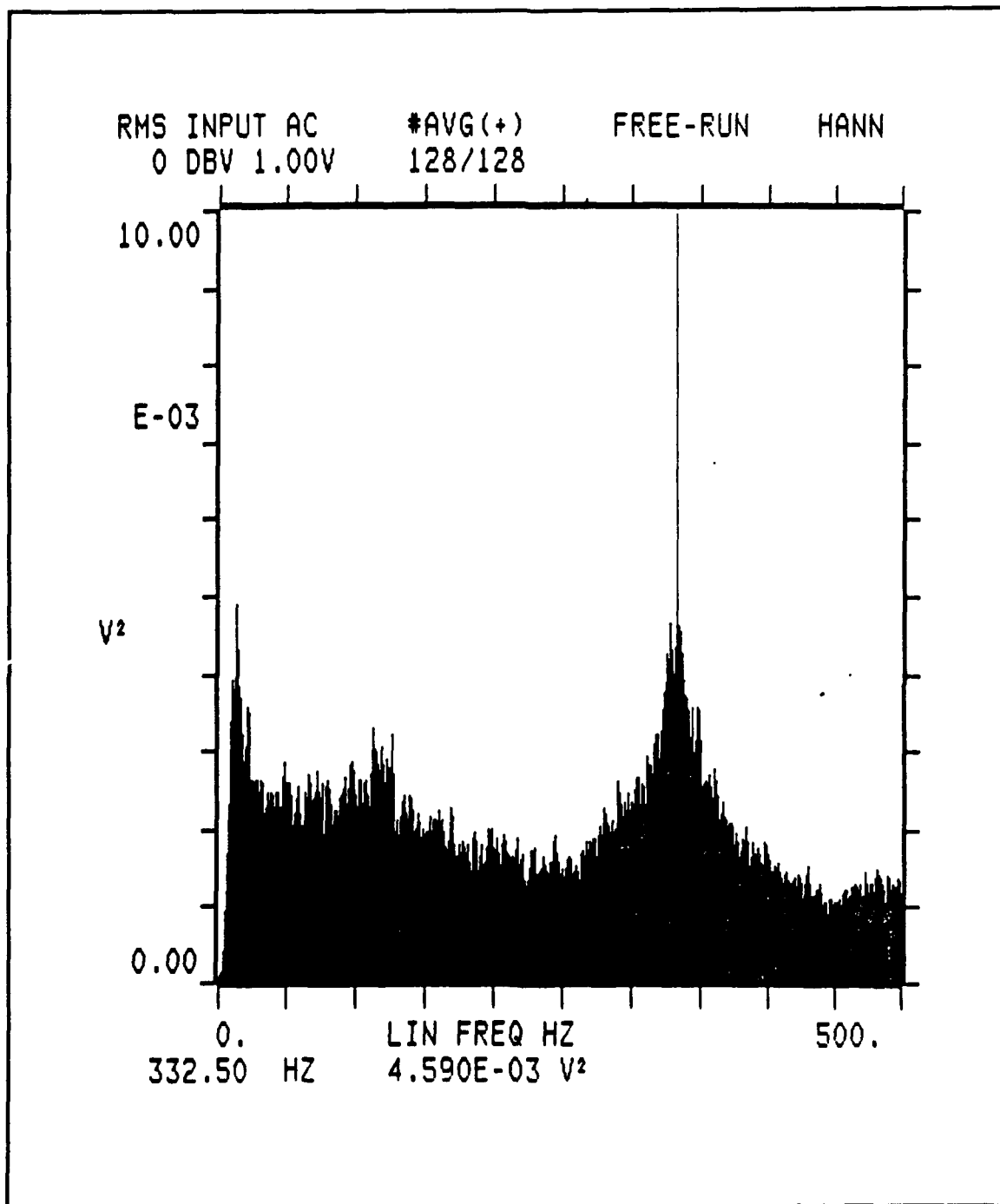


**Figure C19.** Spectrum Analyzer Display for Quasi-two-dimensional Cylinder,  $U_{\infty} = 241.2\text{ft/sec}$ , Probe at Mid-span

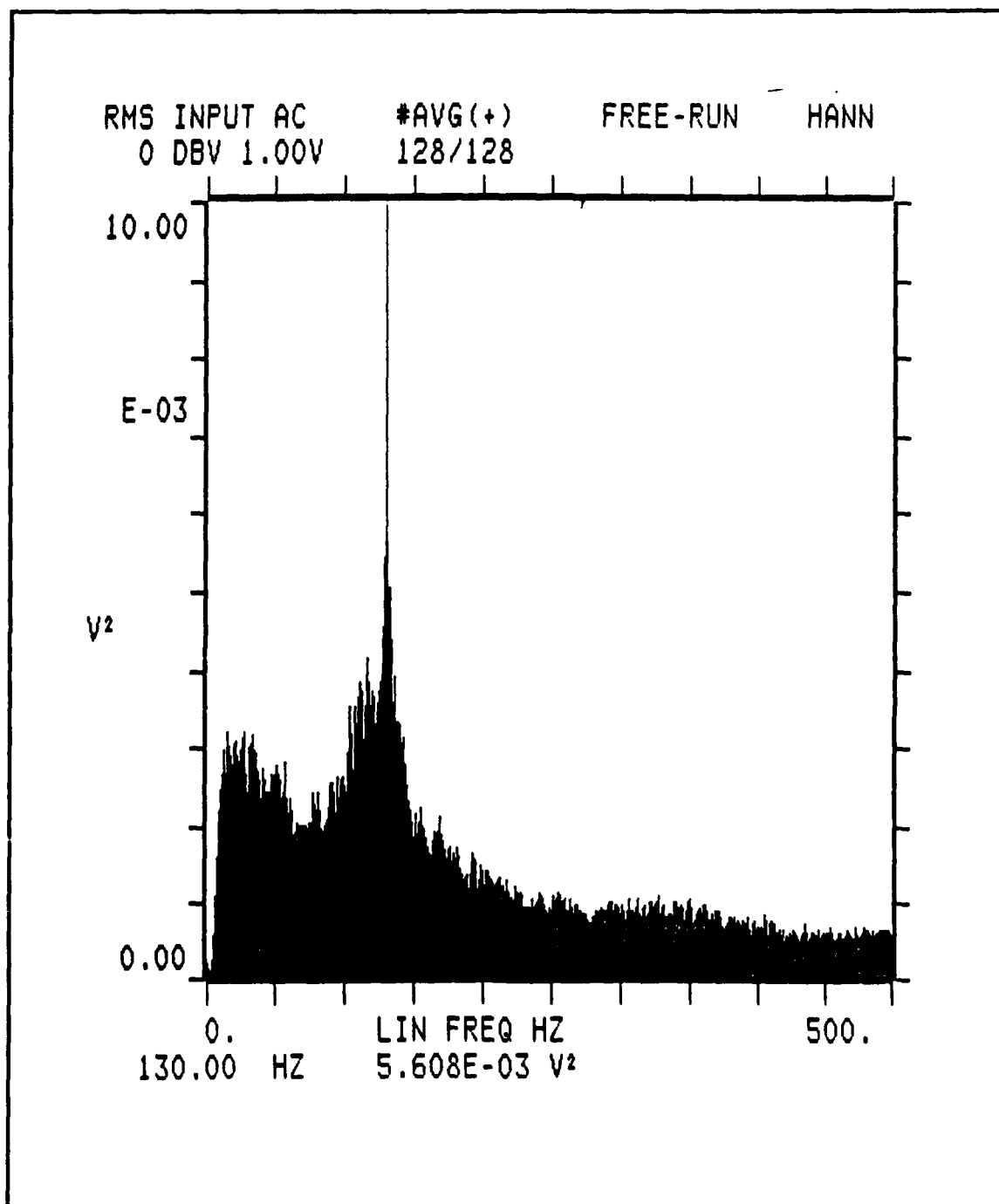
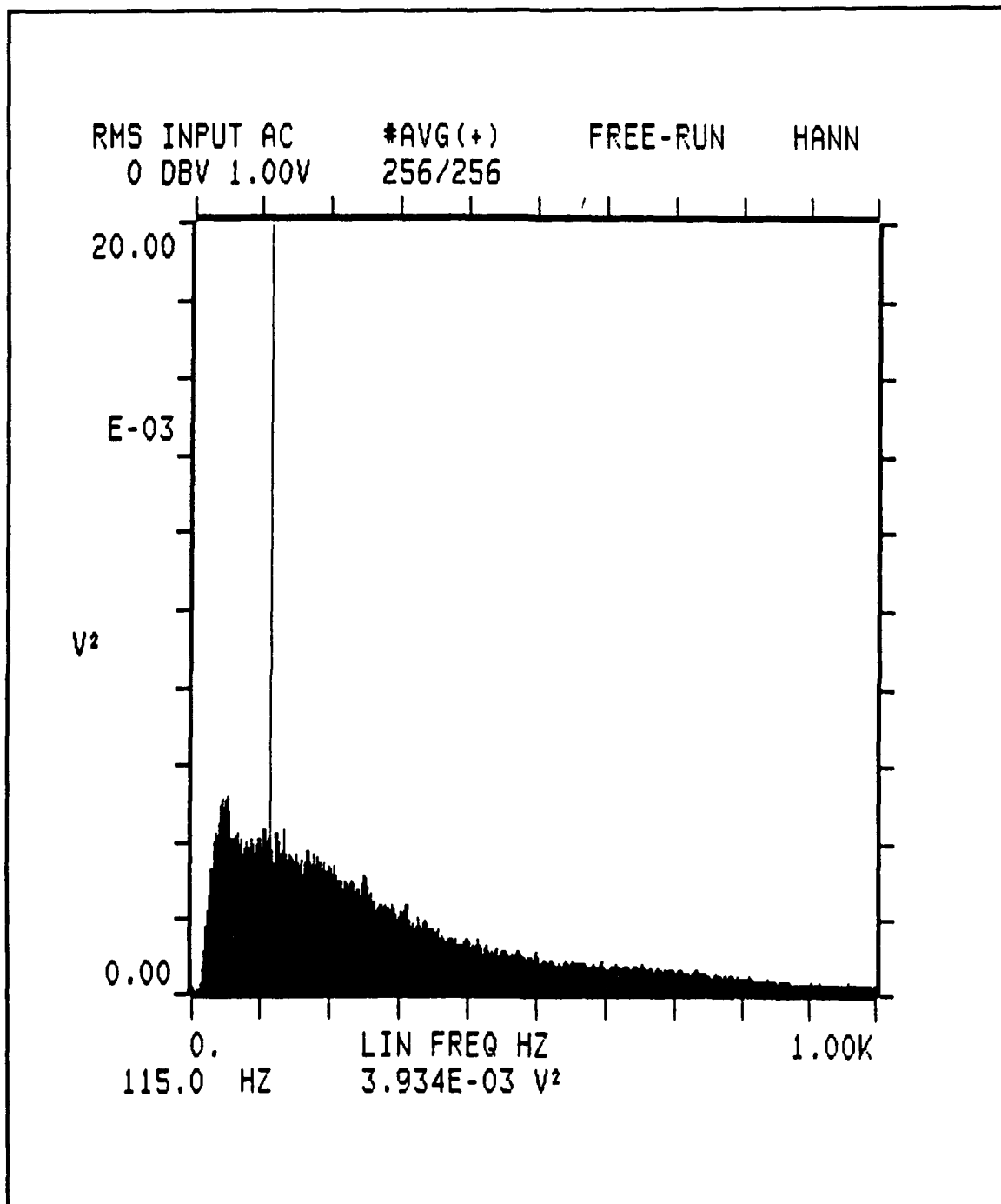
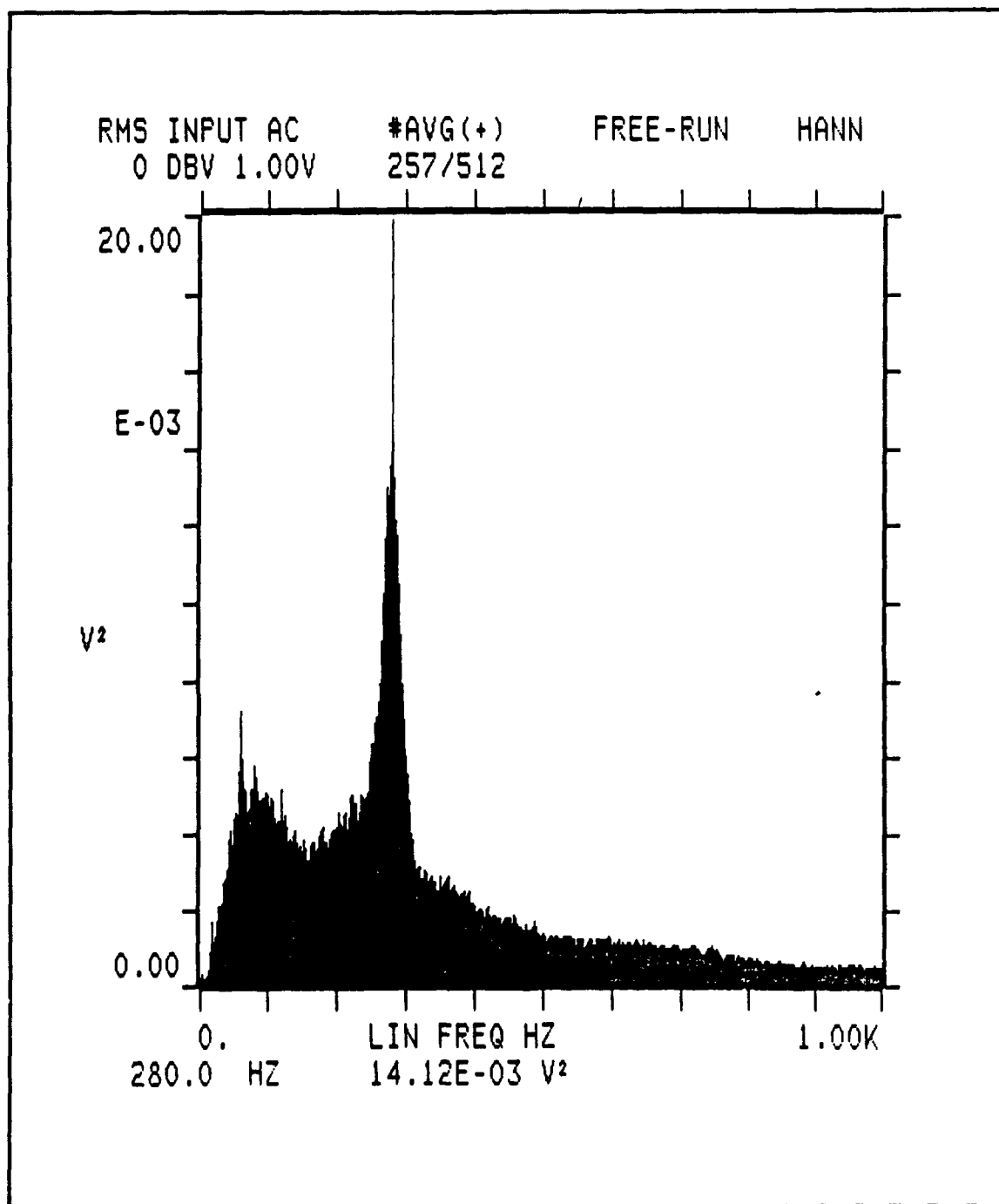


Figure C20. Spectrum Analyzer Display for Quasi-two-dimensional Cylinder without Boundary Layer Tripping,  $U_\infty = 94.0$ ft/sec, Probe at Mid-span



**Figure C21.** Spectrum Analyzer Display for Quasi-two-dimensional Cylinder, with Boundary Layer Tripping,  $U_\infty = 94.0\text{ft/sec}$ , Probe at Mid-span



**Figure C22.** Spectrum Analyzer Display for Quasi-two-dimensional Cylinder,  $U_\infty = 201.0\text{ft/sec}$ , Probe at Low Extreme Position, Approximately 0.5in. Below Mid-span



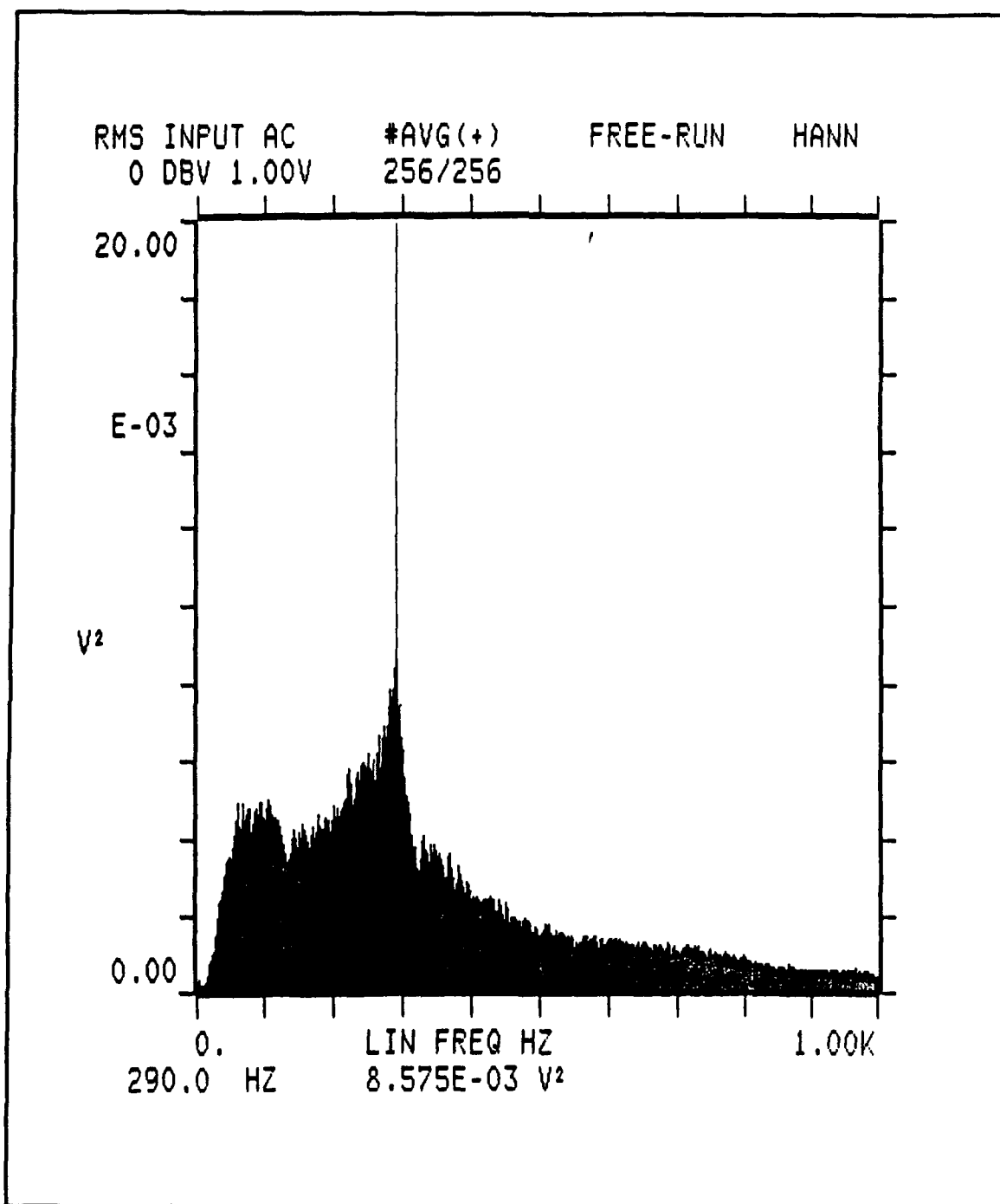


**Figure C23.** Spectrum Analyzer Display for Quasi-two-dimensional Cylinder,  $U_{\infty} = 201.0\text{ft/sec}$ , Probe 2in. Above Low Extreme Position, Approximately 1.5in. Above Mid-span

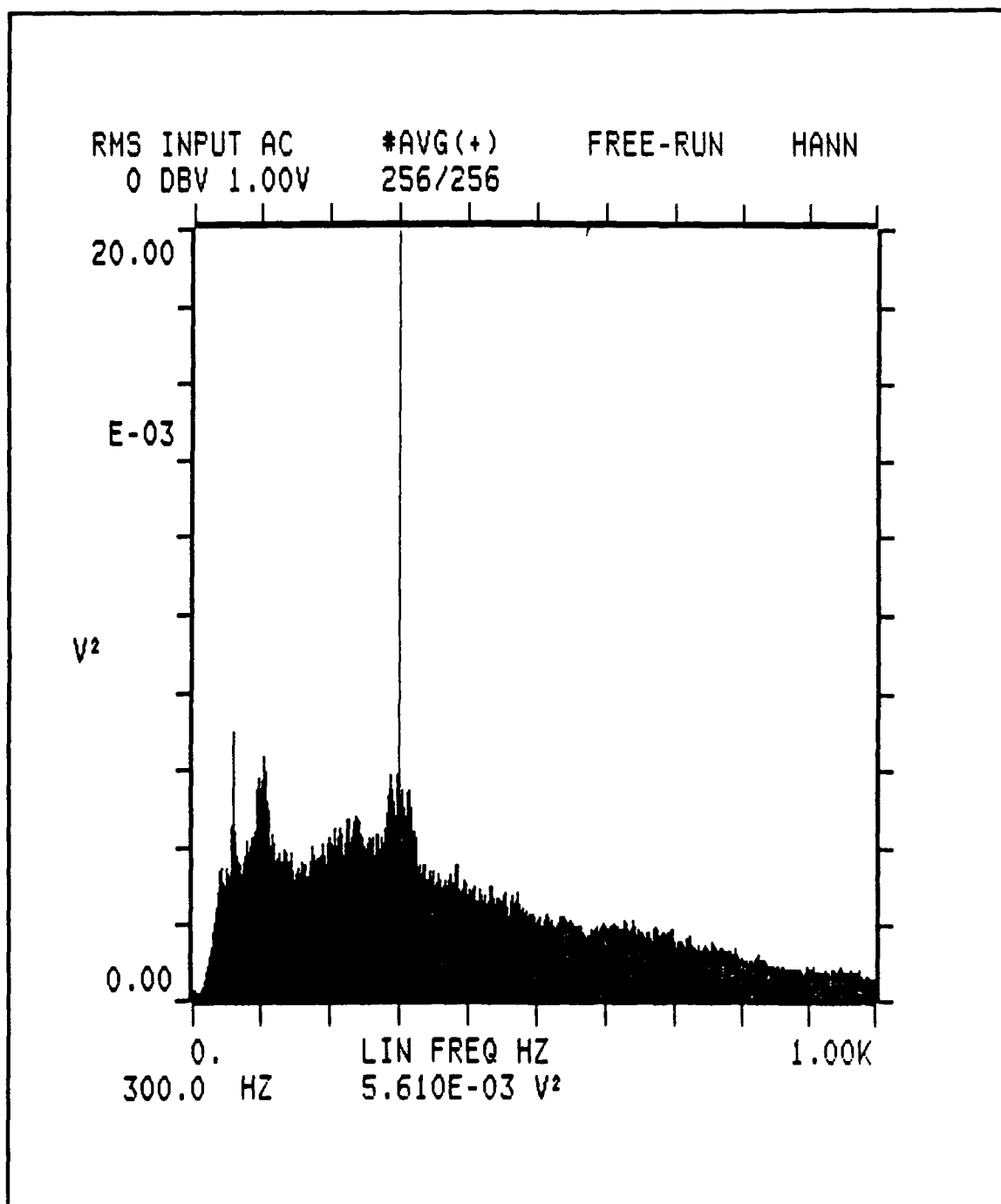


**Figure C24.** Spectrum Analyzer Display for Quasi-two-dimensional Cylinder,  $U_{\infty} = 201.0$  ft/sec, Probe 4 in. Above Low Extreme Position, Approximately 3.5 in. Above Mid-span

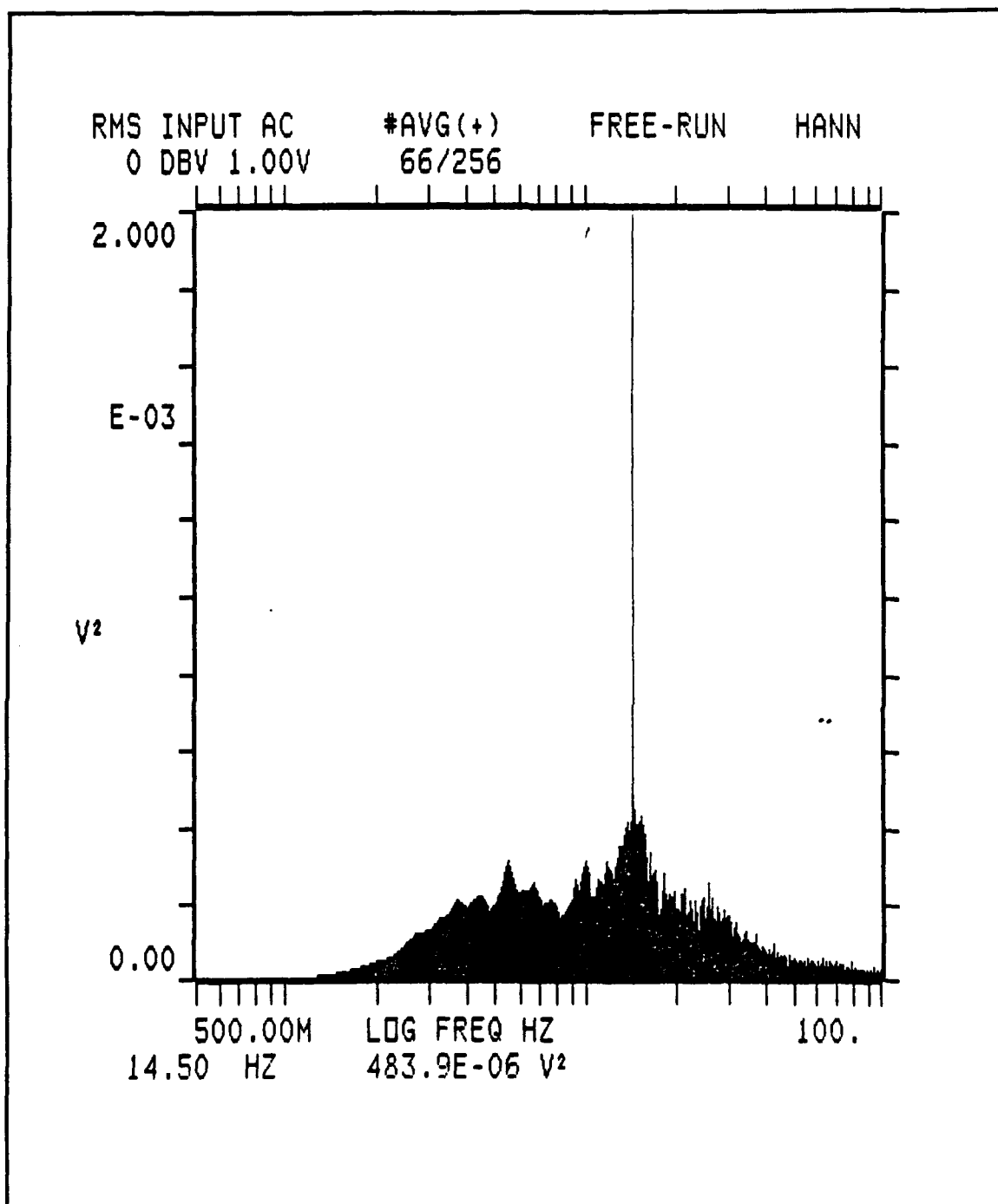


**Figure C25.** Spectrum Analyzer Display, Standard Configuration,  $U_{\infty} = 19.8\text{ft/sec}$

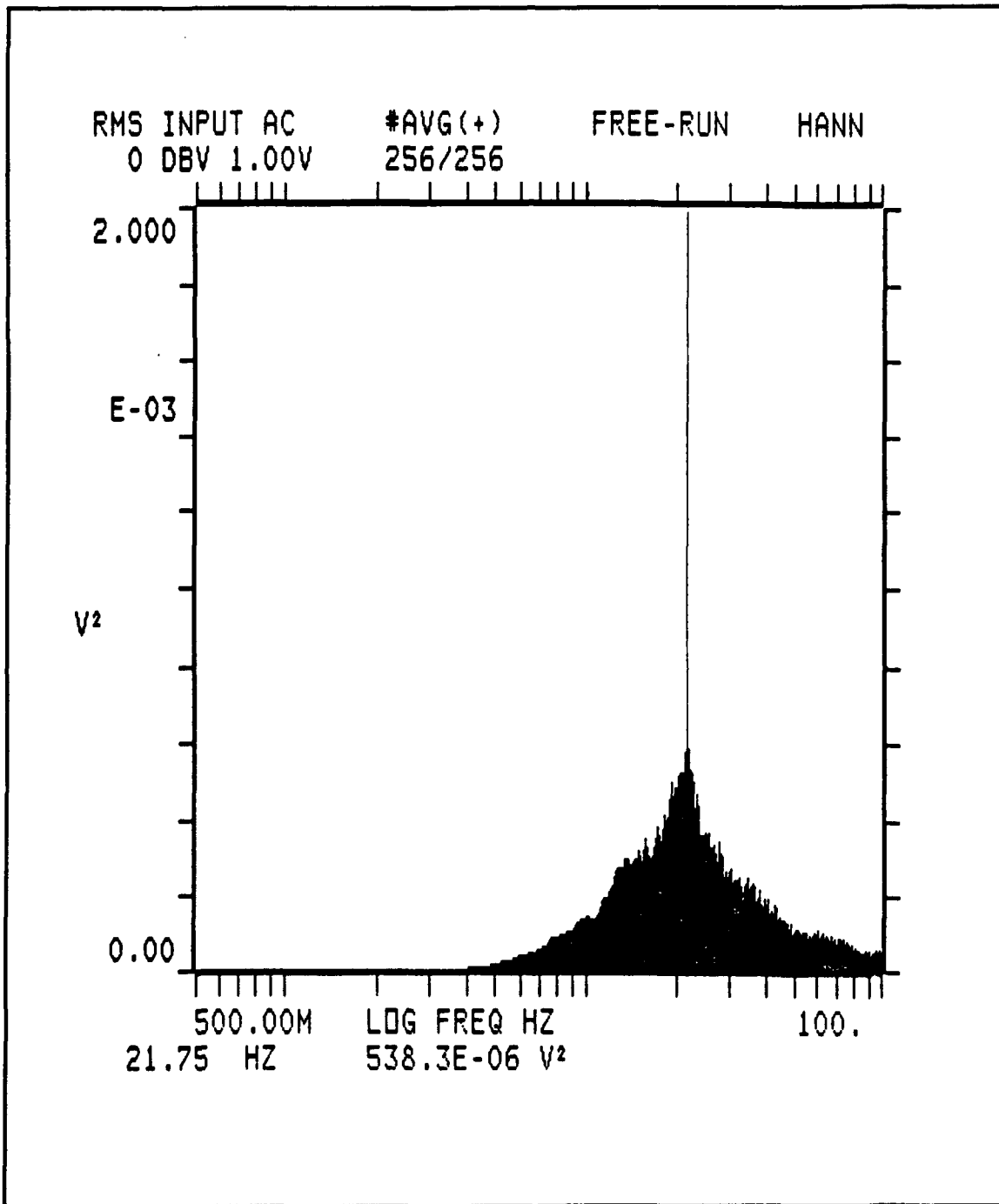


**Figure C26.** Spectrum Analyzer Display, Standard Configuration,  $U_{\infty} = 28.0\text{ft/sec}$

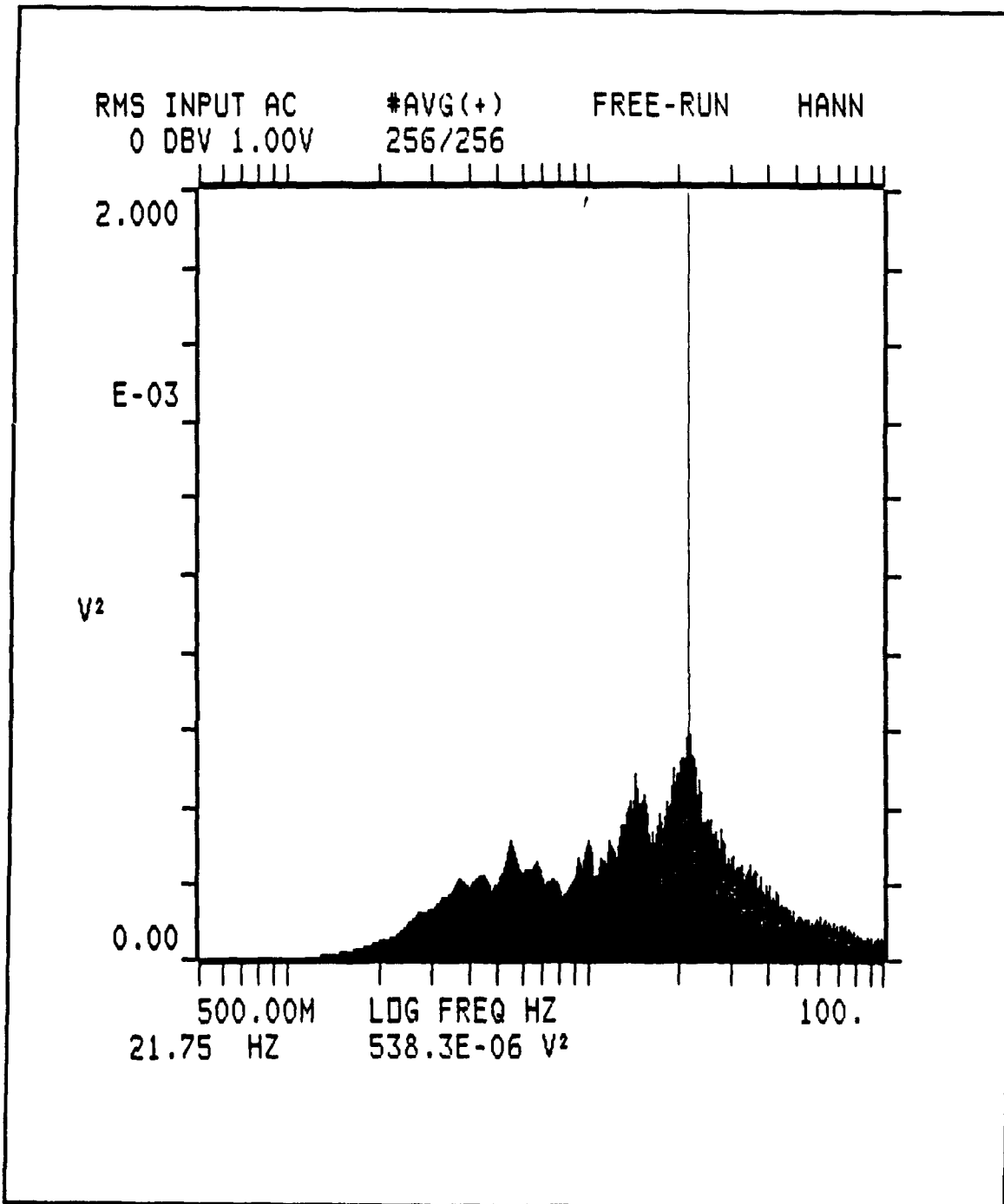


**Figure C27.** Spectrum Analyzer Display, Standard Configuration, Overlaid Plots, Dark Area is for  $U_\infty = 19.8$  ft/sec, Light Area is for  $U_\infty = 28.0$  ft/sec

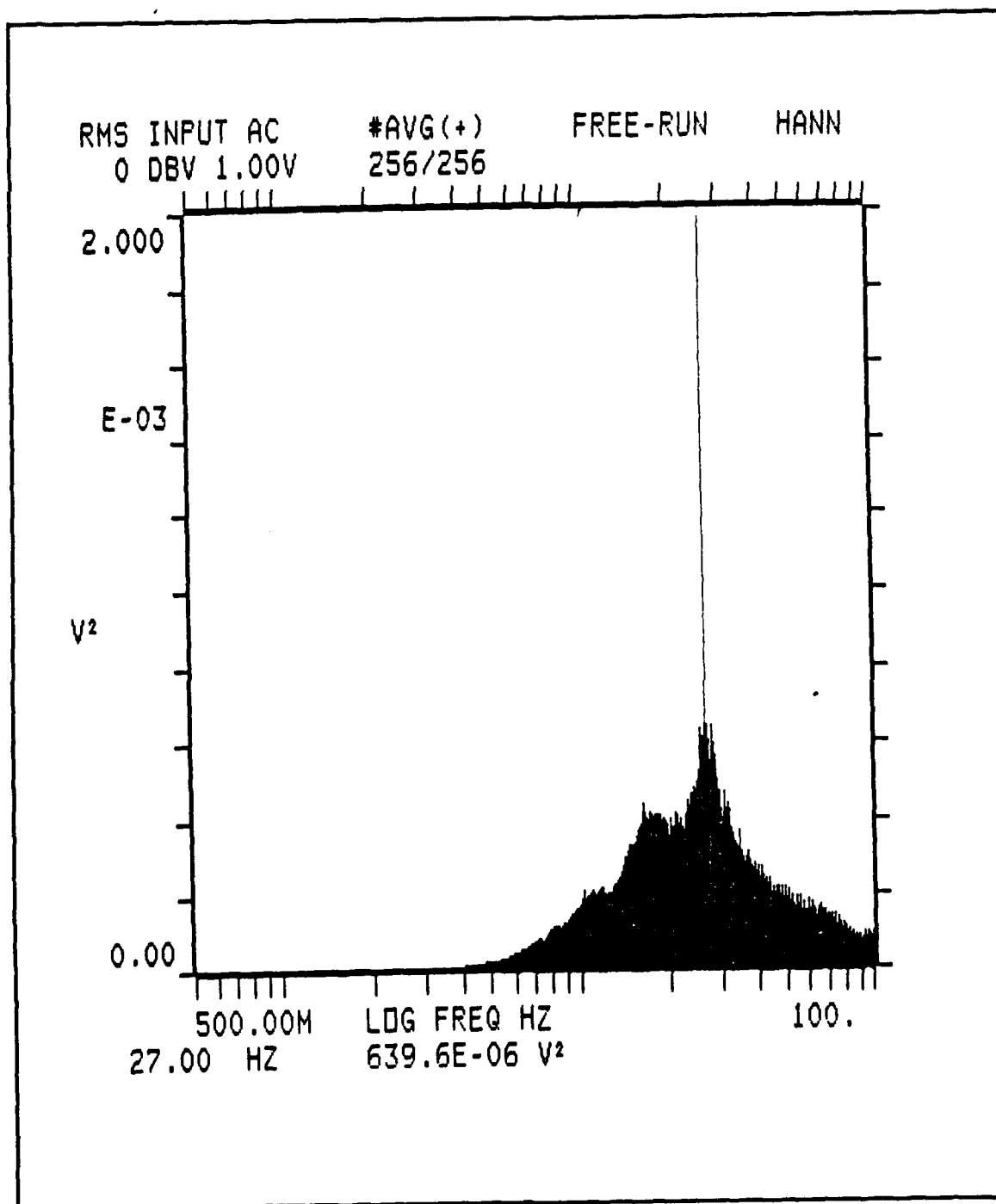
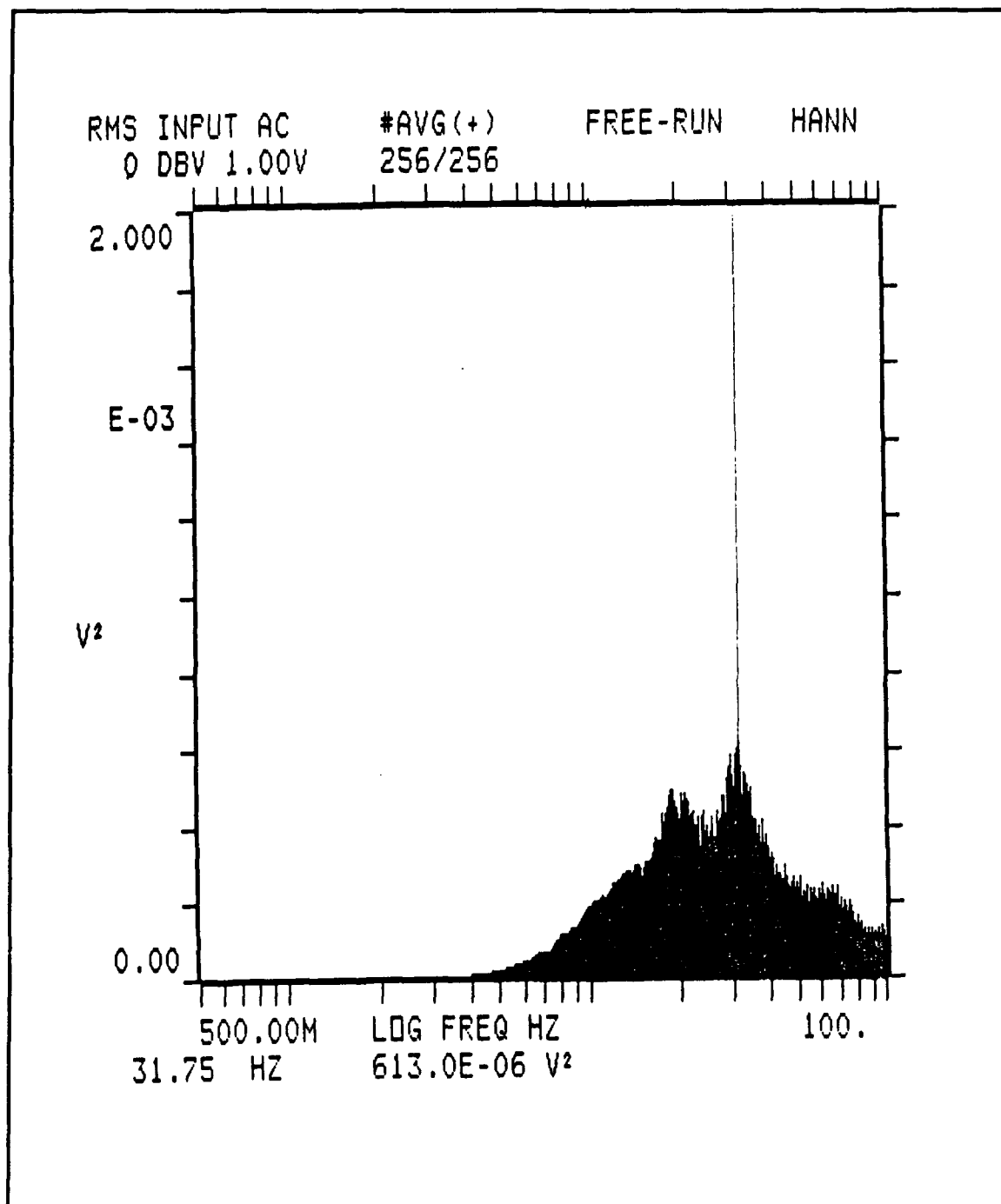


Figure C28. Spectrum Analyzer Display, Standard Configuration,  $U_{\infty} = 34.3\text{ft/sec}$



**Figure C29.** Spectrum Anaylzer Display, Standard Configuration,  $U_{\infty} = 39.6\text{ft/sec}$

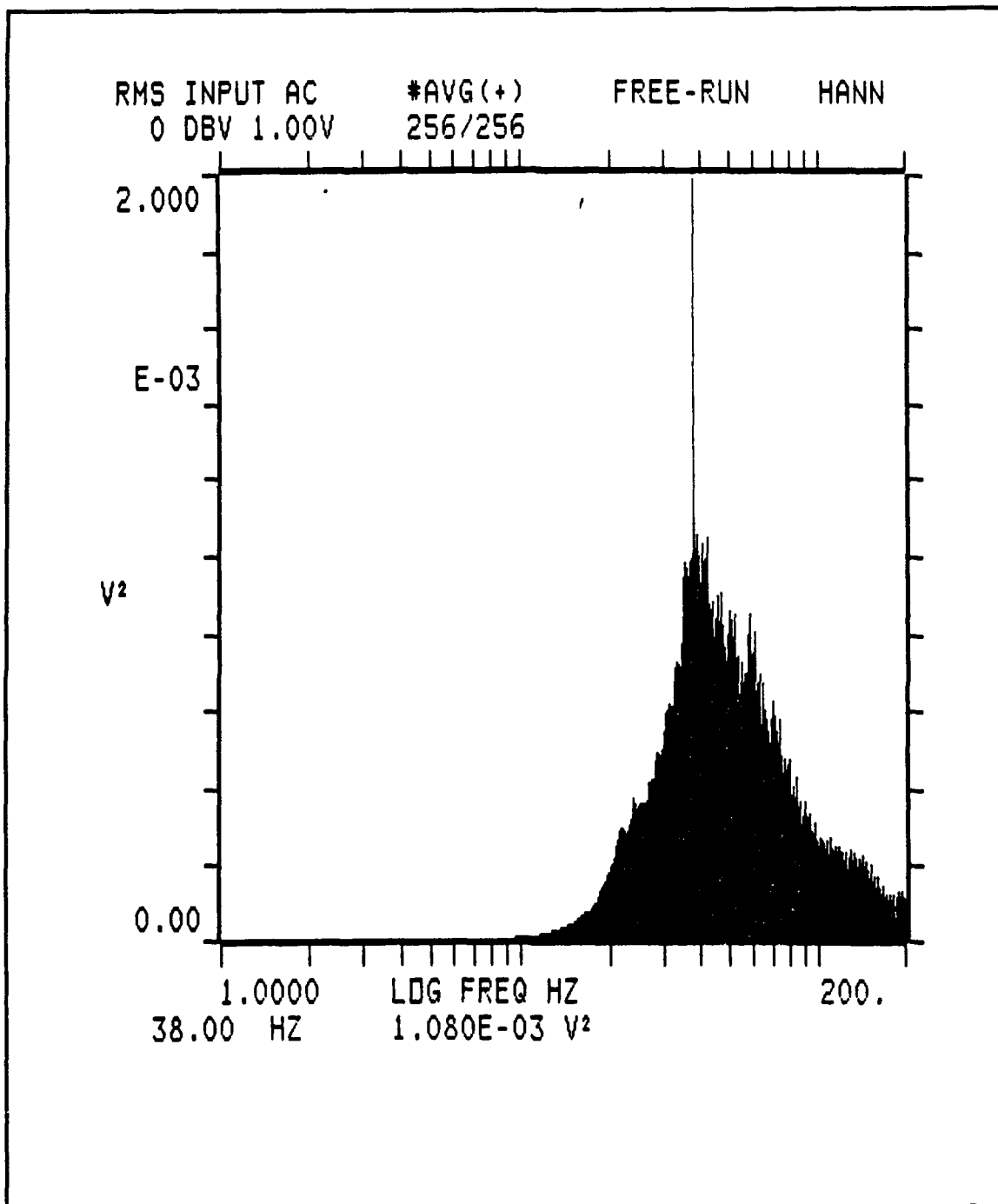
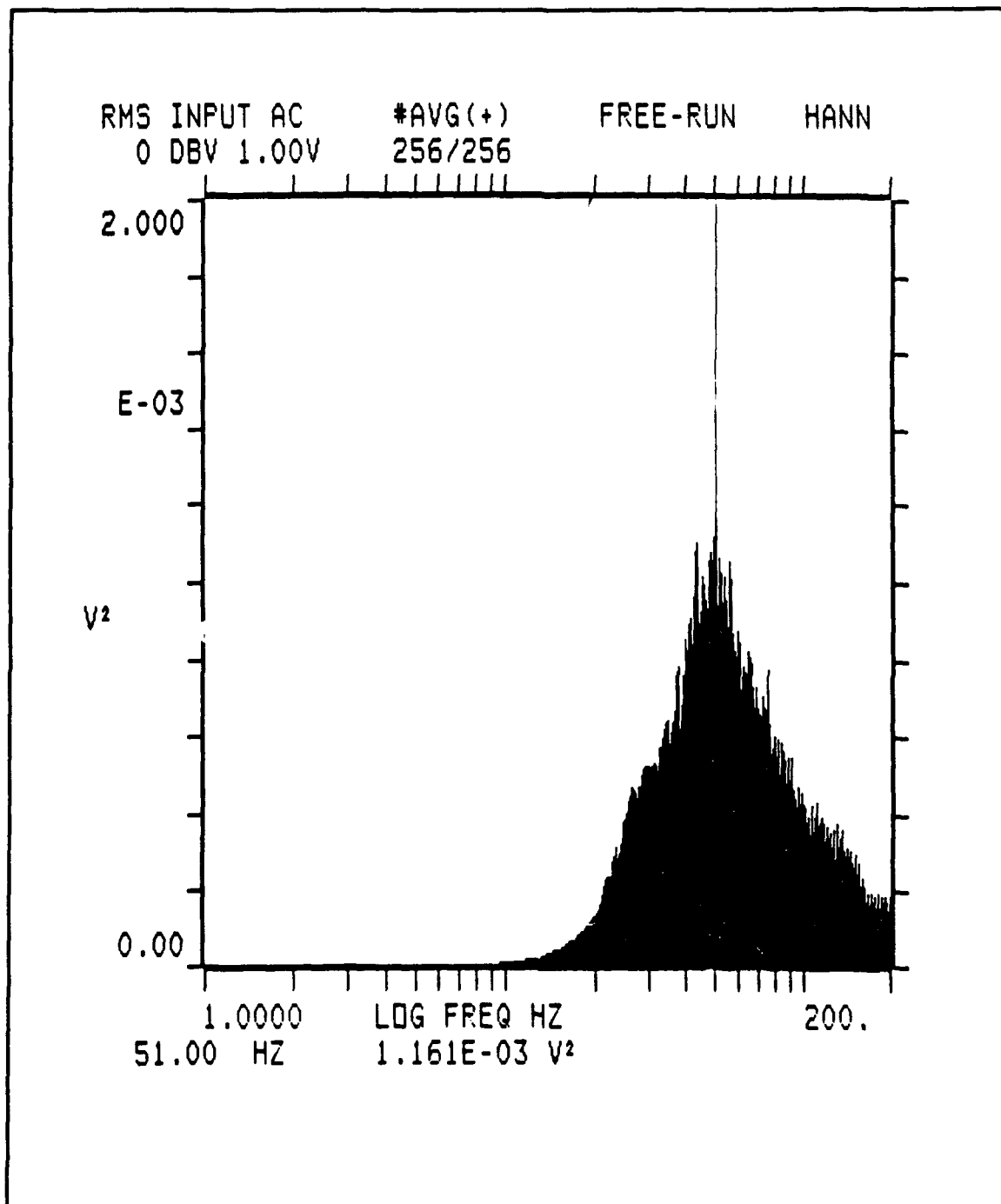


Figure C30. Spectrum Analyzer Display, Standard Configuration,  $U_\infty = 44.2\text{ft/sec}$





**Figure C31.** Spectrum Analyzer Display, Standard Configuration,  $U_{\infty} = 52.4\text{ft/sec}$

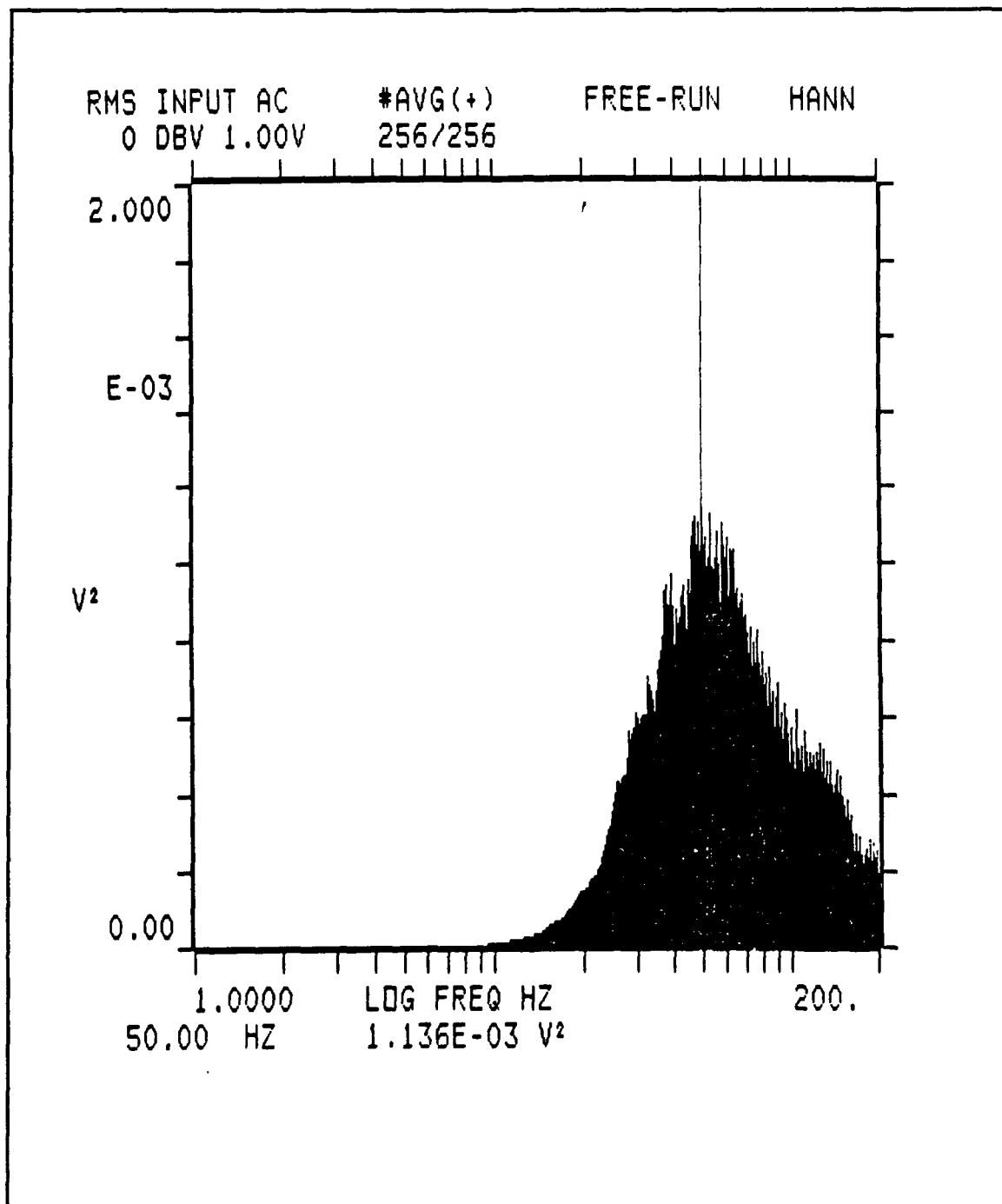


Figure C32. Spectrum Anaylzer Display, Standard Configuration,  $U_{\infty} = 59.4\text{ft/sec}$

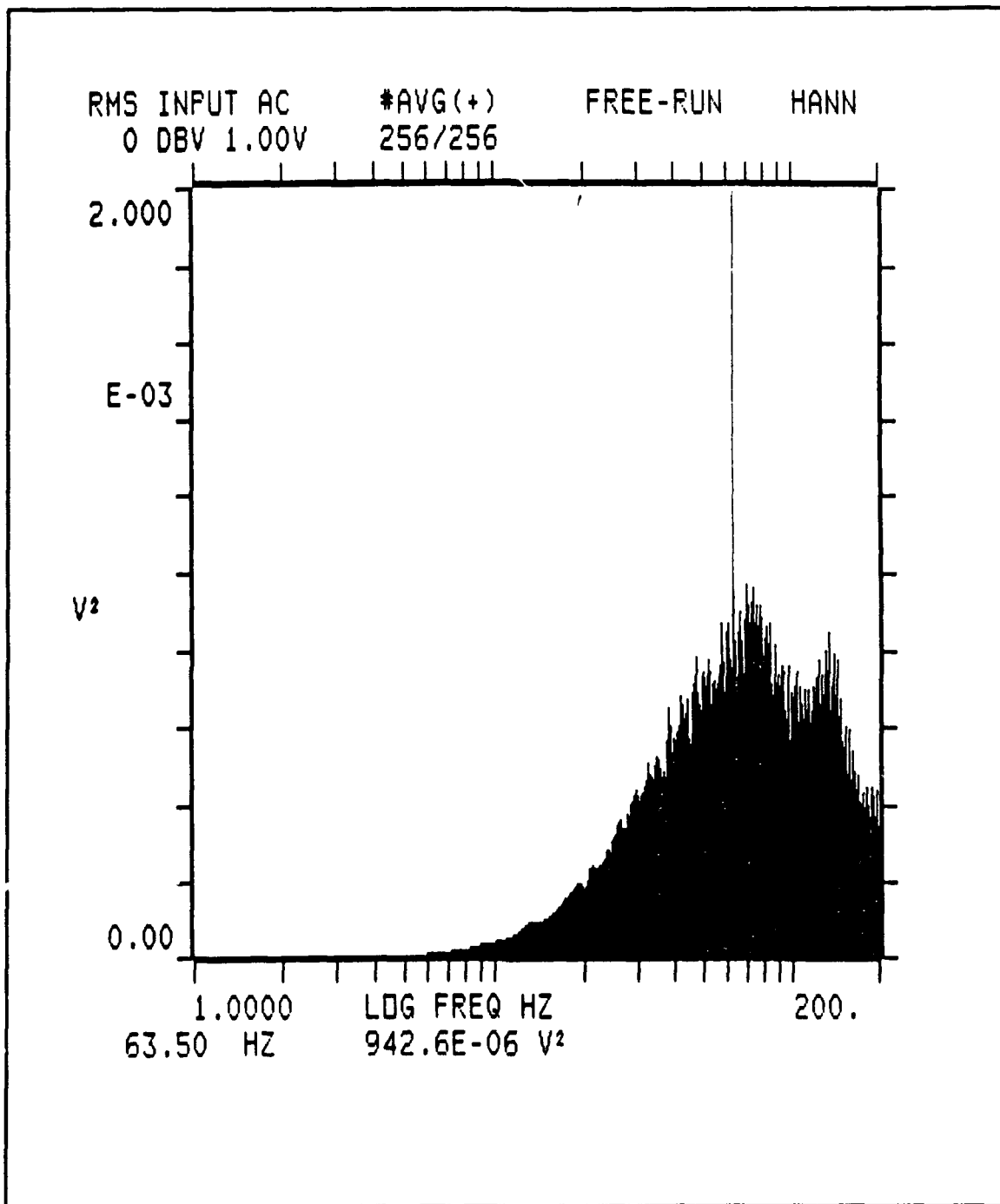


Figure C33. Spectrum Anaylzer Display, Standard Configuration,  $U_{\infty} = 68.5\text{ft/sec}$

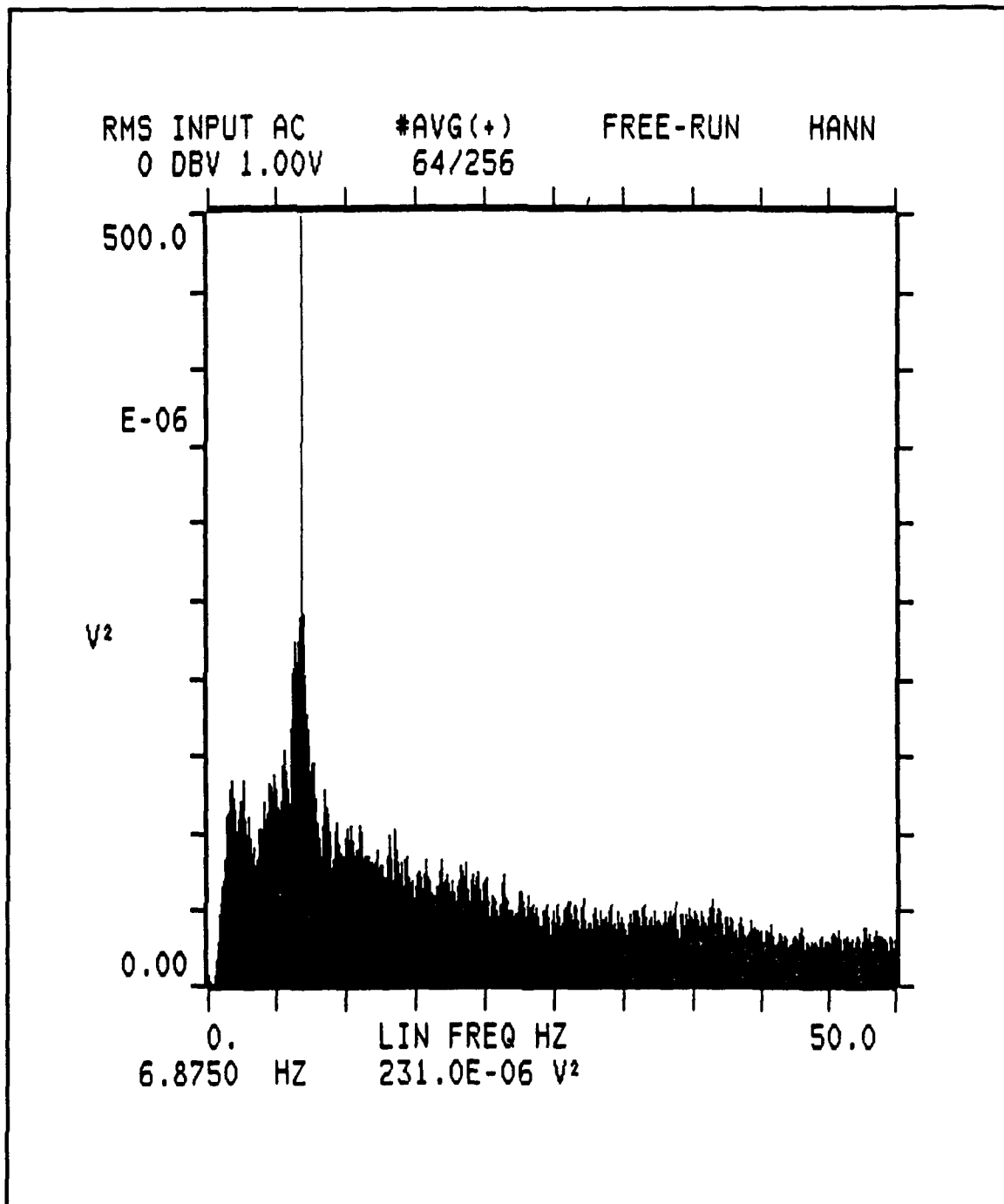
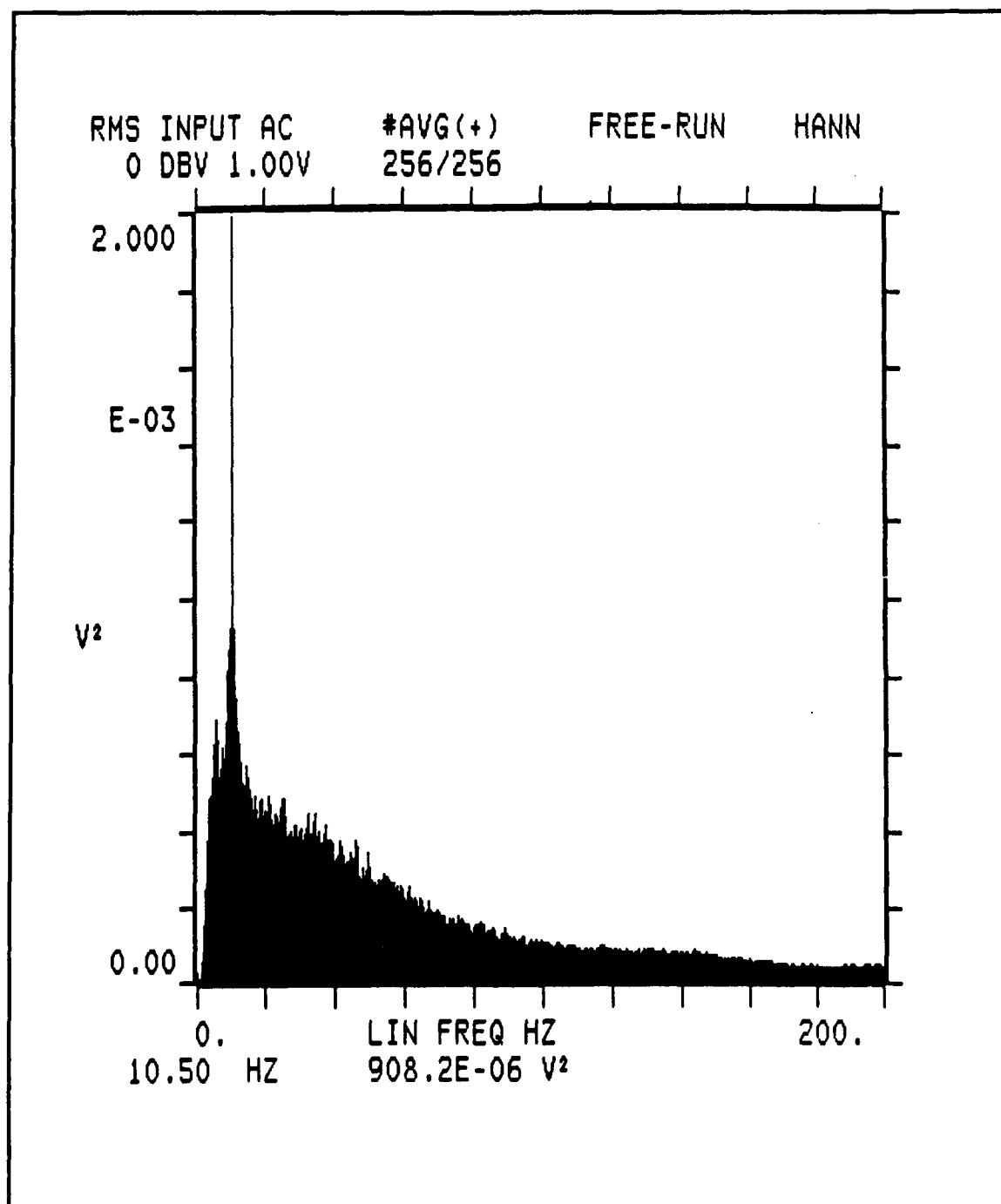


Figure C34. Spectrum Anaylzer Display, Modified Configuration, Radome Wake,  
 $U_{\infty} = 19.8\text{ft/sec}$



**Figure C35.** Spectrum Analyzer Display, Modified Configuration, Radome Wake,  
 $U_{\infty} = 28.0\text{ft/sec}$

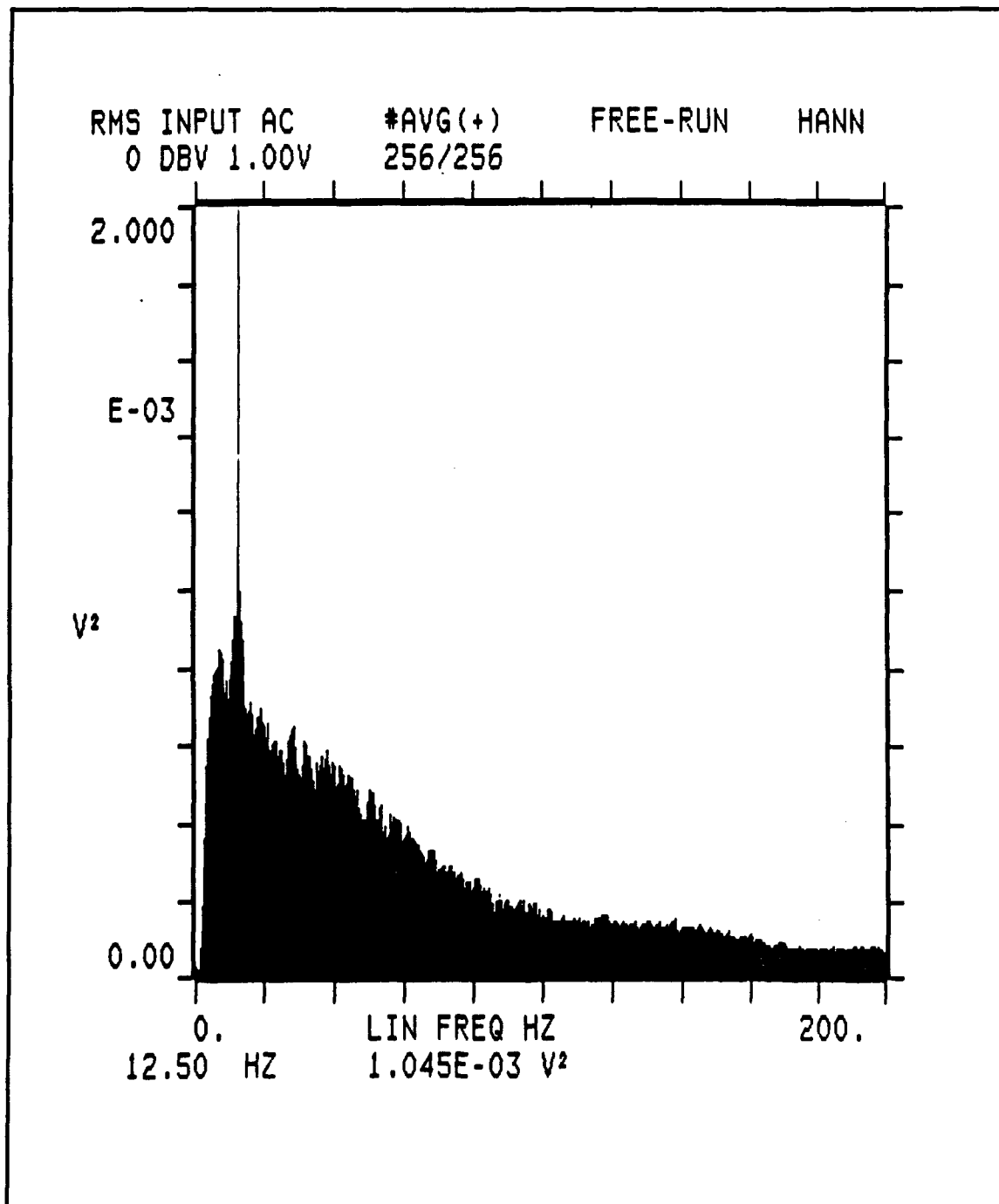
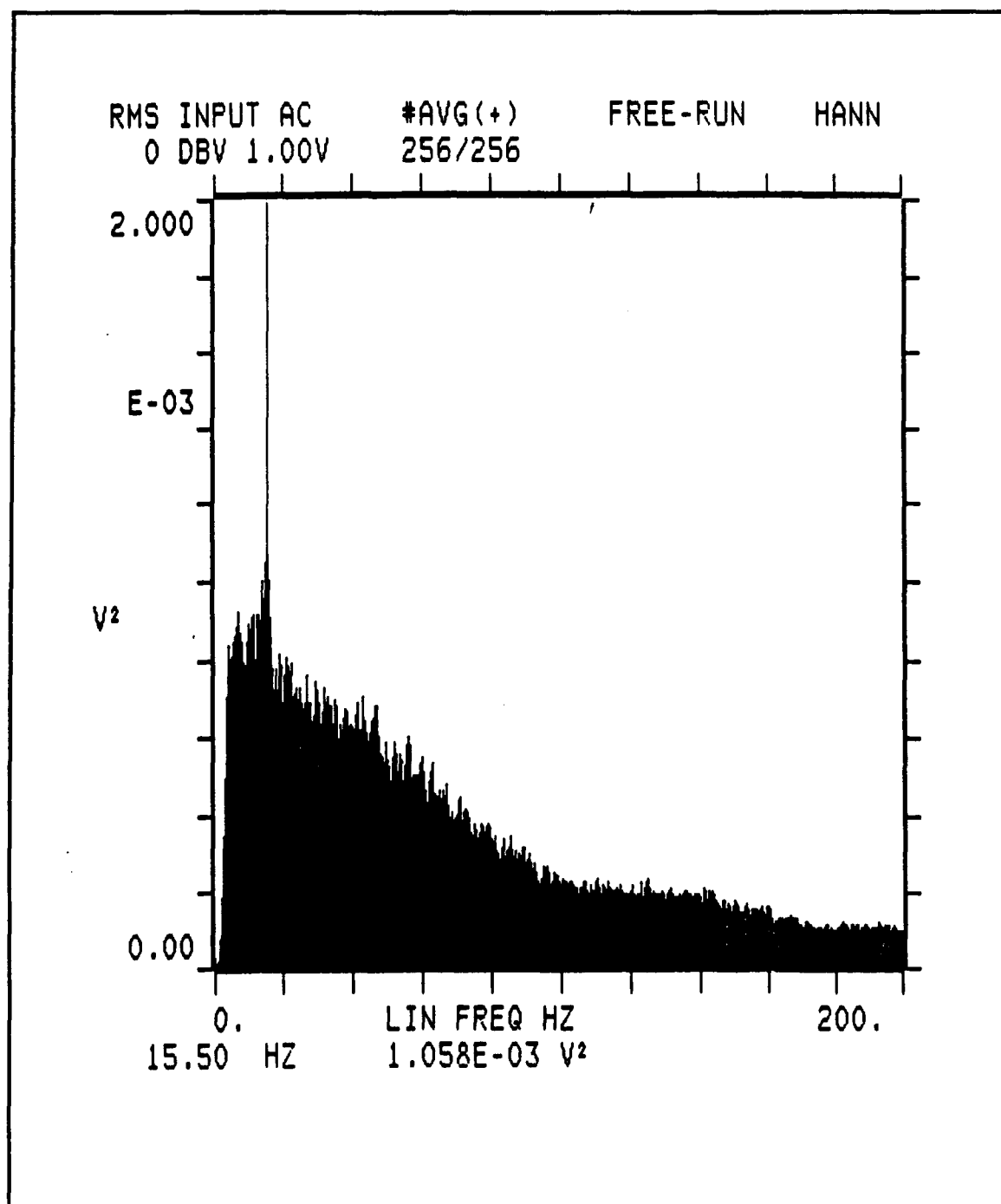
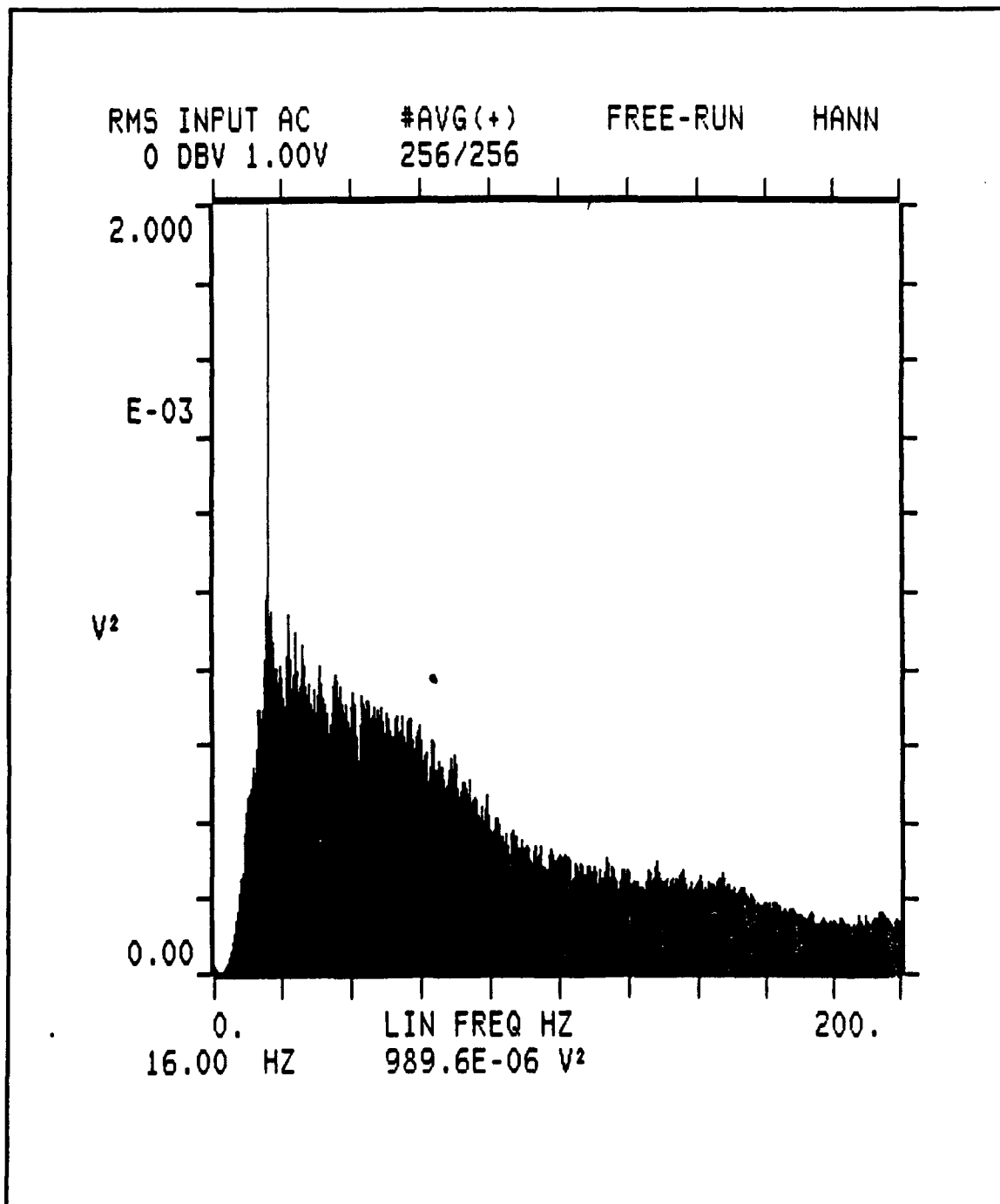


Figure C36. Spectrum Analyzer Display, Modified Configuration, Radome Wake,  
 $U_{\infty} = 34.3\text{ft/sec}$



**Figure C37.** Spectrum Anaylzer Display, Modified Configuration, Radome Wake,  
 $U_{\infty} = 39.6\text{ft/sec}$



**Figure C38.** Spectrum Anaylzer Display, Modified Configuration, Radome Wake,  
 $U_{\infty} = 44.3\text{ft/sec}$



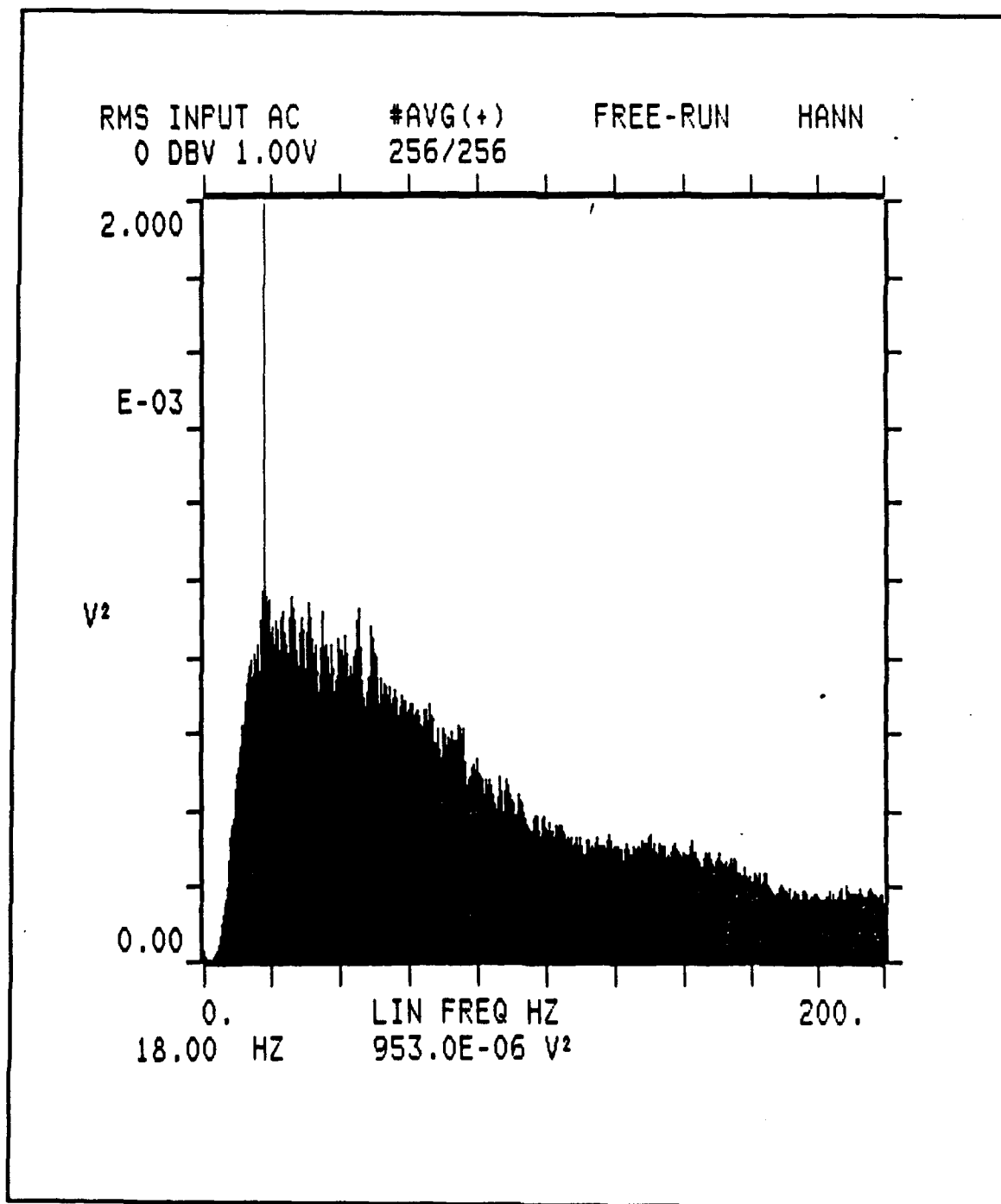


**Figure C39.** Spectrum Anaylzer Display, Modified Configuration, Radome Wake,  
 $U_{\infty} = 48.5\text{ft/sec}$

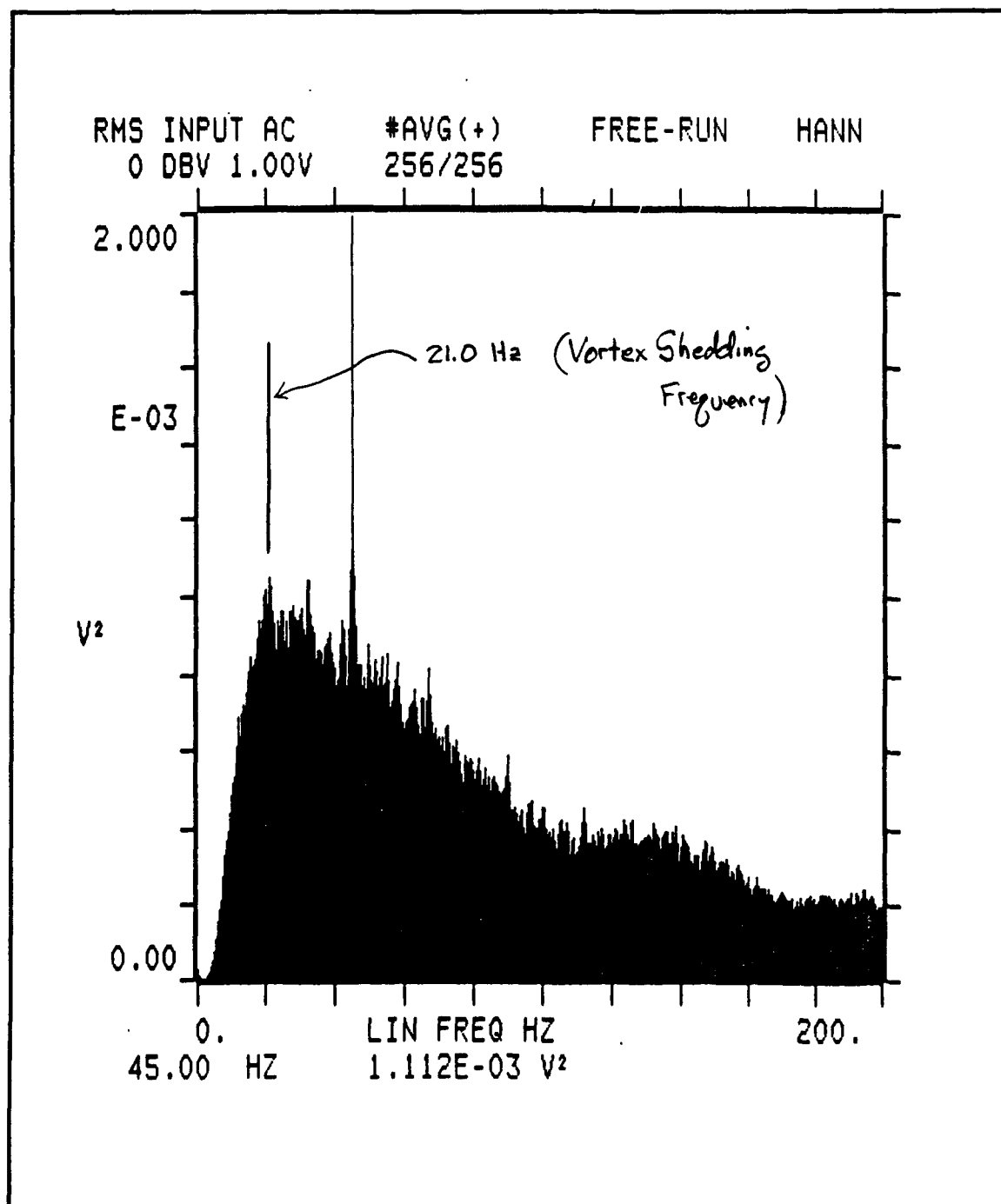


**Figure C40.** Spectrum Anaylzer Display, Modified Configuration, Radome Wake,  
 $U_{\infty} = 52.4\text{ft/sec}$

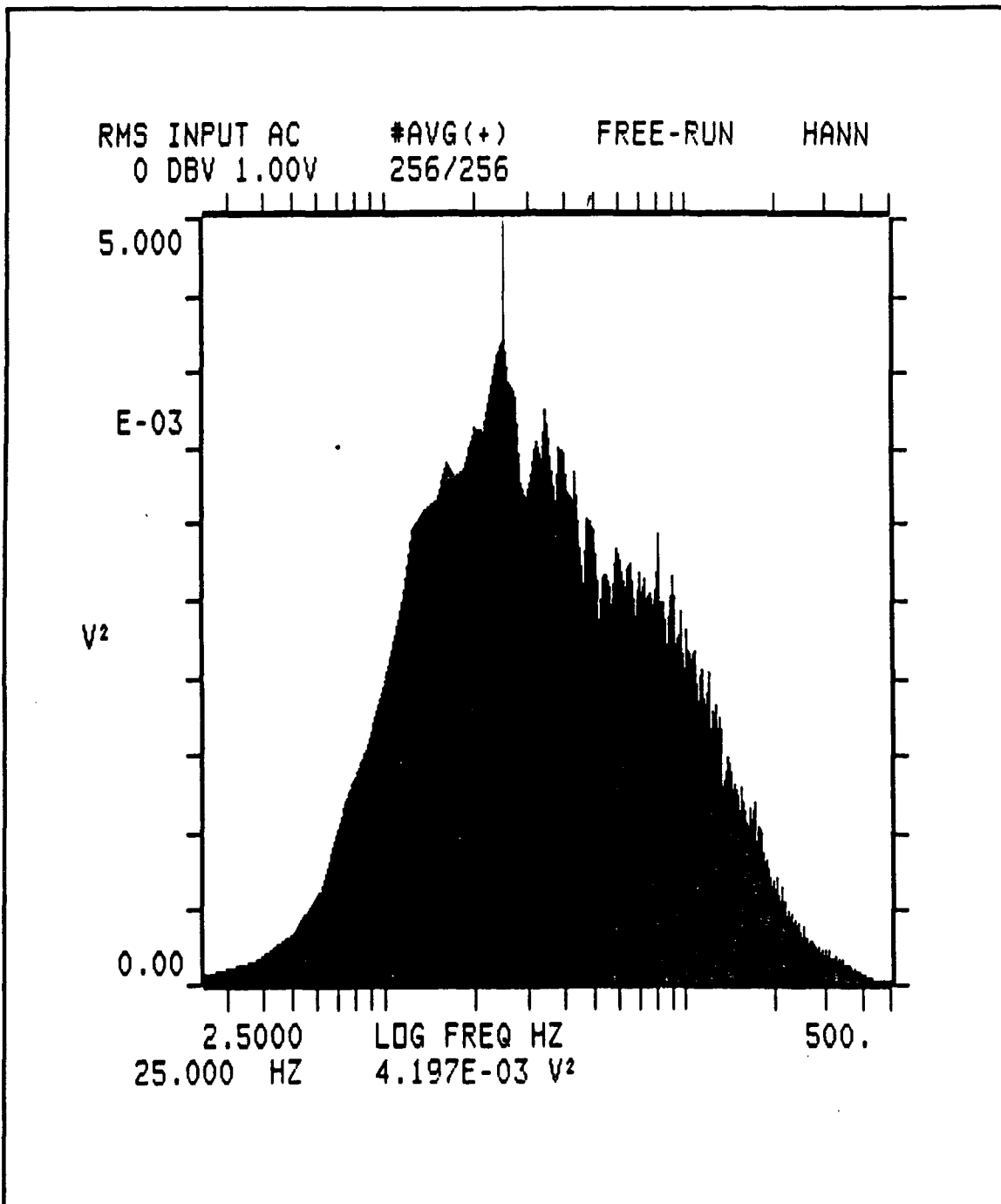


**Figure C41.** Spectrum Analyzer Display, Modified Configuration, Radome Wake,  
 $U_{\infty} = 62.6\text{ft/sec}$

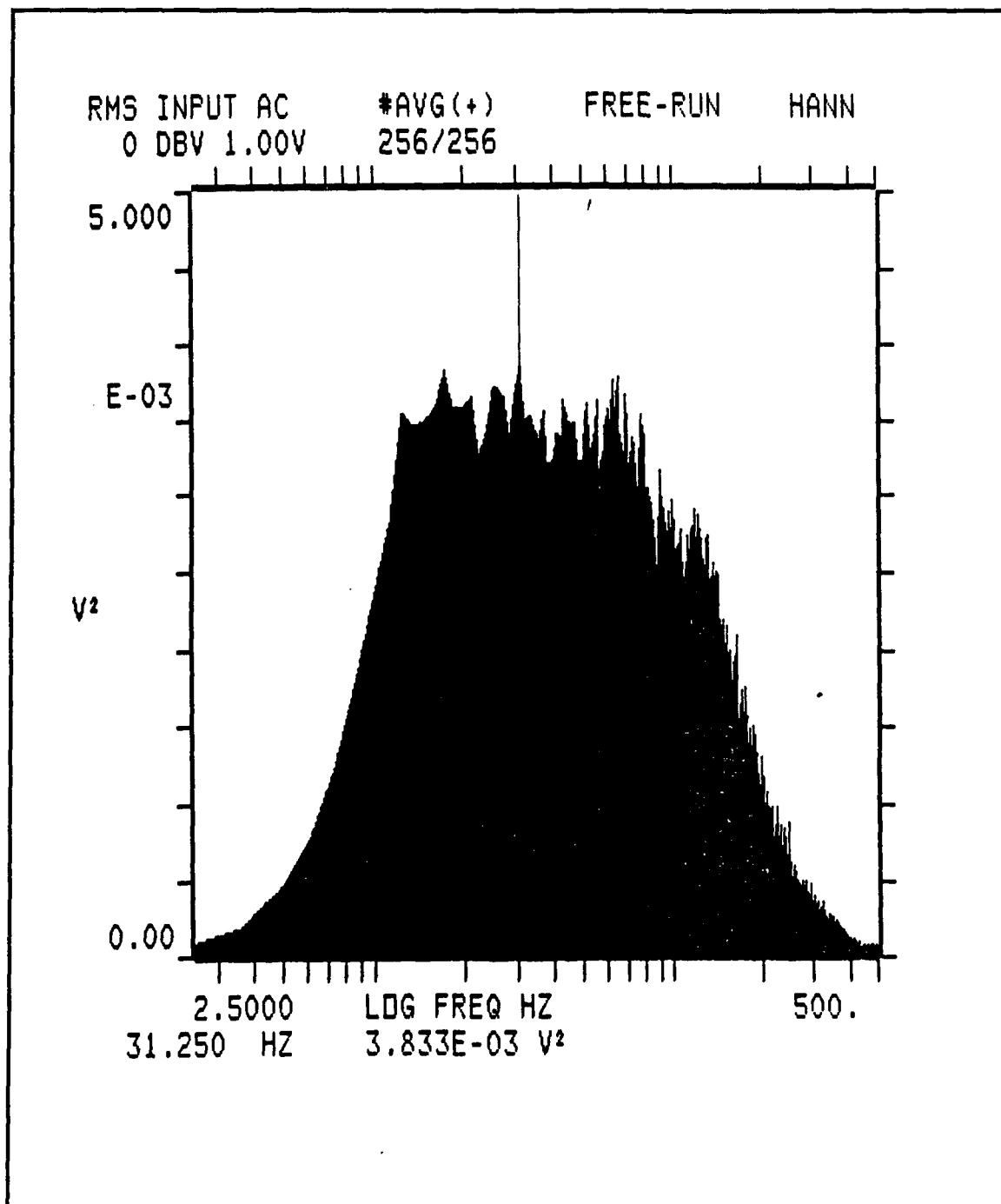


**Figure C42.** Spectrum Analyzer Display, Modified Configuration, Radome Wake,  
 $U_{\infty} = 82.9\text{ft/sec}$

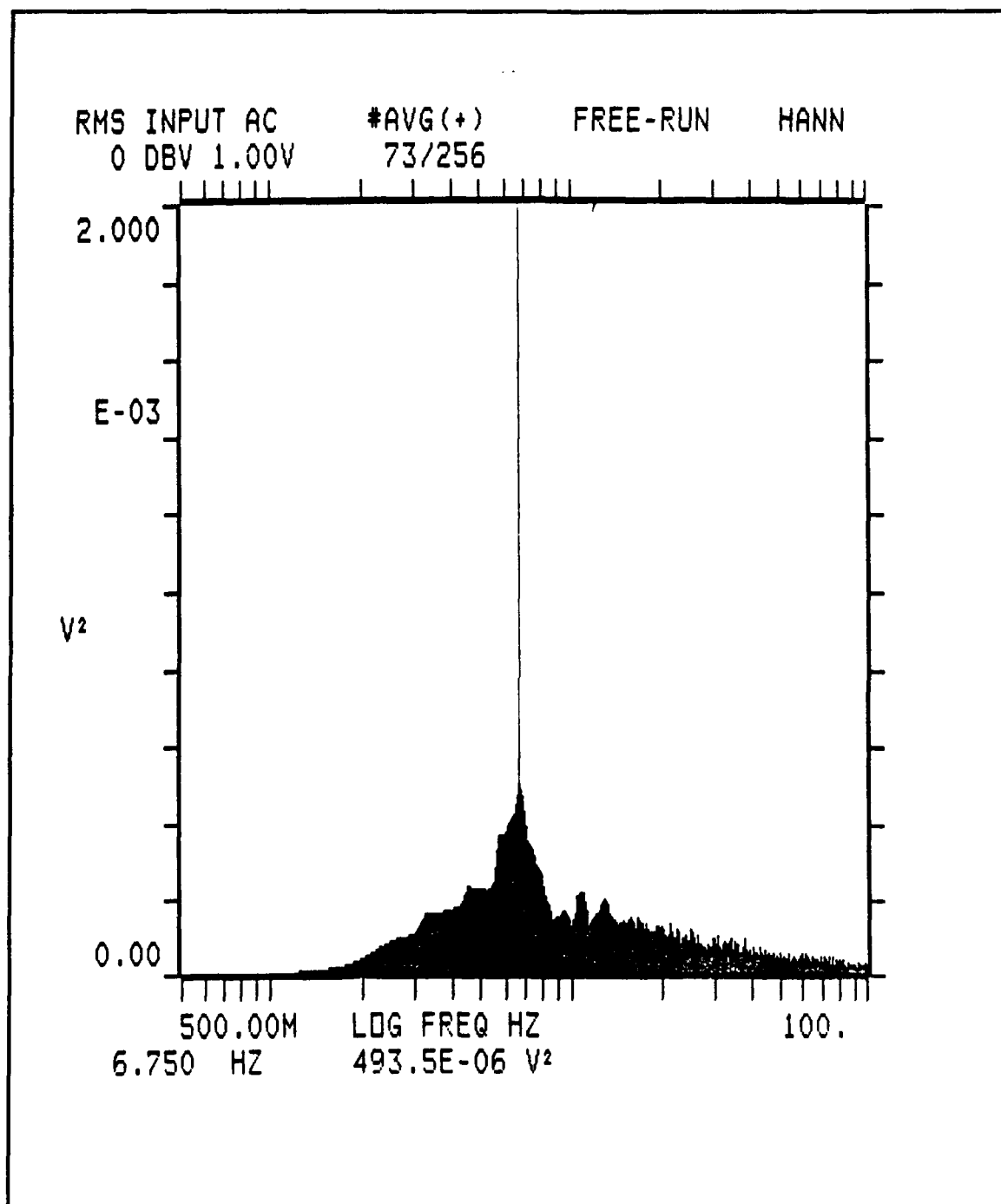


**Figure C43.** Spectrum Analyzer Display, Modified Configuration, Adapter Collar Wake,  $U_{\infty} = 19.8\text{ft/sec}$

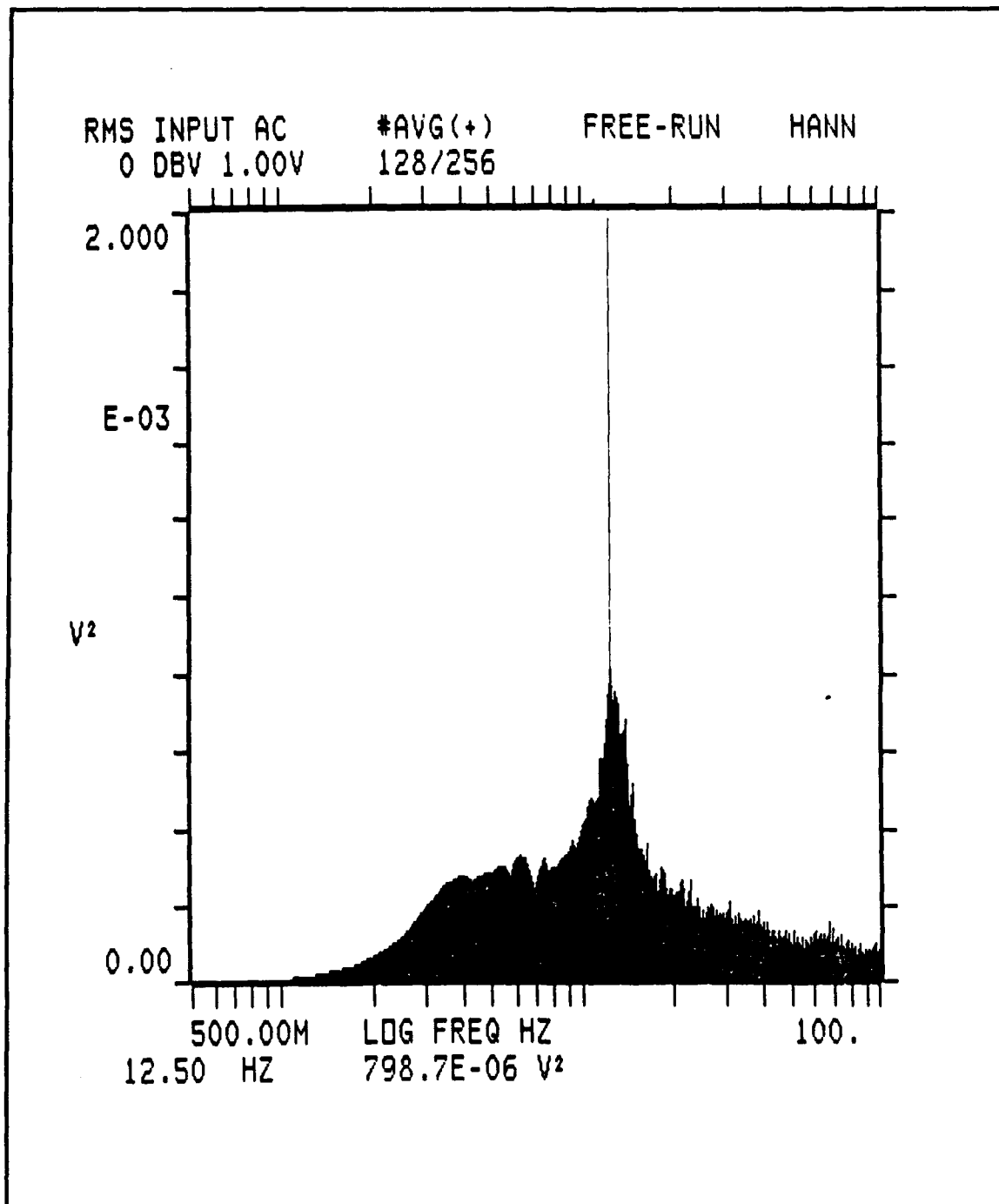


**Figure C44.** Spectrum Analyzer Display, Modified Configuration, Adapter Collar Wake,  $U_{\infty} = 34.3\text{ft/sec}$

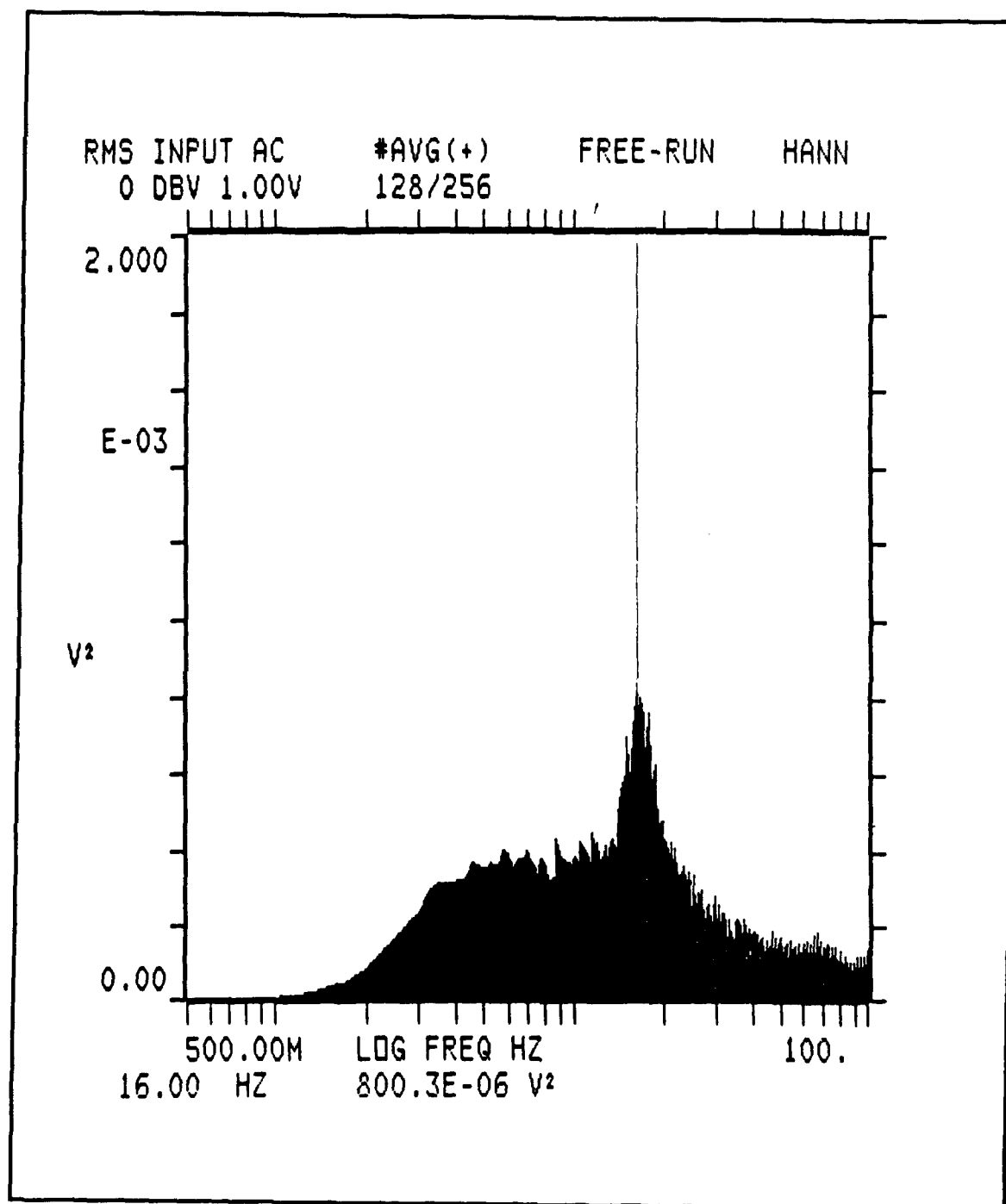


**Figure C45.** Spectrum Analyzer Display, Modified Configuration, Adapter Collar Wake,  $U_{\infty} = 44.3\text{ft/sec}$

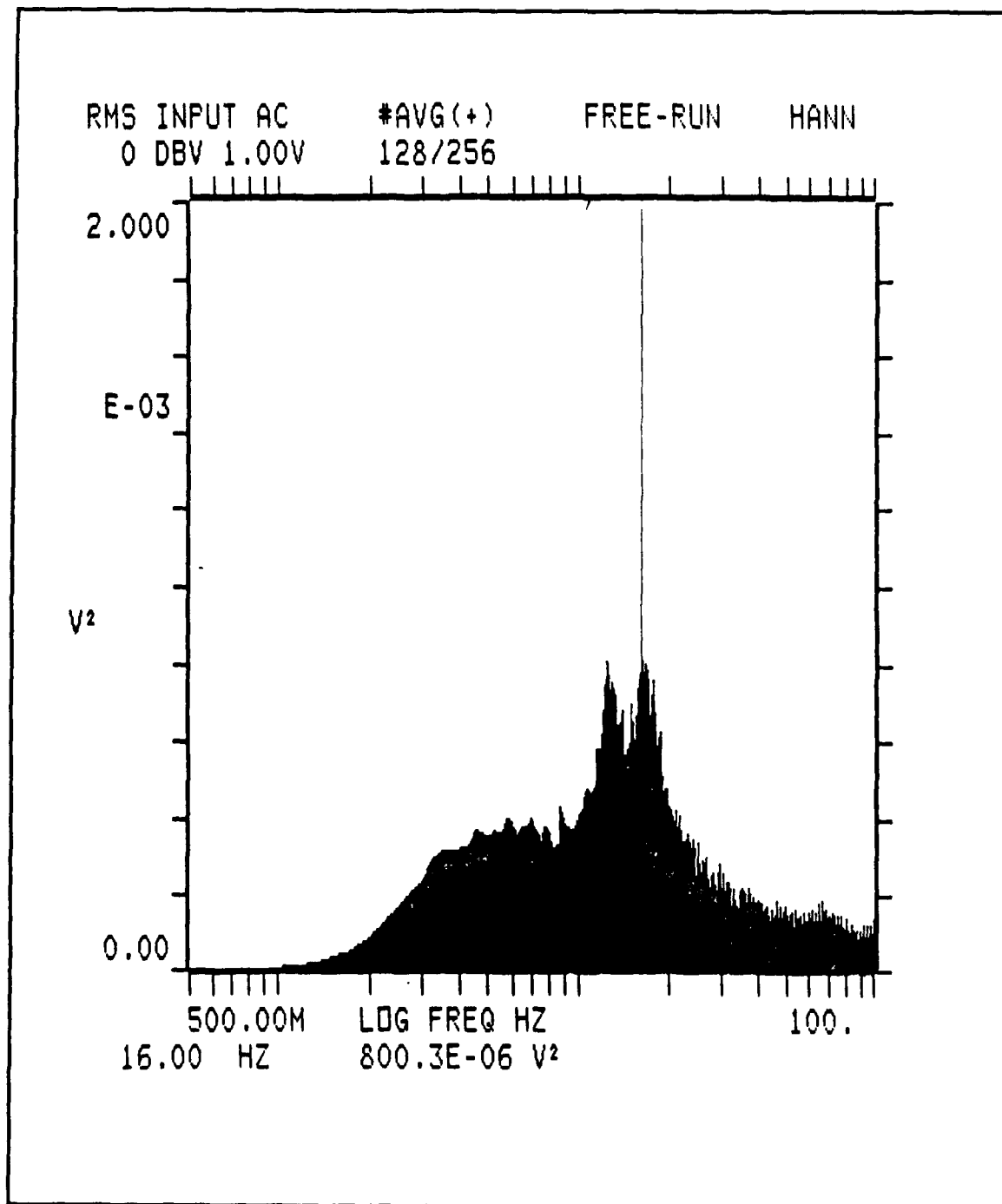


**Figure C46.** Spectrum Analyzer Display, Modified Configuration, Adapter Collar Wake, Overlaid Plots, Dark Area for  $U_{\infty} = 34.3\text{ft/sec}$ , Light Area for  $U_{\infty} = 44.3\text{ft/sec}$



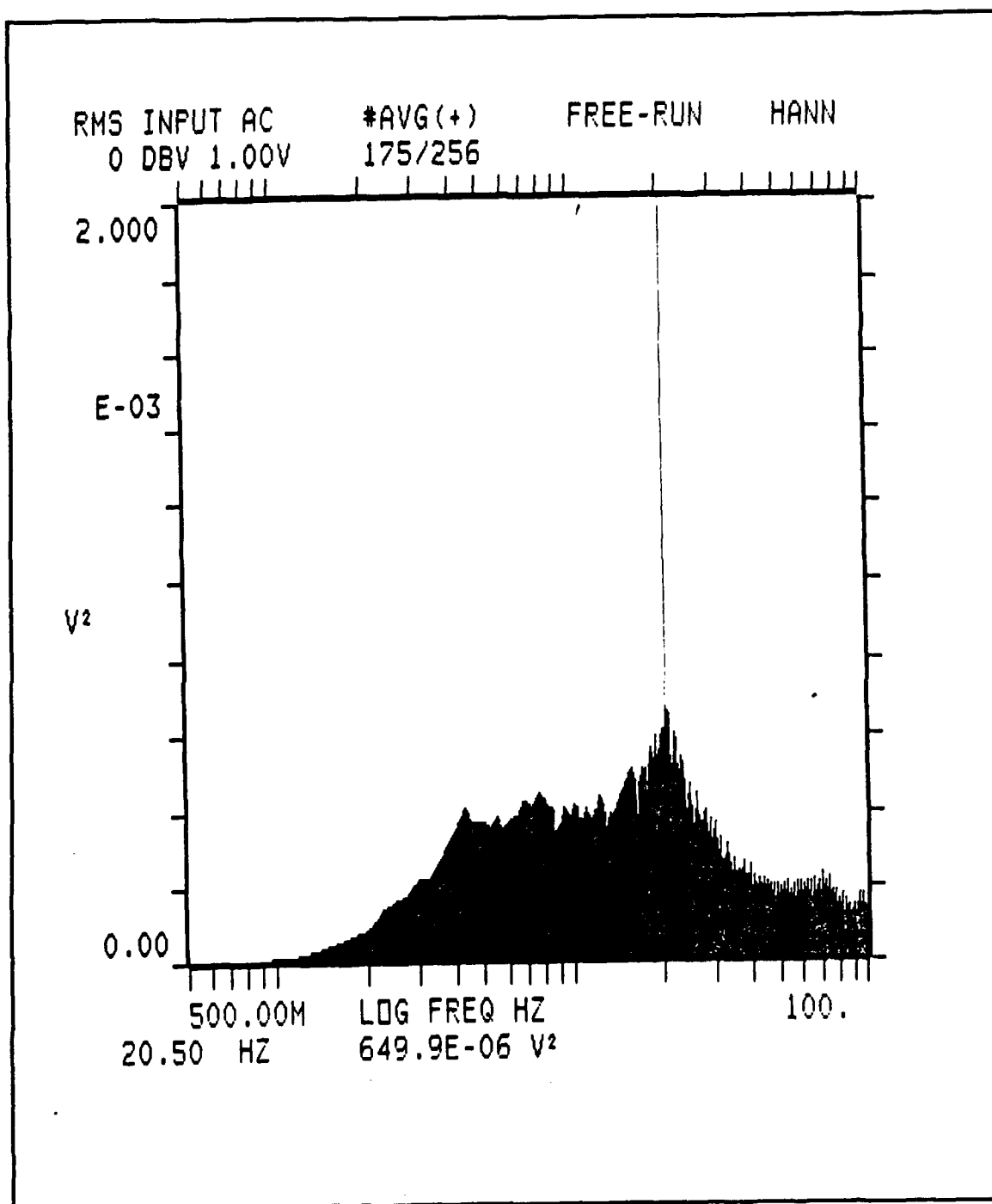


**Figure C47.** Spectrum Analyzer Display, Modified Configuration, Adapter Collar Wake,  $U_{\infty} = 52.4\text{ft/sec}$

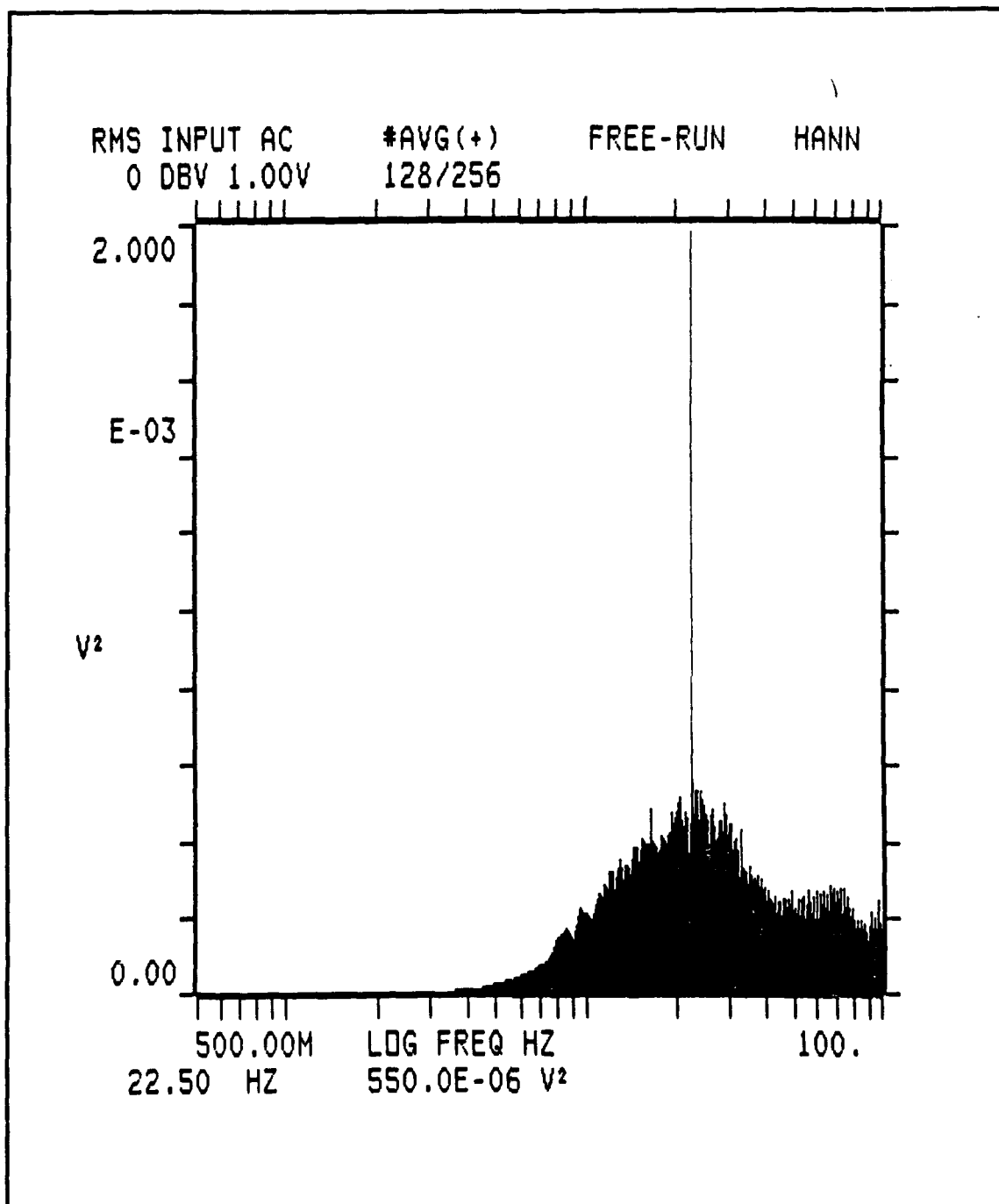


**Figure C48.** Spectrum Analyzer Display, Modified Configuration, Adapter Collar Wake,  $U_{\infty} = 59.4\text{ft/sec}$

**APPENDIX D**  
**FLOW VISUALIZATION IMAGERY**

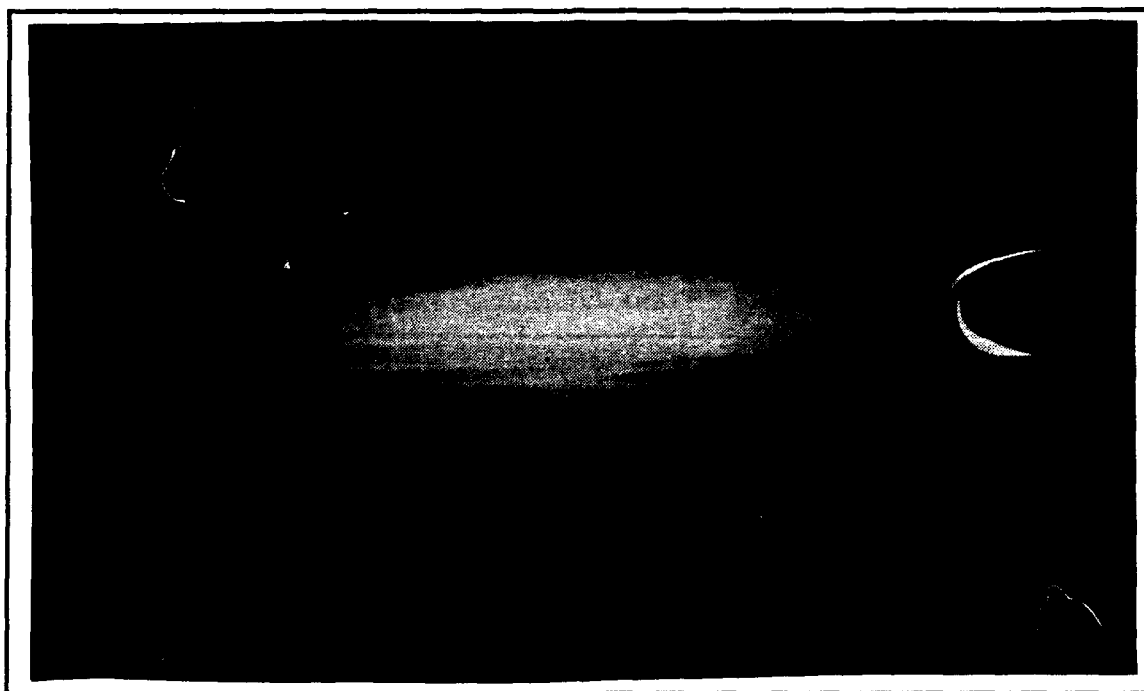


**Figure D1.** Vortex Formation Region, Standard Configuration, Vertical Station 3

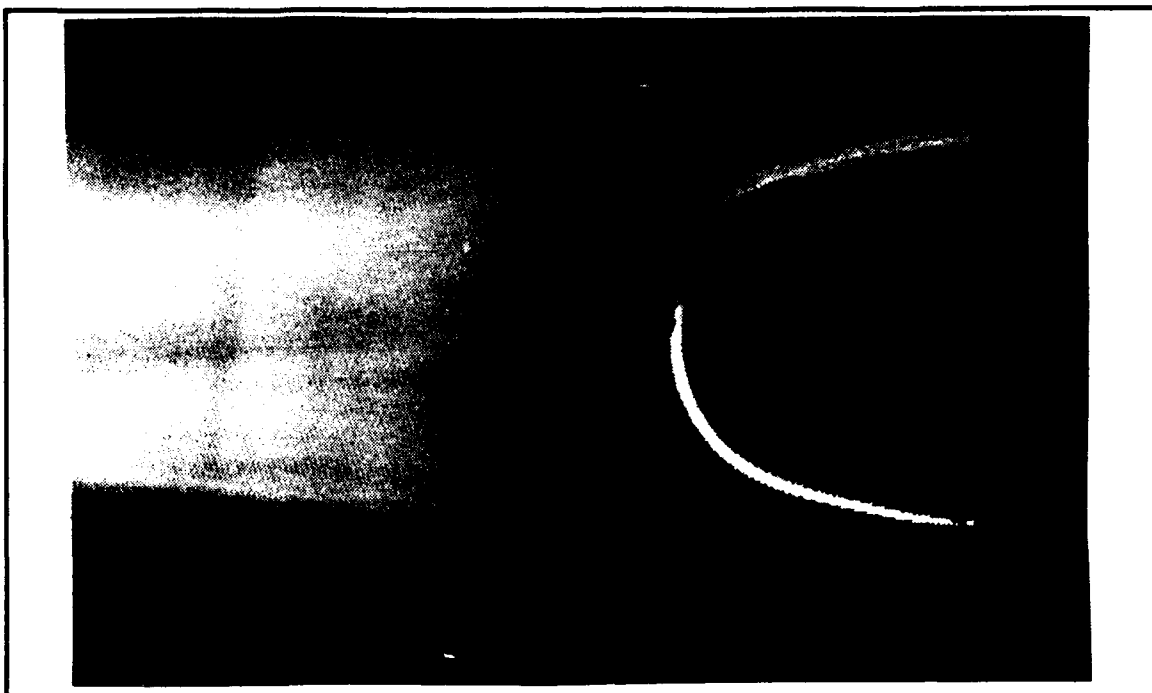


**Figure D2. Vortex Formation Region, Standard Configuration, Vertical Station 4**



**Figure D3. Vortex Formation Region, Modified Configuration, Vertical Station 1**

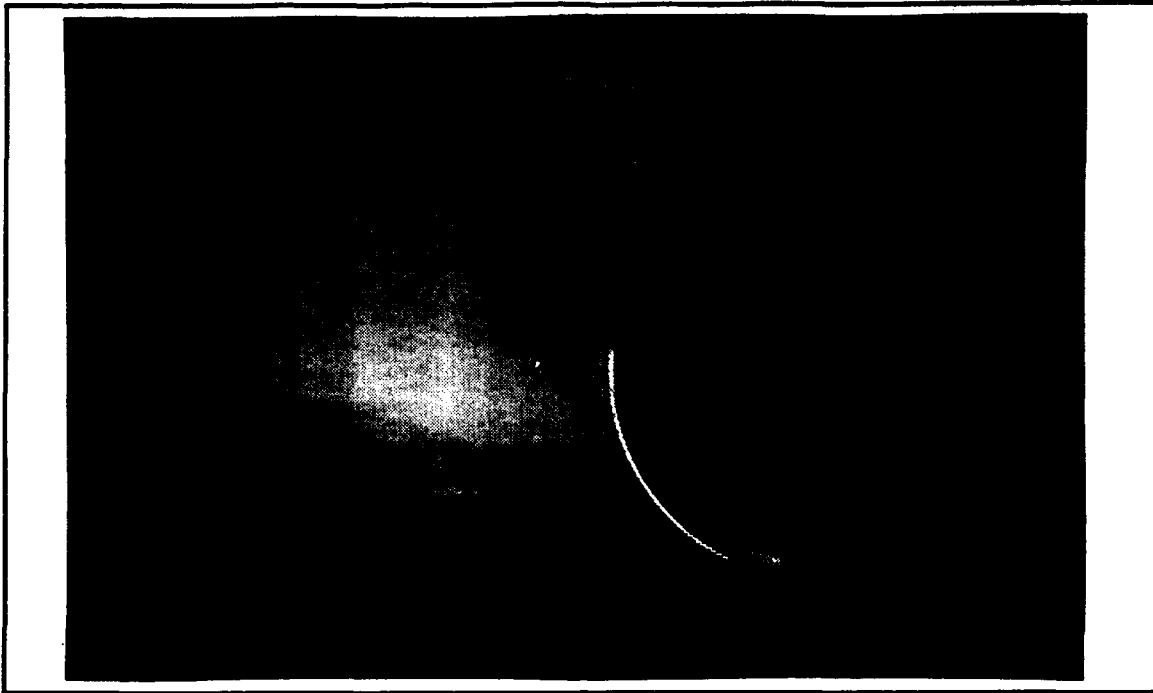


**Figure D4. Vortex Formation Region, Modified Configuration, Vertical Station 2**

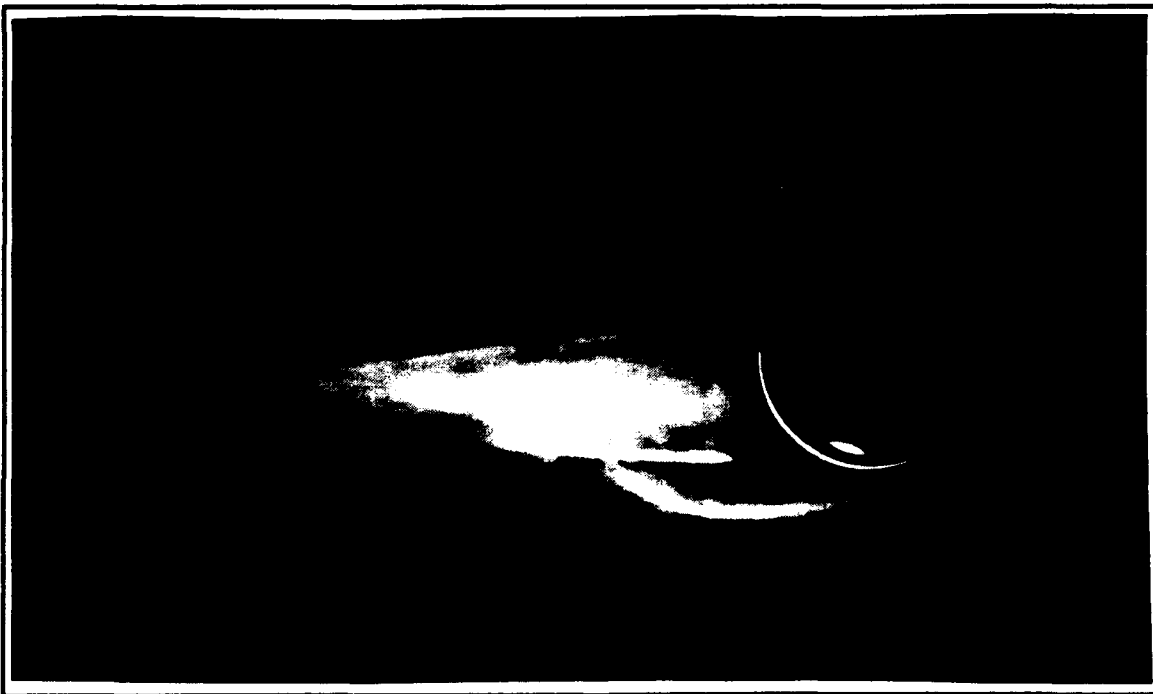


**Figure D5. Vortex Formation Region, Modified Configuration, Vertical Station 3**

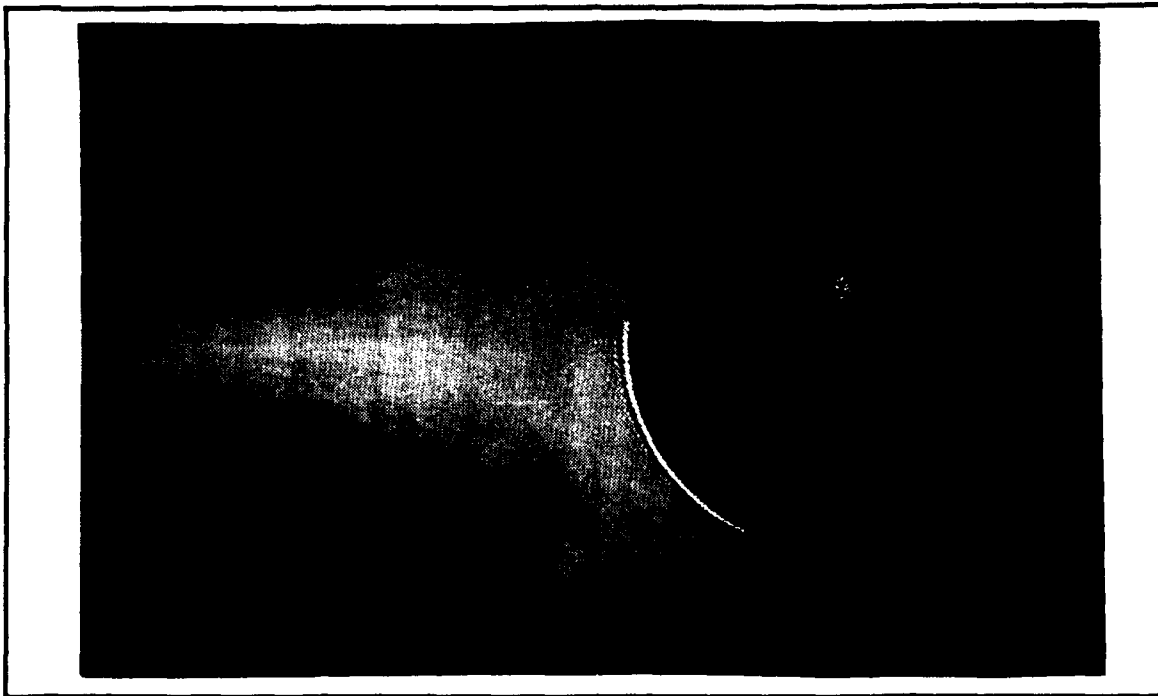


**Figure D6. Vortex Formation Region, Modified Configuration, Vertical Station 4**

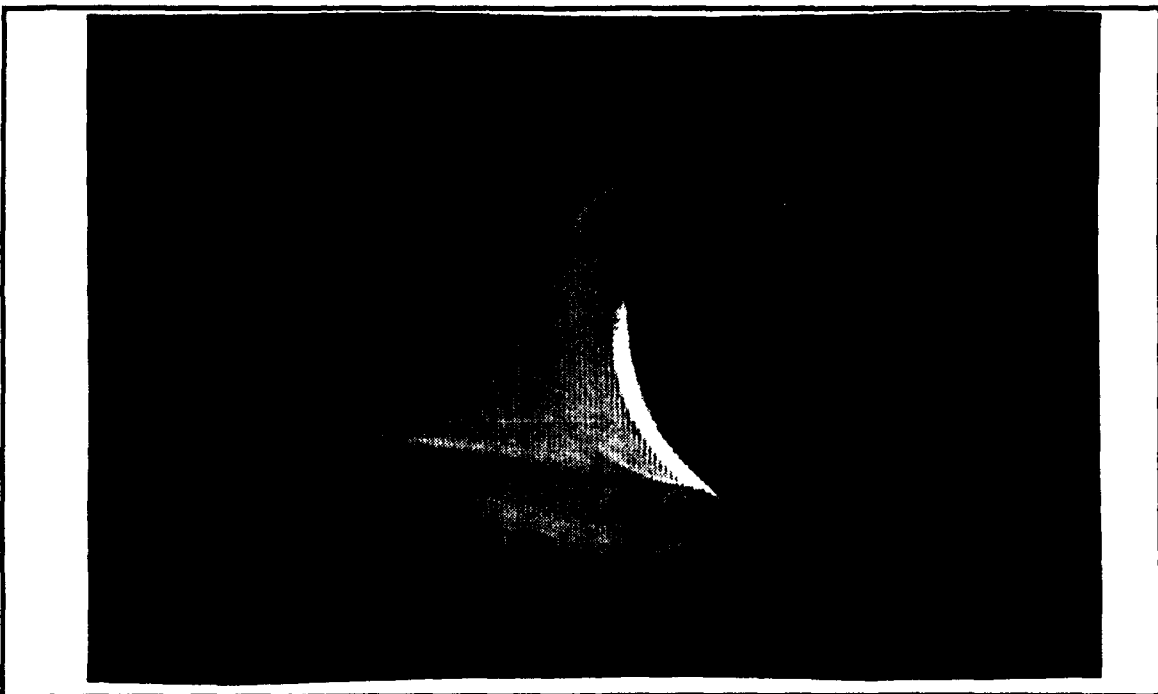


**Figure D7. Vortex Formation Region, Modified Configuration, Vertical Station 5**

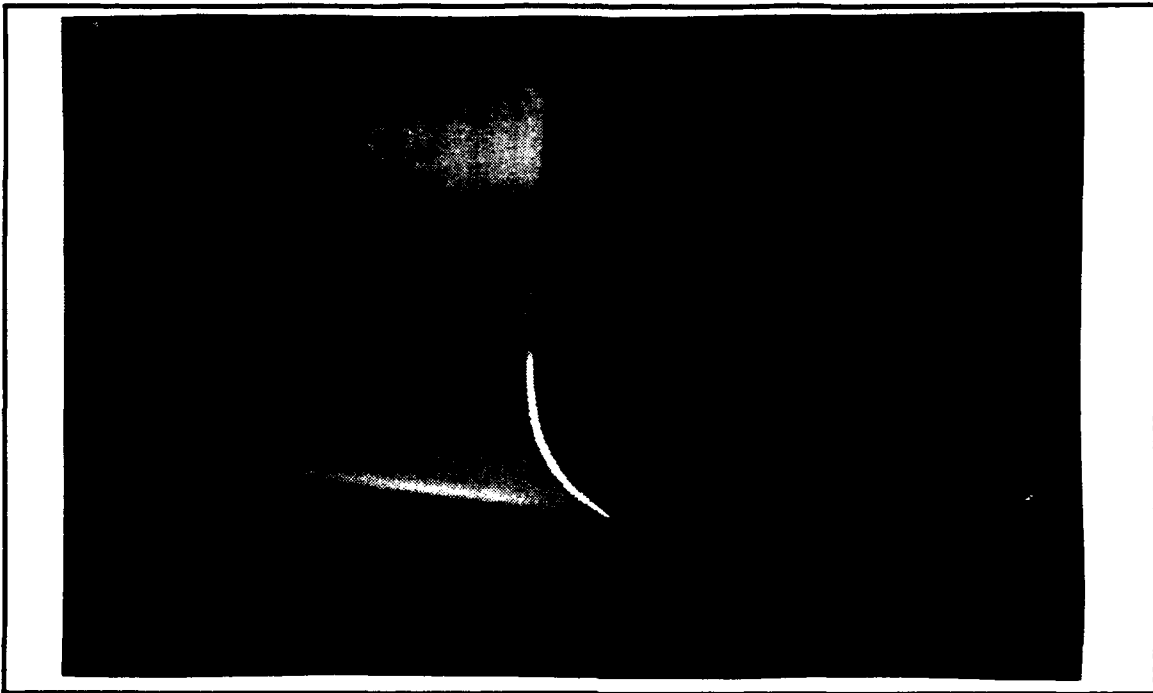


**Figure D8.** Vortex Formation Region, Modified Configuration, Vertical Station 6

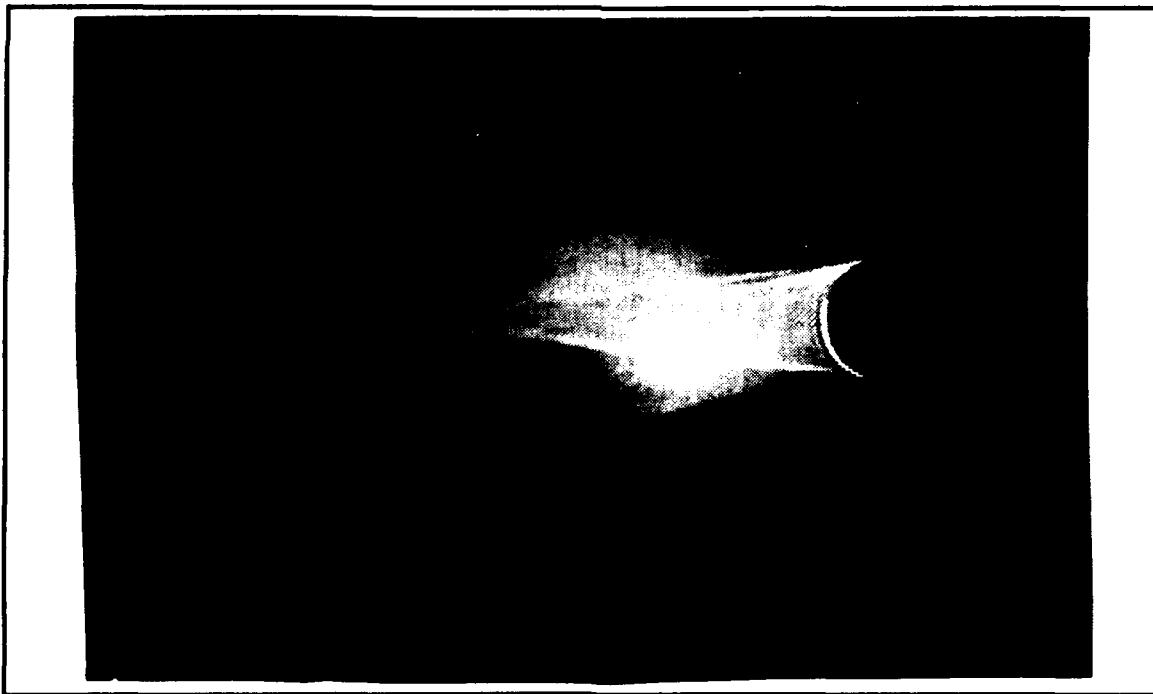


**Figure D9.** Near Wake Region, Modified Configuration, Vertical Station 6



**Figure D10. Near Wake Region, Modified Configuration, Vertical Station 3**



**APPENDIX E**  
**BASE PRESSURE COEFFICIENT PLOTS**

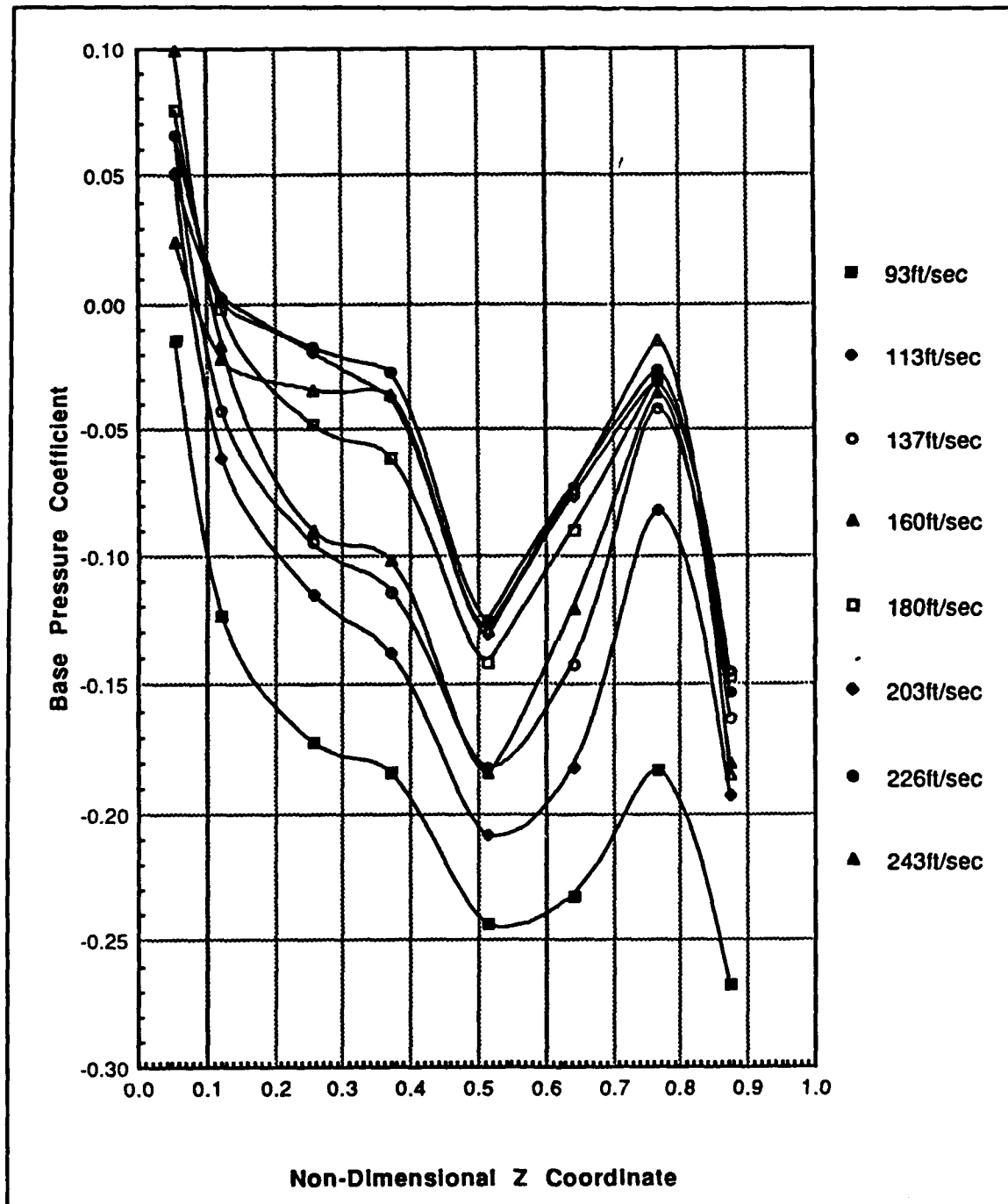


**Figure E1.** Base Pressure Coefficient, Standard Model, Without Boundary Layer Tripping

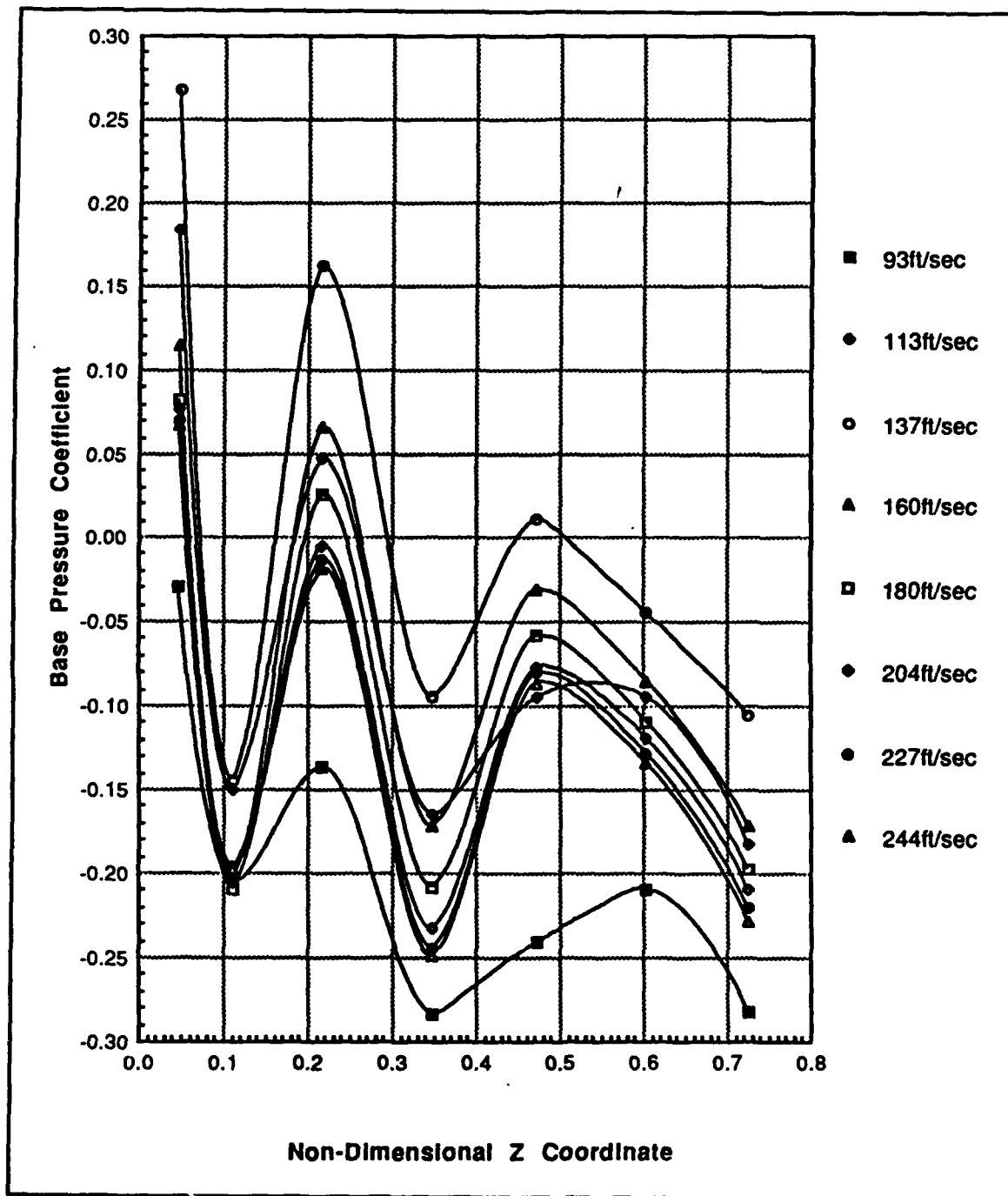


**Figure E2.** Base Pressure Coefficient, Modified Model, Without Boundary Layer Tripping

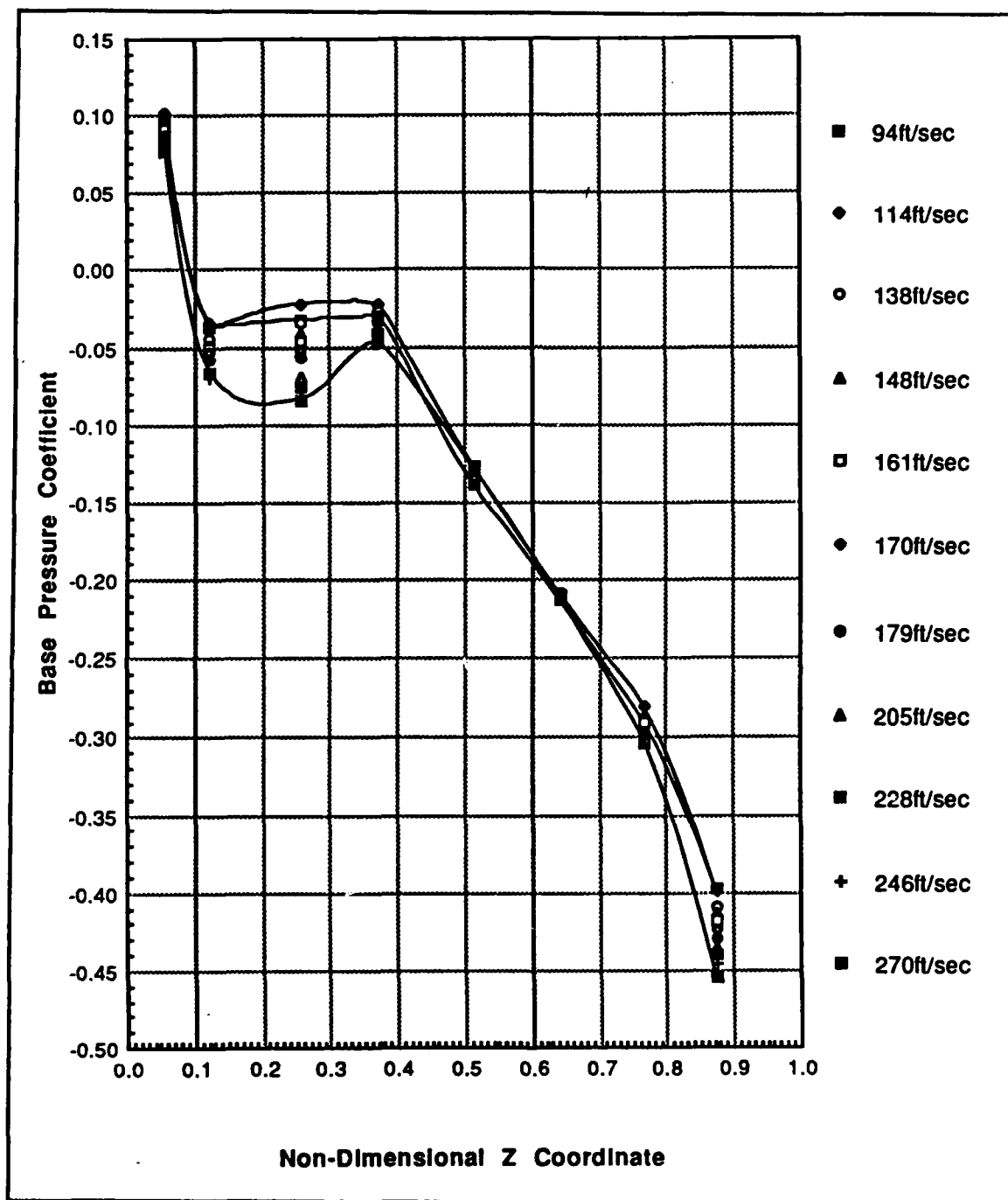


Figure E3. Base Pressure Coefficient, Standard Model, With Boundary Layer Tripping

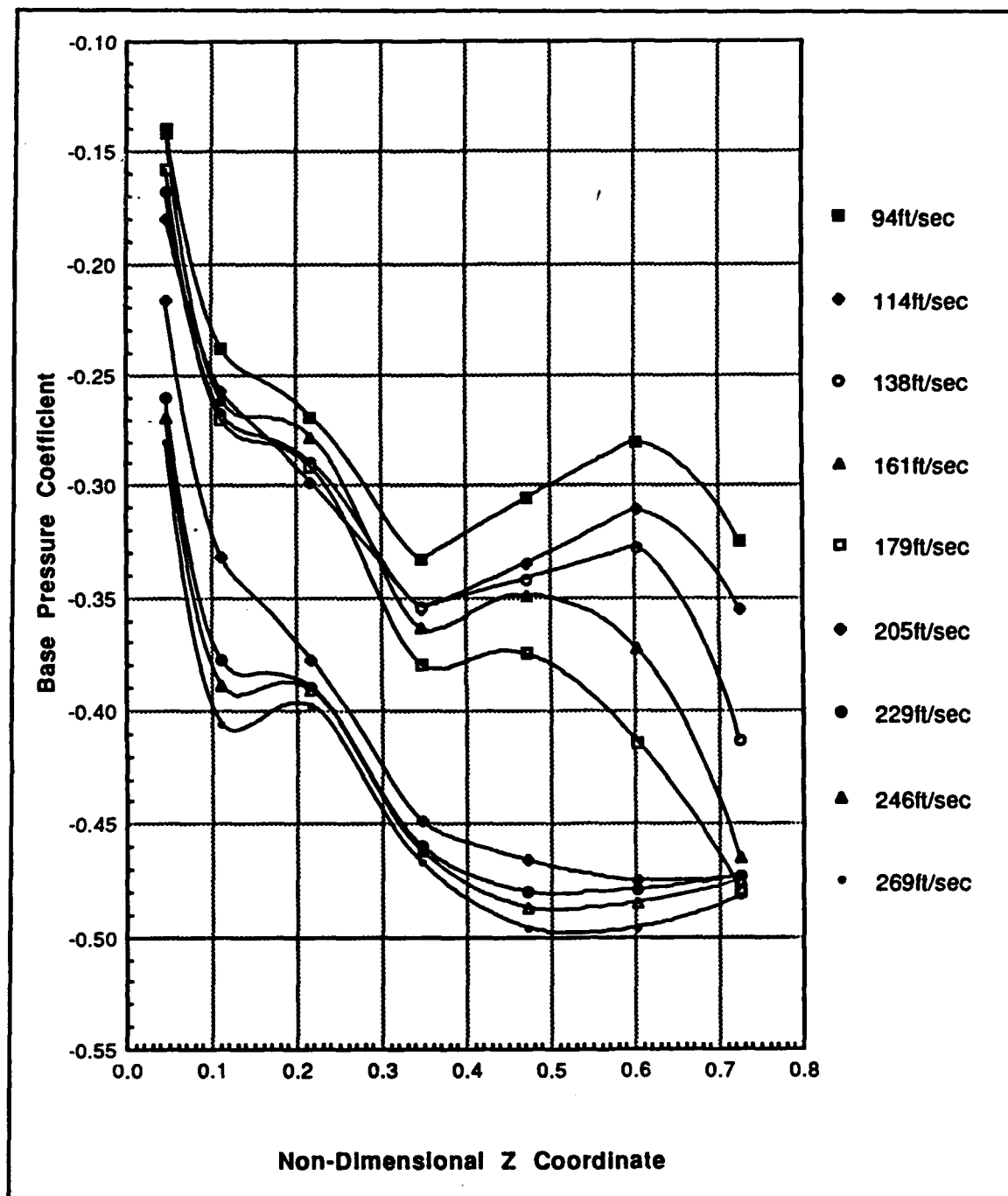
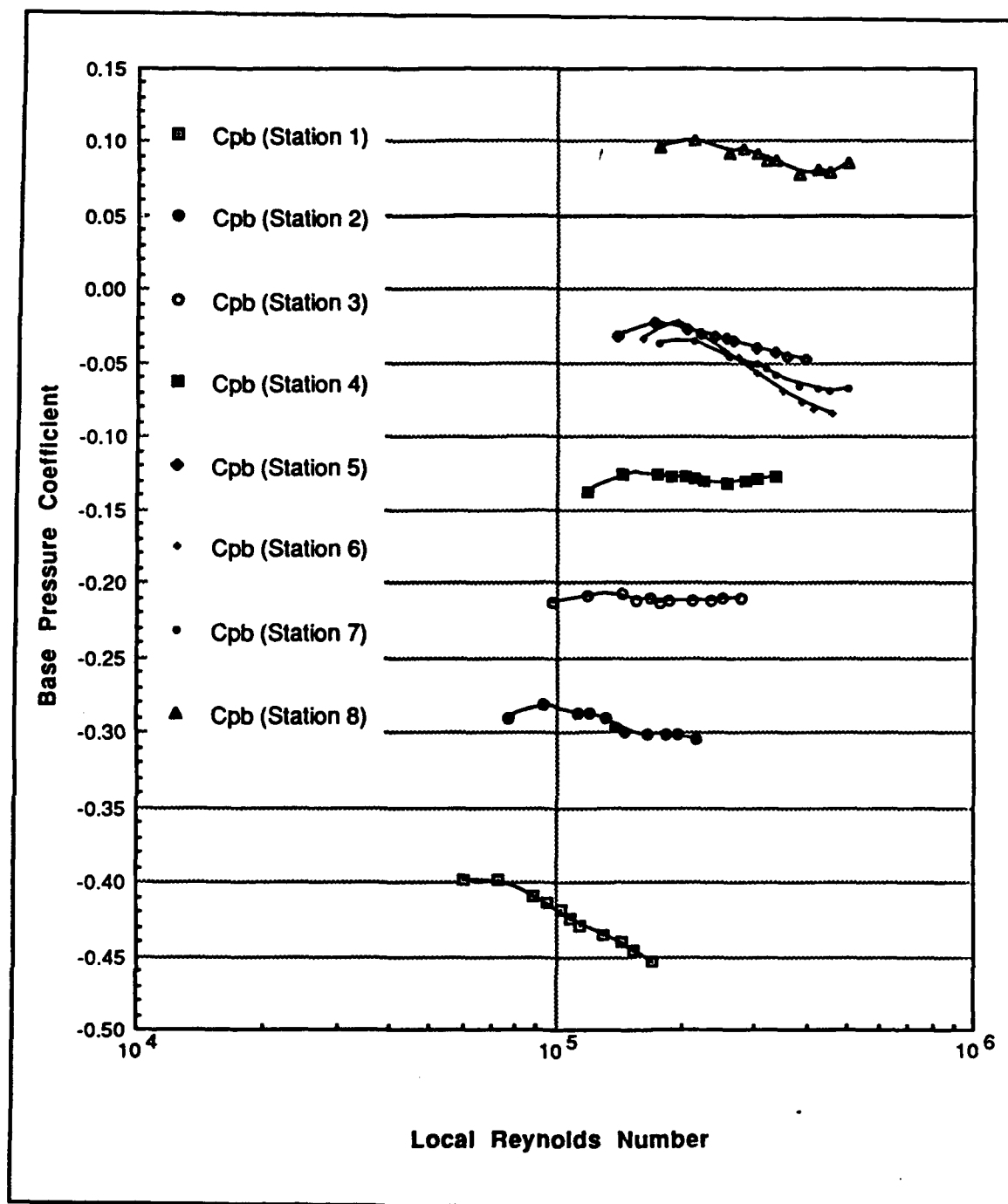
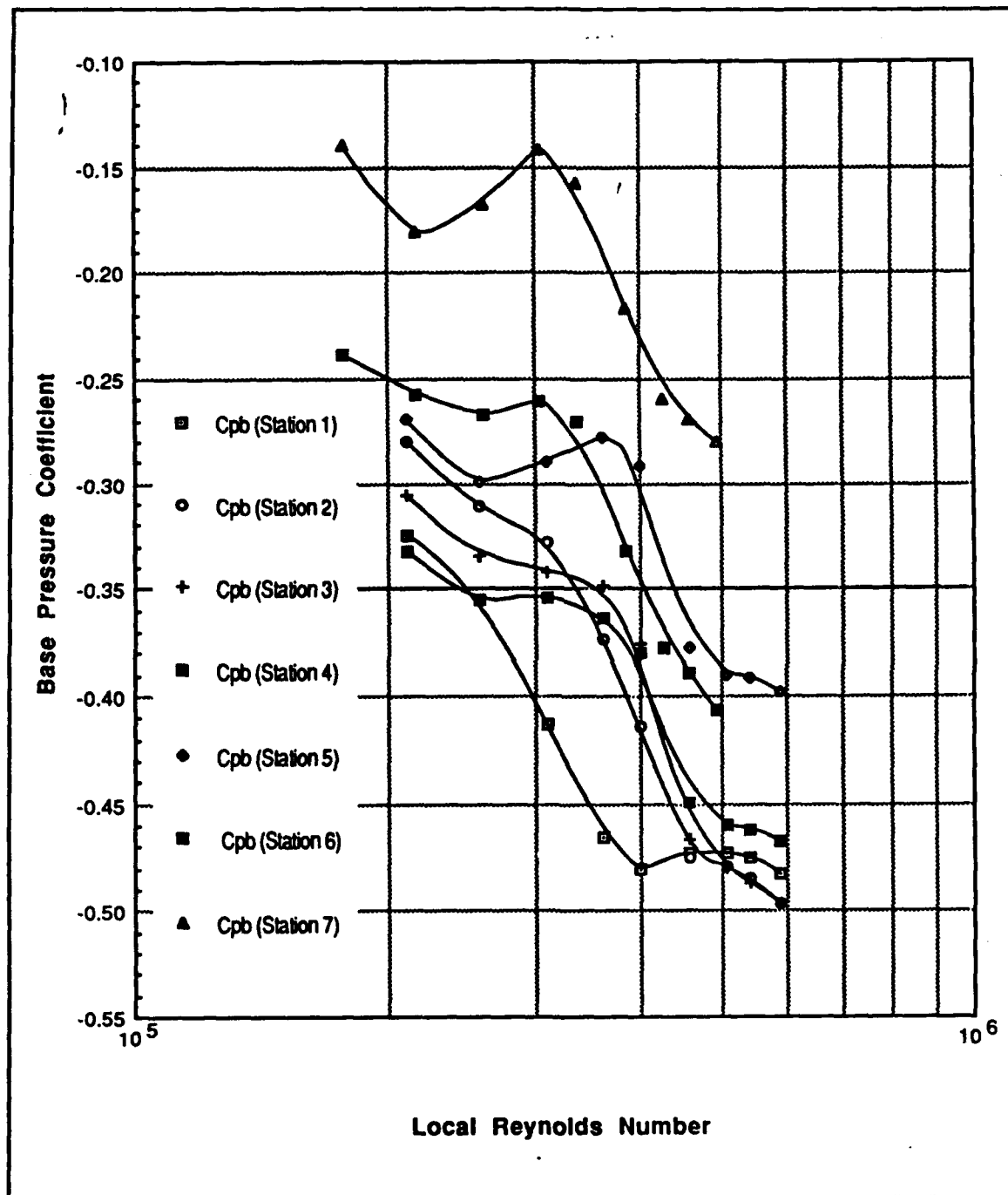


Figure E4. Base Pressure Coefficient, Modified Model, With Boundary Layer Tripping



**Figure E5.** Base Pressure Coefficient vs. Local Reynolds Number, Standard Model, With Boundary Layer Tripping



**Figure E6.** Base Pressure Coefficient vs. Local Reynolds Number, Modified Model, With Boundary Layer Tripping

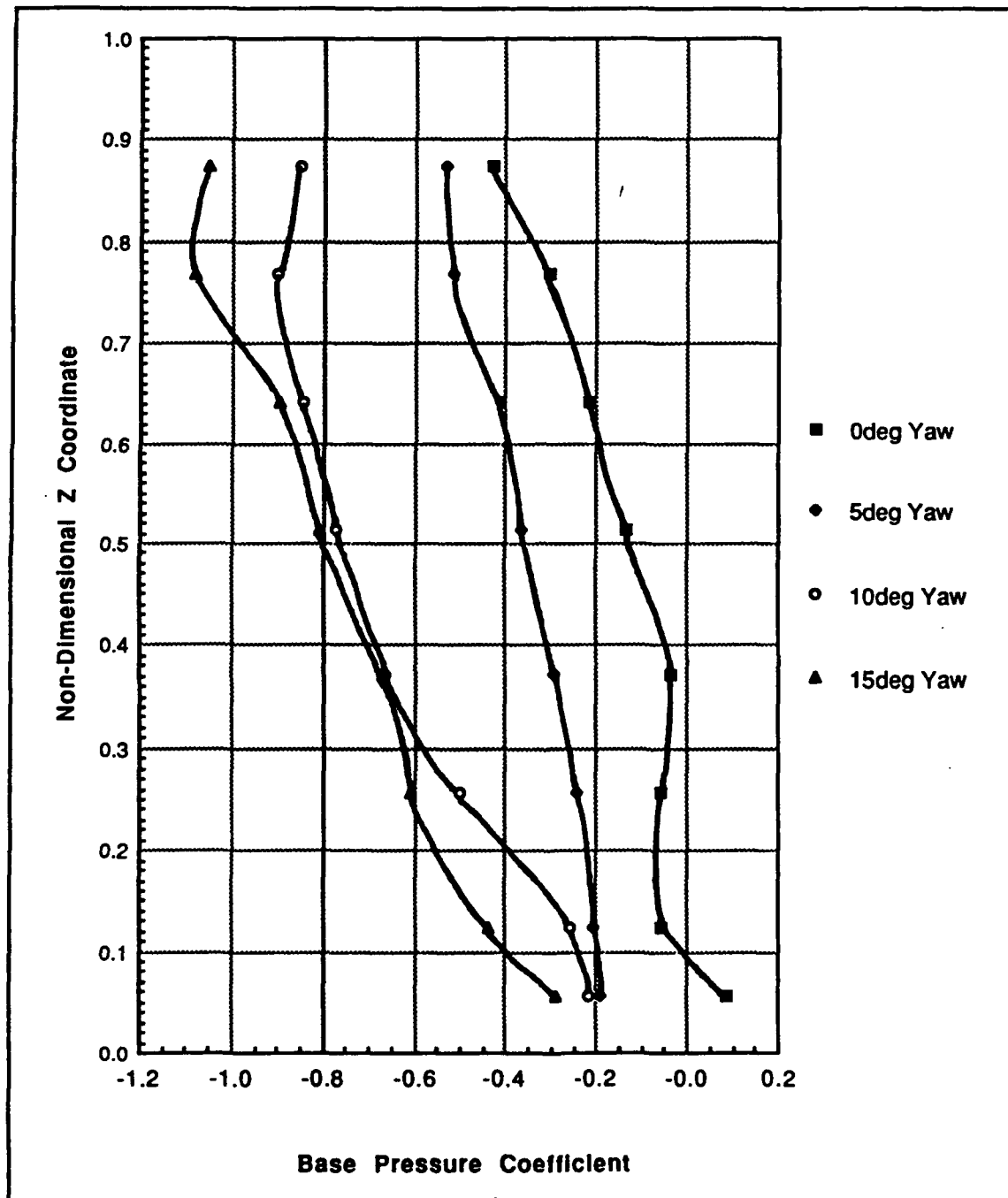


Figure E7. Base Pressure Coefficient Yaw Sensitivity, Standard Model, With Boundary Layer Tripping,  $U_{\infty} = 180\text{ft/sec}$

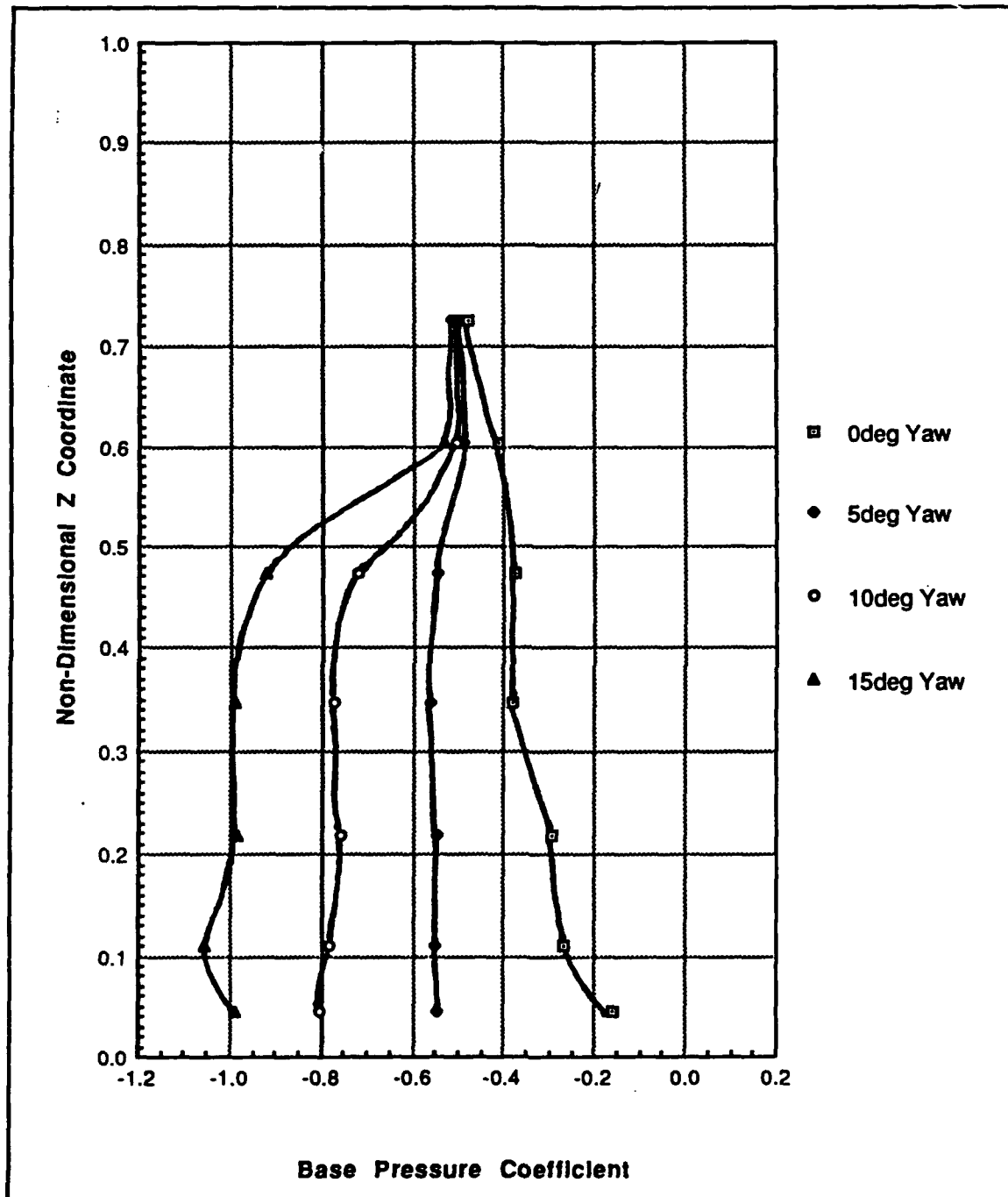


Figure E8. Base Pressure Coefficient Yaw Sensitivity, Modified Model, With Boundary Layer Tripping,  $U_{\infty} = 180\text{ft/sec}$



## BIBLIOGRAPHY

- Achenbach, E., "Vortex Shedding from Spheres," *Journal of Fluid Mechanics*, v. 62, pt. 2, pp. 209-221, 1974.
- Batham, J. P., "Pressure Distributions on Circular Cylinders at Critical Reynolds Numbers," *Journal of Fluid Mechanics*, v. 57, pt. 2, pp. 209-228, 1973.
- Bearman, P. W., "Investigation of the Flow Behind a Two-Dimensional Model with a Blunt Trailing Edge and Fitted with Splitter Plates," *Journal of Fluid Mechanics*, v. 21, pt. 2, pp. 241-255, 1965.
- Bearman, P. W., "On Vortex Shedding from a Circular Cylinder in the Critical Reynolds Number Regime," *Journal of Fluid Mechanics*, v. 37, pt. 3, pp. 577-585, 1969.
- Bearman, P. W., and Graham, J. M. R., "Vortex Shedding from Bluff Bodies in Oscillatory Flow: A Report on Euromech 119," *Journal of Fluid Mechanics*, v. 99, pt. 2, pp. 225-245, 1980.
- Berger, E., and Wille, R., "Periodic Flow Phenomena," *Annual Review of Fluid Mechanics*, v. 4, pp. 313-340, 1972.
- Bishop, R. E. D., and Hassan, A. Y., "The Lift and Drag Forces on a Circular Cylinder in a Flowing Fluid," *Proceedings of the Royal Society, London, Series A*, v. 277, pp. 32-50, 1964.
- Bishop, R. E. D., and Hassan, A. Y., "The Lift and Drag Forces on a Circular Cylinder in a Flowing Fluid," *Proceedings of the Royal Society, London, Series A*, v. 277, pp. 51-75, 1964.
- Buresti, G., and Lanciotti, A., "Vortex Shedding from Smooth and Roughened Cylinders in Cross-flow Near a Plane Surface," *Aeronautical Quarterly*, v. 30, pp. 305-321, 1979.
- Calvert, J. R., "Experiments on the Low-Speed Flow Past Cones," *Journal of Fluid Mechanics*, v. 27, pt. 2, pp. 273-289, 1967.
- Cantwell, B. J., *A Flying Hot Wire Study of the Turbulent Near Wake of a Circular Cylinder at a Reynolds Number of 140,000*, Ph.D. Thesis, California Institute of Technology, October 3, 1975.
- Chen, C. J., Chen, and Holly, F. M., Jr., ed., *Turbulence Measurements and Flow Modeling*, Hemisphere Publishing Corporation, 1987.
- Chlebanowski, J. S., *Flow Visualization by Laser Sheet*, Master's Thesis, Naval Postgraduate School, Monterey, California, March 1988.

- Doremus, G. J., *Flow Field Measurements Using Hotwire Anemometry*, Master's Thesis, Naval Postgraduate School, Monterey, California, September 1987.
- Fiedler, H. E., and Wille, R., "Some Observations in the Near Wake of Blunt Bodies," *AIAA Journal*, v. 8, no. 6, pp. 1140-1141, 1970.
- Fox, M., *Effects of Oscillation Frequency and Amplitude on Separation in an Unsteady Turbulent Flow*, Master's Thesis, Naval Postgraduate School, Monterey, California, September 1980.
- Frost, W., and Moulden, T. H., ed., *Handbook of Turbulence, Volume 1, Fundamentals and Applications*, Plenum Press, 1977.
- Gaster, M., "Vortex Shedding from Slender Cones at Low Reynolds Numbers," *Journal of Fluid Mechanics*, v. 38, pt. 3, pp. 565-576, 1969.
- Gerrard, J. H., "An Experimental Investigation of the Oscillating Lift and Drag of a Circular Cylinder Shedding Turbulent Wakes," *Journal of Fluid Mechanics*, v. 11, pt. 2, pp. 244-257, 1961.
- Griffin, O. M., "The Unsteady Wake of an Oscillating Cylinder at Low Reynolds Number," *Transactions of the American Society of Mechanical Engineers Journal of Applied Mechanics*, v. 38, pp. 729-738, 1971.
- Griffin, O. M., and Koopman, G. H., "The Vortex-Excited Lift and Reaction Forces on Resonantly Vibrating Cylinders," *Journal of Sound and Vibration*, v. 54, pt. 3, pp. 435-448, 1977.
- Griffin, O. M., Skop, R. A., and Koopman, G. H., "The Vortex-Excited Resonant Vibrations of Circular Cylinders," *Journal of Sound and Vibration*, v. 31, pt. 2, pp. 235-249, 1973.
- Harsha, P. T., and Lee, S. C., "Correlations Between Turbulent Shear Stress and Turbulent Kinetic Energy," *AIAA Journal*, v. 8, no. 8, pp. 1508-1510, 1970.
- Hebbbar, K. S., "Mean and Turbulence Measurements in the Boundary Layer and Wake of a Symmetric Airfoil," *Experiments in Fluids*, v. 4, pp. 214-222, 1986.
- Humphreys, J. S., "On a Circular Cylinder in a Steady Wind at Transition Reynolds Numbers," *Journal of Fluid Mechanics*, v. 9, pt. 4, pp. 603-612, 1960.
- Hussaini, M. Y., and Salas, M. D., ed., *Studies of Vortex Dominated Flows*, Proceedings of the Symposium on Vortex Dominated Flows, July 9-11, 1985, NASA Langley Research Center, Hampton, Virginia, Springer-Verlag, 1987.
- Iwan, W. D., "The Vortex Induced Oscillation of Elastic Structural Elements," *Transactions of the ASME Journal of Engineering for Industry*, v. 97, no. 4, pp. 1378-1382, 1975.
- Iwan, W. D., and Blevins, R. D., "A Model for Vortex Induced Oscillation of Structures," *Transactions of the ASME Journal of Applied Mechanics*, v. 41, no. 3, pp. 581-586, 1974.

- Kurosaka, M., and others, "Energy Separation in a Vortex Street," *Journal of Fluid Mechanics*, v. 178, pp. 1-29, 1987.
- Leedy, D. H., *An Experimental Investigation of a Fighter Aircraft Model at High Angles of Attack*, Master's Thesis, Naval Postgraduate School, Monterey, California, September 1988.
- Lewis, R. I., "Surface Vorticity Modelling of Separated Flows from Two-dimensional Bluff Bodies of Arbitrary Shape," *Journal of Mechanical Engineering Science*, v. 23, no. 1, pp. 1-12, 1981.
- Lung, M.-H., *Flowfield Measurements in the Vortex Wake of a Missile at High Angle of Attack in Turbulence*, Master's Thesis, Naval Postgraduate School, Monterey, California, December 1988.
- Mair, W. A., and Maull, D. J., "Bluff Bodies and Vortex Shedding - A Report on Euromech 17," *Journal of Fluid Mechanics*, v. 45, pt. 2, pp. 209-224, 1971.
- Marris, A. W., "A Review of Vortex Streets, Periodic Wakes, and Induced Vibration Phenomena," *Transactions of the ASME Journal of Basic Engineering*, v. 86, pp. 185-193, 1964.
- NACA Report 1191, *On the Development of Turbulent Wakes from Vortex Streets*, by A. Roshko, 1954.
- NACA Technical Note 3169, *On the Drag and Shedding Frequency of Two-Dimensional Bluff Bodies*, by A. Roshko, 1954.
- NASA Technical Report TR R-300, *Aerodynamic Forces on a Stationary and Oscillating Circular Cylinder at High Reynolds Numbers*, by G.W. Jones, Jr., J. J. Cincotta, and R. W. Walker, 1969.
- Naval Postgraduate School Report NPS-69SL79011, *A Discrete Vortex Analysis of Flow About Stationary and Transversely Oscillating Circular Cylinders*, by T. Sarpkaya and R. L. Shoaff, January 1979.
- Oberkampf, W. L., Owen, F. K., and Shivananda, T. P., "Experimental Investigation of the Asymmetric Body Vortex Wake," *AIAA Journal*, v. 19, no. 8, pp. 1025-1032, 1981.
- Perry, A. E., Chong, M. S., and Lim, T. T., "The Vortex Shedding Process Behind Two-Dimensional Bluff Bodies," *Journal of Fluid Mechanics*, v. 116, pp. 77-90, 1982.
- Prasad, J. K., and Gupta, A. K., "Velocity Correlation Structure in the Turbulent Near Wakes of Bluff Bodies," *AIAA Journal*, v. 15, no. 9, pp. 1569-1574, 1977.
- Roshko, A., "Experiments on the Flow Past a Cylinder at Very High Reynolds Number," *Journal of Fluid Mechanics*, v. 10, pp. 345-356, 1960.
- Sarpkaya, T., "In-Line and Transverse Forces on Cylinders in Oscillatory Flow at High Reynolds Numbers," *Journal of Ship Research*, v. 21, no. 4, pp. 200-216, 1977.

- Sarpkaya, T., "Vortex-Induced Oscillations - A Selective Review," *Transactions of the ASME Journal of Applied Mechanics*, v. 46, no. 2, pp. 241-258, 1979.
- Simmons, J. E. L., "Phase Angle Measurements Between Hot-Wire Signals in the Turbulent Wake of a Two-Dimensional Bluff Body," *Journal of Fluid Mechanics*, v. 64, pp. 599-609, 1974.
- Simmons, J. E. L., "Similarities Between Two-Dimensional and Axisymmetric Vortex Wakes," *Aeronautical Quarterly*, v. 28, pp. 15-20, 1977.
- Sommers, J. D., *An Experimental Investigation of Support Strut Interference on a Three-Percent Fighter Model at High Angles of Attack*, Master's Thesis, Naval Postgraduate School, Monterey, California, September 1989.
- Stansby, P. K., "Base Pressure of Oscillating Circular Cylinders," *Journal of Engineering Mechanics Division ASCE*, v. 102, no. EM4, pp. 591-600, 1976.
- Strickland, J. H., Matty, R. R., and Barton, G. H., "Vortex Shedding from Square Plates Perpendicular to a Ground Plane," *AIAA Journal*, v. 18, no. 6, pp. 715-716, 1980.
- Sullerey, R. K., Gupta, A. K., and Moorthy, C. S., "Similarity in the Turbulent Near Wake of Bluff Bodies," *AIAA Journal*, v. 13, no. 11, pp. 1425-1429, 1975.
- Taneda, S., "Experimental Investigation of Vortex Streets," *Journal of the Physical Society of Japan*, v. 20, no. 9, pp. 1714-1716, 1965.
- Tournier, C., and Py, B., "The behaviour of Naturally Oscillating Three-Dimensional Flow Around a Cylinder," *Journal of Fluid Mechanics*, v. 85, pt. 1, pp. 161-186, 1978.
- Wlezien, R. W., and Way, J. L., "Techniques for the Experimental Investigation of the Near Wake of a Circular Cylinder," *AIAA Journal*, v. 17, no. 6, pp. 563-570, 1979.

## INITIAL DISTRIBUTION LIST

- |    |   |   |
|----|---|---|
| 1. | Defense Technical Information Center<br>Cameron Station<br>Alexandria, Virginia 22304-6145  | 2 |
| 2. | Library, Code 52<br>Naval Postgraduate School<br>Monterey, California 93943-5100  | 2 |
| 3. | Professor S. K. Hebbar, Code AA/Hb<br>Department of Aeronautics and Astronautics<br>Naval Postgraduate School<br>Monterey, California 93943-5000  | 3 |
| 4. | E. R. Wood, Chairman<br>Department of Aeronautics and Astronautics<br>Naval Postgraduate School<br>Monterey, California 93943-5000                | 1 |
| 5. | Professor M. F. Platzer, Code AA/Pl<br>Department of Aeronautics and Astronautics<br>Naval Postgraduate School<br>Monterey, California 93943-5000 | 1 |
| 6. | LCDR J. F. Small<br>c/o Woods<br>166 Duval Lane<br>Edgewater, Maryland 21037  | 2 |
| 7. | Commander, Naval Air Systems Command (AIR-546D3B)<br>Washington, D. C. 20361-9320   | 1 |
| 8. | Commander, Naval Air Systems Comand (PMA-240F)<br>Washington, D. C. 20361-9320  | 1 |

- |      |  |   |
|------|--|---|
| 9.   | Director, Force Warfare Aircraft Test Directorate<br>Naval Air Test Center<br>Patuxent River, Maryland 20670-5304<br>Attn: VP Program Office | 1 |
| <br> |  |   |
| 10.  | P-3 Program Office<br>Naval Air Development Center<br>Warminster, Pennsylvania 18974-5000<br>Attn: Mr. C. Rosso                              | 1 |